

Abstract

Title of Dissertation: Computational Investigation of Micro-Scale
Coaxial Rotor Aerodynamics in Hover

Vinod K. Lakshminarayan, Doctor of Philosophy, 2009

Dissertation directed by: Dr. James D. Baeder
Department of Aerospace Engineering

In this work, a compressible Reynolds-Averaged Navier Stokes (RANS) solver is extended to investigate the aerodynamics of a micro-scale coaxial rotor configuration in hover. This required the following modifications to the solver: implementation of a time-accurate low Mach preconditioner, implementation of a sliding mesh interface boundary condition, improvements in the grid connectivity and parallelization of the code.

First, an extensive validation study on the prediction capability of the solver is performed on a hovering micro-scale single rotor, for which performance data and wake characteristics have been measured experimentally. The thrust and power are reasonably well predicted for different leading and trailing geometries. Blunt leading edge geometries show poorer performance compared to the sharp leading edge geometries; the simulations show that this is mainly because of the large pressure drag acting at the blunt front. The tip vortex trajectory and velocity profiles are also well captured. The predicted swirl velocities in the wake

for the micro-rotor are found to be significantly larger as compared to those for a full-scale rotor, which could be one of the reasons for additional power loss in the smaller scale rotors. The use of twist and taper is studied computationally and is seen to improve the performance of micro-rotor blades.

Next, the solver is applied to simulate the aerodynamics of a full-scale coaxial rotor configuration in hover, for which performance data is available from experiments. The global quantities such as thrust and power are predicted reasonably well. In the torque trimmed situation, the top rotor shares significant percentage of the total thrust at lower thrust levels, which decreases to about 55% of the total thrust at higher thrust values. The simulations reveal that the interaction between the rotor systems is seen to generate significant impulses in the instantaneous thrust and power. The characteristic signature of this impulse is explained in terms of the blade thickness effect and loading effect, as well as blade-vortex interactions for the bottom rotor (wake effect).

Finally, the RANS solver is applied to investigate the aerodynamics of a micro-scale coaxial rotor configuration in hover. The overall performance is well predicted. The interaction between the rotor systems is again seen to generate 3–8% fluctuation in the instantaneous thrust and power. The wake effect in the simulation is seen to be very prominent and the phasing of the impingement of the tip vortex from the top rotor upon the bottom rotor plays a significant role in the amount of unsteadiness on the bottom rotor. Interaction of the top rotor vortex and inboard sheet with the bottom rotor results in significant shedding on the bottom rotor blade, and this is believed to be caused by the of sharp leading edge geometry. Significant blade-vortex and vortex-vortex interactions are observed for coaxial systems.

Computational Investigation of Micro-Scale Coaxial Rotor Aerodynamics in Hover

by

Vinod K. Lakshminarayan

Dissertation submitted to the Faculty of the Graduate School of the
University of Maryland at College Park in partial fulfillment
of the requirements for the degree of
Doctor of Philosophy
2009

Advisory Committee:

Dr. James D. Baeder, Chairman/Advisor
Dr. J. Gordon Leishman
Dr. Inderjit Chopra
Dr. Darryll Pines
Dr. Ramani Duraiswami, Dean's Representative

© Copyright by
Vinod K. Lakshminarayan
2009

Dedication

This dissertation is dedicated to my late grandmother for all her
care and support throughout my life.

Acknowledgements

I express my deepest gratitude to my thesis advisor Dr. James D. Baeder for making this work possible. Dr. Baeder, with his unique style of guidance saw me through every aspect of this work and kept me focused to finish this work, while inspiring me to work on many other topics. I would like to thank him for the freedom he allowed in the course of this investigation. It is a pleasure and honor being his student.

I would like to thank Karthik for his guidance that helped me get started with my work. He has provided many insightful suggestions and has been my inspiring role-model throughout these years. I am also grateful to Mani, Shreyas and Brad, for the help they provided in my research and would also like to acknowledge the members of my doctoral committee for their comments and suggestions that helped improve the quality of work.

I have the greatest sense of appreciation to my friends and colleagues Asitav and Arun for their help and company from the days of my undergrad. I would also like to appreciate Brandon, Moble, Ayan, Nitin and Vikram for making the past four and a half years so enjoyable.

Finally, this acknowledgment will not be complete without the mention of my late grandmother. No words are sufficient to describe her tender care, deep love and support. She holds a very special place in my heart. This thesis work is dedicated to her.

Table of Contents

List of Tables	ix
List of Figures	xi
Nomenclature	xxi
1 Introduction	1
1.1 Micro Air Vehicles	1
1.1.1 Current Capabilities of Rotary-Wing MAVs	3
1.1.2 Limitations of Current Rotary-Wing Designs	3
1.2 Previous Work	6
1.2.1 Low Reynolds Number Aerodynamics	7
1.2.2 Rotary-Wing Tip Vortex Studies	11
1.3 Rotary MAV Conceptual Designs	14
1.4 Coaxial Rotors	16
1.5 Previous Studies on Coaxial Rotors	18
1.5.1 Experimental Studies	19
1.5.2 Computational Studies	19
1.6 Motivation	21

1.7	Objectives	23
1.8	Contributions of the Thesis	25
1.9	Scope and Organization of the Thesis	26
2	Computational Methodology	28
2.1	Flow Domain	28
2.2	Mesh Generation	30
2.2.1	Connectivity Approach (Baseline Methodology)	32
2.3	The Flow and its Mathematical Description	36
2.3.1	Navier-Stokes Equations	36
2.3.2	Reynolds Averaged Navier-Stokes Equations	44
2.3.3	Initial and Boundary Conditions	46
2.4	Numerical Solution (Baseline Algorithm)	47
2.4.1	Inviscid Terms	48
2.4.2	Viscous Terms	50
2.4.3	Time Integration	51
2.4.4	Turbulence Modeling	55
2.4.5	Boundary Conditions	57
2.5	Limitations of Current Methodology	60
2.6	Improvements	63
2.6.1	Low Mach Preconditioning	65
2.6.2	Sliding Mesh Boundary Condition	72
2.6.3	Improvements in Grid Connectivity	73
2.6.4	Parallelization	77
2.7	Summary	80

3	Verification and Validation	81
3.1	Low Mach Preconditioning	82
3.1.1	Convection of a 2D Isentropic Vortex	82
3.1.2	Steady Low Speed Flow Over 2D Airfoil	89
3.1.3	Low Speed Fixed-Wing Validation	91
3.2	Grid Connectivity	96
3.2.1	Conventional Hole-cutting versus Implicit Hole-cutting	96
3.2.2	Verification of Improved Blanking Technique	96
3.3	Full-Scale Single Rotor Validation	106
3.4	Summary	110
4	Computational Investigation of Micro-Scale Single Rotor Aerodynamics in Hover	111
4.1	Rotor Configuration	111
4.2	Mesh System	115
4.3	Performance Comparison	117
4.4	Blade Surface Streamlines	119
4.5	Spanwise Loading Distributions	123
4.6	Blade Pressure Distributions	127
4.7	Two-Dimensional Analysis	133
4.8	Sectional Flow Contours	136
4.9	Flow-field Visualizations	144
4.10	Wake Trajectory	150
4.11	Vortex Structure Comparison	153
4.12	Average Velocity Profiles in Wake	157

4.13	Effect of Twist and Taper	161
4.14	Summary	165
5	Computational Investigation of Full Scale Coaxial Rotor Aero-	
	dynamics in Hover	168
5.1	Rotor Configuration	168
5.2	Mesh System	169
5.3	Trimming Procedure	172
5.4	Performance Comparison	175
	5.4.1 Mean Performance	175
	5.4.2 Unsteady Performance	177
5.5	Effect of Rotor Spacing	191
5.6	Wake Trajectory	197
5.7	Flow-field Visualization	199
5.8	Summary	200
6	Computational Investigation of Micro-Scale Coaxial Rotor Aero-	
	dynamics in Hover	206
6.1	Rotor Configuration	206
6.2	Mesh System	207
6.3	Effect of RPM	208
6.4	Effect of rotor spacing	211
	6.4.1 Mean Performance	211
	6.4.2 Unsteady Performance	212
	6.4.3 Effect of Top Rotor Wake on Bottom Rotor	218
	6.4.4 Wake Trajectory	227

6.4.5	Flow-field Visualization	230
6.5	Summary	231
7	Conclusions	238
7.1	Summary	239
7.2	Observations	240
7.2.1	CFD Methodology	240
7.2.2	Micro-Scale Single Rotor	242
7.2.3	Full-Scale Coaxial Rotor	245
7.2.4	Micro-Scale Coaxial Rotor	246
7.3	Recommendations	249
7.4	Future Work	250
	Bibliography	252

List of Tables

1.1	Relative performance of various MAVs.	3
2.1	Limitations of baseline methodology and improvements made in the current work to overcome these limitations.	64
3.1	Comparison of coefficient of forces for NACA 0006 airfoil at different Mach numbers, with and without low Mach preconditioning	89
3.2	Comparison of coefficient of forces for NACA 0012 airfoil using different blanking techniques.	105
5.1	Trim collective settings for the top and bottom rotors of full-scale coaxial system.	174
5.2	Computed mean thrust coefficient for full-scale coaxial system. . .	175
5.3	Computed mean power coefficient for full-scale coaxial system. . .	176
5.4	Computed RMS fluctuation of thrust coefficient for full-scale coaxial system.	178
5.5	Computed RMS fluctuation of power coefficient for full-scale coaxial system.	179
5.6	Effect of rotor spacing for full-scale coaxial system (case 7).	194
6.1	Computed mean torque coefficient for micro-scale coaxial system.	212

6.2	Computed mean thrust coefficient for micro-scale coaxial system.	212
6.3	Computed RMS fluctuation of power coefficient for micro-scale coaxial system.	213
6.4	Computed RMS fluctuation of thrust coefficient for micro-scale coaxial system.	213

List of Figures

1.1	Mass vs Reynolds number for animals and man-made vehicles [2].	6
1.2	University of Maryland “Giant” [41].	14
1.3	University of Maryland “TiShrov” [42].	15
1.4	University of Maryland Micor [2].	16
1.5	Kamov Ka-50 [47].	17
2.1	Sample hyperbolic mesh.	31
2.2	Near body C-O mesh at the blade root and tip.	32
2.3	Sample background mesh.	33
2.4	Schematic of hole cutting. Red circles: Hole points. Blue circles: Hole fringe points. Black circles: Chimera boundary points. . . .	34
2.5	Sample overset grid in a hovering rotor simulation. Red: Blade mesh, Green: Background mesh.	35
2.6	Schematic showing computational cell.	48
2.7	Schematic of one dimensional piecewise reconstruction.	49
2.8	C-mesh topology.	57
2.9	Schematic of point-sink boundary condition.	59
2.10	Schematic of the mesh system and the boundary condition for a 2-bladed coaxial rotor.	73

2.11	Sample domain partitioning for parallel computation.	78
3.1	Computational domain and initial pressure contours for isentropic vortex convection.	84
3.2	Comparison of residual convergence for $M_\infty = 0.0845$ for isen- tropic vortex convection.	86
3.3	Comparison of residual convergence for $M_\infty = 0.000845$ for isen- tropic vortex convection.	87
3.4	Vertical velocity profile along $y = 5$ line at $t = 10$ for isentropic vortex convection.	88
3.5	Pressure contours for flow over NACA 0006 airfoil at $M = 0.05$. . .	90
3.6	Comparison of residue with and without the use of precondition- ing for flow over NACA 0006 airfoil at $M = 0.05$	90
3.7	Computational mesh used for validation with Zuhail experiments [86]	92
3.8	Swirl and axial velocity profile comparison with experimental data [86] at $x/c = 1$, $Re = 9040$	94
3.9	Swirl and axial velocity profile with experimental data [86] at $x/c = 4$, $Re = 9040$	95
3.10	Comparison of grid connectivity in 2D using a fine background mesh.	97
3.11	Comparison of grid connectivity in 2D using a coarse background mesh.	98
3.12	Mesh system used for verification of new blanking technique. . . .	99
3.13	Connectivity using baseline implicit hole-cutting methodology. blue: fringe points of background mesh; black: fringe points of airfoil mesh; green: field points of background mesh.	101

3.14	Comparison of pressure contours for single mesh and two mesh system using baseline implicit hole-cutting. black: single mesh system; red line: airfoil mesh, green line: background mesh.	101
3.15	Connectivity obtained by manually removing fringe points from baseline IHC methodology. blue: fringe points of background mesh; black: fringe points of airfoil mesh; green: field points of background mesh.	102
3.16	Comparison of pressure contours for single mesh and two mesh system using smaller fringe layer thickness and no <i>iblack</i> array. black line: single mesh; red line: airfoil mesh, green line: background mesh.	102
3.17	Comparison of pressure contours for single mesh and two mesh system using smaller fringe layer thickness and <i>iblack</i> = 0 for fringe points. black line: single mesh; red line: airfoil mesh, green line: background mesh.	103
3.18	Comparison of pressure contours for single mesh and two mesh system using smaller fringe layer thickness and <i>iblack</i> = 1 for fringe points. black line: single mesh; red line: airfoil mesh, green line: background mesh.	104
3.19	Comparison of pressure contours for single mesh and two mesh system using smaller fringe layer thickness and <i>iblack</i> = -1 for fringe points. black line: single mesh; red line: airfoil mesh, green line: background mesh.	105
3.20	Computational mesh for Harrington single rotor-2 [49].	107
3.21	Performance comparison for Harrington single rotor-2 [49].	108

3.22	Performance comparison for Harrington single rotor-2 [49] with old hole-cutting method and old blanking technique.	109
4.1	Computational sectional profiles for micro-scale single rotor. . . .	113
4.2	C-mesh near sharp leading edge and blunt trailing edge.	114
4.3	Computational mesh for micro-scale single rotor calculation. . . .	116
4.4	Performance comparison (C_T vs C_Q) with experimental data [29] for micro-scale single rotor.	118
4.5	Performance comparison (FM vs C_T) with experimental data [29] for micro-scale single rotor.	119
4.6	Blade surface streamlines for various geometries at 12° collective setting, micro-scale single rotor.	121
4.7	Spanwise thrust and power distributions for micro-scale single rotor, 12° collective setting.	124
4.8	Sectional L/D distributions for BLTE and SLE geometry of micro-scale single rotor, 12° collective setting.	125
4.9	Spanwise distributions of components of power for micro-scale single rotor, 12° collective setting.	126
4.10	Blade pressure distributions at different spanwise location for micro-scale single rotor, 12° collective setting.	128
4.11	Blade pressure distributions at different spanwise location for micro-scale single rotor, 12° collective setting.	131
4.12	2D and 3D pressure distributions for conditions found at $0.6R$ span location for micro-scale single rotor at 12° collective setting.	134
4.13	L/D versus angle of attack for various geometries using 2D calculation.	135

4.14 Eddy Viscosity contours at $0.4R$ for micro-scale single rotor, 12° collective setting.	138
4.15 Eddy Viscosity contours at $0.6R$ for micro-scale single rotor, 12° collective setting.	139
4.16 Eddy Viscosity contours at $0.8R$ for micro-scale single rotor, 12° collective setting.	140
4.17 Eddy Viscosity contours at $0.95R$ for micro-scale single rotor, 12° collective setting.	141
4.18 Radial Velocity contours along with streamlines at $0.4R$ for micro- scale single rotor, 12° collective setting.	142
4.19 Radial Velocity contours along with streamlines at $0.8R$ for micro- scale single rotor, 12° collective setting.	143
4.20 Iso-surfaces of second invariant of velocity magnitude, $q = 8.0$, at 12° collective setting for micro-scale single rotor.	146
4.21 Contours of streamwise vorticity at 12° collective setting for micro- scale single rotor.	147
4.22 Experimental flow visualization [29].	147
4.23 Iso-surfaces of second invariant of velocity magnitude (colored by vorticity magnitude), $q = 1.0$, at 12° collective setting for micro- scale single rotor, BLTE geometry.	148
4.24 Flow-field comparison.	149
4.25 Comparison of wake trajectory with experimental data [29] for BLTE geometry of micro-scale single rotor at 12° collective setting.	151
4.26 Experimental flow visualization [29].	152

4.27	Vortex swirl velocity profile (non-dimensionalized by tip speed) comparison between computational BLTE geometry and experimental baseline geometry [29] for micro-scale single rotor, 12° collective setting.	154
4.28	Vortex axial velocity profile (non-dimensionalized by tip speed) comparison between computational BLTE geometry and experimental baseline geometry [29] for micro-scale single rotor, 12° collective setting.	155
4.29	Tip vortex viscous core radius (a) and Peak tip vortex swirl velocity (b) comparison with experimental data [29] with wake age for micro-scale single rotor.	156
4.30	Average velocities along radial direction at different planes below the rotor for BLTE geometry for micro-scale single rotor, 12° collective setting.	158
4.31	Average velocities along radial direction at different planes below the rotor for full-scale Harrington single rotor-2 [49], $C_T = 0.004$	160
4.32	Performance comparison for various blade twists for micro-scale single rotor, SLTE geometry.	162
4.33	Average inflow velocity along radial direction at different planes below the rotor for micro-scale single rotor, $\theta_{0.75} = 12^\circ$	163
4.34	Blade taper planforms for micro-scale single rotor.	163
4.35	Performance comparison for various blade taper for micro-scale single rotor, SLTE geometry.	164
4.36	Sectional L/D distributions for SLTE and symmetrically tapered blade of micro-scale single rotor, 12° collective setting.	166

5.1	Computational mesh for full-scale coaxial rotor system.	171
5.2	Comparison of performance with experimental data [49] for full-scale coaxial rotor.	177
5.3	Temporal variation of C_T of the top and bottom rotors over one revolution for all cases for full-scale coaxial system.	180
5.4	Temporal variation of C_Q of the top and bottom rotors over one revolution for all cases for full-scale coaxial system.	181
5.5	Schematic of the loading effect in coaxial system.	182
5.6	Temporal variation of C_T and C_Q of the top and bottom rotors over one revolution for full-scale coaxial system (case 1).	183
5.7	Temporal variation of components of power for the top and bottom rotors and thrust sharing over one revolution for full-scale coaxial system (case 3).	184
5.8	Spanwise thrust distribution at different azimuth locations for full-scale coaxial system (case 3).	186
5.9	Sectional thrust ($R\frac{dC_T}{dr}$) contour for full-scale coaxial system (case 3).	187
5.10	Fluctuation in sectional thrust ($R\frac{dC_T}{dr}$) contour for full-scale coaxial system (case 3).	188
5.11	Temporal variation in sectional thrust ($R\frac{dC_T}{dr}$) at selected spanwise locations for the bottom rotor of full-scale coaxial system (case 3).	189
5.12	Fluctuation in sectional thrust ($R\frac{dC_T}{dr}$) contour for full-scale coaxial system (case 7).	190
5.13	Effect of rotor spacing on the thrust for full-scale coaxial system (case 7).	192

5.14	Effect of rotor spacing on the power for full-scale coaxial system (case 7).	193
5.15	Effect of rotor spacing on the frequency distribution of thrust, normalized by the amplitude of 4/rev frequency of the baseline case, for full-scale coaxial system (case 7).	195
5.16	Effect of rotor spacing on the frequency distribution of power, normalized by the amplitude of 4/rev frequency of the baseline case, for full-scale coaxial system (case 7).	196
5.17	Iso-surfaces of the second invariant of vorticity magnitude for full- scale coaxial system (case 7) when the blades are aligned.	197
5.18	Wake trajectory for full-scale coaxial system (case 7) when the blades are aligned.	198
5.19	Vorticity magnitude contours in a fixed plane in space for full- scale coaxial system at different instances in time for full-scale coaxial system (case 7).	202
5.20	Vorticity magnitude contours in a plane that is at 30° azimuth from the top rotor blade at different instances in time for full- scale coaxial system (case 7).	203
5.21	Vorticity magnitude contours in a plane that is at 30° azimuth from the bottom rotor blade at different instances in time for full-scale coaxial system (case 7).	204
5.22	Vorticity magnitude contours in a fixed plane in space for full- scale coaxial system at different instances in time for full-scale coaxial system (case 3).	205
6.1	Computational mesh for micro-scale coaxial rotor system.	209

6.2	Performance comparison with experimental data [2] at different RPM for micro-scale coaxial rotor.	210
6.3	Temporal variation of C_T of the top and bottom rotors over one revolution for various rotor spacing for micro-scale coaxial system.	214
6.4	Temporal variation of C_Q of the top and bottom rotors over one revolution for various rotor spacing for micro-scale coaxial system.	215
6.5	Effect of rotor spacing on the frequency distribution, normalized by the amplitude of 4/rev frequency of the $h/R = 0.268$ case, for micro-scale coaxial system.	218
6.6	Sectional thrust ($R\frac{dC_T}{dr}$) contour for the bottom rotor of micro-scale coaxial system.	219
6.7	Fluctuation in sectional thrust ($R\frac{dC_T}{dr}$) contour for the bottom rotor of micro-scale coaxial system.	220
6.8	Fluctuation in the surface pressure for the $h/R = 0.268$ case of micro-scale coaxial system.	222
6.9	Fluctuation in the surface pressure for the $h/R = 0.446$ case of micro-scale coaxial system.	223
6.10	Fluctuation in the surface pressure for the $h/R = 0.625$ case of micro-scale coaxial system.	224
6.11	Spanwise pressure contour at $r/R = 0.9$ for micro-scale coaxial system.	225
6.12	Spanwise pressure contour at $r/R = 0.55$ for micro-scale coaxial system.	226
6.13	Iso-surfaces of the second invariant of vorticity magnitude ($q = 0.2$) for micro-scale coaxial system when the blades are aligned.	228

6.14	Wake trajectories for various rotor spacing for micro-scale coaxial system when the blades are aligned.	229
6.15	Vorticity magnitude contours in a fixed plane in space at different instances in time for micro-scale coaxial system, $h/R = 0.446$. . .	233
6.16	Vorticity magnitude contours in the plane of the bottom rotor blade at different instances in time for micro-scale coaxial system, $h/R = 0.268$	234
6.17	Vorticity magnitude contours in the plane of the bottom rotor blade at different instances in time for micro-scale coaxial system, $h/R = 0.446$	235
6.18	Vorticity magnitude contours in the plane of the bottom rotor blade at different instances in time for micro-scale coaxial system, $h/R = 0.625$	236
6.19	Vorticity magnitude contours in a plane that is at 30° azimuth from the top rotor blade at different instances in time for micro-scale coaxial system, $h/R = 0.446$	237

Nomenclature

a	Speed of sound
A	Area of the rotor (πR^2)
c	Chord length of the airfoil
C_d	Drag coefficient
C_l	Lift coefficient
C_m	Moment coefficient
C_p	Pressure coefficient
C_P	Power coefficient = $P/(\rho\pi R^2 U_{tip}^3)$ (Referred to as C_Q)
C_Q	Torque coefficient = $Q/(\rho\pi R^2 U_{tip}^2 R)$ (Equivalent to power coefficient, C_P)
C_{Q_p}	Coefficient of power due to pressure forces
C_{Q_v}	Coefficient of power due to viscous forces
C_T	Thrust coefficient = $T/(\rho\pi R^2 U_{tip}^2)$
$C_{Q_{ideal}}$	Ideal power coefficient = $C_T^{3/2}/\sqrt{2}$
D	Drag
$dC_{Q_{rms}}$	Root mean square fluctuation in power coefficient
$dC_{T_{rms}}$	Root mean square fluctuation in thrust coefficient
e	Internal energy
$iblack$	Blanking array (0, 1 or -1)
J	Jacobian of cell volume
$[J]$	Trim Jacobian matrix
k	Thermal conductivity

L	Lift
M	Mach number
p	Pressure
P	Power
Pr	Prandtl number = 0.72
q	Non-dimensionalized invariant of the velocity gradient tensor $\frac{\partial u_i}{\partial x_j} \frac{\partial u_j}{\partial x_i}$ (normalized by tip speed and blade chord)
Q	Torque = P/Ω
r	Radial location of the blade
R	Radius of the rotor
Re	Reynolds number
T	Thrust
U_r, U_θ, U_z	Radial, swirl and inflow velocities
U_{tip}	Tip speed (ΩR)
u, v, w	Velocity components in the Cartesian directions
x, y, z	Cartesian coordinates
α	Angle of attack
γ	Ratio of specific heats = 1.4
$\Delta t, h$	Time step size
$\Delta \tau$	Dual-time step size
θ_0	Collective setting
θ_{0_1}	Collective setting of the top rotor
θ_{0_2}	Collective setting of the bottom rotor
λ	Eigenvalues
μ	Laminar viscosity

μ_t	Turbulent viscosity
ξ, η, ζ	Computational coordinates
ρ	Density
ψ	Wake age (degrees)
ψ_{b_1}	Wake age of top rotor vortex (degrees)
ψ_{b_2}	Wake age of bottom rotor vortex (degrees)
Ω	Angular velocity of blade rotation

Definitions

chimera points	Points at the boundary where solution is interpolated
hole points	Points in mesh where solution is invalid
field points	Points where solution is computed
fringe points	Points around hole where solution is interpolated

Subscripts

bot	Refers to bot rotor
top	Refers to top rotor
tip	Refers to tip
∞	Refers to free-stream

Abbreviations

2D	Two dimensional
3D	Three dimensional
BLTE	Blunt leading and trailing edge
DL	Disk Loading = T/A

<i>FM</i>	Figure of Merit = (ideal power)/(actual power)
IHC	Implicit hole-cutting
<i>PL</i>	Power Loading = T/P
LHS	Left hand side
RANS	Reynolds averaged Navier-Stokes
RHS	Right hand side
SLE	Sharp leading and blunt trailing edge
SLTE	Sharp leading and trailing edge
STE	Blunt leading and sharp trailing edge

Chapter 1

Introduction

1.1 Micro Air Vehicles

The concept of Micro Air Vehicles (MAVs) was first introduced in 1992 in a Defense Advanced Research Projects Agency (DARPA) workshop titled “Future Technology Driven Revolutions in Military Operations”. MAVs, as defined in the research program of DARPA, are inexpensive flying vehicles with no dimension exceeding 6 inches (15 cm), with a weight of no more than 100 grams. The endurance is encouraged to be one hour and the payload should include a camera or other sensing device. Over the past decade, MAVs have received an increasing amount of attention in military and civilian markets.

For the military, MAVs can provide stealthy surveillance into a complex and possibly dangerous situations without much risk. Common environments for usage include urban areas and inside buildings or in complex terrain such as hills, mountains or inside caves. For civilian applications, MAVs can examine an environment that is harmful due to structural, chemical, electrical, or other hazardous concerns. MAVs can also be used for traffic monitoring.

While there is no perfect MAV for all situations, most of the small flying

vehicles being developed can be divided into three categories. Just like for full size aircraft, the two most successful MAV configurations are fixed-wing and rotary-wing. The third configuration, which mimics nature, is a flapping wing configuration.

Fixed-wing MAVs have so far been the most successful at achieving the longest endurance and greatest speed and range. They are relatively simple, fast, and efficient compared to other categories of MAVs and are well suited for outdoor reconnaissance missions that do not require maneuvering in tightly constrained spaces. However, for missions around or within buildings, hovering vehicles have a clear advantage over fixed-wings configurations.

Both rotary-wing and flapping-wing MAVs provide hovering capabilities. The ability to takeoff and land vertically gives operational flexibility by requiring minimal takeoff and landing zones. Furthermore, perch and stare operations can extend their useful life on station. In addition, the ability to rapidly change flight direction is ideal for use in pursuit or search missions, where the flight path is dynamic. However, due to their complex kinematics, hovering flapping-wing vehicles have very poor mechanical efficiency. On the other hand, rotary-wing vehicles can adapt some of the technology used in full-scale vehicles and require simpler mechanics, thereby keeping the mechanical losses to a minimum. Finally, most rotary-wing MAVs can also better withstand crosswind gusts that may destabilize flapping-wing MAVs. These characteristics make the rotary-wing configurations specially attractive for MAV applications. This thesis focuses on the aerodynamics of rotary-wing MAVs.

1.1.1 Current Capabilities of Rotary-Wing MAVs

Table 1.1 shows the performance, in terms of weight and endurance, of a series of rotary-wing MAVs along with selected fixed-wing small-scale vehicles. It can be clearly seen that the objective set by DARPA is far from being reached. Fixed-wing vehicles meet size and weight constraints, but are lacking in endurance. For rotary-wing vehicles, even with larger and heavier designs, endurance times are shorter than for the fixed-wing configurations.

Table 1.1: Relative performance of various MAVs.

Name	Type	Weight (g)	Endurance (min)
Micor UMD	Rotary-wing	150	15
Commercial Electric Heli	Rotary-wing	350	15
Kolibri Lutronix	Rotary-wing	440	< 10
Honeywell iSTAR	Rotary-wing	1800	15
Aerovironment Black Widow	Fixed-wing	80	25
Lockhead-Sanders Microstar	Fixed-wing	110	25

1.1.2 Limitations of Current Rotary-Wing Designs

The main difficulty in achieving a better performance with a rotary-wing vehicle comes from the large hover power requirements. Hover is an intrinsically high-power flight state with considerably larger energy requirements; this fact is independent of scale. If hover extends for a significant fraction of the mission duration, hover efficiency becomes a key vehicle characteristic that must be carefully addressed.

Hovering efficiency, which directly determines the endurance achieved, can

be quantified analytically using Simple Momentum Theory [1], where the rotor is assumed as an actuator disk and the flow is assumed to be steady and inviscid.

For a rotor producing thrust (T), the minimum average induced velocity through the plane of the rotor disk is given by:

$$v_{ideal} = \sqrt{\frac{T}{2\rho A}} = \sqrt{\frac{DL}{2\rho}} \quad (1.1)$$

where DL is the disk loading (T/A), A is the area of the rotor and ρ is the density.

The ideal power required to hover is then given by:

$$P_{ideal} = T v_{ideal} = \frac{T^{3/2}}{\sqrt{2\rho A}} \quad (1.2)$$

The aerodynamic efficiency of a hovering rotor is measured in terms of the figure of merit (FM), which is defined as the ratio of ideal power to actual power and is given by:

$$FM = \frac{P_{ideal}}{P} \quad (1.3)$$

The total efficiency of a hovering rotary-wing vehicle can be quantified in terms of effective power loading (PL), which is defined as the ratio of thrust (equal to the vehicle weight) to power required to hover (T/P). The figure of merit can be rewritten in terms of power loading as

$$FM = PL \sqrt{\frac{DL}{2\rho}} \quad (1.4)$$

Therefore,

$$PL = \frac{\sqrt{2\rho}FM}{\sqrt{DL}} \quad (1.5)$$

where FM accounts for all sources of non-ideal losses including the profile losses due to viscosity. This means that the best hovering efficiency is obtained when the effective disk loading is a minimum and also when the FM is a maximum. Therefore, the key to endurance for a rotary-wing MAV is to have a low effective disk loading and have good aerodynamic efficiency.

However, currently available rotary MAVs have relatively poor aerodynamic efficiency compared to full-scale vehicles. MAV rotors have achieved a maximum FM around 0.6 while full-scale helicopters may have a maximum FM near 0.80 or even slightly higher. This degraded performance for MAVs is due to the adverse effects of the low Reynolds numbers at which the MAVs operate. Figure 1.1 shows Reynolds number vs. Mass for a wide range of aircraft. MAVs generally fly in the Reynolds number range of 1,000 to 120,000 (whereas full size helicopters and airplanes experience Reynolds numbers on the order of 10^7). Rotary-wing MAVs generally fly in the 20,000 to 70,000 Reynolds number range, although the smallest rotary-wing MAVs may fly at a Reynolds number below 10,000.

At these low Reynolds numbers, viscous effects in the flow are dominant over the inertial ones, boundary layers are thick and undergo several complex phenomena. Separation, transition, and reattachment can all occur within a short chordwise distance, forming laminar separation bubbles that have a strong adverse effect on the lifting surface characteristics. As a result of the poor airfoil performance, small-scale rotors have lower efficiency than full-scale ones.

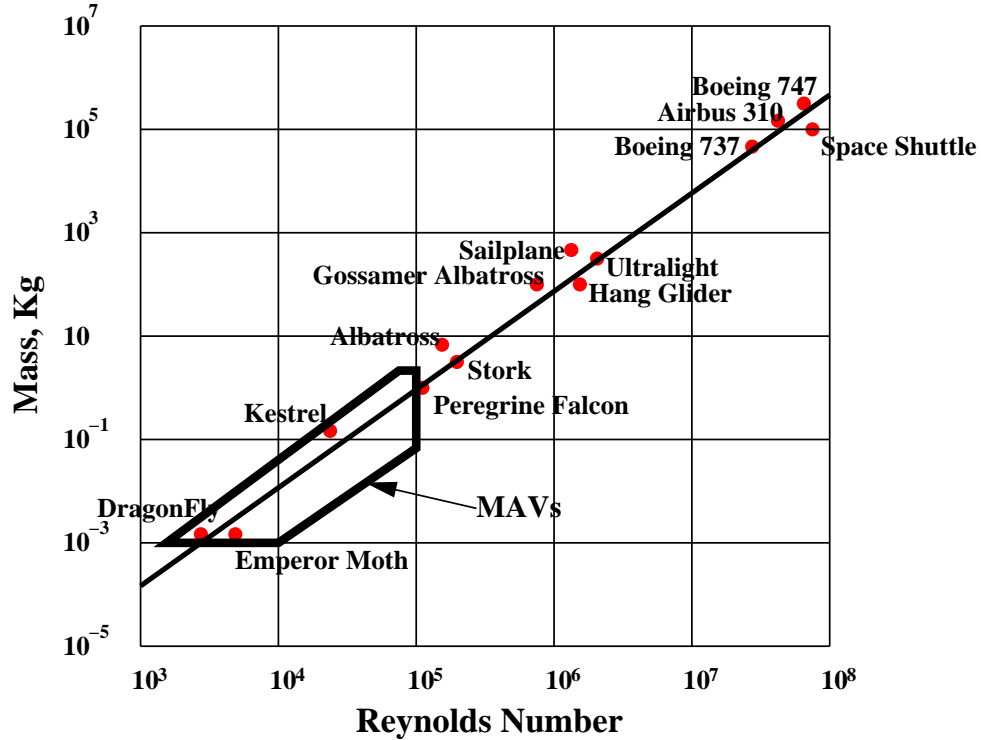


Figure 1.1: Mass vs Reynolds number for animals and man-made vehicles [2].

1.2 Previous Work

Several studies have been done in the past to improve the aerodynamic efficiency of MAV rotors. Primary focus has been on airfoil aerodynamics. For the MAV rotors, the selection of airfoils is extremely important. A good airfoil choice for MAVs will try to accomplish several goals: to delay the onset of the laminar separation bubble and therefore flow separation, to achieve a high maximum lift coefficient, and to keep profile drag at a minimum.

While good aerodynamic efficiency requires the design of blade airfoil sections with low drag and high lift-to-drag ratios, another major source of performance loss for a rotor is contained within the structure of its blade wake, i.e., the induced losses. Therefore, it is very important to have a good understanding of the

micro-rotor wake. Comprehensive rotor wake measurements and detailed computational studies have been carried out to help understand the source of these losses for rotors at larger scales. However, there is very limited experimental and computational studies on MAV-scale rotors.

Previous studies on low Reynolds number aerodynamics and rotary-wing tip vortex are detailed below.

1.2.1 Low Reynolds Number Aerodynamics

Experimental Studies

One of the most influential publications in the field was published by Schmitz [3] in 1941. Schmitz performed his research in a wind tunnel with turbulence levels similar to those found in free flight (0.1%). Under such flow conditions, he was able to observe for the first time the hysteresis loops in the lift and drag of airfoils at Reynolds numbers between 40,000 and 160,000. He also identified the reduction in the Reynolds number at which flow transitions from laminar to turbulent due to the added turbulence produced by placing a wire upstream of the leading edge.

In 1980 a comprehensive airfoil catalog was published by Althaus [4]. The measurements were made in a low turbulence wind tunnel. It consisted of lift and drag coefficients as a function of angle of attack for 30 airfoils at Reynolds numbers ranging between 40,000 and 250,000.

A comprehensive study on low Reynolds number flow physics and pre-1981 low Reynolds number data can be found in the work of Carmichael [5]. This reference also contains a good qualitative description of the flow physics in different Reynold number flight regimes.

Mueller [6–8] conducted extensive experimental studies on 2D and 3D flow around flat plates and cambered airfoils at Reynolds numbers ranging from 60,000 to 200,000. The data showed that cambered plates offer better aerodynamic performance characteristics than flat plates. Additionally, it was shown that the trailing edge geometry has little effect on the lift and drag on thin wings at low Reynolds numbers.

Selig has been working over the last 20 years on systematic wind tunnel testing of more than 200 airfoils at Reynolds numbers between 40,000 and 500,000. This set of data is especially valuable since all tests were performed at the same facility with the same methodology, making quantitative comparison within the set very accurate. Results have been compiled in a series of 3 volumes [9, 10]. Selig has also worked on inverse design methodologies and optimization of airfoils at low Reynolds numbers [11, 12].

Results from Laitone [13, 14] suggest that a good airfoil for use in flow with Reynolds numbers less than 70,000 should be a thin plate with 5% circular arc camber. This type of airfoil had a better L/D at low Reynolds numbers compared to a NACA 0012, and a reversed NACA 0012, among others. Additionally, the thin, cambered airfoil geometry produced a higher total lift for all angles of attack. Sharpening the leading edge resulted in the largest lift curve slope, similar to the findings in [12].

Hein and Chopra [15], as well as Bohorquez [2], measured the performance of a hovering rotor using different airfoils and showed that a thin circular arc airfoil geometry improved the figure of merit of the rotor. Bohorquez also studied the effect of twist and tip taper on the performance. Performance gains were obtained by introducing tip taper in a manner such that large negative twist

angles over short radial distances at the blade tips. Linear twist (negative) was not found to be effective in increasing performance. A parametric study of various blade geometries resulted in maximum figures of merit of 0.65 as compared to a value of 0.35 using NACA airfoil having rectangular planform. Following this, Bohorquez explored the performance of coaxial micro-rotor at torque equilibrium. These results form the basis for validating micro-scale coaxial rotor simulations in this thesis.

Recently, Ramasamy et al. [29,30] obtained performance data for a hovering rotor at a tip Reynolds number of 32,400 at different blade collective settings. Thin circular airfoils were used with different leading and trailing edge geometries (sharp and blunt). It was found that sharpening the leading and trailing edge improved the performance of the rotor. Ramasamy et al. also studied the effect of twist and taper on these blades. It was found that, while twist improved the performance, taper did not provide any benefit. In addition to the performance data, high resolution flow-field data was also obtained in this study. As a result, these results form the basis for validating micro-scale single rotor simulations in this thesis.

Computational Studies

The following are some relevant studies that cover the development and use of Computational Fluid Dynamics (CFD) tools in the low Reynolds number regime.

Singh et al. [16], performed computations using XFOIL [17] over several airfoils at $Re = 80,000$. XFOIL, which is a freeware program, is a two dimensional panel method code. It can compute basic airfoil performance characteristics with extension to viscous flows using a boundary layer method with a transition

model. Results from Singh et al. showed that a thin, cambered airfoil (8.89%) from Selig had the best lift and drag characteristics over thicker, less cambered Wortmann and NACA symmetric airfoils.

Kellogg and Bowman [18] completed a parametric computational study using the thickness of MAV airfoils for the Reynolds numbers of 60,000, 100,000, and 150,000 and found that decreasing the Reynolds number also decreased the optimal thickness with respect to L/D . Thus, an airfoil designed for use in low Reynolds number flow should be relatively thin.

Bohorquez [2] implemented a rotor design tool that integrated a BEMT rotor model with a CFD calculated 2D airfoil database. The effect of spanwise twist, taper and airfoil shape (restricted to circular arcs) on hover performance were modeled. The model was able to predict the thrust within margins of experimental error. However, the power predictions were not satisfactory, agreeing with experiments only over a limited collective range.

Schroeder and Baeder [19,20] examined the use of TURNS [21] (modified to include steady low Mach preconditioner [22]) in 2D and 3D around thin, highly cambered airfoils commonly found on MAVs. The predictions agreed reasonably well with experimental data for the static 2D lift and drag data for both an Eppler 387 and the airfoil of Mueller. The predicted lift and drag curves for the 3-D wing of Mueller agreed extremely well with the experimental results. The current studies will build upon the work of Schroeder and Baeder to develop methodologies, which will aid in simulation of micro-scale rotors.

1.2.2 Rotary-Wing Tip Vortex Studies

Experimental Studies

Comprehensive wake measurements have been carried out for various scales of rotor. For rotorcraft, the scale is defined based on the radius of the rotor. Full-scale rotors have radius ranging from approximately 9 – 60 feet, model-scale rotors have radius ranging from approximately 3 – 6 feet, sub-scale rotors have radius of approximately 1 – 2 feet and micro-scale rotors have radius on the order of 0.25 feet or smaller.

Caradonna and Tung [23] performed hot wire velocity measurements in the wake of a two bladed model-scale hovering rotor. The measured peak swirl velocities were found to reach a maximum of 40% of the tip speed and the initial vortex core radius was found to be around 4% of the blade chord. In addition, pressure measurements were made on the blade surface.

Tangler et al. [24] conducted a comprehensive study of the effects of tip shape, airfoil section, tip Mach number and collective pitch on the tip vortex structure of a sub-scale hovering rotor. For the range of collective pitch that was tested, the tip vortex swirl velocity was found to be of the order of 20%–50% of the tip speed.

Thompson et al. [25] performed detailed measurements with a laser Doppler velocimeter in the tip region and in the tip vortex core of a single-bladed sub-scale rotor in hover. The data exhibited evidence of secondary structure inside the rotational core of the vortex.

Martin and Leishman [26] measured the swirl and axial velocities in the vortex system trailed from an isolated sub-scale blade in hover. The measured data in select planes over one rotor revolution was corrected for wandering. The

peak swirl velocity was found to decay at a rate that was much slower than that for the measured axial velocity deficit. The effects of blade tip shape modification were also evaluated.

Ramasamy & Leishman [27] and McAlister [28] measured velocity profiles for an isolated sub-scale rotor in hover. They were able to show that the swirl velocity and circulation profiles are approximately self-similar with wake-age.

As mentioned previously, Ramasamy et al. [29, 30] obtained high-resolution flow visualization, performance data and particle image velocimetry (PIV) flow-field data for a micro-scale rotor operating at a tip Reynolds number of 32,400. It was seen that the vortex sheets trailing the rotor blades were much thicker than their higher chord Reynolds number counterparts. Similarly, the viscous core sizes of the tip vortices were relatively large as a fraction of blade chord compared to those measured at higher vortex Reynolds numbers. The initial core size was found to be $0.05c$ compared to $0.02c$ at higher Reynolds numbers. On the other hand, the rate of core growth was found to be comparable to higher Reynolds numbers. These results form the basis for validating micro-scale single rotor simulations in this thesis.

Computational Studies

Compared to fixed-wing calculations, it is very difficult to come across numerical validation of tip vortex structure with experiments for rotating blades.

Russell et al. [31, 32] have performed RANS simulations using the Baldwin-Lomax turbulence model to validate the experimental hover measurements of McAlister et al. [33]. Computed vortex velocity profiles are compared with measurements at distances of 0.5 and 3 chord lengths behind the trailing edge. The

axial velocity excess is overpredicted and the swirl velocity is underpredicted. The computed core radius is seen to be larger by 60% compared to the measurement at the 3 chord lengths downstream location.

Usta [34] used upto eighth order accurate symmetric TVD schemes [35] (for inviscid terms) with the Spalart-Allmaras turbulence model to simulate the Caradonna and Tung [23] 2 bladed hovering rotor. Though high order schemes performed better than the low order schemes in predicting blade surface pressures, numerical diffusion was found to reduce the vortex strength significantly.

Tang [36] used a high order accurate Euler solver with adaptive mesh refinement and compared the evolution of the peak swirl velocity with wake-age for the isolated hovering rotor test case of Martin et al [26]. The use of high order accuracy and mesh adaption was seen to reduce numerical dissipation. No details of the vortex velocity profile were compared with experiments.

Recently, Duraisamy & Baeder [37,38] used the high order accurate overset RANS code, OVERTURNS, to simulate the same experiment. For the first time, detailed validations of the swirl and axial velocities were achieved up to one full revolution of the wake (roughly 60 chords of evolution). In addition, the aerodynamic loading was validated on single rotor systems. Duraisamy & Baeder, in collaboration with Ramasamy & Leishman [39] also studied the formation and rollup of a tip vortex for the hovering rotor test case in Ref. [27] and showed the presence of secondary and tertiary vortices resulting from crossflow separations near the blade tip. This thesis will build upon the methodologies developed by Duraisamy & Baeder for capturing rotary-wing tip vortices in large scales and extend it for the micro-scale rotors.

1.3 Rotary MAV Conceptual Designs

Apart from improvements in blade/airfoil design for MAVs, various conceptual designs of rotary MAVs have evolved over the period of time to meet the target set by DARPA. These concepts differ mainly in their anti-torque mechanism. One design is simply to scale down conventional helicopters (with a large main rotor and a small tail rotor) such as the Precision Heli Micron V2 helicopter [40]. The benefits of this conventional design are simplicity and familiarity in construction and control. The tail rotor and boom, however, add to the vehicle dimensions and are a detriment to the goal of compactness.

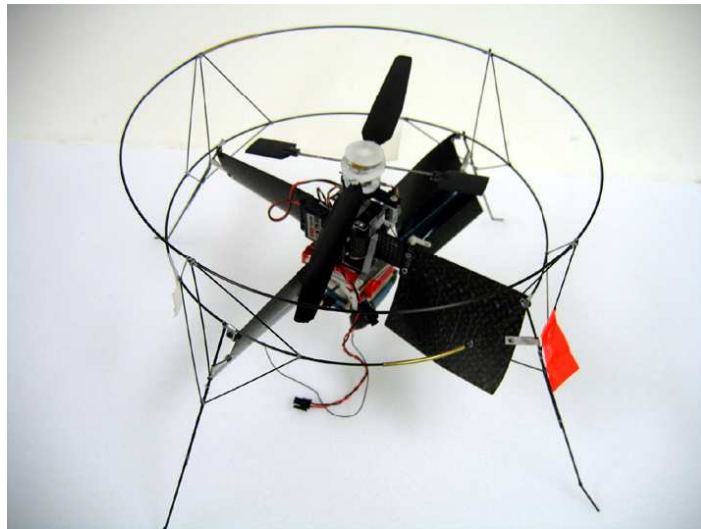


Figure 1.2: University of Maryland “Giant” [41].

To meet the goal of a compact and simple design, some MAVs utilize a single rotor with vanes in the downwash to counteract the torque required by the main rotor. As the main rotor torque and thrust increase, the anti-torque from the vanes also increases due to the increased downwash. Three examples of vanes used as a stable method of control and torque counteraction are the Honeywell

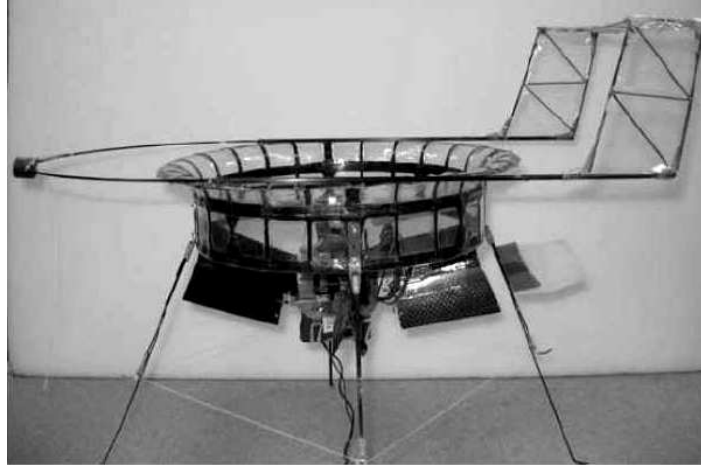


Figure 1.3: University of Maryland “TiShrov” [42].

iSTAR [43] and the Giant and the TiShrov at the University of Maryland [41, 42]. The Giant and the TiShrov, respectively shown in Figures 1.2 and 1.3, are similar vehicles, but the TiShrov further utilizes a shrouded rotor. The shroud has a curved inlet that increases aerodynamic efficiency by reducing tip losses and providing additional thrust due to the accelerated airflow over the inlet. However, the thrust benefits of the shroud have not yet exceeded the shroud’s weight. The disadvantage of the current design of Giant’s vanes and TiShrov’s shroud is that they cause more drag than a conventional rotor.

Another concept, which appears attractive because of its inherent compactness, is the coaxial design. Coaxial rotors are a pair of counter-rotating rotors mounted one above the other. Examples of coaxial MAVs are the Seiko Micro Flying Robot [44] and the Micor [2], developed at the University of Maryland (as seen in Figure 1.4). The disadvantages of this design include the aerodynamic interference between the two rotors, mechanical complexity and the added weight of a dual rotor system. However, because of their compactness, the current work looks into the aerodynamics of MAVs that utilize a coaxial rotor design.

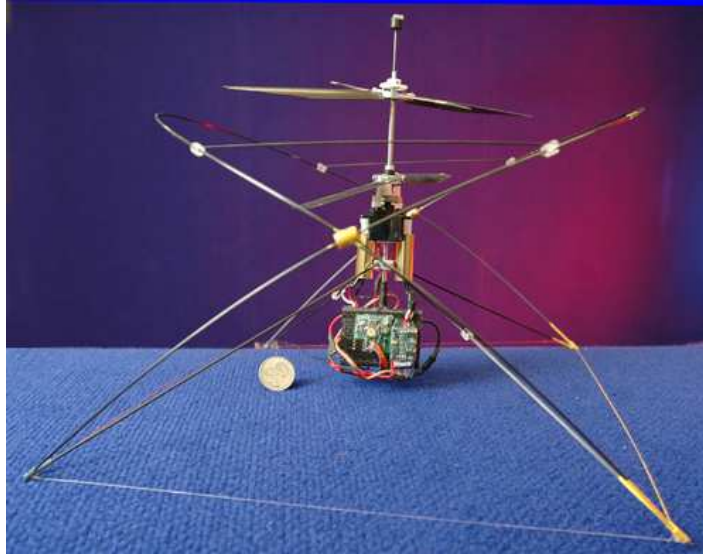


Figure 1.4: University of Maryland Micor [2].

1.4 Coaxial Rotors

The concept of coaxial rotors has been used since the beginning of experiments with helicopters in the nineteenth century. Contemporary sources [45,46] suggest that at least 35 prototype helicopters that used coaxial rotors had been built (but not necessarily flown successfully) prior to 1945. However, only the Kamov company from Russia has been successful in placing coaxial rotor configurations into production, starting with the Ka-6 and Ka-8 helicopters in the late 1940s through to the Ka-50 (see Figure 1.5) in the 1990s. In recent years, there has been renewed interest in the coaxial configuration in other countries as well.

Conceptually, the coaxial rotor configuration offers substantial design advantages over the conventional main rotor tail-rotor configuration. Perhaps most significantly, the additional power requirements and weight associated with the tail rotor and transmission system may be reallocated for additional payload capability. Additionally, the asymmetry of lift associated with a single rotor in



Figure 1.5: Kamov Ka-50 [47].

forward flight is mitigated, offering the potential for a faster and more stable vehicle. Another advantage of the conceptual coaxial configuration is the reduction in noise arising from interactions between the airflows from the main and tail rotors.

From the perspective of MAV, the most attractive feature of a coaxial design is the resulting compactness in the vehicle. Since two rotors produce the net thrust, instead of a single rotor in the conventional design, the diameter of the rotors can be reduced to carry the same amount of weight. Secondly, eliminating the tail rotor results in a smaller and lighter vehicle. Additionally, since the MAVs do not need to operate at high forward speeds, the horizontal and vertical fins required for stability in full-scale helicopters can also be eliminated, making it further compact.

However, the principal disadvantage of the coaxial rotor configuration is the increased mechanical complexity of the rotor hub required to drive two rotor discs in opposite directions. In addition, a long mast can result in high drag at large forward flight speeds. However, since MAVs operate only at low speeds,

the drag due to mast may not be significant. Aerodynamically, the two rotors and their wakes interact with each other, producing a more complicated flow field than is found in a single rotor system. A major portion of the lower rotor continually operates in the wake system of the upper rotor. This has a significant effect on the inflow distribution of the overall system, and also on the boundary layer of the lower rotor blades. This interacting flow can, in general, result in a loss of net rotor system aerodynamic efficiency. Additionally, this can result in an undesired unsteadiness in the flow-field, even under hovering conditions. Therefore, a good understanding of the flow physics is required to analyse the feasibility of such a system for MAVs.

1.5 Previous Studies on Coaxial Rotors

There has been very limited experimental or computational study, not only for the MAV scale, but also for the full size helicopter scale, on coaxial rotor aerodynamics. A NASA report that gives a broad perspective of the aerodynamic issues and state of the art of coaxial helicopters technology was published by Coleman in [48]. His survey summarizes the main publications on the topic from American, Russian, Japanese, British and German sources. Experimental data and analysis that address rotor separation distance, load sharing between the rotors, wake structure, solidity effects and the unique characteristics of the coaxial configuration are presented.

1.5.1 Experimental Studies

Few experimental measurements of coaxial rotor performance are available in the literature. These include the full-scale tests performed by Harrington [49] and Dingledein [50] in the Langley full-scale wind tunnel, and the data presented by Nagashima in [51]. Harrington performed hover tests on two different rotors, referred to as rotor-1 and rotor-2. The results of Harrington rotor-2 will form the basis for validating full-scale coaxial rotors in hover for this work.

Recently, McAlister et al. [52] assessed the hover performance of a three-bladed sub-scale tilt rotor. The study comprises of sweeps of varying rotor spacing distance at constant rotor speed, and sweeps of varying ground distance at constant rotor spacing. Performance degradation of the bottom rotor was clearly identified in out of ground effect compared to single rotor. In ground effect, the performance of the bottom rotor was seen to improve as the rotor approached the ground.

As mentioned previously, at the University of Maryland, coaxial micro rotor performance at torque equilibrium was explored by Bohorquez [2]. It was found that the upper rotor was only marginally affected by the lower one at spacings larger than 35% of the rotor radius, and that it produced about 60% of the total thrust. These results form the basis for validating micro-scale coaxial rotor simulations in this thesis.

1.5.2 Computational Studies

Various approaches that generally combine momentum theory, blade element theory, vortex, and lifting line models have been implemented in an attempt to calculate the power requirements of coaxial rotors. Generally a good predictive

capability has been achieved. However, most of the algorithms require empirical models of the wake geometry.

Leishman [1,53] derived the simple (global) momentum theory and the blade element momentum theory (BEMT) for a coaxial rotor system in hover. The BEMT was found to agree well with measured coaxial rotor performance of Harrington rotors [49], and gave better results when compared to experiments than the simple momentum theory alone. The results from the BEMT were further validated using a free-vortex wake analysis of the coaxial rotor, also with good agreement.

Griffiths and Leishman [54] studied the dual-rotor interference in ground effect using the Free Vortex Method. Rotor performance was determined for dual-rotor systems under different combinations of vertical and horizontal spacing. The results showed that there was no substantial benefits for overlapping rotors.

Recently, Syal [55] used simple momentum theory, blade element momentum theory and a Free Vortex Method (FVM) to help design an aerodynamically optimum coaxial rotor system starting from the Harrington rotor-1 [49] setup. The effect of changes in inter-rotor spacing, blade twist and blade planforms on both top and bottom rotors were studied. The results showed that the performance of the coaxial rotor system can be improved significantly by having different blade geometries on the top and bottom rotors. It was seen that, the performance of both the top and the bottom rotors degrade due to interference effects between the two rotors, and increasing inter-rotor spacing was found to reduce these effects.

Kim and Brown [56] used the Vorticity Transport Model (VTM) to study the

coaxial rotor system. In this approach, the wake vorticity is determined from a lifting line-based approach and is evolved in the flow-field using an Eulerian solution of the inviscid, incompressible vorticity transport equations. The representation of the wake is of a much higher quality, and as a result, very accurate predictions of the performance of Harrington rotors were reported.

Lim et. al [57] applied the comprehensive analysis code, CAMRAD II to the scaled coaxial rotor experimental setup of McAlister et al. [52]. In this study, each rotor's wake were modeled separately using a vortex lattice method. The results compared reasonably well with the experimental hover performance results. As a general trend, the thrust was overpredicted, while the power was predicted correctly.

Recently, Ruzicka and Strawn [58] modeled the coaxial rotor setup of McAlister et al. [52] using the Reynolds-averaged Navier-Stokes solver, Overflow2. The simulations did not use any low Mach preconditioner, even though the tip Mach number is as low as 0.15. The performance results did not agree as well with the experiments as the results from CAMRAD II [57] did with the experimental data. The over-prediction in thrust was even more pronounced. But, the power prediction was still reasonably good. The most important outcome of this work is the observation of the unsteadiness in the performance data, whose frequency is 6/rev (twice the number of blades per rev).

1.6 Motivation

CFD can be used to aid in the airfoil selection process for low Reynolds number flows, where experiments are challenging. Past computational studies at low Reynolds numbers are limited to 2D airfoils and 3D fixed-wings. However, in

order to come up with a good overall rotor design, it is essential to account for the three-dimensionality of the flow, which is typical in a rotor environment. Additionally, significant variation of Reynolds number is found along the span of rotors (typically a factor of 5, if 20% root cut-out). The airfoil characteristics do not change much from root to tip when the scale is large. However, at the low Reynolds numbers found in small scale rotors, the drag characteristics change significantly with Reynolds number. Therefore, in order to design MAV blades using 2D analysis, one now also needs to obtain airfoil data at different Reynolds number, thus making it more challenging.

Further, as mentioned earlier, a major source of performance loss for a micro rotor maybe contained within the structure of its blade wake. However, there is very limited experimental and computational studies on MAV-scale rotors. This lack of data is not only because of the experimental complexities associated with measuring rotor flows at any scale, but also from the specific measurement challenges that are unique at the MAV scale. This includes, but is not limited to, the physical size of the flow structures that are present, which are often too small to be sufficiently resolved with most types of flow diagnostic methods. Due to these difficulties, accurate computational results are of critical importance for MAV research.

As discussed before, coaxial configurations are particularly suited for MAVs. However, a good understanding of the flow physics is required to improve the aerodynamic efficiency of such a system. But, there has been very limited experimental or computational studies on coaxial rotor aerodynamics, not only for the MAV scale, but also for the full size helicopter scale. Traditionally, for multiple rotor systems in full-scale, simple analyses that can provide a qualitative

understanding of the phenomena have been used. Though the aforementioned methods are efficient and are capable of predicting global performance results reasonably well, the following limitations have been observed:

- A certain degree of empiricism is involved. For instance, in FVM, initial core-radius size and vortex rollup position are required.
- These models are inviscid, and therefore, the drag information is required and the vortex/wake decay is either ignored or modeled.
- Since the blade is represented as a lifting line, the surface information is lost, and hence effects due to the blade thickness and vortex-surface interaction cannot be captured. Furthermore, in general this requires 2D tables of C_l , C_d and C_m as a function of angle of attack, Mach number and Reynolds number.

CFD can be used to study the performance and flow physics of a coaxial rotor. In this approach, the solution of the more fundamental fluid flow conservation equations coupled with an accurate representation of the blade geometry can be expected to provide further insight into the aerodynamics and performance of the coaxial system.

1.7 Objectives

The main objective of this work is to develop a computational platform that can be used to study the performance and flow physics of conventional and a non-conventional (coaxial) micro-scale rotor configurations in hover. As a first step, an existing solver will be extended for the analysis of low Mach number flows. The methodology will be used to obtain detailed understanding of

the flow physics of a micro-scale single rotor. Following this, a computational methodology to handle coaxial rotor configuration will be developed, which will be validated for a full-scale system. Finally, calculations will be done for a micro-scale coaxial rotor, which will help in determining the feasibility of utilizing a coaxial configuration for MAVs. Following are the detailed objectives of the dissertation:

- Extend the applicability of a compressible Reynolds Averaged Navier-Stokes (RANS) solver for analysis of the flow physics to the low Mach number and low Reynolds number regime; a condition that has not been studied adequately using CFD. To facilitate this, a low Mach preconditioning algorithm will be implemented for both the steady and the unsteady Navier-Stokes equations.
- Verification and validation of the low Mach preconditioning will be done in a rigorous manner. Initially, the performance of the preconditioner will be investigated based on the numerical solution of a 2D isentropic vortex convecting in a free-stream. The effectiveness of the preconditioner will also be verified by applying it to 2D steady low speed flow over an airfoil. This will be followed by validation using 3D fixed-wing predictions at similar flow conditions. Finally, complete validation of the performance and the flow-field will be done for a hovering micro-rotor. As part of this validation, the effects of the leading edge and the trailing edge geometries on performance will be detailed.
- Extend the applicability of a compressible RANS solver to study the performance and flow physics of a coaxial rotor system. To achieve this, a

sliding mesh boundary condition with high order interpolation will be implemented. A coarse-grain parallelization of the solver will be performed to handle the enormous grid size required to capture the wake accurately. Improvements will also be made to the grid connectivity for better transfer of information between various overset meshes.

- Validation of the CFD model will be done by comparing the performance of a full-scale hovering coaxial rotor system with experiments. A detailed study of the flow physics will be done to understand the unsteadiness in the flow-field.
- Finally, the methodologies developed for simulating a micro-scale single rotor and a full-scale coaxial rotor will be combined to simulate a micro-scale coaxial rotor. The performance predictions will be validated with available experimental data. The flow physics will be studied in detail and some of the key differences in flow-field between full-scale and micro-scale coaxial systems will be identified. The effect of rotor spacing on the unsteadiness will be investigated.

1.8 Contributions of the Thesis

The key contributions of this research include:

1. Extension of an existing compressible RANS solver to study low Mach number and low Reynolds number flow by implementing time-accurate low Mach preconditioner.
2. Improvements in grid connectivity methodology to allow better transfer of

information between various overset meshes. This involves implementation of an improved blanking methodology.

3. Validation of performance and wake data of micro-scale single rotor with experiment for different leading and trailing edge geometries.
4. Validation of mean performance of full-scale and micro-scale coaxial rotor with experimental data.
5. Understanding the effect of twist and taper for micro-rotors.
6. Detailed analysis of flow physics of the micro-scale single rotor, full-scale coaxial rotor and micro-scale coaxial rotor.
7. Understanding the similarities and differences between full-scale and micro-scale coaxial systems in terms of unsteadiness and effect of rotor spacing.

1.9 Scope and Organization of the Thesis

This thesis is focused on extending an existing computational methodology to enable the simulation of a micro-scale coaxial rotor configuration and then analyzing the resulting airloads and flow-field. This forms an important stepping stone in the direction of the development of a computational platform that can be used to study various rotary-wing MAV configurations, which in turn can help build MAVs that meet the targets set by DARPA.

Chapter 2 describes the computational methodology for the solution of the RANS equations. The improvements to an existing solver in terms of the implementation of low Mach preconditioning, sliding mesh interface condition, grid connectivity approach and parallelization are detailed. It should be noted that

although the current development of the CFD methodology is mainly driven by MAV research, the methodologies are also valid for other diverse applications.

The verification and validation of the methodology developed is presented in the third chapter. The performance and effectiveness of low Mach preconditioning is investigated using 2D model problems and a 3D fixed-wing calculation. The advantages of improvements in grid connectivity is demonstrated using a simplified 2D problem. The baseline methodology in the existing solver is validated using a full-scale hovering rotor simulation.

The investigation of micro-scale single rotor aerodynamics in hover is performed in Chapter 4. The computational methodology is validated by comparing the performance and flow-field data with those from experiments. The effect of leading and trailing edge geometries is investigated by looking at blunt and sharp profiles. Performance improvements due to change in planform shapes are studied.

Chapter 5 presents the results for hovering full-scale coaxial rotor simulations. Following the validation of the performance data with those from experiments, the effects causing unsteadiness in the flow-field is identified. Detailed understanding of the flow physics is obtained.

The results for hovering micro-scale coaxial rotor are presented in Chapter 6. Validation is again done by comparing the performance data with the experimental results. The differences in the flow-field between full-scale and micro-scale coaxial system are identified. A study on the effect of rotor spacing on unsteadiness is conducted.

Conclusions and observations noted during the development, validation and application of the methodologies developed are summarized in the final chapter.

Chapter 2

Computational Methodology

In this chapter, the fundamental fluid dynamic equations along with the numerical solution algorithms are described. The chapter will initially identify the flow domain that is being studied. Following this, the details of the mesh system and the connectivity approach is discussed. Subsequently, the flow equations and methodologies available in the existing flow solver are described. Next, the deficiencies of some of these methodologies for the current problem are characterized. Finally, specific improvements made in the solver for the present study are detailed.

2.1 Flow Domain

The focus of the current work is to simulate the flow-field of hovering rotors. The rotor consists of one or more blades, whose surfaces can be treated as a solid wall. The far-field extent of the modeled domain is limited to a few rotor radii from the blades in any direction, because of practical reasons. The size of the domain is further reduced for multi-bladed hovering rotor systems because of the inherent periodicity in the flow-field, which allows the simulation of the

entire system using just one blade for each rotor.

Even within the finite domain of interest, the flow solution can be represented only at finite locations. This is achieved by decomposing the flow domain into smaller domains (cells) by generating a grid. The flow variables represented at each of these grid points constitute the flow solution. The accuracy of the solution is determined by the quality of the grid.

A common difficulty in simulating complex geometries is that a single, contiguous grid will not be sufficient to represent the flow features well enough. For hovering rotors, it is very difficult to obtain a single structured mesh which can represent the blade surfaces and also preserve important off-surface flow features, like tip vortices. In such cases, the common approaches used are unstructured meshes, multiblock structured meshes or overlapping chimera structured meshes.

Unstructured meshes are generally considered to be easily adaptable to complex configurations, but they require more memory and are less efficient compared to structured meshes. Using block structured grids, the grid interfaces have to be matched and this makes the grid generation process very complicated. Overset structured grids have the advantage in that different grids can be generated independent of each other and can be placed in the region of interest without any distortion. Due to these advantages, the current work employs overset meshes.

The penalty to pay however, is the additional work required in identifying points of overlap between meshes and interpolation of the solution in this overlap region. Additionally, there is a possibility of a loss of the conservation property of the numerical scheme. However, the resulting errors can be minimized by making sure discontinuous features like shocks and shear layers do not cross the

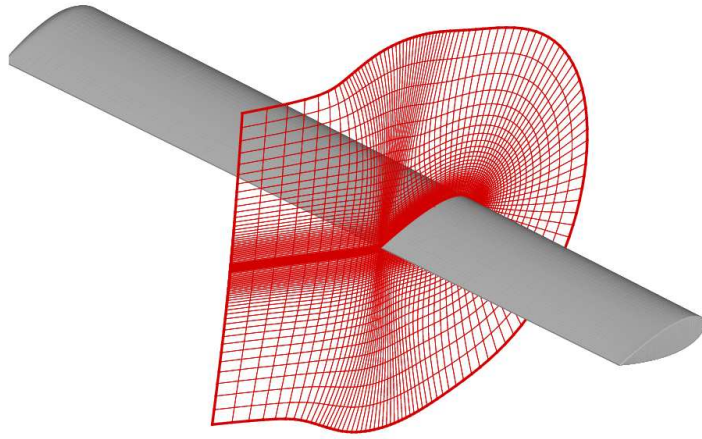
overlap boundaries and furthermore, ensuring that the mesh cell sizes are of commensurate size in the overlap region.

Details of the baseline grid generation/overset methodology are presented in section 2.2. The improvements made in the current work to the connectivity methodology is later provided in section 2.6.3.

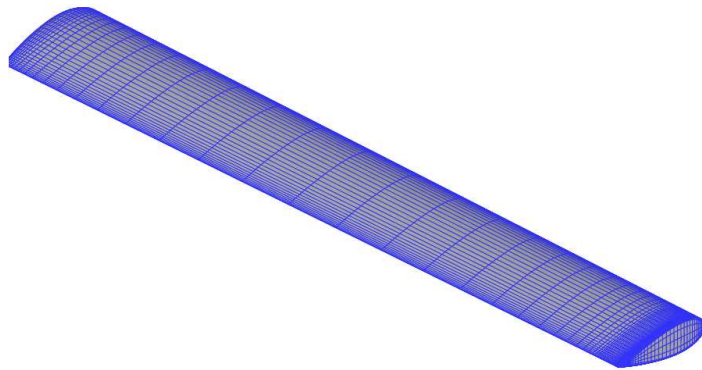
2.2 Mesh Generation

To accurately represent blade surfaces, body conforming structured curvilinear meshes are required. In this study, a hyperbolic mesh generation technique [59] is used to generate 2D C-type meshes around the airfoil sections at the various spanwise locations, shown in Fig. 2.1. The C-type meshes are free of a geometrical singularity at the trailing edge, which is a major disadvantage of O-type meshes. Also, the grid clustering at the trailing edge provides good resolution for capturing the shed wake. The C-meshes obtained are stacked in the spanwise direction. Near the root and the tip regions, the spanwise sections are rotated and collapsed, thus defining a C-O topology, see Fig. 2.2. Details of the collapsing technique are described in Ref. [37].

For rotor problems, the blade mesh is itself overset in one or more background meshes, in order to resolve any tip vortices. In the current work, a background mesh consists of identical planes that are rotated in the azimuthal direction. A sample background mesh for a 2-bladed single rotor is shown in Fig. 2.3. Note that, only one blade is simulated because of the periodicity. The structure and placement of these meshes will be introduced for specific cases in Chapters 4, 5 and 6.



(a) Spanwise 2D section



(b) Stacking in spanwise direction

Figure 2.1: Sample hyperbolic mesh.

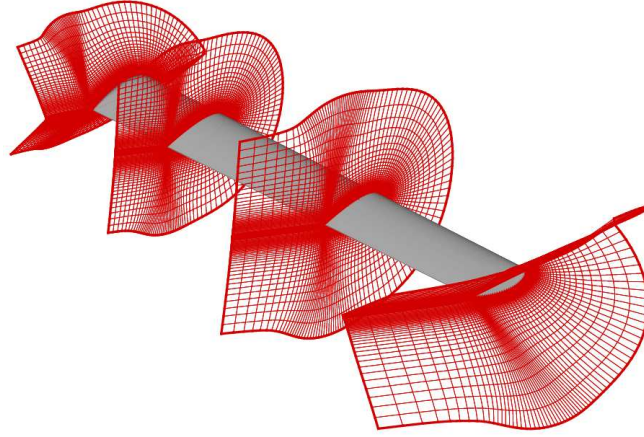
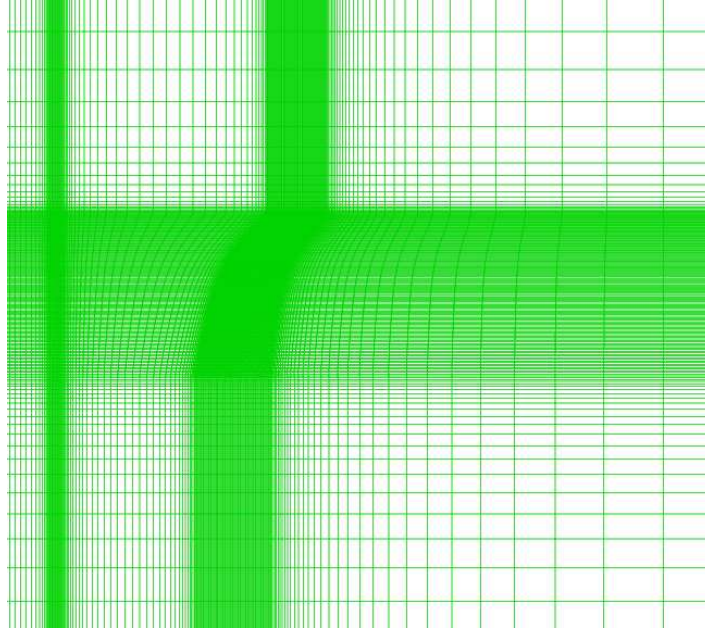


Figure 2.2: Near body C-O mesh at the blade root and tip.

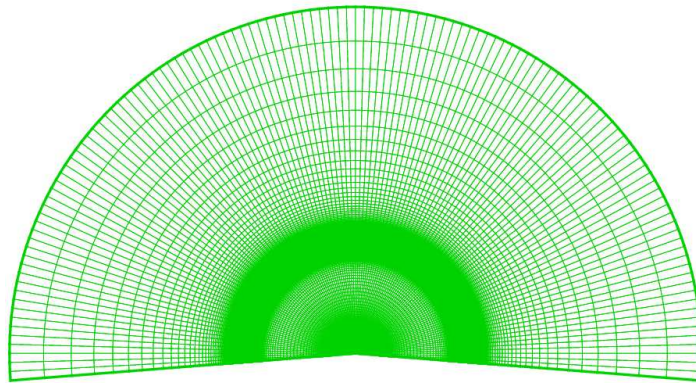
2.2.1 Connectivity Approach (Baseline Methodology)

Once the overlapping meshes are generated, the chimera methodology involves three distinct steps, namely: hole cutting, identification of hole fringe and chimera boundary points and finally, finding donor cells and interpolation factors. For purposes of description, a simple geometry as shown in Fig. 2.4 will be used. The inner circular mesh is the body mesh and the outer mesh is the background mesh.

First, a hole-cutting technique is chosen and used to identify those points that are inside a given hole region with any arbitrary shape (that describes the blade surface geometry for example). These points are blanked out, i.e. identified in an array *iblack*, which indicates the inside/outside status of all grid points for all given hole regions. The flow equations are not solved at these points. The points at the fringe of this initial minimum-size hole are not suitable to receive hole boundary values because of the large differences in grid resolution. The hole



(a) Azimuthal plane



(b) Top View

Figure 2.3: Sample background mesh.

is then expanded or re-sized so that a better grid overlap is achieved. The red circles in Fig. 2.4 shows the hole points of the background grid in the vicinity of the solid surface.

As mentioned before, for typical rotor simulations, a blade mesh is itself over-set in a background mesh and hence the background mesh needs to be hole cut.

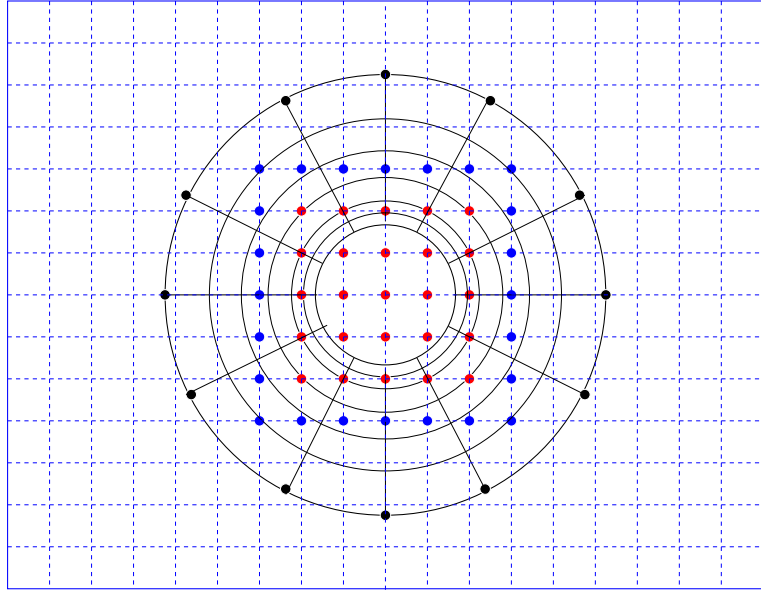


Figure 2.4: Schematic of hole cutting. Red circles: Hole points. Blue circles: Hole fringe points. Black circles: Chimera boundary points.

Instead of using a generalized method, the simplified geometry of the background mesh is utilized. Knowing the approximate dimensions of the solid body, a box enclosing the solid body is defined in the background grid. All the points inside this box are checked as to whether they lie inside the overset grid and the points that do not are labeled as hole points. Using the neighbor information, this hole region is extended at least one layer outwards.

After obtaining the hole points, a list of hole fringe points that require information from other grids to serve as boundary conditions can be easily extracted. The number of fringe layers depends on the stencil of the spatial scheme. For instance, if a third order upwind scheme (described later in section 2.4.1) is used, at least two hole fringe layers are necessary. The blue circles in Fig. 2.4 show one layer of hole fringe points. Chimera points are defined as those boundary points on the body mesh that require information from the background mesh. These

are usually explicitly specified by the user. The black circles in Fig. 2.4 shows the chimera boundary points. The number of layers in the chimera boundary again depends on the stencil of the spatial scheme.

After finding the hole fringe and chimera boundary points, donor cells of the other grid are found and the information is interpolated using the interpolation factors. Typically, linear interpolation is used. The donor cell is found using the "stencil walking" procedure [22]. In this procedure, the search is started at an arbitrary donor cell and the next guess for the donor is made based on the direction in which the boundary point lies, finally ending at the correct donor cell. Once the donor cell is identified, the linear interpolation factors in the three coordinate directions are found by using tri-linear mapping.

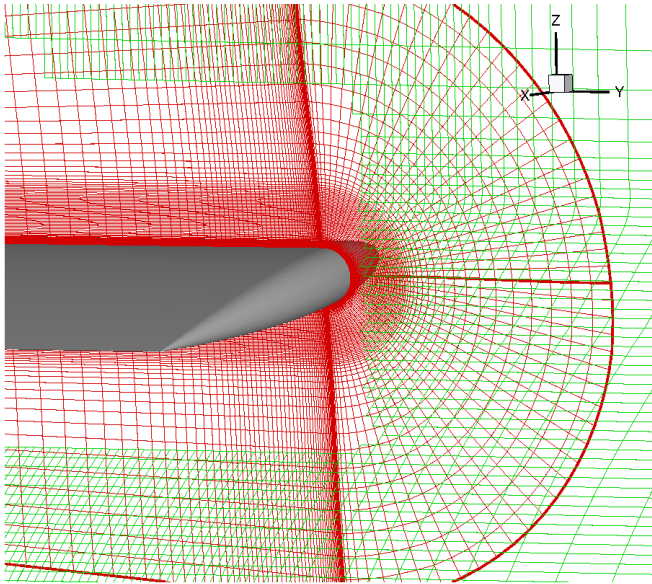


Figure 2.5: Sample overset grid in a hovering rotor simulation. Red: Blade mesh, Green: Background mesh.

A sample overset grid with hole for a hovering rotor simulation is shown in Fig. 2.5. Note that, the current work does not use the connectivity approach

described in this section. Instead, an improved methodology called implicit hole cutting (discussed later in section 2.6.3) is used. However, the concept of hole points, fringe points and field points are retained along with chimera boundary points and donor cells.

2.3 The Flow and its Mathematical Description

The flow-field information at each grid point is obtained by solving the equations of fluid flow, which represent mathematical statements of the conservation laws of physics

1. the conservation of mass,
2. the conservation of momentum, and
3. the conservation of energy.

These conservation laws can be gathered into a single system of partial differential equations called the Navier-Stokes equations, which can be numerically discretized and solved with necessary boundary conditions for the specified geometry. Additional algebraic or differential equations (e.g. equation of state, Stokes hypothesis or turbulent eddy viscosity equation) may be required for closure.

2.3.1 Navier-Stokes Equations

The strong conservation-law form of the 3-dimensional unsteady compressible Navier-Stokes equations in Cartesian coordinates are given by:

$$\frac{\partial Q}{\partial t} + \frac{\partial F_i}{\partial x} + \frac{\partial G_i}{\partial y} + \frac{\partial H_i}{\partial z} = \frac{\partial F_v}{\partial x} + \frac{\partial G_v}{\partial y} + \frac{\partial H_v}{\partial z} + S \quad (2.1)$$

where Q is the vector of conserved variables, F_i , G_i , H_i are vectors representing inviscid fluxes, F_v , G_v , H_v are vectors that represent the viscous fluxes, and S represents the source terms that have to be included to account for the centrifugal and Coriolis accelerations if the equations are formulated in a non-inertial frame of reference. The vector of conserved variables is given by

$$Q = \left\{ \begin{array}{c} \rho \\ \rho u \\ \rho v \\ \rho w \\ e \end{array} \right\} \quad (2.2)$$

where ρ is the density, (u, v, w) are the Cartesian velocity components and e is the total energy per unit volume. The flux vectors are given by

$$F_i = \left\{ \begin{array}{c} \rho u \\ \rho u^2 + p \\ \rho uv \\ \rho uw \\ u(e + p) \end{array} \right\} \quad (2.3)$$

$$G_i = \left\{ \begin{array}{c} \rho v \\ \rho v u \\ \rho v^2 + p \\ \rho v w \\ v(e + p) \end{array} \right\} \quad (2.4)$$

$$H_i = \left\{ \begin{array}{c} \rho w \\ \rho w u \\ \rho w v \\ \rho w^2 + p \\ w(e + p) \end{array} \right\} \quad (2.5)$$

$$F_v = \left\{ \begin{array}{c} 0 \\ \tau_{xx} \\ \tau_{yx} \\ \tau_{zx} \\ u\tau_{xx} + v\tau_{xy} + w\tau_{xz} - q_x \end{array} \right\} \quad (2.6)$$

$$G_v = \left\{ \begin{array}{c} 0 \\ \tau_{xy} \\ \tau_{yy} \\ \tau_{zy} \\ u\tau_{yx} + v\tau_{yy} + w\tau_{yz} - q_y \end{array} \right\} \quad (2.7)$$

$$H_v = \left\{ \begin{array}{c} 0 \\ \tau_{xz} \\ \tau_{yz} \\ \tau_{zz} \\ u\tau_{zx} + v\tau_{zy} + w\tau_{zz} - q_z \end{array} \right\} \quad (2.8)$$

where q_x , q_y and q_z are the thermal conduction terms, which can be represented in terms of temperature (T) and coefficient of thermal conductivity (k), given by:

$$q_i = -k \frac{\partial T}{\partial x_i} \quad (2.9)$$

The pressure (p) is determined by the equation of state for a perfect gas, given by

$$p = (\gamma - 1) \left\{ e - \frac{1}{2} \rho (u^2 + v^2 + w^2) \right\} \quad (2.10)$$

where γ is the ratio of specific heats, generally taken as 1.4. For a perfect gas, $T = \frac{p}{\rho R}$, where R is the gas constant. With the assumption of Stokes' hypothesis [60], the mean stresses can be represented by:

$$\tau_{ij} = \mu \left[\left(\frac{\partial u_i}{\partial x_j} + \frac{\partial u_j}{\partial x_i} \right) - \frac{2}{3} \frac{\partial u_k}{\partial x_k} \delta_{ij} \right] \quad (2.11)$$

where μ is the laminar viscosity, which can be evaluated using simple algebraic Sutherland's Law [60].

Non-dimensionalization of Navier-Stokes Equations

Equations of fluid motion are non-dimensionalized to achieve dynamic and energetic similarity for geometrically similar situations. The solutions of such equations also should provide values on the order of one. Generally, a characteristic dimension such as the chord of an airfoil is selected to non-dimensionalize the length scale, while free-stream conditions are used to non-dimensionalize the dependant variables. The non-dimensional variables (with superscript $*$) are given below:

$$\begin{aligned}
 t^* &= \frac{ta_\infty}{c} & x^* &= \frac{x}{c} & y^* &= \frac{y}{c} & z^* &= \frac{z}{c} \\
 \mu^* &= \frac{\mu}{\mu_\infty} & u^* &= \frac{u}{a_\infty} & v^* &= \frac{v}{a_\infty} & w^* &= \frac{w}{a_\infty} \\
 \rho^* &= \frac{\rho}{\rho_\infty} & T^* &= \frac{T}{T_\infty} & p^* &= \frac{p}{\rho_\infty a_\infty^2} & e^* &= \frac{e}{\rho_\infty a_\infty^2}
 \end{aligned} \tag{2.12}$$

where c is the chord of the airfoil, a is the speed of sound and subscript ∞ represents free-stream condition.

The non-dimensional parameters are defined as:

$$\begin{aligned}
 \text{Reynolds Number :} & & Re_\infty &= \frac{\rho_\infty V_\infty c}{\mu_\infty} \\
 \text{Mach Number :} & & M_\infty &= \frac{V_\infty}{a_\infty} \\
 \text{Prandl Number :} & & Pr &= \frac{\mu C_p}{k}
 \end{aligned} \tag{2.13}$$

where C_p is the specific heat at constant pressure. For all computations in this work, $Pr = 0.72$ is assumed. V_∞ is the free-stream total velocity given by $\sqrt{u_\infty^2 + v_\infty^2 + w_\infty^2}$.

The Navier-Stokes equations in non-dimensional form can again be represented as eqn. 2.1, if the superscript $*$ is ignored. The non-dimensional inviscid and viscous flux terms will also have identical form as before. Differences arise in the non-dimensional stress and conduction terms, which now become a function of the non-dimensional parameters (Reynolds number and Prandtl number). The non-dimensional mean stresses are given by:

$$\tau_{ij} = \frac{\mu M_\infty}{Re_\infty} \left[\left(\frac{\partial u_i}{\partial x_j} + \frac{\partial u_j}{\partial x_i} \right) - \frac{2}{3} \frac{\partial u_k}{\partial x_k} \delta_{ij} \right] \quad (2.14)$$

And the non-dimensional thermal conduction terms are given by:

$$q_i = - \frac{\mu M_\infty}{Re_\infty Pr(\gamma - 1)} \frac{\partial T}{\partial x_i} \quad (2.15)$$

Note that, all the variables in eqns. 2.14 and 2.15 are non-dimensional. The superscript $*$ is purposefully neglected.

Rotating Reference Frame

For computation of unsteady flows involving moving bodies, the governing equations are usually solved in the inertial frame of reference. This requires computation of the metric terms and connectivity information of the overset grids (if any) at every time-step. This additional cost can be avoided for hovering rotors if the equations are solved in the rotating reference frame [21]. To account for the non-inertial reference frame, the fluxes in eqn. 2.1 become:

$$F_i = \left\{ \begin{array}{c} \rho(u - u_g) \\ \rho u(u - u_g) + p \\ \rho(u - u_g)v \\ \rho(u - u_g)w \\ (u - u_g)(e + p) \end{array} \right\} \quad (2.16)$$

$$G_i = \left\{ \begin{array}{c} \rho(v - v_g) \\ \rho(v - v_g)u \\ \rho(v - v_g)v + p \\ \rho(v - v_g)w \\ (v - v_g)(e + p) \end{array} \right\} \quad (2.17)$$

$$H_i = \left\{ \begin{array}{c} \rho(w - w_g) \\ \rho(w - w_g)u \\ \rho(w - w_g)v \\ \rho(w - w_g)w + p \\ (w - w_g)(e + p) \end{array} \right\} \quad (2.18)$$

where, $U = \{u, v, w\}$ is the vector of physical velocities in the inertial frame and $U_g = \{u_g, v_g, w_g\} = \Omega \times r$ is the rotational velocity vector. Ω is the angular velocity vector given by $\{0, 0, \Omega_z\}$ for a hovering rotor, rotating about z -axis and r is the relative position vector from the axis of rotation. Thus, for a hovering rotor rotating about z -axis, U_g becomes $\{-\Omega_z y, \Omega_z x, 0\}$. In addition, the relative acceleration terms have to be included as a source term vector S in eqn. 2.1; and for the hovering rotor can be simplified to:

$$S = \begin{pmatrix} 0 \\ \rho v \Omega_z \\ -\rho u \Omega_z \\ 0 \\ 0 \end{pmatrix} \quad (2.19)$$

Transformation to Generalized Curvilinear Coordinates

The governing equations can be expressed in strong conservation law form in generalized body-conforming curvilinear coordinate system with the aid of the chain rule of partial derivatives. In effect, the equations after being transformed to the computational coordinates ξ, η, ζ are as follows:

$$\frac{\partial \hat{Q}}{\partial t} + \frac{\partial \hat{F}}{\partial \xi} + \frac{\partial \hat{G}}{\partial \eta} + \frac{\partial \hat{H}}{\partial \zeta} = \hat{S} \quad (2.20)$$

where,

$$\hat{Q} = \frac{1}{J} Q \quad (2.21)$$

$$\hat{F} = \frac{1}{J} [\xi_t Q + \xi_x (F_i - F_v) + \xi_y (G_i - G_v) + \xi_z (H_i - H_v)] \quad (2.22)$$

$$\hat{G} = \frac{1}{J} [\eta_t Q + \eta_x (F_i - F_v) + \eta_y (G_i - G_v) + \eta_z (H_i - H_v)] \quad (2.23)$$

$$\hat{H} = \frac{1}{J} [\zeta_t Q + \zeta_x (F_i - F_v) + \zeta_y (G_i - G_v) + \zeta_z (H_i - H_v)] \quad (2.24)$$

$$\hat{S} = \frac{1}{J} S \quad (2.25)$$

where J is the Jacobian of the coordinate transformation (i.e., $J = \det \left(\frac{\partial(\xi, \eta, \zeta)}{\partial(x, y, z)} \right)$)

2.3.2 Reynolds Averaged Navier-Stokes Equations

The solution of the governing equations, eqn. 2.20, do not raise any fundamental difficulties in the case of inviscid or laminar flows. However, all the flows encountered in engineering practice are turbulent. Turbulent flow is characterized by chaotic motion of molecules, leading to increased momentum and energy exchange between various layers of fluid and also between the fluid and the wall. Although these chaotic fluctuations of the flow variables are of deterministic nature, the number of grid points needed for sufficient spatial resolution of all the scales of these fluctuations present a significant problem. Despite the performance of modern supercomputers, a direct simulation of turbulence by the time-dependent Navier-Stokes equations eqn. 2.20, called Direct Numerical Simulation (DNS), is still possible only for rather simple flow cases at low Reynolds numbers.

A first level of approximation of turbulence is achieved using the Large-Eddy Simulation (LES) approach. The development of LES is founded on the observation that the small scales of turbulent motion possess a more universal character than the large scales, which transport the turbulent energy. Thus, the idea is to resolve only the large eddies accurately and to approximate the effects of the small scales by a relatively simple subgrid-scale model. Since LES requires significantly less grid points than DNS, the investigation of turbulent flows at much higher Reynolds numbers becomes feasible. But because LES is inherently three-dimensional and unsteady, it remains computationally still very demanding. Thus, LES is still far from becoming an engineering tool.

The next level of approximation is represented by the so-called Reynolds-Averaged Navier-Stokes equations (RANS). This approach, which was presented

by Reynolds in 1895, is based on the decomposition of the flow variables into mean and fluctuating parts. The motivation behind this is that in most engineering and physical processes, one is only interested in the mean quantities. Therefore, any flow variable, ϕ , can be written as:

$$\phi = \bar{\phi} + \phi' \quad (2.26)$$

where $\bar{\phi}$ is the mean part and ϕ' is the fluctuating part. The mean part, $\bar{\phi}$, is obtained using Reynolds averaging given by

$$\bar{\phi} = \frac{1}{\bar{\chi}} \lim_{\Delta t \rightarrow \infty} \frac{1}{\Delta t} \int_0^{\Delta t} \chi \phi(t) dt \quad (2.27)$$

where $\chi = 1$, if ϕ is density or pressure and $\chi = \rho$, if ϕ is other variables such as velocity, internal energy, enthalpy and temperature. By definition, the Reynolds average of the fluctuating part is zero.

The decomposed variables are then inserted into the Navier-Stokes equations (eqn. 2.20) and the equations are Reynolds averaged to obtain the mathematical description of the mean flow properties. If the overbar on the mean flow variables is dropped, the resulting equations are identical to the instantaneous Navier-Stokes equations with the exception of additional terms in the momentum equation and the energy equation (not present if heat transfer is neglected). The extra terms in the momentum equation accounts for the additional stress due to turbulence and are called the **Reynolds-stress tensor**. These stresses add to the viscous stress terms given in eqn. 2.11 and are given by:

$$\tau_{ij}^R = -\overline{\rho u_i' u_j'} \quad (2.28)$$

However, with the introduction of Reynolds-stress terms, we obtain six additional unknowns in the Reynolds-averaged momentum equations. In order to close the RANS equation, the Reynolds stress terms are approximated using a turbulence model. Details of turbulence modeling will be briefly discussed in section 2.4.4.

2.3.3 Initial and Boundary Conditions

The governing equations described in the previous section are very generic and do not change from one problem to another. Therefore, apart from these conservation equations, we need additional criteria, namely initial and boundary conditions to define a problem.

Initial conditions are specified by assigning the density, flow velocities and pressure everywhere in the solution region before the start of the solution procedure. Typically for a hovering rotor simulation, the initial conditions are set such that the density and pressure are freestream values and the flow velocities are zero.

The two common boundary conditions for an external flow are the wall boundary condition and the far-field boundary condition. Wall boundaries are natural boundaries of the physical domain which arise from the wall surfaces being exposed to the flow. For a viscous fluid which passes a solid wall, the relative velocity between the surface and the fluid directly at the surface is zero. The truncation of the physical domain or system for the purpose of numerical simulation leads to artificial far-field boundaries, where certain physical quantities have to be prescribed. The far-field boundary condition has to fulfill two basic requirements. First, the truncation of the domain should have no notable

effects on the flow solution as compared to the infinite domain. Second, any outgoing disturbances must not be reflected back into the flow-field.

Additional boundaries become manifest in the numerical simulation due to the mesh system and grid topology, namely, wake-cut boundary, periodic boundary, boundary between blocks, chimera boundary etc. All of these boundaries are numerical in nature rather than physical.

The numerical implementation of both the physical and numerical boundary conditions will be discussed in section 2.4.5.

2.4 Numerical Solution (Baseline Algorithm)

The baseline flow solver is the Transonic Unsteady Rotor Navier-Stokes (TURN) research code which has been applied to a variety of helicopter rotor problems [21]. The TURN code solves the compressible RANS equations on 2 or 3 dimensional single block structured grids. The differential eqn. 2.20 is discretized in space and time in a finite volume approach. In this approach, fictitious volumes are created around each grid point. A fictitious volume is created around a point using the midpoints of the lines joining the adjacent grid points to the grid point. The faces of this new volume lie exactly in the middle of two grid points. This volume is treated as a control volume and fluxes are evaluated at the faces of the volume, resulting in conservation equations for the volume.

The semi-discrete conservative approximation of eqn. 2.20 can be written as:

$$\frac{\partial \hat{Q}}{\partial t} = -\frac{\hat{F}_{j+\frac{1}{2}} - \hat{F}_{j-\frac{1}{2}}}{\Delta \xi} - \frac{\hat{G}_{k+\frac{1}{2}} - \hat{G}_{k-\frac{1}{2}}}{\Delta \eta} - \frac{\hat{H}_{l+\frac{1}{2}} - \hat{H}_{l-\frac{1}{2}}}{\Delta \zeta} + \hat{S}_{j,k,l} \quad (2.29)$$

where, (j, k, l) are the indices corresponding to the (ξ, η, ζ) directions in the

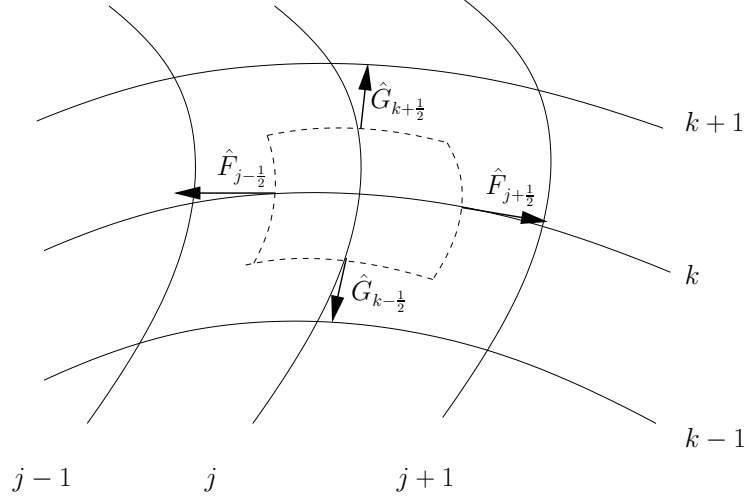


Figure 2.6: Schematic showing computational cell.

transformed coordinate system and $(j \pm \frac{1}{2}, k \pm \frac{1}{2}, l \pm \frac{1}{2})$ define the cell-interfaces of the control volumes as shown in Fig. 2.6 (2D cell shown for simplicity). The spatial discretization (consisting of the inviscid and viscous fluxes) reduces to evaluating the interfacial fluxes $\hat{F}_{j+\frac{1}{2}}, \hat{G}_{k+\frac{1}{2}}, \hat{H}_{l+\frac{1}{2}}$ for every cell (j, k, l) in the domain.

2.4.1 Inviscid Terms

The inviscid part of the interfacial flux is computed using upwind schemes [61]. Upwind schemes have the advantage that the wave propagation property of the inviscid equations is accounted for (albeit approximately) in the flux calculation. To evaluate the interfacial fluxes, the Monotone Upstream-Centered Scheme for Conservation Laws (MUSCL) [61] approach is used. This procedure involves two steps.

The first step is the evaluation of the left state and the right state at each interface, as shown in Fig. 2.7. It can be seen from the figure that left and right states are calculated at the interface $(j + 1/2)$ using the reconstruction in cell j

and $j + 1$. The order of accuracy of the evaluation of the left and right states is governed by the stencil used (number of neighboring points). Piecewise cubic reconstruction with Koren's limiter [62] is used in the baseline TURNS.

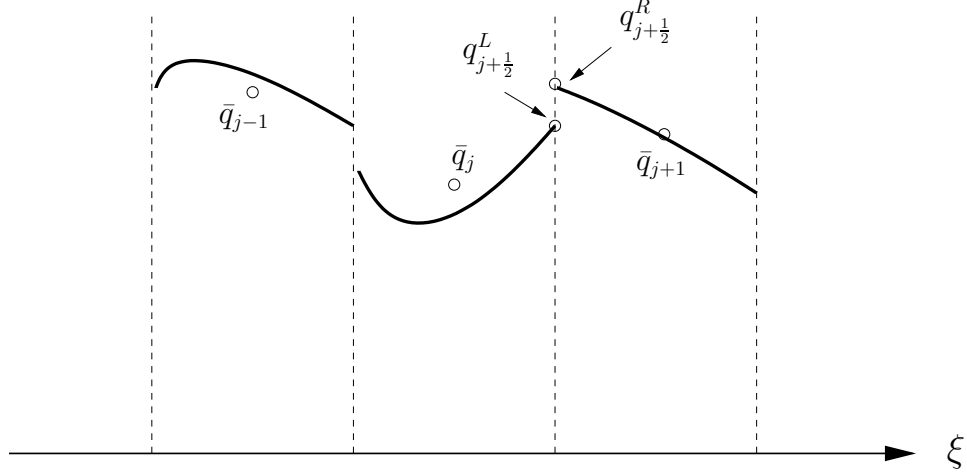


Figure 2.7: Schematic of one dimensional piecewise reconstruction.

After evaluation of the left and right states at the cell interface, the next step is to calculate the fluxes at the interface. The left and right states can be used to define a local Riemann problem and the interfacial flux can be obtained using any flux splitting scheme. The baseline TURNS code uses the Roe flux difference splitting [63] in which, the interfacial flux is given by:

$$F(q^L, q^R) = \frac{F(q^L) + F(q^R)}{2} - |\hat{A}(q^L, q^R)| \frac{q^R - q^L}{2} \quad (2.30)$$

where \hat{A} is the Roe-averaged Jacobian matrix.

Third Order Differencing using Koren's Limiter

Koren's differentiable limiter [62] is used to limit the high order reconstruction, so that the resulting scheme is third order accurate in smooth regions and is

progressively lower order accurate (down to first order at a solution discontinuity) in high gradient regions. Given cell averaged values $\{\bar{q}_{i+1}, \bar{q}_i, \bar{q}_{i-1}\}$, the cell reconstruction is such that the interface value $q_{i+1/2}^L$ and $q_{i-1/2}^R$ are given by:

$$q_{i+1/2}^L = \bar{q}_i + \phi_i \left[\frac{1}{3}(\bar{q}_{i+1} - \bar{q}_i) + \frac{1}{6}(\bar{q}_i - \bar{q}_{i-1}) \right] \quad (2.31)$$

$$q_{i-1/2}^R = \bar{q}_i - \phi_i \left[\frac{1}{3}(\bar{q}_{i+1} - \bar{q}_i) + \frac{1}{6}(\bar{q}_i - \bar{q}_{i-1}) \right] \quad (2.32)$$

where, ϕ is the differentiable limiter which is defined by:

$$\phi_i = \frac{3\Delta\bar{q}_i\nabla\bar{q}_i + \epsilon}{2(\Delta\bar{q}_i - \nabla\bar{q}_i)^2 + 3\Delta\bar{q}_i\nabla\bar{q}_i + \epsilon} \quad (2.33)$$

where, ϵ is a small number used to prevent division by zero and Δ and ∇ are forward and backward difference operators defined by $\Delta\bar{q}_i = (\bar{q}_{i+1} - \bar{q}_i)$ and $\nabla\bar{q}_i = (\bar{q}_i - \bar{q}_{i-1})$.

2.4.2 Viscous Terms

Typically, in the baseline TURNS code, the Thin-layer approximation is used while discretizing the viscous terms. In this approximation, only the terms that have a very strong dependence on the derivative in the wall-normal direction are considered. The basis for this argument is the fact that for attached flows, the boundary layer is very thin and the streamwise and spanwise gradients are much smaller than the wall-normal gradients. This approximation is valid in the near-wall region for high Reynolds number attached flows. However, for low Reynolds number small-scale flows where there are thick boundary layers and massive separation, the thin layer assumption fails and one has to consider

the full viscous terms. A complete listing of the viscous terms after coordinate transformation can be found in [64]. Numerical discretization of these terms involve expressions of the form:

$$\frac{\partial}{\partial \xi} \left(\alpha \frac{\partial \beta}{\partial \eta} \right) \quad (2.34)$$

These terms are computed using second order accurate central differencing. Thus, the above expression will be discretized as:

$$\frac{1}{\Delta \xi} \left(\left[\alpha_{j+\frac{1}{2},k} \frac{\beta_{j+\frac{1}{2},k+1} - \beta_{j+\frac{1}{2},k}}{\Delta \eta} \right] - \left[\alpha_{j-\frac{1}{2},k} \frac{\beta_{j-\frac{1}{2},k} - \beta_{j-\frac{1}{2},k-1}}{\Delta \eta} \right] \right) \quad (2.35)$$

where

$$\delta_{j+\frac{1}{2},k} = \frac{\delta_{j,k} + \delta_{j+1,k}}{2}, \quad (\delta = \alpha, \beta) \quad (2.36)$$

2.4.3 Time Integration

Once, the right hand side (RHS) of the eqn. 2.29 is evaluated (including viscous fluxes and source terms), the conservative variables, Q are evolved in time. There are mainly two types of methods to evolve the solution in time, explicit or implicit. The explicit methods only use information at the previous time step to calculate the conservative variables at the new time step, where as the implicit methods indirectly use information at the new time step and require matrix inversion of large sparse matrices. Explicit methods have restrictions on time step size based on the mesh size and flow quantities. However, most implicit methods do not have such restrictions. Hence, implicit methods are preferred for RANS

calculations with fine meshes at the wall surfaces. The baseline TURNS code uses the implicit Lower Upper Symmetric Gauss Siedel Scheme (LUSGS) [65,66] along with Newton sub-iterations [67] in order to remove factorization errors and to fully recover time accuracy.

If an index for time step is included in eqn. 2.29, an implicit scheme can be written as the following.

$$\frac{\partial \hat{Q}^{n+1}}{\partial t} = -\frac{\hat{F}_{j+\frac{1}{2}}^{n+1} - \hat{F}_{j-\frac{1}{2}}^{n+1}}{\Delta \xi} - \frac{\hat{G}_{k+\frac{1}{2}}^{n+1} - \hat{G}_{k-\frac{1}{2}}^{n+1}}{\Delta \eta} - \frac{\hat{H}_{l+\frac{1}{2}}^{n+1} - \hat{H}_{l-\frac{1}{2}}^{n+1}}{\Delta \zeta} + \hat{S}_{j,k,l}^{n+1} \quad (2.37)$$

In the equation above, all the quantities are desired at the new time step ($n+1$), but the fluxes are not known at the ($n+1$) time step, so there is a need for them to be linearized and expressed in terms of fluxes and conservative variables at step (n). The nonlinear terms are linearized in time about \hat{Q}^n by Taylor Series as:

$$\hat{F}^{n+1} = \hat{F}^n + \hat{A} \Delta \hat{Q}^n + O(h^2) \quad (2.38)$$

$$\hat{G}^{n+1} = \hat{G}^n + \hat{B} \Delta \hat{Q}^n + O(h^2) \quad (2.39)$$

$$\hat{H}^{n+1} = \hat{H}^n + \hat{C} \Delta \hat{Q}^n + O(h^2) \quad (2.40)$$

where $\hat{A} = \frac{\partial \hat{F}}{\partial \hat{Q}}$, $\hat{B} = \frac{\partial \hat{G}}{\partial \hat{Q}}$ and $\hat{C} = \frac{\partial \hat{H}}{\partial \hat{Q}}$. The source terms can also be linearized with respect to the conservative variables. Note that the linearization are second order accurate and so if a second order time scheme is chosen (typically used in TURNS), the linearization would not degrade the time accuracy.

If the linearized fluxes are substituted in eqn. 2.37 along with assuming first order Euler implicit time discretization ($\partial_t \hat{Q}^{n+1} = \frac{\Delta \hat{Q}^n}{\Delta t}$), the equation can be written in 'delta form' as:

$$\left[I + \Delta t(\delta_\xi \hat{A}^n + \delta_\eta \hat{B}^n + \delta_\zeta \hat{C}^n) \right] \Delta \hat{Q}^n = -\Delta t \left[\delta_\xi \hat{F}^n + \delta_\eta \hat{G}^n + \delta_\zeta \hat{H}^n - \hat{S}^n \right] \quad (2.41)$$

which is simplified as

$$\text{LHS } \Delta \hat{Q}^n = -\Delta t \text{ RHS} \quad (2.42)$$

The right hand side (RHS) captures the physics, while, the left hand side (LHS) is numerics, which determines the rate of convergence. It can be easily shown that the implicit algorithm produces a large banded system of algebraic equations. The matrix is sparse, but it would be very expensive to solve the algebraic system in order to obtain a solution for ΔQ^n . Further approximations to the LHS are necessary for ease of inversion of the matrix, but the penalty comes in some loss in the speed of convergence.

One such approximation is made in the LUSGS algorithm. In the LUSGS algorithm, the LHS is factorized by grouping together terms depending upon whether they lie in the lower portion, along the diagonal, or in the upper portion of the unfactored LHS. By treating the left hand side using first order split flux Jacobians and neglecting the viscous contribution, one obtains:

$$L = \Delta t(-\hat{A}_{j-1,k,l}^+ - \hat{B}_{j,k-1,l}^+ - \hat{C}_{j,k,l-1}^+) \quad (2.43)$$

$$D = I + \Delta t(\hat{A}_{j,k,l}^+ - \hat{A}_{j,k,l}^- + \hat{B}_{j,k,l}^+ - \hat{B}_{j,k,l}^- + \hat{C}_{j,k,l}^+ - \hat{C}_{j,k,l}^-) \quad (2.44)$$

$$U = \Delta t(\hat{A}_{j+1,k,l}^- + \hat{B}_{j,k+1,l}^- + \hat{C}_{j,k,l+1}^-) \quad (2.45)$$

Now, one can write the resulting LUSGS scheme as a lower-upper splitting that takes the following form:

$$\begin{aligned}
[L + D + U]\Delta\hat{Q}^n &= D[D^{-1}L + I + D^{-1}U]\Delta\hat{Q}^n \\
&\approx D[I + D^{-1}L][I + D^{-1}U]\Delta\hat{Q}^n \\
&= [D + L]D^{-1}[D + U]\Delta\hat{Q}^n \\
&= -\Delta t [RHS^n]
\end{aligned} \tag{2.46}$$

This can be solved by a forward and a backward sweep using a two-factor scheme that can be written as:

$$\begin{aligned}
[D + L]\Delta\bar{Q} &= -\Delta t[RHS] \\
[D + U]\Delta\hat{Q} &= D\Delta\bar{Q}
\end{aligned} \tag{2.47}$$

Additional simplifications are made by approximating the split flux Jacobians (e.g., \hat{A}^+ and \hat{A}^-) in terms of spectral radius (e.g., σ_ξ) as $\hat{A}^+ = \frac{1}{2}(\hat{A} + \sigma_\xi)$ and $\hat{A}^- = \frac{1}{2}(\hat{A} - \sigma_\xi)$. This reduces D to a diagonal matrix and the matrix inversion reduces to a scalar inversion. Note that, the above derivation is strictly valid for Euler equations. The contribution of viscous fluxes can be approximated by adding a scalar term to the spectral radius (e.g. $\sigma_\xi + \sigma_\xi^v$), where

$$\sigma_\xi^v = \frac{2\mu (\xi_x^2 + \xi_y^2 + \xi_z^2)}{\rho} \tag{2.48}$$

Approximation of the LHS results in factorization errors. In order to remove these factorization errors and to fully improve time accuracy, the baseline TURNS performs Newton sub-iterations at each physical time step. Details are provided in section. 2.6.1. It should be mentioned that, the LUSGS scheme can be easily extended to 2^{nd} order backward difference in time (BDF2) by substituting $\partial_t\hat{Q}^{n+1} = \frac{3\hat{Q}^{n+1} - 4\hat{Q}^n + \hat{Q}^{n-1}}{2\Delta t}$, the scheme employed in TURNS.

2.4.4 Turbulence Modeling

The turbulence modeling problem is to close the RANS equation by approximating the **Reynolds stress term** (eqn. 2.28). With the assumption of isotropic eddy viscosity, the Reynolds stresses can be represented by:

$$\tau_{ij}^R = \mu_t \left[\left(\frac{\partial u_i}{\partial x_j} + \frac{\partial u_j}{\partial x_i} \right) - \frac{2}{3} \frac{\partial u_k}{\partial x_k} \delta_{ij} \right] \quad (2.49)$$

where μ_t is the turbulent viscosity. The evaluation of turbulent viscosity is not trivial. Various turbulence models, which aim at obtaining the turbulent viscosity field have been developed in the past. The models range from zero equation algebraic turbulence models (Baldwin-Lomax [68]), four equation turbulence models ($\nu^2 - f$ model [69]) to Reynolds Stress models. The zero equation model developed by Baldwin and Lomax calculates the turbulent viscosity as an algebraic function of the conservative variables. On the other hand, the $\nu^2 - f$ model by Durbin solves four differential equations to obtain four scalar field variables (k , ϵ , ν^2 and f). The turbulent viscosity is obtained as an algebraic function of these four variables. Apart from the possible increase in stiffness of the differential equations, it is imperative from the above discussion that the additional computational time to obtain the solution of turbulent viscosity will be extremely high in the four equation model as opposed to the zero equation algebraic model.

The baseline TURNS code uses the algebraic Baldwin-Lomax [68] turbulence model. The applicability of this model, is however restricted to steady and attached flows (as seen, for instance in [70]). However, in practice it is a reasonable first approach even when these conditions are not strictly achieved. Another option in the baseline code is the one equation model of Spalart and

Allmaras [71]. Though relatively recent, the Spalart-Allmaras (SA) model has gained enormous popularity in the aerospace flow problems as it was developed with such applications in mind. As a result, the SA model is used in all the computations in this work.

Spalart-Allmaras (SA) Turbulence Model

In the SA model, the Reynolds stresses are related to the mean strain by the isotropic relation, $\overline{u'_i u'_j} = -2\nu_t S_{ij}$, where ν_t is the turbulent eddy viscosity, which is obtained by solving a PDE for a related variable ($\overline{\nu}$), given by:

$$\frac{\partial \overline{\nu}}{\partial t} + V \cdot (\nabla \overline{\nu}) = \frac{1}{\sigma} [\nabla \cdot ((\overline{\nu} + \nu) \nabla \overline{\nu}) + c_{b2} (\nabla \nu)^2] + c_{b1} \overline{S} \overline{\nu} - c_{w1} f_w \left[\frac{\overline{\nu}}{d} \right]^2 \quad (2.50)$$

The eddy viscosity ν_t is related to by the relation,

$$\nu_t = \overline{\nu} f_{v1} \quad (2.51)$$

where f_{v1} is a function of $\overline{\nu}$ and the molecular viscosity ν and is defined as:

$$f_{v1} = \frac{\chi^3}{\chi^3 + c_{v1}^3} \quad (2.52)$$

with $\chi = \frac{\overline{\nu}}{\nu}$ and $c_{v1} = 7.1$. The left hand side of equation 2.50 accounts for the convection of the working variable at the mean flow velocity V . The first term on the right hand side represents the diffusion, followed by the production and destruction terms. Further details and expressions for \overline{S} , d , σ , c_{b1} , c_{b2} , c_{w1} and f_w are provided in Ref. [37].

2.4.5 Boundary Conditions

There are several types of boundary conditions commonly encountered in the solution of the Navier-Stokes equations. Physical boundary conditions arising during the solution procedure were described in section 2.3.3. Apart from these, the grid topology presents additional numerical boundary conditions. This section describes the numerical treatment of both types of these boundary conditions. Note that this section only includes boundary conditions from the baseline TURNS code and does not include those implemented as a part of the current work.

Typical boundaries found in the solution of the Navier-Stokes equations can be shown on a schematic C-mesh, Fig. 2.8. They include wall boundary, far-field boundary and wake cut boundary. Additionally, a periodic boundary is very commonly used in hovering rotor simulations. A brief numerical description of these boundaries are given below:

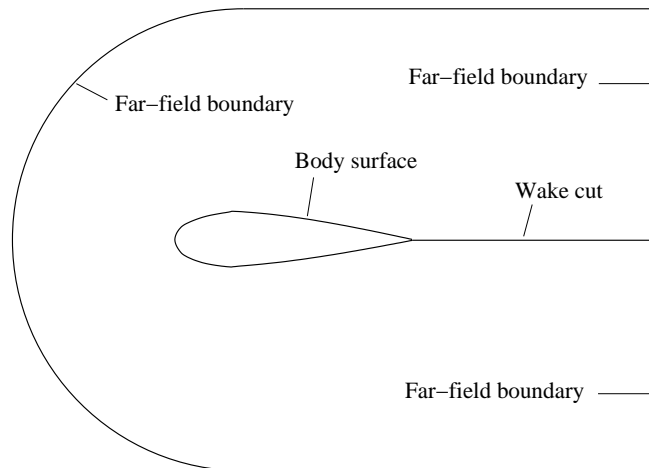


Figure 2.8: C-mesh topology.

Wall Boundary Condition

In this work, all the solid walls are treated as viscous wall. Therefore no-slip condition is applied, which requires the fluid velocity at the wall be equal to the surface velocity. At the solid wall, the density (ρ) is extrapolated (zeroth order) from the interior of the domain. The pressure (p) is then obtained from the normal momentum equation.

Far-field Boundary Condition

Ideally, the far-field boundaries should be placed far enough (typically 20 – 30 chord lengths) from body surfaces such that the prevailing conditions are very close to free-stream, so that no spurious wave reflections occur at the boundary. To determine the boundary conditions, characteristic-based Riemann invariants [72] are used. In this approach, based on the direction of the velocity vector and the sonic velocity, the corresponding Riemann invariants are extrapolated either from the interior or from the free-stream.

For a hovering rotor, the wake vortices stay under the blade at all times and the resulting induced velocities can be expected to be significant at distances of a few rotor radii. For computational efficiency, the far-field boundaries are held to less than five rotor radii away from the blade surface. In this case, the linearized characteristic free-stream boundary condition cannot be used since the flow velocities are large. In this work, the point-sink boundary condition approach of Srinivasan et. al. [21] is used. A schematic of this approach is shown in Fig. 2.9. It is well known from momentum theory [1] that the asymptotic contraction of the vortex wake of a hovering rotor is approximately $R/\sqrt{2}$ and the non-dimensional downwash velocity, resulting from the thrust of the rotor,

at such a downstream section is approximately $2\sqrt{C_T}/2$. As shown in the figure, this is used as the outflow velocity in the region marked "Outflow" in the far-field boundary.

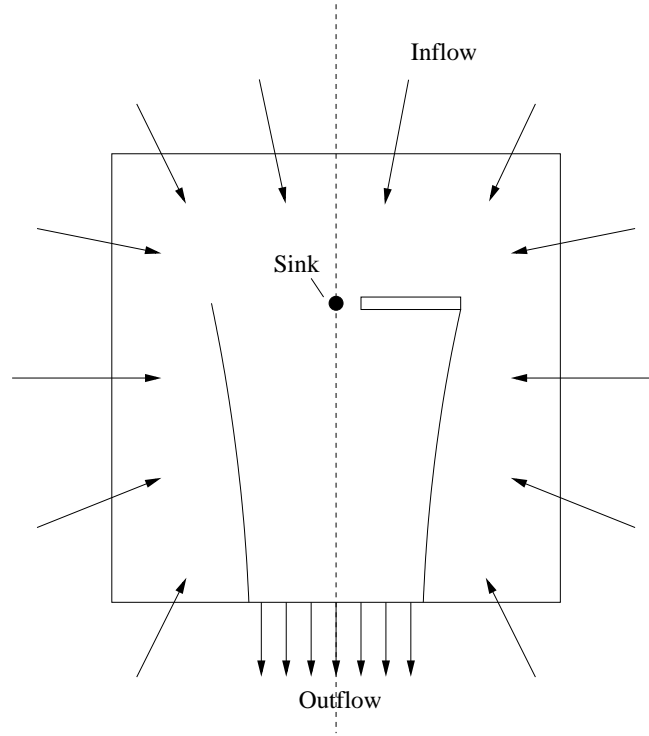


Figure 2.9: Schematic of point-sink boundary condition.

In order to satisfy global mass conservation, the rest of the far-field boundary is then assumed to be an inflow, the velocities of which are assumed to be induced by a point sink placed on the rotor hub. The magnitude of this spherically symmetric induced velocity is given by:

$$\frac{V_{induced}}{\Omega R} = \frac{1}{4} \sqrt{\frac{C_T}{2}} \left(\frac{R^2}{x^2 + y^2 + z^2} \right) \quad (2.53)$$

where, x, y, z is the position vector relative to the placement of the sink. Linearized Riemann invariants are then used to determine the conserved variables at the boundary.

Note that for a coaxial rotor simulation, the sink is placed on the hub of the top rotor. Even though this is not fully correct, this does not create any additional error considering the fact that the sink-outflow boundary condition is just an approximation of the actual physics.

Wake Cut Boundary Condition

At the wake cut region, grid planes collapse on to each other. Along these planes, an explicit simple average of the solution from either side is used. Similar boundaries are present at the root and tip of a C-O grid and are treated in the same manner.

Periodic Boundary Condition

The hovering rotor calculation can be simplified by assuming periodicity, thereby performing the entire calculation by simulating just one blade. The interaction with the remaining blades is enforced via rotational periodic boundary conditions. The periodic boundary condition is implemented by creating dummy cells at the boundary, where the vector quantities are prescribed using coordinate rotation and the scalar quantities are set identical.

2.5 Limitations of Current Methodology

The baseline methodology has certain limitations when applied to micro and coaxial rotors. These limitations are described in this section.

Micro Rotors

Micro-scale rotors typically operate at low rotational tip Mach numbers. It is well known that classical numerical methods for the simulation of compressible viscous flows from the solution of the Reynolds Averaged Navier-Stokes (RANS) equations perform in a satisfying way for most flow regimes, from medium subsonic flow to hypersonic flow. However, in the low subsonic flow regime these methods give poor results in terms of convergence rate to steady state (or within a time step for unsteady flows) and solution accuracy.

The difficulty in convergence of the compressible equations for low Mach numbers are associated with the large ratio between the acoustic wave speeds and the material waves convected at the fluid speed. The time step size for the solver is restricted by the stability limit imposed by the acoustic wave. However, the material waves travel a very short distance compared to the acoustic waves for the same time step size. To obtain a converged solution, all the waves should travel to the boundary (in reality, they also need time for any reflections to settle down). Since the material waves move very slowly, they result in it taking a long time for the solution to converge.

The other issue with compressible flow solvers for low Mach numbers is the solution inaccuracy. At low Mach numbers, the Roe scheme presents an excess of artificial viscosity and as a result leads to excess dissipation. Roe flux splitting was given in eqn. 2.30. It can be shown that the dissipation for the Roe scheme is proportional to $|\hat{A}|$, while the fluxes are proportional to \hat{A} , where \hat{A} is the Roe-averaged Jacobian matrix.

After manipulating terms of $|\hat{A}|$ and \hat{A} in one-dimension for low Mach numbers ($M \rightarrow 0$), along with having flow velocity and density of order 1, one

obtains:

$$\hat{A} \sim \begin{bmatrix} 0 & O(1) & 0 \\ O(1) & O(1) & O(1) \\ O(\frac{1}{M^2}) & O(\frac{1}{M^2}) & O(1) \end{bmatrix} \quad (2.54)$$

$$|\hat{A}| \sim \begin{bmatrix} O(1) & O(M) & O(M) \\ O(\frac{1}{M}) & O(\frac{1}{M}) & O(M) \\ O(\frac{1}{M}) & O(\frac{1}{M}) & O(\frac{1}{M}) \end{bmatrix} \quad (2.55)$$

It can be noted that several terms in $|\hat{A}|$ have different order of Mach number from terms in \hat{A} . This difference in order of Mach number leads to large dissipation terms (evident from the momentum equation, where \hat{A} has $O(1)$, and $|\hat{A}|$ has $O(1/M)$; in the energy equation the dissipation terms are too small) for low Mach number flows and is a major source of inaccuracy in such flow regimes.

Coaxial Rotors

A major difficulty in RANS-based CFD simulations of coaxial rotor computations is the enormous computational cost required to handle the counter-rotating system. Additionally, in order to capture the blade-vortex and vortex-vortex interactions correctly, it is important to accurately represent the formation and evolution of the wake. Hence, along with using accurate numerical schemes and reliable turbulence models, we need to have sufficient grid resolution to resolve the details of the flow physics. This requires months of computational time with the existing solver and therefore makes it impractical.

An additional difficulty in coaxial rotor simulations arise in the information transfer between the blade and the background mesh. It is preferred not to

overlap the blade meshes of the two rotor systems due to two main reasons. Firstly, the current connectivity routine in OVERTURNS requires one mesh to be completely embedded in the other, which will not hold true here. Secondly, even if the connectivity routine could handle overlapping meshes, this will require determining connectivity information dynamically, which will increase the computational time. As a result, the extent of the outer boundary of the blade meshes is limited by the inter-rotor spacing. Typically, the spacing between the rotors is about 1 – 5 chords, which means the extent of outer boundary of the blade meshes is limited to half that value. Additionally, we also want to ensure that the blade mesh is not stretched too rapidly in the wall normal direction. As an outcome of this, the grid spacing at the outer boundary of the blade mesh ends up being much smaller than the grid spacing in the background mesh. Information transfer between unequal sized meshes can lead to severe loss of accuracy. This problem can be solved by using a finer intermediate background mesh to transfer information from the blade to the outer background mesh. The resulting overset system will be a 3-mesh overset system. However, the current overset methodology implemented in OVERTURNS can handle only overset system consisting of two meshes and therefore, does not permit the use of intermediate background mesh.

2.6 Improvements

To extend the capability of the baseline TURNS solver to simulate flow over small scale hovering coaxial rotors, several modification and additions are made to the flow solver. These modifications along with the limitations with the baseline methodology are tabulated in table 2.1. In order to remove the limitations

Table 2.1: Limitations of baseline methodology and improvements made in the current work to overcome these limitations.

Limitations of baseline methodology	Improvements made in current work
Convergence and accuracy of low Mach number flow calculations	Implementation of time-accurate low Mach preconditioner
Handling counter-rotating systems	Implementation of sliding mesh boundary condition
Large computational time for fine mesh calculations	Coarse-grain parallelization of the solver
Solution inaccuracy in overset methodology (mainly for coaxial rotor simulations)	Use of implicit hole-cutting method and implementation of improved blanking method

imposed by low Mach numbers, low Mach preconditioning is implemented. To allow coaxial rotor simulation, a sliding mesh interface condition is implemented which allows simulation of multi-bladed rotor systems using just one blade from each rotor system. The code is also parallelized to a certain extent, which enabled performing simulations using fine meshes in a reasonable amount of time. Finally, a few improvements are made in grid connectivity to ensure better transfer of solution from one mesh to another. All of the improvements are discussed in detail below:

2.6.1 Low Mach Preconditioning

Low Mach preconditioning has become the most popular methods to alleviate the issues associated with local low Mach compressible flows. Many of the low Mach number preconditioning methods have been summarized by Turkel [73–75]. The present work implements a preconditioned dual-time scheme in the diagonalized approximate factorization framework, described by Buelow et al. [76] and Pandya et al. [77]. The preconditioning is based on the one developed by Turkel [73]. To put into effect the low Mach preconditioning, the diagonalized algorithm and dual time-stepping is implemented.

Diagonalized Algorithm (DADI)

The diagonalized algorithm developed by Pulliam Chaussee [78] forms an alternative to LUSGS for implicit time inversion. In this algorithm, the left hand side of eqn. 2.41 is rewritten as given by Beam and Warming [79] for first order implicit in time:

$$\left[I + \Delta t(\delta_\xi \hat{A} + \delta_\eta \hat{B} + \delta_\zeta \hat{C}) \right] \Delta \hat{Q} = \left[I + \Delta t \delta_\xi \hat{A} \right] \left[I + \Delta t \delta_\eta \hat{B} \right] \left[I + \Delta t \delta_\zeta \hat{C} \right] \Delta \hat{Q} \quad (2.56)$$

The computational work can be decreased by introducing a diagonalization of the blocks in the implicit operators as developed by Pulliam and Chaussee [78]. The eigensystem of the flux Jacobians \hat{A} , \hat{B} and \hat{C} are used in this construction.

The inviscid flux Jacobians \hat{A}_i , \hat{B}_i and \hat{C}_i each have real eigenvalues and a complete set of eigenvectors. Therefore, the inviscid flux Jacobian matrices can be diagonalized as:

$$\begin{aligned}
\Lambda_\xi &= T_\xi^{-1} \hat{A}_i T_\xi \\
\Lambda_\eta &= T_\eta^{-1} \hat{B}_i T_\eta \\
\Lambda_\zeta &= T_\zeta^{-1} \hat{C}_i T_\zeta
\end{aligned} \tag{2.57}$$

where T_ξ is the left set of eigenvectors of matrix \hat{A}_i and T_ξ^{-1} is the right set of eigenvectors of matrix \hat{A}_i . Similarly, T_η and T_ζ are matrices corresponding to matrices \hat{B}_i and \hat{C}_i , respectively. The set of eigenvalues of matrix \hat{A}_i are given in matrix Λ_ξ . Similarly, Λ_η and Λ_ζ contain eigenvalues of \hat{B}_i and \hat{C}_i .

Ignoring the viscous contribution on the LHS, eqn. 2.41 can be rewritten as:

$$\begin{aligned}
& [T_\xi T_\xi^{-1} + \Delta t \delta_\xi (T_\xi \Lambda_\xi T_\xi^{-1})] [T_\eta T_\eta^{-1} + \Delta t \delta_\eta (T_\eta \Lambda_\eta T_\eta^{-1} \hat{B})] [T_\zeta T_\zeta^{-1} + \Delta t \delta_\zeta (T_\zeta \Lambda_\zeta T_\zeta^{-1})] \Delta \hat{Q}^n \\
& \approx T_\xi [I + \Delta t \delta_\xi \Lambda_\xi] T_\xi^{-1} T_\eta [I + \Delta t \delta_\eta \Lambda_\eta] T_\eta^{-1} T_\zeta [I + \Delta t \delta_\zeta \Lambda_\zeta] T_\zeta^{-1} \Delta \hat{Q}^n \\
& = -\Delta t [RHS^n]
\end{aligned} \tag{2.58}$$

The approximation assumes the eigenvectors of matrices \hat{A}_i , \hat{B}_i and \hat{C}_i to be constant spatially in the neighborhood of (j,k,l). The diagonal algorithm reduces the block tridiagonal inversion to 5×5 matrix multiplications and scalar tridiagonal inversions.

The diagonal algorithm as presented above is really only rigorously valid for the Euler equations. This is because we have neglected the implicit linearization of the viscous fluxes. The viscous flux Jacobians are not simultaneously diagonalizable with the inviscid flux Jacobians and therefore an approximation to the viscous Jacobian eigenvalues have to be used and is given by:

$$\begin{aligned}
\lambda_v(\xi) &= \overline{\mu J^{-1} (\xi_x^2 + \xi_y^2 + \xi_z^2)} J \rho^{-1} \\
\lambda_v(\eta) &= \overline{\mu J^{-1} (\eta_x^2 + \eta_y^2 + \eta_z^2)} J \rho^{-1} \\
\lambda_v(\zeta) &= \overline{\mu J^{-1} (\zeta_x^2 + \zeta_y^2 + \zeta_z^2)} J \rho^{-1}
\end{aligned} \tag{2.59}$$

The new form of diagonal algorithm is given by:

$$\begin{aligned}
&T_\xi [I + \Delta t(\delta_\xi \Lambda_\xi - \delta_{\xi\xi} \lambda_v(\xi))] T_\xi^{-1} T_\eta [I + \Delta t(\delta_\eta \Lambda_\eta - \delta_{\eta\eta} \lambda_v(\eta))] T_\eta^{-1} \\
&T_\zeta [I + \Delta t(\delta_\zeta \Lambda_\zeta - \delta_{\zeta\zeta} \lambda_v(\zeta))] T_\zeta^{-1} \Delta \hat{Q}^n = -\Delta t [RHS^n]
\end{aligned} \tag{2.60}$$

The first derivatives on the LHS of the above equation are discretized using upwind differencing and the second derivative are discretized using central differencing.

Dual Time-Stepping

Approximation of the LHS results in factorization errors. To remove these factorization errors and to recover time accuracy, one must perform sub-iterations at each physical time step. To carry out these iterations, eqn. 2.20 can be modified to consider a term that also contains a fictitious pseudo time (τ).

$$\frac{\partial \hat{Q}}{\partial \tau} + \frac{\partial \hat{Q}}{\partial t} + \frac{\partial \hat{F}}{\partial \xi} + \frac{\partial \hat{G}}{\partial \eta} + \frac{\partial \hat{H}}{\partial \zeta} = \hat{S} \tag{2.61}$$

Convergence of the pseudo-time(sub-iterations) at each physical time step is important for obtaining an accurate transient solution. Discretizing eqn. 2.61 with first order finite difference for both artificial and physical time results in:

$$\frac{\hat{Q}^{k+1} - \hat{Q}^k}{\Delta\tau} + \frac{\hat{Q}^{k+1} - \hat{Q}^n}{\Delta t} + \partial_\xi \hat{F}^{k+1} + \partial_\eta \hat{G}^{k+1} + \partial_\zeta \hat{H}^{k+1} = \hat{S}^{k+1} \quad (2.62)$$

where k is the pseudo-iteration counter and n is the time step counter. After linearization one gets:

$$\left[\frac{1}{\Delta\tau} + \frac{1}{\Delta t} + \delta_\xi \hat{A}^k + \delta_\eta \hat{B}^k + \delta_\zeta \hat{C}^k \right] \Delta \hat{Q}^k = - \left[\delta_\xi \hat{F}^k + \delta_\eta \hat{G}^k + \delta_\zeta \hat{H}^k - \hat{S}^k + \frac{\hat{Q}^k - \hat{Q}^n}{\Delta t} \right] \quad (2.63)$$

Defining $h = \frac{\Delta t}{1+(\Delta t/\Delta\tau)}$ and rearranging the above equation, one obtains:

$$\left[I + h(\delta_\xi \hat{A}^k + \delta_\eta \hat{B}^k + \delta_\zeta \hat{C}^k) \right] \Delta \hat{Q}^k = -h \left[\delta_\xi \hat{F}^k + \delta_\eta \hat{G}^k + \delta_\zeta \hat{H}^k - \hat{S}^k + \frac{\hat{Q}^k - \hat{Q}^n}{\Delta t} \right] \quad (2.64)$$

The above equation has similar form as eqn. 2.41 and therefore can be solved either using LUSGS or DADI scheme. The unsteady residual at each time step is given by:

$$\delta_\xi \hat{F}^k + \delta_\eta \hat{G}^k + \delta_\zeta \hat{H}^k - \hat{S}^k + \frac{\hat{Q}^k - \hat{Q}^n}{\Delta t} \quad (2.65)$$

This term should approach zero as the solution converges during the sub-iterations. Typically, a drop in the unsteady residual on the order of one to two orders of magnitude may be considered to be sufficient to ensure that the iteration error is less than the other remaining discretization errors.

If the pseudo time size is made very large ($\Delta\tau \rightarrow \infty$), then $h \rightarrow \Delta t$ and we obtain a Newton sub-iteration scheme. Furthermore, if one doesn't do any

sub-iterations then one recovers the traditional Euler implicit method described in eqn. 2.41. Similarly, dual time-stepping can be applied with 2^{nd} order backward difference in time (BDF2) by substituting $\partial_t \hat{Q}^{k+1} = \frac{3\hat{Q}^{k+1} - \hat{Q}^n + 4\hat{Q}^{n-1}}{2\Delta t}$ into eqn. 2.61, the scheme employed in TURNS.

Preconditioned Dual-Time Algorithm

In the preconditioned dual-time algorithm, the pseudo-time term in eqn. 2.61 is written in terms of the primitive variable vector, \hat{Q}_p , and the preconditioning matrix, Γ_p , and is given by:

$$\Gamma_p \frac{\partial \hat{Q}_p}{\partial \tau} + \frac{\partial \hat{Q}}{\partial t} + \frac{\partial \hat{F}}{\partial \xi} + \frac{\partial \hat{G}}{\partial \eta} + \frac{\partial \hat{H}}{\partial \zeta} = \hat{S} \quad (2.66)$$

Primitive variable vector, \hat{Q}_p , is given by $(p, u, v, w, T)/J$, where p is the pressure, u, v and w are velocity components in x, y and z directions, respectively and T is the temperature. The preconditioning matrix, Γ_p , is defined as:

$$\Gamma_p = \begin{bmatrix} \rho'_p & 0 & 0 & 0 & \rho_T \\ u\rho'_p & \rho & 0 & 0 & u\rho_T \\ v\rho'_p & 0 & \rho & 0 & v\rho_T \\ w\rho'_p & 0 & 0 & \rho & w\rho_T \\ (\rho h_p + h_0 \rho'_p - 1) & \rho u & \rho v & \rho w & \rho h_T + h_0 \rho_T \end{bmatrix} \quad (2.67)$$

where $\rho'_p = \frac{1}{\epsilon_p a^2}$, a is the speed of sound, h is the enthalpy and h_0 is the stagnation enthalpy. Here $\epsilon_p = \frac{M_p^2}{1+(\gamma-1)M_p^2}$ and M_p is the preconditioning parameter, which is typically chosen to be a value close to the freestream Mach number.

Discretizing eqn. 2.66 with first order finite difference for both artificial and physical time and linearizing with primitive variables gives:

$$\left[\frac{\Gamma_p}{\Delta\tau} + \frac{\Gamma_e}{\Delta t} + \delta_\xi \hat{A}_p^k + \delta_\eta \hat{B}_p^k + \delta_\zeta \hat{C}_p^k \right] \Delta \hat{Q}_p^k = - \left[\delta_\xi \hat{F}^k + \delta_\eta \hat{G}^k + \delta_\zeta \hat{H}^k - \hat{S}^k + \frac{\hat{Q}^k - \hat{Q}^n}{\Delta t} \right] \quad (2.68)$$

where \hat{A}_p , \hat{B}_p and \hat{C}_p are flux Jacobians with respect to \hat{Q}_p , and $\Gamma_e = \frac{\partial Q}{\partial Q_p}$.

The key step in the derivation of a diagonalized scheme rests in combining the pseudo-physical time-derivative terms on the left hand side into a single matrix. Accordingly, we define $S_p = \Gamma_p + \frac{\Delta\tau}{\Delta t} \Gamma_e$. Eqn. 2.68 can be rewritten as:

$$\begin{aligned} \left[S_p + \Delta\tau(\delta_\xi \hat{A}_p^k + \delta_\eta \hat{B}_p^k + \delta_\zeta \hat{C}_p^k) \right] \Delta \hat{Q}_p^k &= -\Delta\tau \left[\delta_\xi \hat{F}^k + \delta_\eta \hat{G}^k + \delta_\zeta \hat{H}^k - \hat{S}^k + \frac{\hat{Q}^k - \hat{Q}^n}{\Delta t} \right] \\ &= R^k \end{aligned} \quad (2.69)$$

Multiplying through by $\Gamma_e S_p^{-1}$ and converting back to the conservative system, we get

$$\left[I + \Delta\tau \Gamma_e S_p^{-1} \delta_\xi \hat{A}^k + \Delta\tau \Gamma_e S_p^{-1} \delta_\eta \hat{B}^k + \Delta\tau \Gamma_e S_p^{-1} \delta_\zeta \hat{C}^k \right] \Delta \hat{Q}^k = \Gamma_e S_p^{-1} R^k \quad (2.70)$$

Applying approximate factorization,

$$\left[I + \Delta\tau \Gamma_e S_p^{-1} \hat{A}^k \delta_\xi \right] \left[I + \Delta\tau \Gamma_e S_p^{-1} \hat{B}^k \delta_\eta \right] \left[I + \Delta\tau \Gamma_e S_p^{-1} \hat{C}^k \delta_\zeta \right] \Delta \hat{Q}^k = \Gamma_e S_p^{-1} R^k \quad (2.71)$$

Now, the scheme can be diagonalized similar to eqn. 2.58 to obtain

$$\Gamma_e X_\xi \left[I + \Delta\tau \delta_\xi \tilde{\Lambda}_\xi \right] X_\xi^{-1} X_\eta \left[I + \Delta\tau \delta_\eta \tilde{\Lambda}_\eta \right] X_\eta^{-1} X_\zeta \left[I + \Delta\tau \delta_\zeta \tilde{\Lambda}_\zeta \right] X_\zeta^{-1} \Gamma_e^{-1} \Delta \hat{Q}^k = \Gamma_e S_p^{-1} R^k \quad (2.72)$$

where X_ξ and $\tilde{\Lambda}_\xi$ are respectively, the eigenvector matrix and the eigenvalue matrix of $S_p^{-1}\hat{A}_p$. The eigenvalue matrix ($\tilde{\Lambda}_\xi$) is given by

$$\tilde{\Lambda}_\xi = \begin{bmatrix} \lambda_1 & 0 & 0 & 0 & 0 \\ 0 & \lambda_2 & 0 & 0 & 0 \\ 0 & 0 & \lambda_3 & 0 & 0 \\ 0 & 0 & 0 & \lambda_4 & 0 \\ 0 & 0 & 0 & 0 & \lambda_5 \end{bmatrix}$$

$$\begin{aligned} \lambda_{1,2,3} &= bU \\ \lambda_{4,5} &= \frac{b}{2} \left[U(1 + \beta') \pm \sqrt{U^2(1 - \beta')^2 + 4a^2\beta'} \right] \end{aligned} \quad (2.73)$$

where $\beta' = \frac{M_p^2}{b - M_p^2(b-1)}$, a is the speed of sound and $b = \frac{\Delta t/\Delta\tau}{1 + \Delta t/\Delta\tau}$

The values of M_p^2 and b control the behavior of the preconditioner. The parameter b switches the behavior of the preconditioner from unsteady to steady. For steady flows, $b = 1$ and $\beta' = M_p^2$. Using $M_p = 1$ switches off the preconditioner. It should be noted that when β' is close to the local Mach number, the eigenvalues are of similar magnitude and therefore the preconditioning provides improved convergence. Note that, characteristic boundary conditions also have to be modified to account for the modified eigenvalues, refer [73].

Due to preconditioning, the Roe flux scheme described in eqn. 2.30 gets modified to:

$$F(q^L, q^R) = \frac{F(q^L) + F(q^R)}{2} - P^{-1}|P\hat{A}(q^L, q^R)|\frac{q^R - q^L}{2} \quad (2.74)$$

where $P = \Gamma_e S_p^{-1}$. The dissipation term for the scheme is now proportional to $P^{-1}|P\hat{A}|$. In the limits of low Mach number, this is given by:

$$P^{-1}|P\hat{A}| \sim \begin{bmatrix} O(1) & O(1) & 0 \\ O(1) & O(1) & O(1) \\ O(\frac{1}{M^2}) & O(\frac{1}{M^2}) & O(\frac{1}{M^2}) \end{bmatrix} \quad (2.75)$$

The order of terms as a function of Mach number is similar to order of terms in \hat{A} matrix (eqn. 2.54). This characteristic of the dissipation matrix keeps the terms bounded even at low Mach numbers, improving the accuracy of the system for low Mach number flows.

2.6.2 Sliding Mesh Boundary Condition

Sliding mesh boundary condition is implemented to allow handling of counter-rotating system. With this, each rotor system of the coaxial system is simulated using its own blade and background mesh overset system. The outer background mesh of each rotor system is allowed to slide past each other and the information between the outer background meshes are exchanged using a one-dimensional interpolation. Because of its low cost, higher order can be used for the interpolation.

Further, for hovering coaxial rotor, complete simulation can be done using just one blade mesh in each rotor system by utilizing the periodicity of the flow-field. Figure 2.10 shows a schematic of the blade surfaces and the blade and background mesh boundaries. The solid lines show the meshes for the simulated blade and the dotted lines depict periodicity. The sliding boundary condition for the simulated background mesh of any of the two rotors is implemented by exchanging information with either the simulated background mesh or the periodic mesh of the other rotor. This type of interface condition, though novel

in helicopter calculations, is routinely used in simulations of gas turbine rotor-stator flow-fields. Since, the solution transfer between the sliding meshes is one-dimensional,

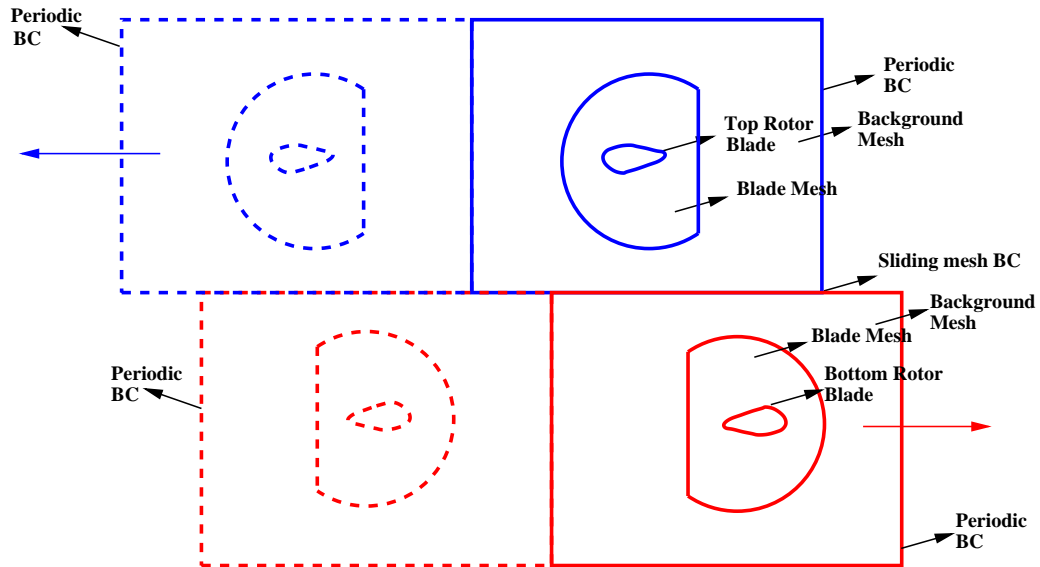


Figure 2.10: Schematic of the mesh system and the boundary condition for a 2-bladed coaxial rotor.

2.6.3 Improvements in Grid Connectivity

The hole-cutting technique used in the baseline OVERTURNS is a simplified algorithm, which can handle two overset meshes (blade and background) and requires the blade mesh to be completely embedded in the background mesh. The algorithm involves cutting a hole by specifying a box around the blade and extracting a list of hole fringe points that require information from other grids to serve as boundary conditions. Refer section 2.2.1 for more details.

There are many difficulties associated with this approach. First of all, the algorithm can handle only two overset meshes and requires one mesh to be com-

pletely embedded in the other. This poses severe restrictions on the type of meshes used, especially when the problem gets complicated (as in coaxial rotor simulation). Secondly, in order to cut the hole, the box around the body has to be specified explicitly. This is particularly challenging when the body surface is not well defined. Note that, this problem is common to all traditional hole-cutting techniques. Additionally, defining an arbitrary box around the body has the undesirable effect of cutting the hole at the same location regardless of possibly large differences in grid resolution. This could, in some cases, potentially result in hole fringe points interpolating from donors whose cell volumes are drastically different from those of the receivers, thus deteriorating the accuracy of the interpolation. In more complicated algorithms, an optimum hole is determined by marching the hole away from the body till the grid sizes become comparable. However, this comes with additional computational cost. Finally, in order to utilize the increasing number of available computational nodes with time, CFD codes need to have parallel capability. Load balancing in the parallel execution of traditional overset connectivity codes is much harder than that of the flow solver due to the unknown number of fringe points and the amount of work needed to find all donor cells. Researchers have found that a partitioning strategy that gives optimal parallel performance in the flow solution does not necessarily give optimal performance in the connectivity solution, and vice-versa and one must derive alternative parallel implementation approaches to attain scalable performance on large numbers of processors (see Ref. [80–83]).

The Implicit Hole Cutting (IHC) approach for overset grids developed recently by Lee and Baeder [84] alleviates some of the problems faced by traditional connectivity algorithms. The primary advantage for the current work being, the

ability to use intermediate background mesh for better transfer of information from the blade mesh to the outer background mesh in coaxial rotor simulation. Additionally, in the IHC approach, the inter-grid boundary points list and *iblack* arrays can be obtained without explicitly knowing where the holes are, cutting them out and expanding them. The IHC method routes through every point in the grid system to test and select the best quality cells in multiple overlapped regions, leaving the rest as hole points. In other words, at any point, the solution is computed on the cell having the smallest volume and interpolated at other points. The presence of the body is felt either by the progressively smaller cell sizes towards the wall or by the grid topology (for example, if all walls are located at $k = 1$). Since the hole cutting is determined by cell size, the resultant hole from the IHC algorithm is automatically optimum. Also, load balancing in a parallel implementation of IHC is considerably simpler. Since the two main loops in IHC are over grids, the work load can be distributed grid-by-grid just as in the coarse-grain parallelization of the flow solver. For a more detailed discussion, see Ref. [84].

Because of these advantages, all the connectivity in this work is done using the IHC approach. Minor modifications were made to the original IHC code developed by Lee and Baeder [84] to handle C-O type meshes. Further, *iblack* array is handled in a novel way, which will be described below:

In traditional hole-cutting techniques, in order to avoid contamination of the solution due to the invalid hole points, an array of integers (*iblack*) is defined corresponding to the grid points. *iblack* is set as 0 for hole points and hole fringe/chimera points, and as 1 for the field points. The solution is not updated by the solver, when a point is blanked out. On the other hand, the original

implementation of IHC does not require an *iblack* array. It relies on having thick enough hole fringe layers so that they completely enclose the body to prevent contamination from invalid points. However, it is not always possible to ensure sufficiently thick fringe layers. Furthermore, the original implementation of IHC then requires a large number of interpolations. Therefore, the current work borrows the idea of an *iblack* array from the traditional hole-cutting technique to be used along with the IHC technique.

However, the conventional blanking technique is not fully correct. Apart from preventing contamination from invalid points, traditional blanking technique also prohibits the use of valid solutions from the blanked out hole fringe/chimera points in the flux calculations. Instead, if the hole fringe/chimera points are not blanked out, the solution gets contaminated during an implicit time update. During this step of the solution procedure, the variables are not yet interpolated from other grids onto the inter-grid boundary points and therefore, the solution at these points are incorrect. As a result, the inaccuracies can spread to other grid points during the line inversion procedure.

This problem can be resolved by blanking out hole fringe/chimera points during implicit inversion and by including them while calculating the fluxes. This is achieved by setting the *iblack* array to -1 at these points. The hole points and the field points have similar *iblack* values as before. In the solution procedure, a function of the *iblack* array is multiplied to the time step corresponding to each grid point (for e.g., h in eqn. 2.64). The time step in the LHS of the equation is multiplied by $\max(\textit{iblack}, 0)$ and that in the RHS is multiplied by $\textit{abs}(\textit{iblack})$. As a result of this, the contribution of the hole points is blanked out in both the LHS and RHS, while that of hole fringe and chimera boundary points are

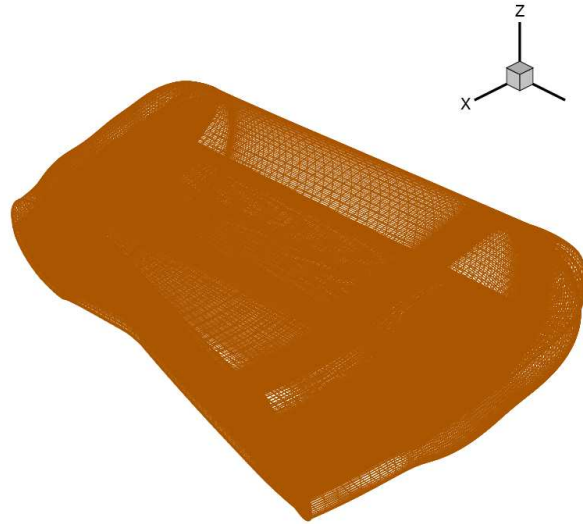
blanked out only in the LHS. This prevents the propagation of inaccuracies from the hole points to the flow solution.

2.6.4 Parallelization

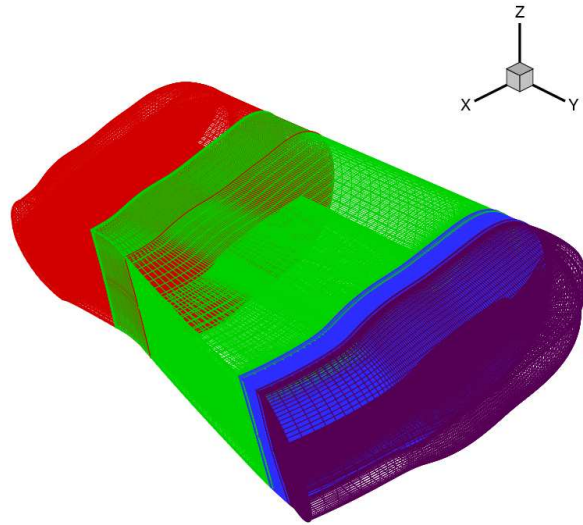
With the requirement to resolve tip vortex formation and evolution accurately for single and coaxial hovering systems, the mesh sizes can become very large. Severe limitations on the mesh sizes can be imposed by the available memory. Even if a reasonable mesh is made which meets the memory limitation, restrictions come from limited processing speed. Using a single processor, a typical hovering rotor calculation takes several weeks to complete. Such a limitation is undesirable and therefore, in this work, the TURNS/OVERTURNS code is parallelized to a certain extent.

The message passing interface system (MPI) is used to perform parallel computations and communications between processors. Solution for the entire domain, is obtained by solving the smaller sub-domain problems collaboratively and "patching together" the sub-domain solutions. This numerical method is known as the domain decomposition method. The partitioning of the domain is done by splitting each grid into equal number of sub-grids along one direction. Load balancing is achieved by having similar sizes of sub-grids for different meshes in the overset system. Typically, the blade meshes are split along the spanwise direction and the background meshes are split in the vertical direction. Figure 2.11 shows an example of domain partitioning, where the blade mesh is divided into four along the spanwise direction. Note that, sufficient overlap is ensured between the split meshes to maintain the spatial accuracy. An artificial internal boundary condition is created in the overlap region, where the solution

from one domain is directly copied to the other.



(a) Sample blade mesh



(b) Split blade meshes

Figure 2.11: Sample domain partitioning for parallel computation.

The current parallelization method is limited to the flow solver. Parallel execution of the connectivity routine is not yet implemented. As a result, the current code does not provide any benefit when the meshes in the overset system move relative to each other with time. However, when there is no relative motion between various overset meshes (which is true for all the simulations in this work), the connectivity has to be done only once at the beginning and the solution can be interpolated at each time step between various meshes using this information. Therefore, the code can provide parallel capability with additional communication of chimera interpolation data at each time step, which is described below.

The connectivity information for each grid (or sub-grid) is stored in the format (FORTRAN77 code) given below [85]:

```

write(1) nfringe,ndonor,iieptr,iisptra
write(1) (idonor(n,1),n=1,ndonor), (idonor(n,2),n=1,ndonor),
        (idonor(n,3),n=1,ndonor), (frac(n,1),n=1,ndonor),
        (frac(n,2),n=1,ndonor), (frac(n,3),n=1,ndonor)
write(1) (imesh(n,1),n=1,nfringe), (imesh(n,2),n=1,nfringe),
        (imesh(n,3),n=1,nfringe), (ibc(n),n=1,nfringe)
write(1) (((iblack(j,k,l),j=1,jmax),k=1,kmax),l=1,lmax)

```

where *nfringe* is the number of chimera/hole fringe boundary points in this grid, and *ndonor* is the number of interpolation points (or stencils) in this grid, used by chimera/hole fringe boundary points in any other grid. *iisptra* and *iieptr* give start and end pointers for interpolated data from this grid into the global *qbc* array. (*idonor(n,1)*, *idonor(n,2)*, *idonor(n,3)*) gives the three coordinates of the donor cell for interpolation data with (*frac(n,1)*, *frac(n,2)*, *frac(n,3)*)

as linear weights between $idonor(n, 1)$ and $idonor(n, 1) + 1$, etc. The result of these interpolations gets stored into qbc elements $iisptr$ through $ieptr$. The three coordinates of the boundary point which receives interpolated data from qbc element ibc are given by $(imesh(n, 1), imesh(n, 2), imesh(n, 3))$. The $iblack$ array was described before in sections 2.2.1 and 2.6.3.

At every iteration (or sub-iteration) during parallel runs, each processor calculates the interpolated data required by the other processors using $idonor$ and $frac$ and sends it to the first processor. The first processor collects this information and updates the qbc array. Subsequently, all the processors request appropriate interpolated data from the first processor based on ibc array. Following, the solution is updated based on the $imesh$ array.

2.7 Summary

In this chapter, the computational methodology for the solution of the RANS equations was presented. The improvements to an existing solver in terms of implementation of low Mach preconditioning, sliding mesh interface condition, grid connectivity approach and parallelization were detailed.

Chapter 3

Verification and Validation

Before applying the newly implemented methodology to the actual MAV rotor problems, it is necessary first to apply them to simpler problems to gain confidence in the solution algorithm. The current chapter is focused on this issue of verification and validation. Firstly, the performance of the low Mach preconditioning algorithm is evaluated based on the numerical solution of a two-dimensional vortex convection. The effectiveness of the preconditioner is further verified by applying it to two-dimensional steady flow over an airfoil. Following this, the algorithm is validated for a steady 3D finite-span wing by comparing predicted vortex velocity profiles with the experimental data. This is then followed by the demonstration of the advantages of implicit hole-cutting and the new blanking technique. Finally, the baseline methodology in OVERTURNS with the addition of the use of implicit-hole cutting, is validated for rotors by comparing the performance data obtained for a full-scale single rotor simulation with those from experiments.

3.1 Low Mach Preconditioning

3.1.1 Convection of a 2D Isentropic Vortex

In this section, the performance of the low Mach preconditioning is evaluated for the numerical solution of vortex convection in terms of convergence and accuracy. The model problem involves the isentropic convection of a two dimensional vortex in a uniform inviscid flow-field [35]. The initial conditions are set up such that:

- The spatial entropy gradient is zero,
- The velocity, pressure and density fields correspond to an exact solution to the 2D Euler equations,

The exact solution to the above problem would then be the pure advection of the vortex at the free-stream velocity without any decay. Hence, the effects of numerical diffusion and dispersion can be evaluated.

A 41×41 uniform grid is used in a domain of $0 \leq x \leq 10$, $0 \leq y \leq 10$. Periodic conditions are assumed on all four grid boundaries. This is done in order to remove any effects of boundary inaccuracies and also to keep the domain small. Perturbations are added to the free-stream such that there is no entropy gradient in the flow-field.

Free-stream conditions are $\rho = 1$, $u = u_\infty$, $v = 0$ and $p = 1$. The perturbations are given by:

$$(\delta u, \delta v) = \frac{\beta}{2\pi} e^{\frac{1-r^2}{2}} (-(y - y_0), (x - x_0)) \quad (3.1)$$

$$\rho = \left[1 - \frac{(\gamma - 1)\beta^2}{8\gamma\pi} e^{1-r^2} \right]^{\frac{1}{\gamma-1}} \quad (3.2)$$

$$p = \rho^\gamma \quad (3.3)$$

where, β , set as u_∞ , is the vortex strength and r is the distance from the vortex center $(x_0, y_0) = (5, 5)$.

Two cases, corresponding to u_∞ of 0.1 and 0.001, are studied. The corresponding free stream Mach numbers are respectively 0.0845 and 0.000845. The domain and initial pressure contours for the case of $u_\infty = 0.1$ are shown in Fig. 3.1. In Pandya et al. [77], an unsteady scale which depends on the unsteady length scale is used to define the preconditioning parameter. However, the unsteady length scale is quite arbitrary and cannot be defined easily for a practical problem. Therefore, in the present work, a different approach is used to control the preconditioning parameter, which is done by changing the pseudo time step ($\Delta\tau$). It was shown in section 2.6.1 that $\Delta\tau \rightarrow \infty$ is equivalent to no-preconditioning. As the value of $\Delta\tau$ is decreased, the effect of the preconditioning increases. However, a smaller value of $\Delta\tau$ would require a sufficiently large number of sub-iterations to converge. Therefore, an appropriate value of $\Delta\tau$ has to be chosen.

To study the performance of the scheme with and without preconditioning, the sub-iteration convergence is studied for two different physical time steps. The time step is characterized by $CFL_u = \frac{u\Delta t}{\Delta x}$, where u is the speed of propagation, Δt is the physical time step and Δx is the grid size. Figure 3.2 shows the residual convergence for the case of $M_\infty = 0.0845$ for two different time steps. For the preconditioning case, results are obtained for four different values of $\Delta\tau$. For $CFL_u = 0.1$, the no-preconditioning case shows the best convergence. The preconditioning cases show improving convergence as $\Delta\tau$ is increased and for $\Delta\tau = 100 \Delta t$ the convergence becomes very similar to that of the no-preconditioning case. For the larger physical time step ($CFL_u = 1.0$), the preconditioning cases with higher $\Delta\tau$ (10 Δt , 100 Δt) show better convergence

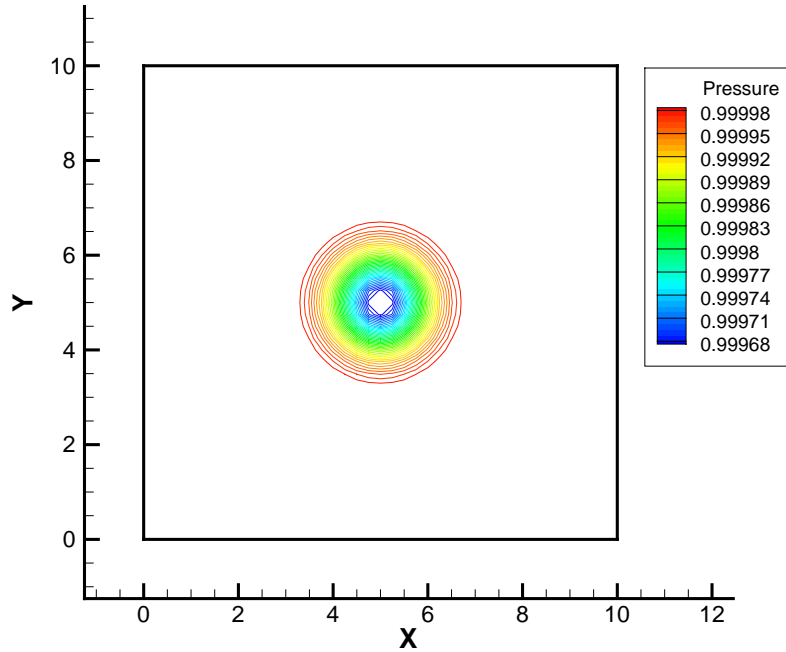


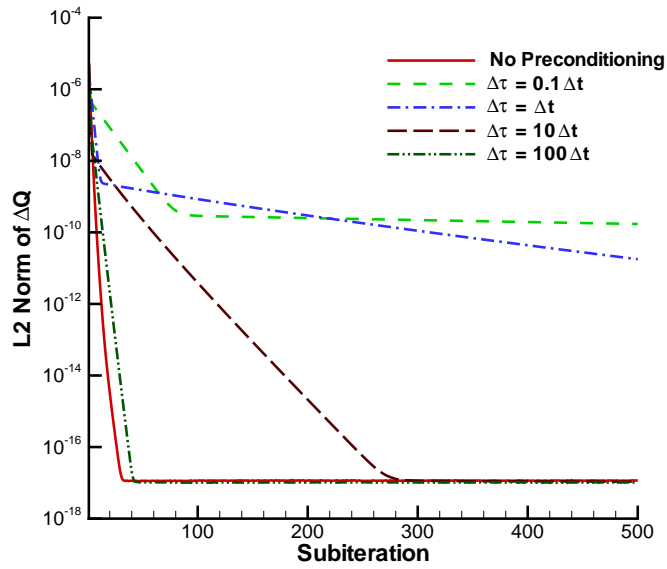
Figure 3.1: Computational domain and initial pressure contours for isentropic vortex convection.

compared to the no-preconditioning case.

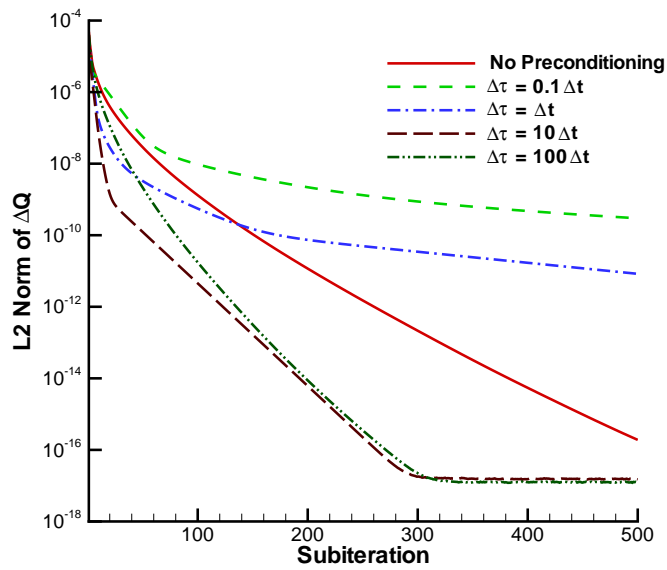
Figure 3.3 shows similar plots for the case of $M_\infty = 0.000845$; the advantages of the low Mach preconditioning can be clearly seen at the speed of $u_\infty = 0.001$. For this case, the no-preconditioning case shows very poor convergence for both the physical time steps. In fact, for $CFL_u = 1.0$, the no-preconditioning case fails to converge. On the other hand, the preconditioning cases show good convergence. As a general trend, higher pseudo time step shows better convergence. It has to be mentioned here that for all cases when the pseudo time step is made very large, the convergence is similar to that of the no-preconditioning case (when no-preconditioning converges). Therefore, from the convergence point of view,

$\Delta\tau = 100 \Delta t$ seems to be a good choice. However, practical computations do not require that the sub-iterations be converged to machine zero. Typically, the residue is converged to 3 to 4 orders of magnitude or the number of sub-iterations is fixed to a value, typically 20 or less. By looking only at the convergence of various cases in the first 20 sub-iterations, it can be seen that the preconditioning cases with $\Delta\tau = \Delta t, 10 \Delta t$ and $100 \Delta t$ show equally good results, with the residues dropping by 3 to 4 orders of magnitude for all the cases. Therefore, the choice of $\Delta\tau$ cannot be determined just by looking at the convergence.

Figure 3.4 shows the vertical velocity profile along a line cut through the center of the vortex at $t = 10$. The results are obtained with a time step of $CFL_u = 0.1$ and using 20 sub-iterations for both free-stream speeds. The plot also shows the exact solution. For both the speeds, the preconditioning with smaller $\Delta\tau$ has lower dissipation. However, for the choice of $\Delta\tau = 0.1 \Delta t$, the solution is not converged sufficiently for both the cases. The no-preconditioning case is more dissipative compared to the preconditioning cases for $u_\infty = 0.1$. For $u_\infty = 0.001$, the no-preconditioning case does not converge and therefore is not plotted. Clearly, $\Delta\tau = \Delta t$ is seen to give the best result and therefore can be considered the optimum choice. Therefore, for all the calculations to be shown in this thesis, the value of $\Delta\tau = O(\Delta t)$ will be used.

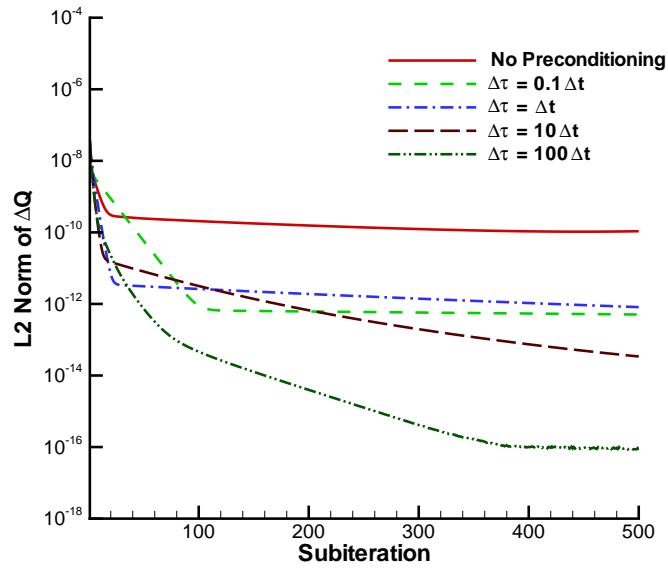


(a) $CFL_u = 0.1$

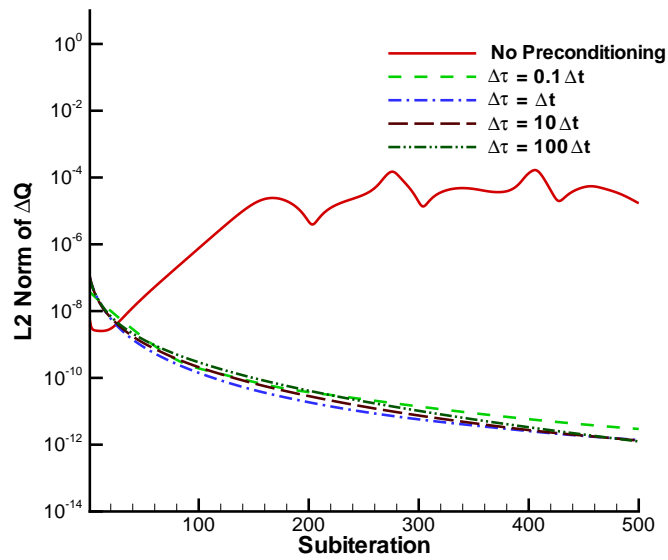


(b) $CFL_u = 1.0$

Figure 3.2: Comparison of residual convergence for $M_\infty = 0.0845$ for isentropic vortex convection.

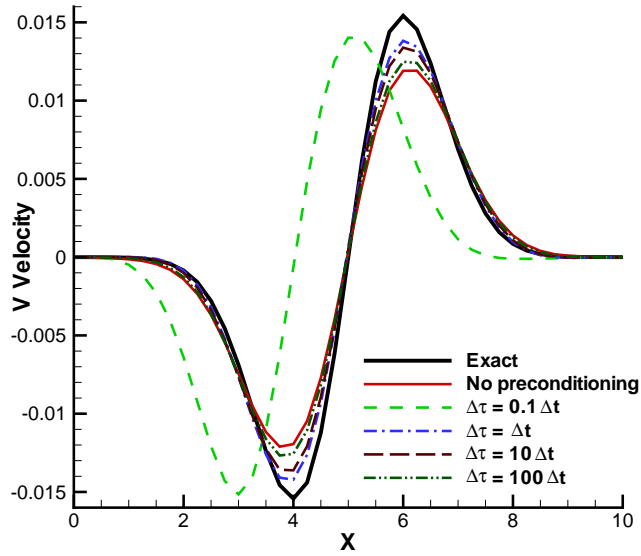


(a) $CFL_u = 0.1$

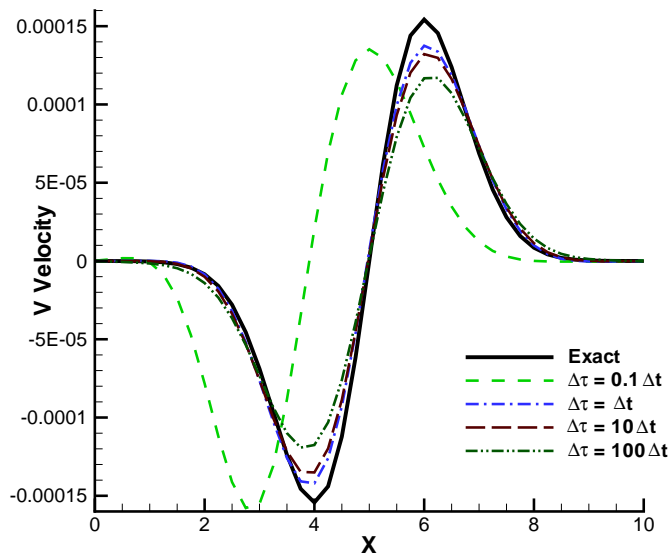


(b) $CFL_u = 1.0$

Figure 3.3: Comparison of residual convergence for $M_\infty = 0.000845$ for isentropic vortex convection.



(a) $M_\infty = 0.0845, CFL_u = 0.1$



(b) $M_\infty = 0.000845, CFL_u = 0.1$

Figure 3.4: Vertical velocity profile along $y = 5$ line at $t = 10$ for isentropic vortex convection.

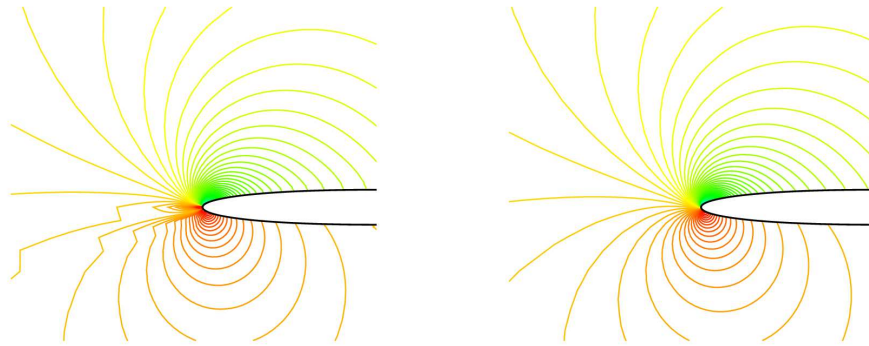
3.1.2 Steady Low Speed Flow Over 2D Airfoil

Effectiveness of the low Mach preconditioning in a steady flow is demonstrated by simulating the flow over a NACA 0006 airfoil at 5° angle of attack at low speeds. The Reynolds number is set as 3×10^6 . Table 3.1 compares the calculated lift and drag coefficients at free-stream Mach numbers of 0.3, 0.2, 0.1 and 0.05, with and without using low Mach preconditioning. It can be seen that at $M = 0.3$, results obtained for the preconditioned and non-preconditioned cases are identical. However, at lower Mach numbers, the results are seen to be different; the non-preconditioned case predicts lower lift coefficient and much larger drag coefficient compared to the preconditioned case.

Table 3.1: Comparison of coefficient of forces for NACA 0006 airfoil at different Mach numbers, with and without low Mach preconditioning

Mach Number	No Preconditioning		Preconditioning	
	C_l	C_d	C_l	C_d
0.30	0.551	0.0128	0.551	0.0128
0.20	0.538	0.0131	0.537	0.0124
0.10	0.525	0.0148	0.530	0.0120
0.05	0.508	0.0178	0.529	0.0118

The differences in the solution can be identified by looking at the pressure contours near the leading edge of the airfoil for the $M = 0.05$ case, see Fig. 3.5. The pressure contours are smoother with the application of preconditioning as compared to the case without the preconditioner. This clearly shows that the difference in results obtained using preconditioned and non-preconditioned cases arise due to inaccuracy in the solution of the non-preconditioned case. The



(a) No preconditioning

(b) With preconditioning

Figure 3.5: Pressure contours for flow over NACA 0006 airfoil at $M = 0.05$.

accuracy of the preconditioned case is further confirmed by the fact that the predicted forces approximately scale by the Prandtl-Glauert compressible factor as the Mach number changes.

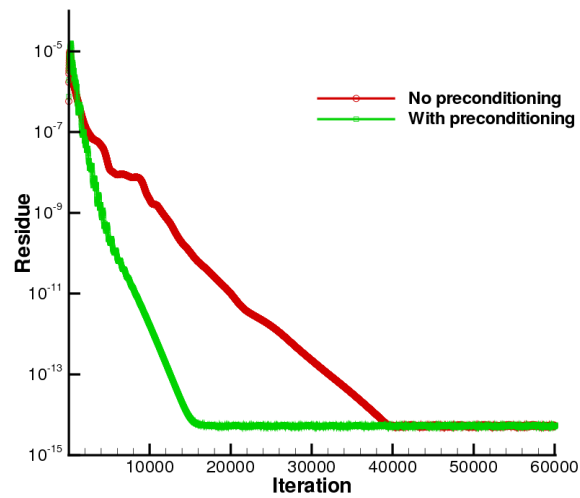


Figure 3.6: Comparison of residue with and without the use of preconditioning for flow over NACA 0006 airfoil at $M = 0.05$.

Improvements in convergence due to preconditioning can be studied by looking at the residue plot. Figure 3.6 shows the plot of residue versus iteration number at $M = 0.05$ for both preconditioned and non-preconditioned cases. The residues for both the cases drop to machine precision by the end of the simulation, however, the preconditioned case clearly shows a much faster and smoother convergence rate.

3.1.3 Low Speed Fixed-Wing Validation

The low Mach preconditioning algorithm is validated in the finite-span case using measurements made by Zuhail [86] on a NACA 0012 wing of aspect ratio 4.61 (span of 41.91 cm and chord of 9.1 cm) with a rectangular tip. Vortex velocity profiles were obtained using 2 and 3-component PIV techniques at $x = 1, 2, 3$ and 4 chords downstream of the trailing edge. Experiments were conducted at a Reynolds number of 9040, Mach number of 0.004 (free-stream of 1.5 m/s) and at angles of attack ranging from $\alpha = 0^\circ$ through 10° . For these lower Reynolds numbers, the viscous forces become significant and Batchelor’s analysis [87] shows that the viscous head loss term can overpower the inviscid acceleration mechanism and lead to an axial velocity deficit. In the present validation, the Zuhail experimental data shows the expected core axial velocity deficit in all cases. Computations are performed on a mesh of $369 \times 121 \times 111$ streamwise, spanwise and normal points, respectively (Fig. 3.7). To help ensure an accurate, stable and efficient simulation, OVERTURNS was run at a Mach of 0.05 rather than the lower experimental value. Since the Mach numbers involved in these studies are well within the incompressible limit, it is expected that small variations in Mach number will not have a significant effect on the final results.

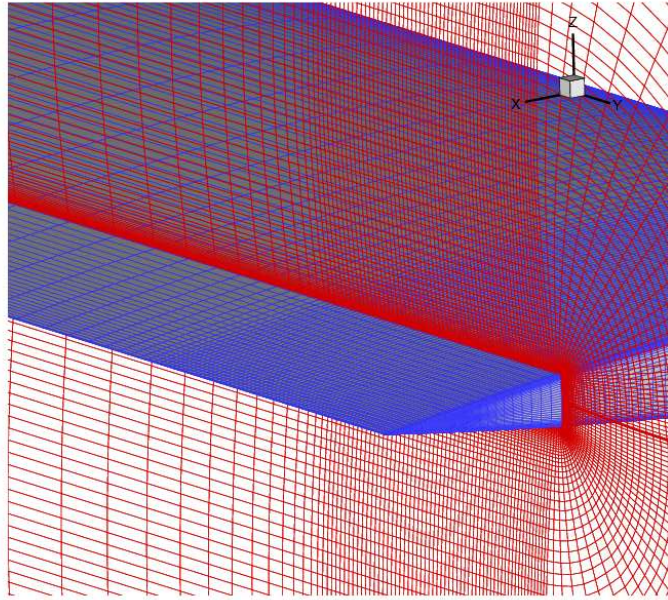


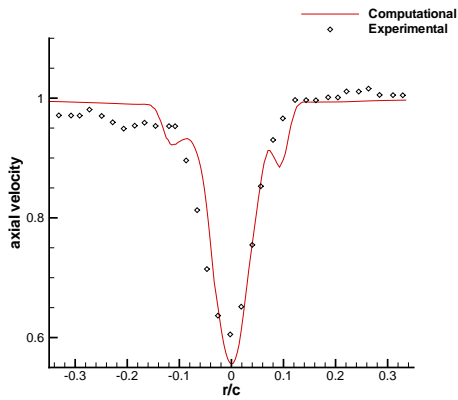
Figure 3.7: Computational mesh used for validation with Zuhai experiments [86]

As mentioned previously, because of the increased tendency for flow separation, MAV usually employ thin airfoil sections. Thus, as one might expect with the relatively thick NACA 0012, regions of flow separation exist along much of the span, especially at low angles of attack. Spanwise shedding interacts with the developing tip vortex causing it to deform, resulting in some of the oscillations in the velocity profiles shown in Fig. 3.8. At high angles of attack, the strength of the tip vortex is sufficient to generally outweigh the effect of these interactions. However, at angles of attack near 4° and below, the computed strength of the forming vortex is of the same order of magnitude as the spanwise shed vorticity. This causes a significant delay in the formation of a coherent vortex to streamwise locations of up to 3 chords downstream. Because the experimental profiles are obtained by an ensemble average of instantaneous velocities, closer to the wing, these unsteady interactions are probably not accurately represented. For the purposes of validation, only the instantaneous profiles of the relatively

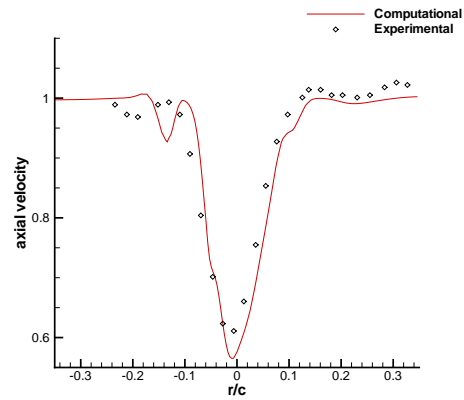
steady tip vortex at angles of attack greater than 4 degrees are presented here.

The computed axial and swirl velocity profiles in the tip vortex at $x/c = 1$ are given for $\alpha = 6, 8$ and 10 degrees in Fig. 3.8. Similar plots at $x/c = 4$ are shown in Fig. 3.9. In general, the computed axial velocity profiles show good agreement with the experiment aside from a tendency to slightly overpredict the magnitude of the axial velocity deficit. There is also an overprediction of the effect of a secondary structure as can be seen on the inboard side ($r/c < 0$) of the axial velocity profiles at the $x/c = 1$ stations. Although especially pronounced for the 8 and 10 degree cases, these disturbances weaken by $x/c = 4$ producing smooth profiles between $r/c = -0.1$ to $r/c = -0.2$ for all angles of attack.

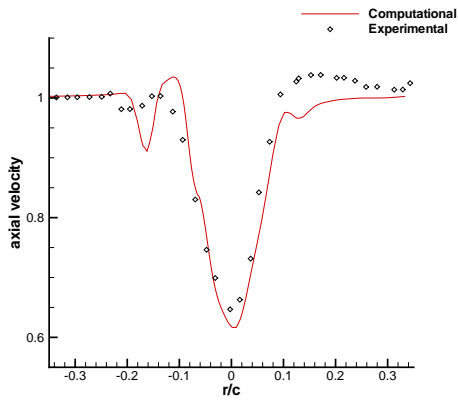
Note the relatively large core radius sizes resulting from the low Reynolds number. A typical core radius for a moderate Reynolds number of 200,000 may be on the order of $0.04c$ [88]. As seen in Fig. 3.8, the core radius is significantly larger ($r \approx 0.1c$) at the $x/c = 1$ station. The core radius and peak swirl velocities are notably underpredicted at 6 degrees angle of attack, however the core radius is captured well at 8 degrees and both the swirl and radius size are in good agreement with the experiment at 10 degrees. The underpredictions may result from underresolving the vortex formation region at the blade tip. Although the magnitude of the swirl velocities is underpredicted outside of the core flow region, it is worth noting that the velocity gradients in this zone are predicted quite well in all cases. Again, the trend of improving results with increasing angle of attack may be attributed to the increasing margin between the strength of the tip vortex and the strength of the spanwise shedding.



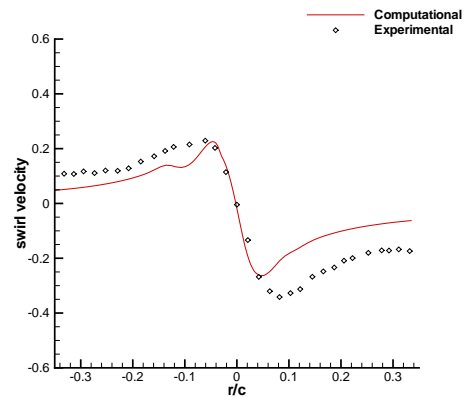
(a) $\alpha = 6^\circ$



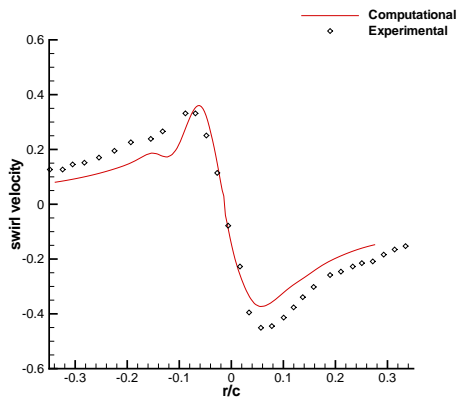
(b) $\alpha = 8^\circ$



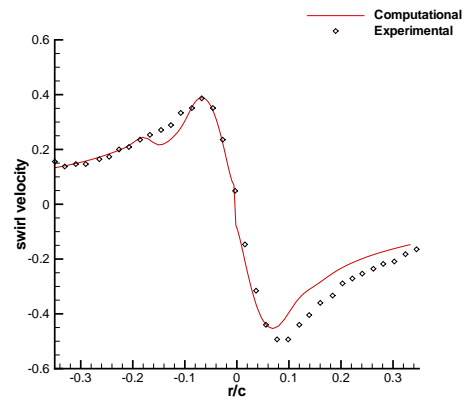
(c) $\alpha = 10^\circ$



(d) $\alpha = 6^\circ$

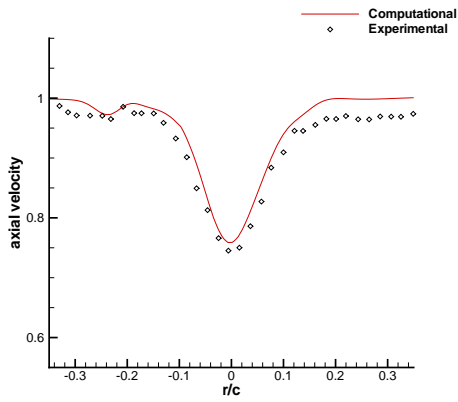


(e) $\alpha = 8^\circ$

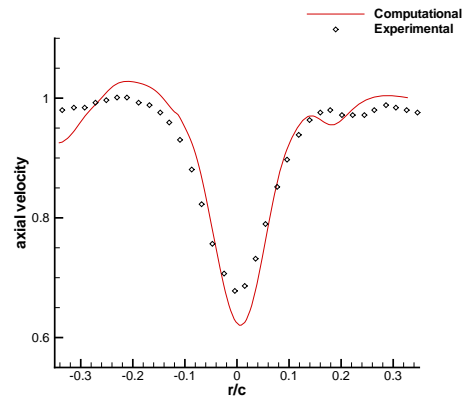


(f) $\alpha = 10^\circ$

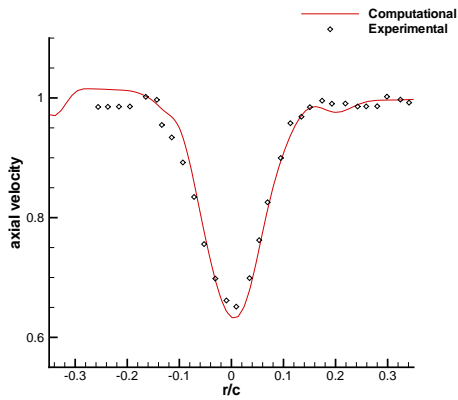
Figure 3.8: Swirl and axial velocity profile comparison with experimental data [86] at $x/c = 1$, $Re = 9040$.



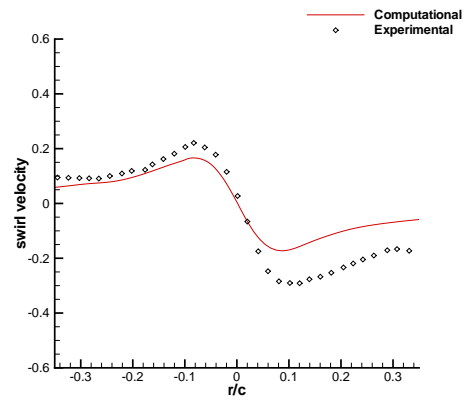
(a) $\alpha = 6^\circ$



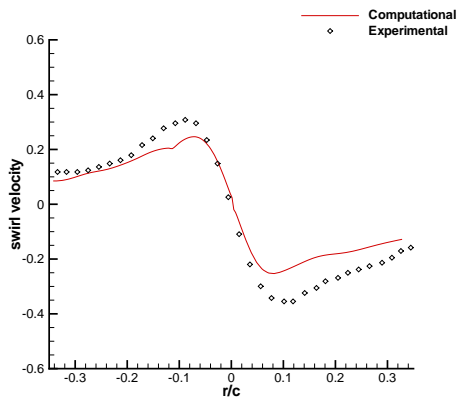
(b) $\alpha = 8^\circ$



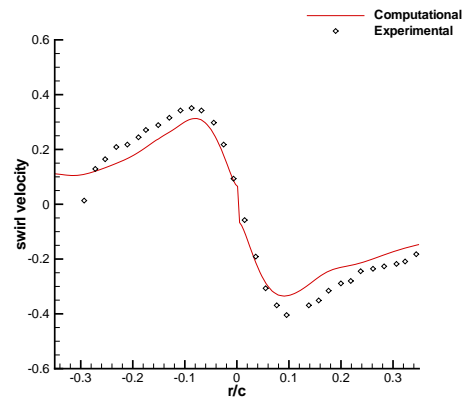
(c) $\alpha = 10^\circ$



(d) $\alpha = 6^\circ$



(e) $\alpha = 8^\circ$



(f) $\alpha = 10^\circ$

Figure 3.9: Swirl and axial velocity profile with experimental data [86] at $x/c = 4$, $Re = 9040$.

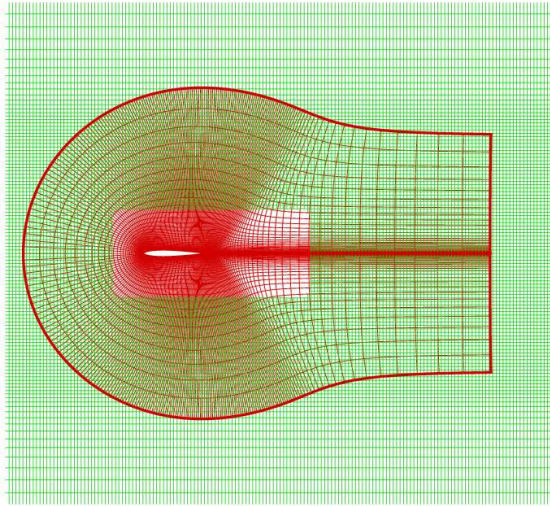
3.2 Grid Connectivity

3.2.1 Conventional Hole-cutting versus Implicit Hole-cutting

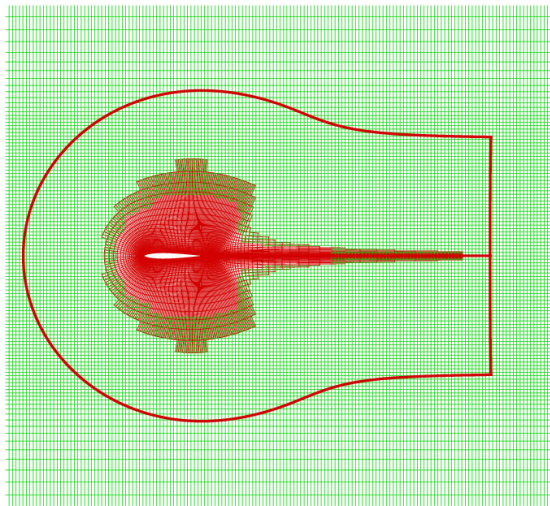
The advantages of implicit hole-cutting over conventional hole-cutting are demonstrated in 2D using an airfoil and a Cartesian background mesh in Fig. 3.10. The conventional hole-cutting technique, which is implemented in OVERTURNS, cuts a hole that is defined by a rectangular box, whereas implicit hole-cutting chooses the appropriate cell based on its size. The advantages of implicit hole-cutting become more apparent when the background mesh is coarsened, keeping the blade mesh the same (see Fig. 3.11). It can be seen that the hole defined by the conventional hole-cutting technique is fixed in location, while the fringe points obtained using implicit hole-cutting changes appropriately. With the conventional hole-cutting technique, the solution is calculated in certain areas using the coarser background mesh even while the finer blade mesh oversets the regions, which could lead to solution inaccuracy.

3.2.2 Verification of Improved Blanking Technique

To demonstrate the improvements due to the changes in blanking technique, flow over a NACA 0012 airfoil is simulated using two different mesh systems - one with a single airfoil mesh (327×85) and another with a two mesh system consisting of an airfoil mesh (267×65) and Cartesian background mesh (151×151). The meshes are shown in Fig. 3.12. The Mach number for the simulation is 0.3, the angle of attack is 10° and the Reynolds number is 3×10^6 .

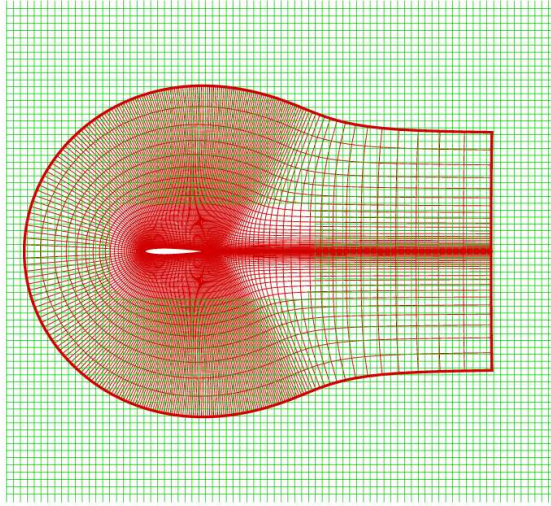


(a) Conventional hole-cutting

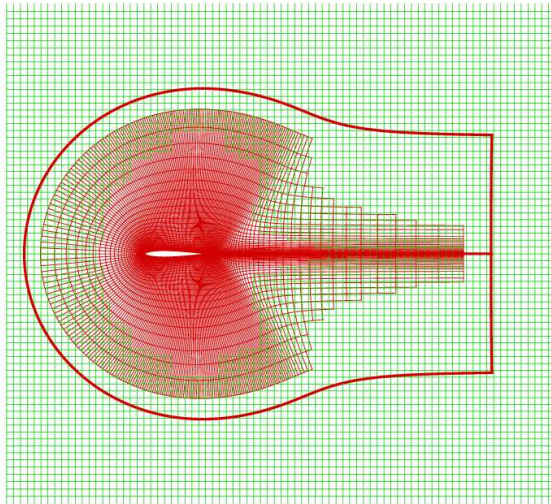


(b) Implicit hole-cutting

Figure 3.10: Comparison of grid connectivity in 2D using a fine background mesh.

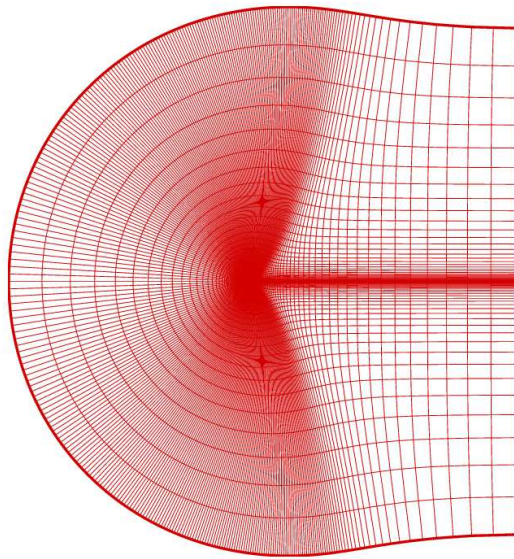


(a) Conventional hole-cutting

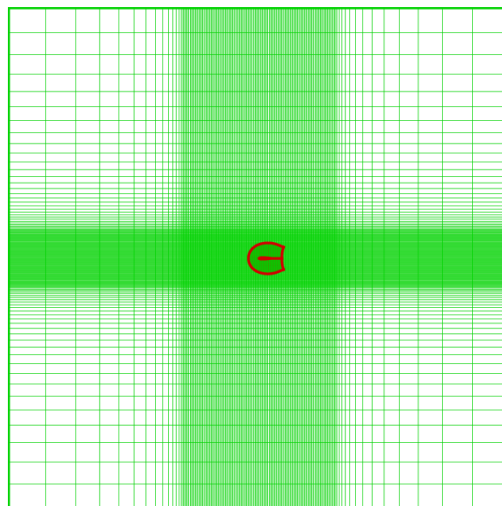


(b) Implicit hole-cutting

Figure 3.11: Comparison of grid connectivity in 2D using a coarse background mesh.



(a) Single mesh system (327×85)



(b) Two mesh system (267×65 airfoil mesh and 151×151 background mesh)

Figure 3.12: Mesh system used for verification of new blanking technique.

Figure 3.13 shows the grid connectivity using the baseline implicit hole-cutting. Blue and black regions respectively, show the fringe/chimera points for the airfoil and background meshes. The green region represents the field points of the background mesh. Since implicit hole-cutting does not use *iblack* array, there is a small region of field points within the airfoil. The solution in this region is not accurate. Any contamination from this region is prevented by the thick fringe layer (blue region). Figure 3.14 compares the pressure contours near the airfoil for both the single and the two mesh systems. The black lines show the contours for the single mesh system, red and green lines, respectively show the contours for the airfoil and background meshes of the two mesh system. The contours for the two mesh system are almost identical to that of the single mesh (away from the airfoil surface), thus validating the baseline implicit hole-cutting methodology.

However, it is seen that the number of fringe points in the baseline implicit hole-cutting can become very large, especially for 3D problems, which can severely increase the communication time when the code is run in parallel. This can be prevented, if the fringe layer thickness is kept small enough to just maintain the spatial order of accuracy. However, if the thickness of the fringe layer is reduced, then the solution can get corrupted by the invalid points, if *iblack* array is not used. This is shown in the following case, where a few layers of fringe points near the airfoil are manually removed. The new connectivity is plotted in Fig. 3.15. Figure 3.16 shows the pressure contours using this connectivity information. Note that, the solution is computed without any use of *iblack* array. The plot clearly shows the contamination in the solution.

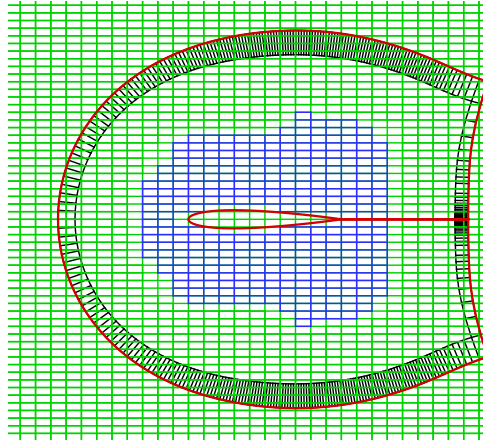


Figure 3.13: Connectivity using baseline implicit hole-cutting methodology. blue: fringe points of background mesh; black: fringe points of airfoil mesh; green: field points of background mesh.

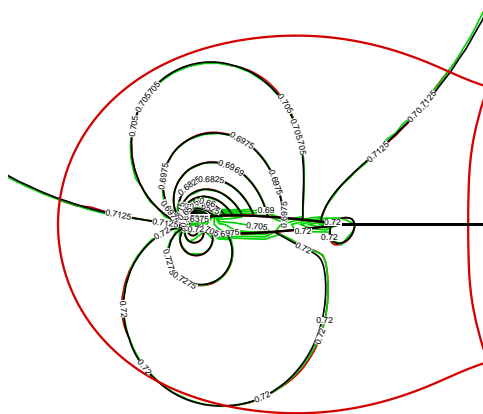


Figure 3.14: Comparison of pressure contours for single mesh and two mesh system using baseline implicit hole-cutting. black: single mesh system; red line: airfoil mesh, green line: background mesh.

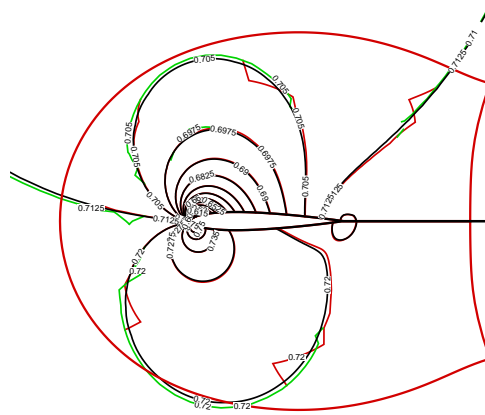


Figure 3.17: Comparison of pressure contours for single mesh and two mesh system using smaller fringe layer thickness and $iblack = 0$ for fringe points. black line: single mesh; red line: airfoil mesh, green line: background mesh.

The connectivity shown in Fig. 3.15 is identical to one obtained using a conventional hole-cutting technique with an optimal hole. The only difference is in the use of *iblack* array. In conventional hole-cutting techniques, the invalid hole points are blanked out by assigning an *iblack* value of 0. The field points are assigned a value of 1, whereas the fringe points are assigned a value of either 0 or 1. The same blanking technique can be adapted to implicit hole-cutting method to avoid having very thick fringe layers. Pressure contours obtained using *iblack* array are plotted in Figs 3.17 and 3.18. In Fig. 3.17, the *iblack* value for the fringe points are set as 0, whereas in Fig. 3.18, it is set as 1. Clearly, both the contours correlate better to the single grid contour compared to that obtained without any *iblack* array. However, the contours still show some inaccuracy in the form of wiggles near the interpolation points. The reason for this inaccuracy

was discussed before in section 2.6.3. Note that, such a problem is present even when using a conventional hole-cutting technique.

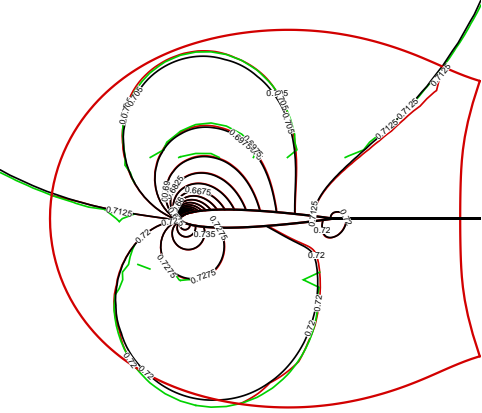
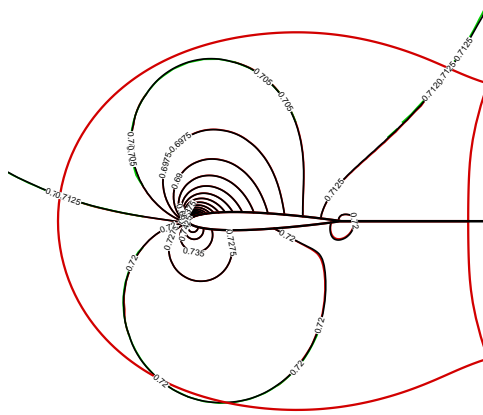


Figure 3.18: Comparison of pressure contours for single mesh and two mesh system using smaller fringe layer thickness and $iblack = 1$ for fringe points. black line: single mesh; red line: airfoil mesh, green line: background mesh.

As discussed before in section 2.6.3, this problem can be solved by treating fringe points as field points in the RHS of the solution procedure and as hole points in the LHS. This is achieved by assigning $iblack = -1$ for the fringe points. Contours obtained using this new blanking method are shown in Fig. 3.19. Now, the contours obtained using the single mesh and the two mesh system are almost indistinguishable, thus proving the correctness of the new blanking technique.

The results from the various blanking methods can be better compared by looking at the force coefficients, see table 3.2. From the table, it can be seen that the results obtained using the baseline implicit hole-cutting compares reasonably well with the single mesh results. However, the implicit hole-cutting method

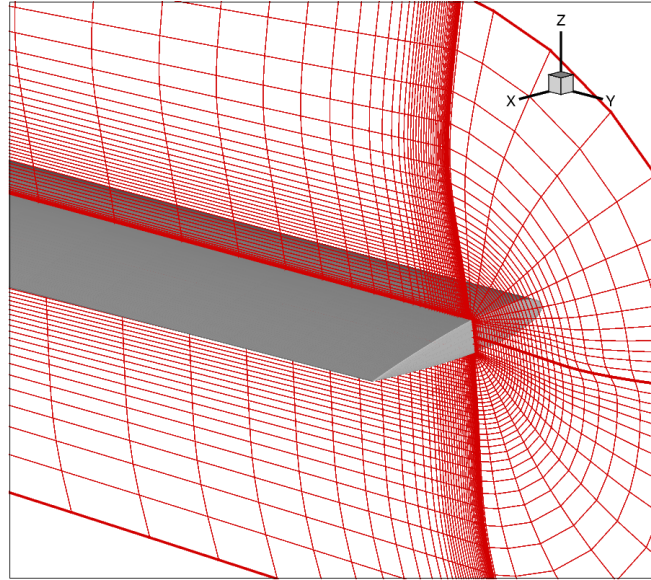


The current implementation of blanking technique shows the best comparison (less than 2% error in C_d and less than 0.5% error in C_l and C_m). Reduction in the number of fringe points for the cases with the use of *iblack* array results in a corresponding reduction in the communication and interpolation costs.

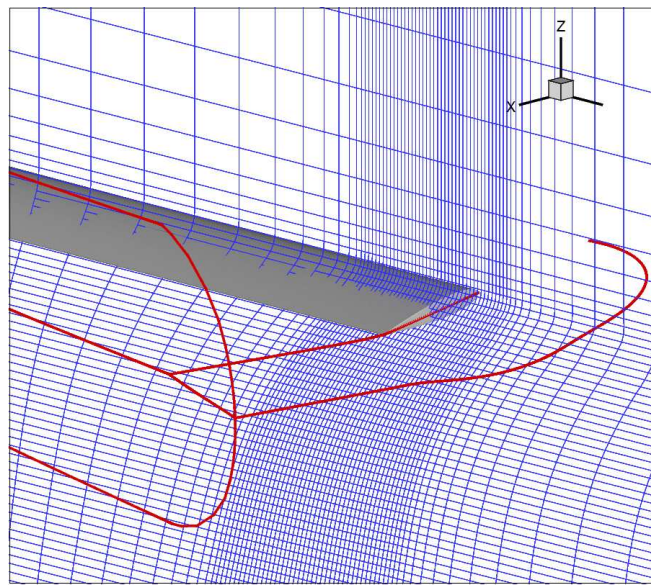
3.3 Full-Scale Single Rotor Validation

In order to validate the baseline methodology in OVERTURNS in combination with the implicit hole-cutting method, the full-scale single rotor experimental setup of Harrington [49] (referred to as Rotor-2) is simulated. The experimental setup consists of a two-bladed rigid rotor with an aspect ratio of 8.33. The diameter of the blade is 25 feet and the blade chord is 18 inches. The blade uses a NACA airfoil with a linearly varying thickness of 27.5% at $0.2R$ to 15% at R . The tip speed of the rotor is 392 ft/sec. The corresponding tip Reynolds number is 3.5×10^6 and the tip Mach number is 0.352. Collective pitch settings from 2° to 12° were used to obtain the variation of thrust with power. A two mesh overset system with a body-conforming blade mesh and a cylindrical background mesh are used for all the cases. The periodicity of the flow-field is utilized and hence, only half the computational domain is simulated. The blade mesh has $267 \times 78 \times 56$ points in the streamwise, spanwise and normal directions, respectively and the background cylindrical mesh has $127 \times 116 \times 118$ points in the azimuthal, radial and vertical directions, respectively (see Figure 3.20). Performance quantities were found to be insensitive to further mesh refinement for the isolated rotor.

Figure 3.21(a) shows the computed performance along with the experimental results and those from momentum theory [89]. All three results show excellent



(a) Blade meshes

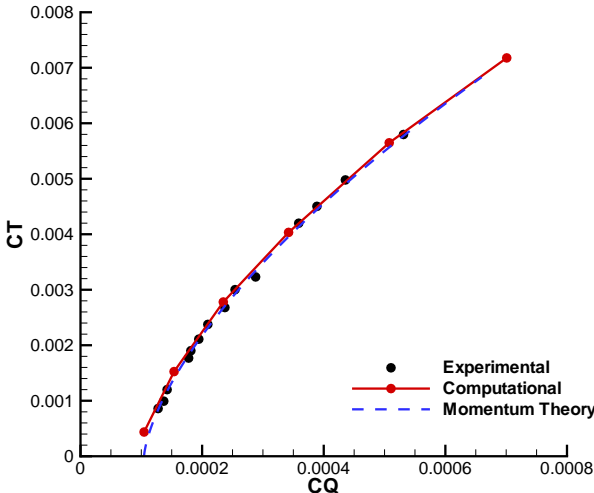


(b) Cylindrical meshes with blade mesh boundaries

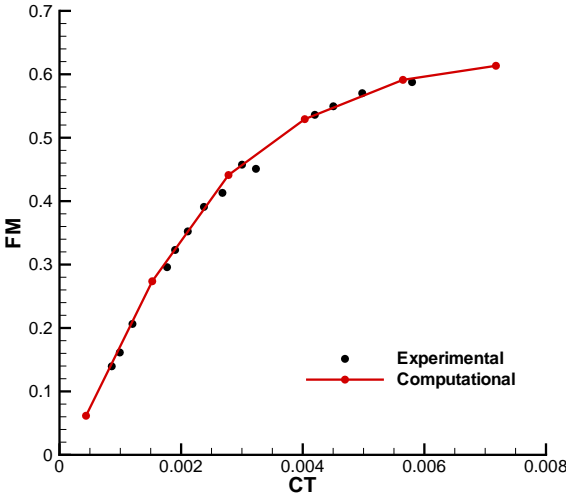
Figure 3.20: Computational mesh for Harrington single rotor-2 [49].

agreement at all thrust levels. Figure 3.21(b) shows the variation of Figure of Merit (FM) with thrust obtained using both the experiment and computations. The agreement can be seen to be very good (within 3%) and therefore, clearly

establishes the reliability of the code. It should be noted that with the old hole-cutting method and old blanking technique, the agreement was only fair ($\sim 20\%$ difference at lower thrust coefficient levels), see Fig. 3.22.

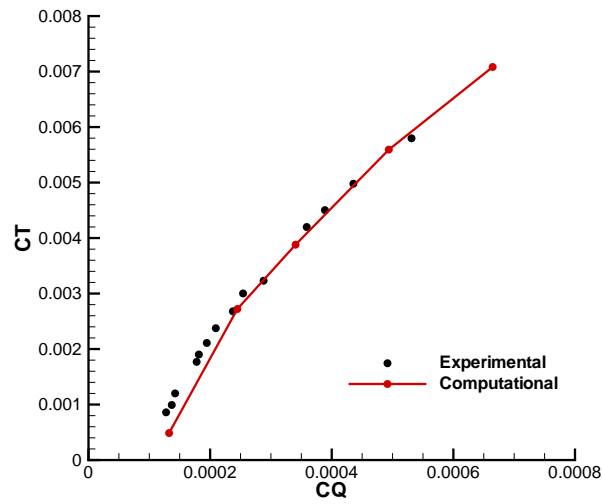


(a)

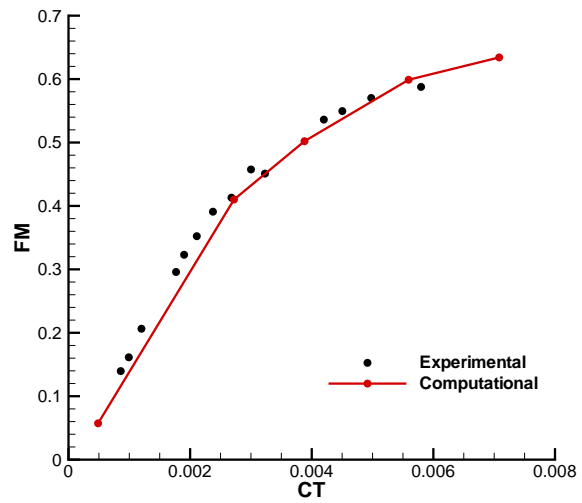


(b)

Figure 3.21: Performance comparison for Harrington single rotor-2 [49].



(a)



(b)

Figure 3.22: Performance comparison for Harrington single rotor-2 [49] with old hole-cutting method and old blanking technique.

3.4 Summary

In this chapter, improvements made to the computational methodology for the solution of the RANS equations are verified and validated. The baseline methodology in OVERTURNS is also tested with implicit hole-cutting and improved blanking method. Specifically, the following observations are noted:

- Best overall results for the dual-time stepping preconditioner are obtained for $\Delta\tau = O(\Delta t)$, in terms of accuracy and convergence. This is used throughout this work.
- The use of low Mach preconditioner increases accuracy near stagnation points, increases the convergence rate, and results in lift coefficients that scale with the Prandtl-Glauert compressible factor for the steady 2D flow over an airfoil.
- The ability to capture the tip vortex formation and evolution is verified for the experimental configuration of Zuhai at low Mach and Reynolds number.
- The new blanking technique for dealing correctly with the fringe points on both the left hand side and right hand side of implicit time marching methods is seen to maintain accuracy of thick fringes while having the reduced communication time and interpolation costs of optimally thin fringes on a steady 2D airfoil flow.
- The use of implicit hole-cutting and improved blanking results in improved performance predictions for the Harrington single rotor-2 as compared to previous predictions.

Chapter 4

Computational Investigation of Micro-Scale Single Rotor Aerodynamics in Hover

In this chapter, computations are performed on a hovering micro-scale single rotor. The performance data is validated with experimental results for different leading and trailing edge profiles. Subsequently, detailed analysis of the flow physics is performed and the differences obtained from the various leading and trailing edge profiles are examined and explained. Finally, a preliminary study of the effect of twist and taper on MAV blades is conducted.

4.1 Rotor Configuration

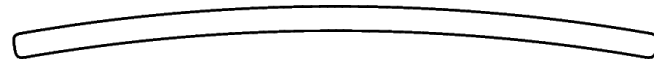
With validation of the predictive capability of OVERTURNS for a low Mach number and Reynolds number 3D fixed-wing case (shown in Chapter 3), the extension is made to the rotor case by exploring the experimental results obtained by Ramasamy et al. [29] on a two-bladed hovering rotor having a radius of 86

mm and a blade chord of 19 mm, resulting in an aspect ratio of 4.52. The rotor was operated at rotational frequency of 50 Hz. The corresponding tip speed is 27 m/s, tip Reynolds number is 32,400 and tip Mach number is 0.08. The resulting rotor solidity is 0.145. The untwisted rectangular blades use a 3.3% curvature circular arc airfoil with a thickness of 3.7%. The baseline section has a blunt leading as well as trailing edge. Experiments were also performed on sections which were slightly different from the baseline section. One of them is the baseline section with sharpened leading edge (SLE) and the other is the baseline section with sharpened leading edge and trailing edge (SLTE). Performance data is available at various collective angles. High resolution flow visualization and particle image velocimetry (PIV) flow-field data are available for the case with a collective angle of 12° using the baseline sectional profile.

Computations are performed on rotor blades with four different sectional profiles, see Fig. 4.1, listed below:

1. Blunt leading and trailing edge (BLTE)
2. Sharp leading edge and blunt trailing edge (SLE)
3. Blunt leading edge and sharp trailing edge (STE)
4. Sharp leading and trailing edge (SLTE)

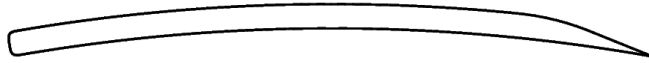
The modeled geometries are mostly similar to the corresponding experimental geometries. Minor modifications are made to the geometries to allow simulation using a C-type grid. The geometries with sharp leading edge are modeled using a slightly rounded leading edge and the geometries with blunt trailing edge are modeled with marginally smoothed trailing edge. Figure 4.2 shows a close up of a mesh near a sharp leading edge and a blunt trailing edge. It should be noted



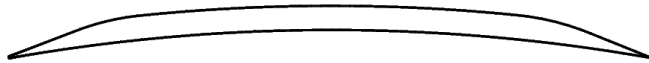
(a) Blunt leading and trailing edge (BLTE)



(b) Sharp leading and blunt trailing edge (SLE)



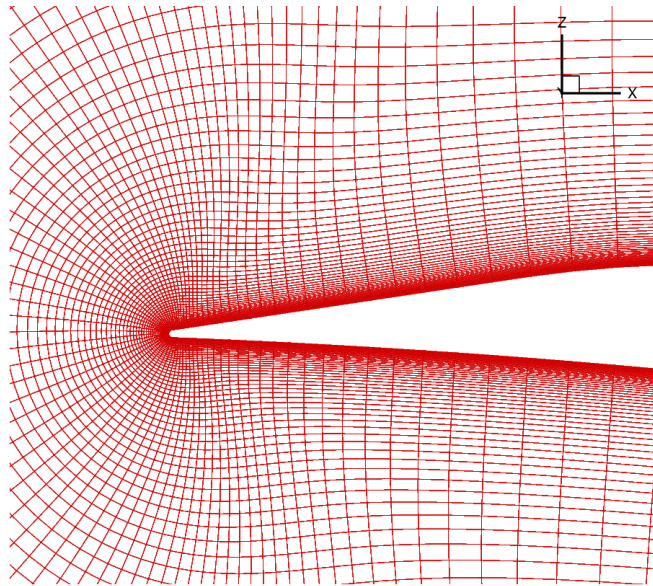
(c) Blunt leading and sharp trailing edge (STE)



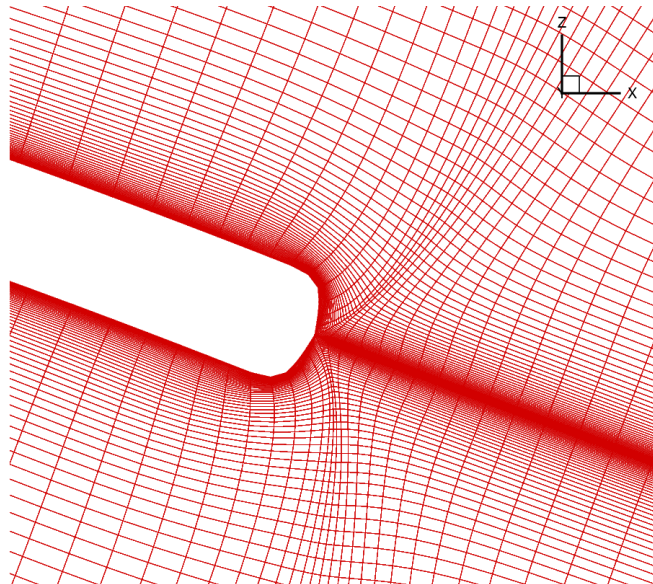
(d) Sharp leading and trailing edge (SLTE)

Figure 4.1: Computational sectional profiles for micro-scale single rotor.

that the differences in the modeled geometry are so small that it is not expected to have any significant influence on the solution.



(a) Leading edge

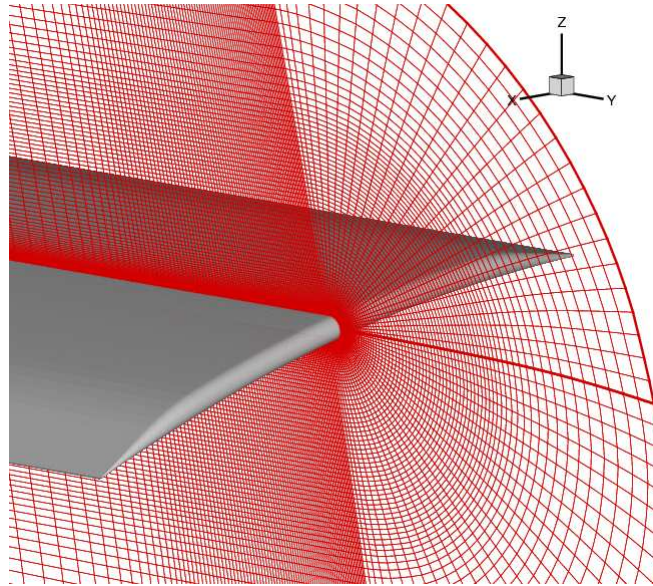


(b) Trailing edge

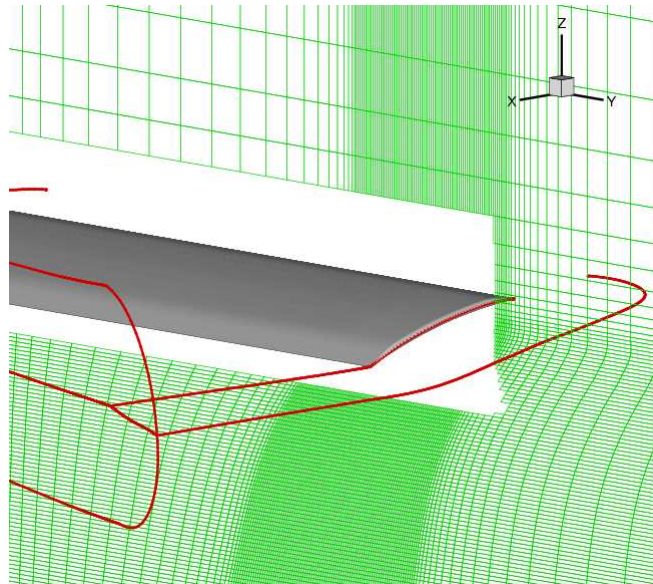
Figure 4.2: C-mesh near sharp leading edge and blunt trailing edge.

4.2 Mesh System

A two mesh overset system with a body conforming blade mesh and a cylindrical background mesh is used for the computations. A hole-cutting technique is used to blank out the portion of the background mesh that overlaps with the blade mesh. Information is exchanged from one grid to the other by means of interpolation. For 12° collective setting cases, where the flow-field is compared with the experiments, computations are performed on a fine mesh with the blade mesh having $267 \times 185 \times 99$ points in the streamwise, spanwise and normal directions respectively and the background cylindrical mesh having $127 \times 186 \times 198$ points in the azimuthal, radial and vertical directions respectively, see Fig. 4.3. Thus, the total number of mesh points used is about 10 million. A spacing of $2.5 \times 10^{-4}c$ is used in the wall normal direction, which corresponds to y^+ value of around 0.5. In the most refined regions, the background mesh has a grid spacing of 0.02 chords in both the radial and the vertical directions. Along the azimuthal direction, a grid plane is spaced every 1.5° . For all the other collective settings, where only performance data is compared, computations are performed on a coarser mesh obtained by leaving out every other point in the spanwise and normal direction. The chosen time-steps correspond to 0.125° of azimuth for the fine mesh and 0.25° of azimuth for the coarse mesh calculations. At each time step, 6 sub-iterations are used in the dual-time procedure. In the fine mesh, the calculations take about 20 days when run in parallel on 8 Intel Xeon 3.20GHz processors. The coarse mesh calculations take one-eighth of the time taken for the fine mesh calculations.



(a) Blade mesh ($267 \times 195 \times 99$)



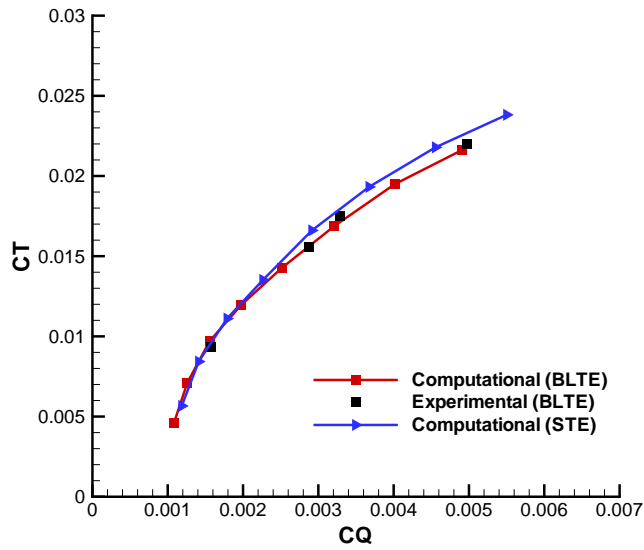
(b) Cylindrical mesh ($127 \times 195 \times 198$) with blade mesh boundary

Figure 4.3: Computational mesh for micro-scale single rotor calculation.

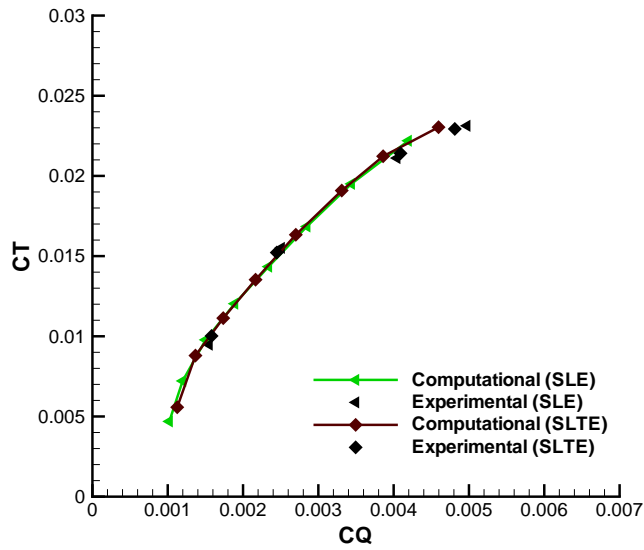
4.3 Performance Comparison

Figure 4.4 compares the computed performance with the experimentally measured values [29]. Note that the computed performance data showed 1 – 2% RMS fluctuation due to flow separation. The results shown here are the mean values obtained by averaging the thrust and power over one revolution. It can be seen that the computed performance for all geometries (BLTE, SLE and SLTE) show good agreement with the experimental results. At higher thrust levels, the power is under-predicted by about 4 – 5% for the SLE and SLTE geometries and over-predicted by 1 – 2% for the BLTE geometry. The differences at higher thrust values can be more clearly seen in figure of merit (FM), see Fig. 4.5, where the predicted maximum FM is slightly higher in comparison with experimental measurements for the sharp leading edge geometries and marginally lower for the BLTE geometry. However, the overall comparison between the computational and the experimental results is reasonably good and, therefore, demonstrate the capability of the current computational study to provide good performance predictions.

Comparing the performance of various geometries, it can be seen that the profiles with a blunt leading edge show degraded performance at all thrust levels compared to a geometry with a sharp leading edge. Also, interestingly, sharpening the trailing edge is seen to improve the performance of the geometry with blunt leading edge, but not for the geometry with a sharp leading edge. Looking at the computational results, it can be seen that while the BLTE and STE geometries achieve a maximum FM of about 0.48 and 0.52, respectively, the sharp leading edge profiles attain a maximum FM greater than 0.55. The maximum FM is achieved at a thrust coefficient level of about 0.015 – 0.02 for the blunt



(a) Blunt leading edge geometries



(b) Sharp leading edge geometries

Figure 4.4: Performance comparison (C_T vs C_Q) with experimental data [29] for micro-scale single rotor.

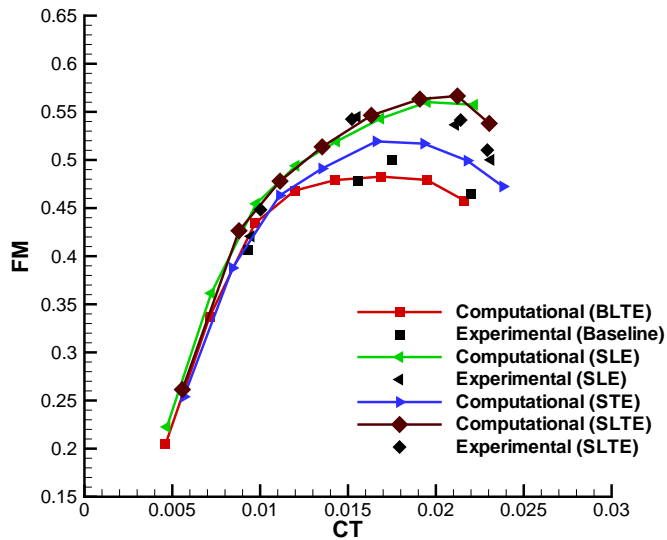


Figure 4.5: Performance comparison (FM vs C_T) with experimental data [29] for micro-scale single rotor.

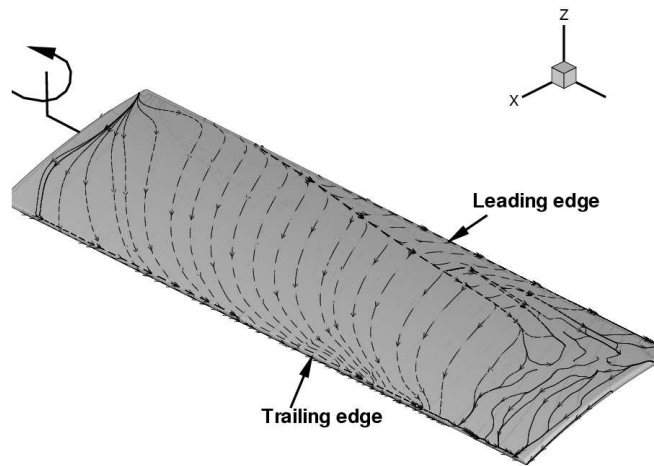
leading edge geometries and at a thrust coefficient level greater than 0.02 for the sharp leading edge geometries. The reason for the differences in performance will be studied in detail in the following sections.

It should be noted that the performance results obtained using the fine mesh for the 12° collective setting are comparable to the coarse mesh results and, therefore, shows grid convergence in the performance data.

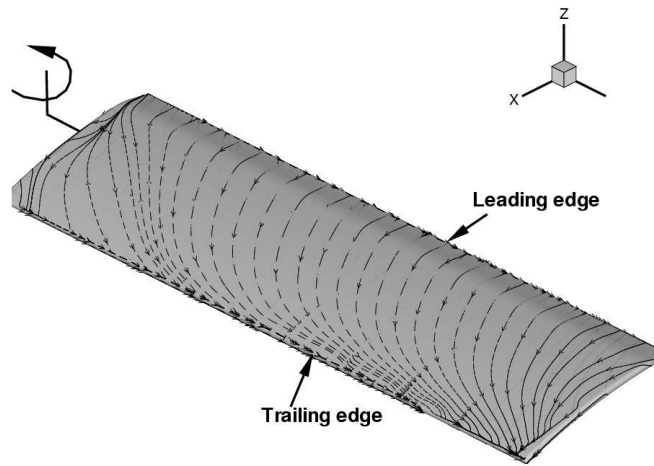
4.4 Blade Surface Streamlines

Separation patterns on the blade surfaces are used to highlight and gain insight into some of the differences resulting from the various cross-section geometries. Figure 4.6 shows the surface streamlines on the blades for 12° collective setting for all four geometries. The results shown are obtained for the fine mesh cal-

culations. Most of the flow is attached for the sharp leading edge geometries, especially the one with a blunt trailing edge. For the profile with a sharp trailing edge, the flow separates near the trailing edge at about 80% chord position. The inboard stations show a small portion of leading edge separation which reattaches with fairly strong radial cross-flow. In contrast, the blunt leading edge geometries result in a leading edge separation that increases in chordwise extent as one goes towards the tip, with the flow completely separating at the tip. The reattachment downstream of the leading edge separation bubble then seems to extend to almost the same positions as for the geometries with sharp leading edge with identical trailing edge profile. It should be noted that, the predicted length of separation bubble and amount of separation may not be very accurate in the present calculations, because of the limitations in the Spalart-Allmaras turbulence model. However, the results can be expected to be qualitatively correct, especially since the performance is predicted reasonably well. Transition modelling might be required to provide a better quantitative prediction of the separation pattern.

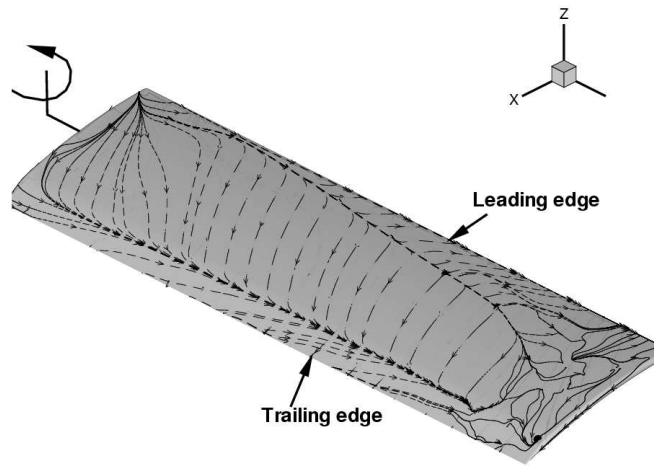


(a) BLTE geometry

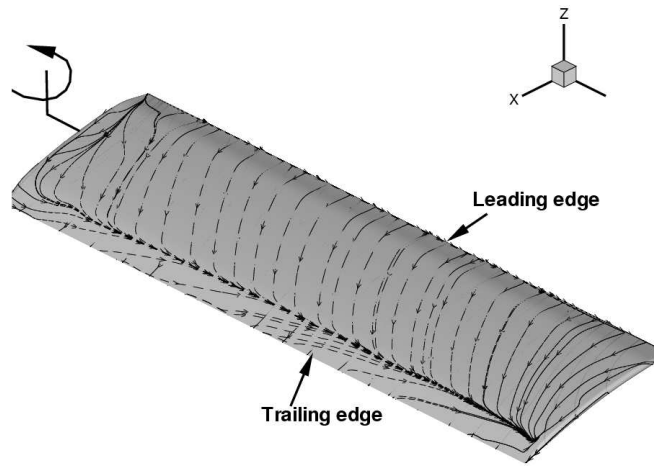


(b) SLE geometry

Figure 4.6: Blade surface streamlines for various geometries at 12° collective setting, micro-scale single rotor.



(c) STE geometry



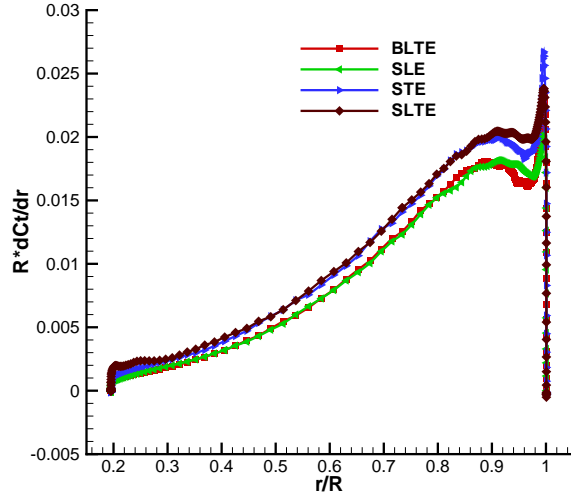
(d) SLTE geometry

Figure 4.6: Blade surface streamlines for various geometries at 12° collective setting, micro-scale single rotor. (cont'd)

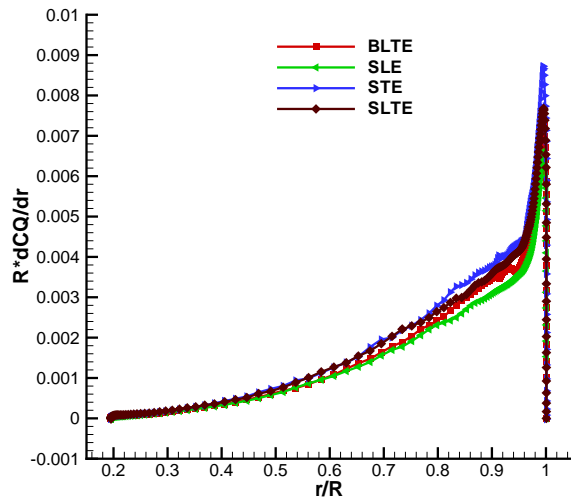
4.5 Spanwise Loading Distributions

The differences in the performance of various geometries can be better understood by looking at the spanwise loading distributions. Figure 4.7(a) shows the spanwise thrust distribution for 12° collective setting for all four geometries. The distribution for the geometries with identical trailing edge profile are comparable through most of the span except near the tip (outboard of $0.9R$). For geometries with identical leading edge, the blunt trailing edge profiles produce a smaller thrust distribution compared to that with sharp trailing edge throughout the span (and thus a smaller overall total thrust). Comparing the power for the geometries with identical trailing edge, see Fig. 4.7(b), the spanwise distribution is similar only in the inboard regions (inboard of $\sim 0.75R$). Blunt leading edge geometries result in a higher power distribution at most of the span locations as compared to sharp leading edge geometries with the same trailing edge profile (and thus a larger total power). The differences are more clearly highlighted in the spanwise distribution of sectional L/D for the blunt and sharp leading edge geometries (with blunt trailing edge), shown in Fig. 4.8. The blunt leading edge geometry clearly has lower sectional L/D through most of the span.

Comparing the power for geometries having identical leading edge profile in Fig. 4.7(b), sharp trailing edge geometries are seen to have higher spanwise power distribution as compared to blunt trailing edge geometries. This could be misinterpreted that sharpening the trailing edge results in performance degradation. However, it should be noted that the results are compared at different thrust levels and it was seen previously in Figs. 4.4 and 4.5 that sharpening the trailing edge improves the overall performance of the blunt leading edge geometry, while it does not affect the performance of the sharp leading edge geometry.



(a) Thrust



(b) Power

Figure 4.7: Spanwise thrust and power distributions for micro-scale single rotor, 12° collective setting.

Isolating the power into components due to viscous forces (viscous power, C_{Q_v}) and pressure forces (pressure power, C_{Q_p}) can provide a better under-

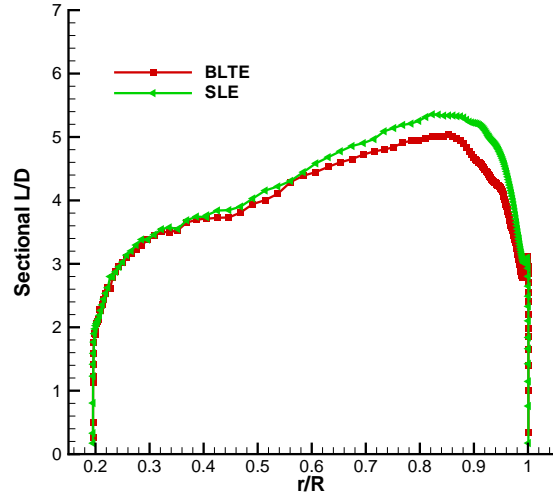
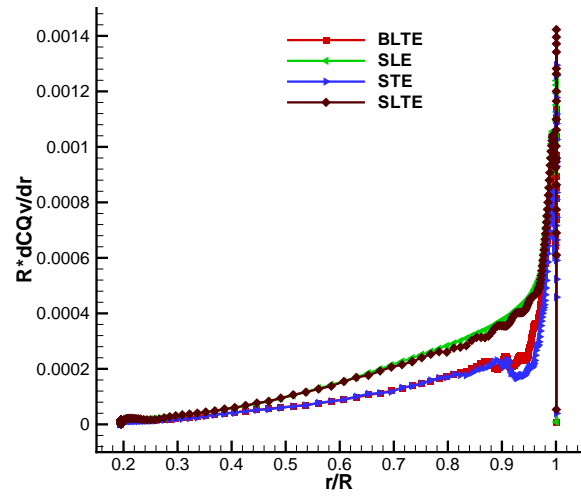
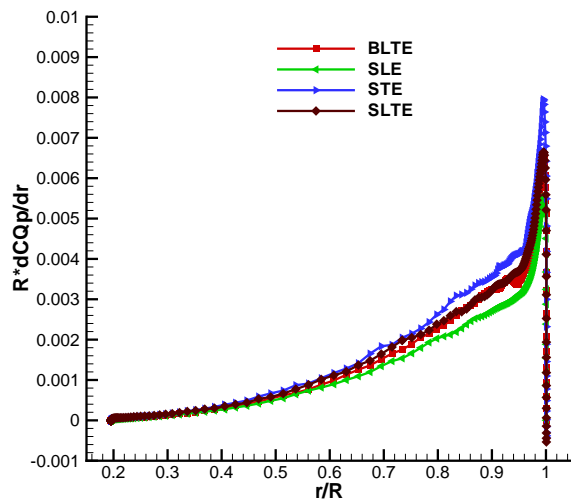


Figure 4.8: Sectional L/D distributions for BLTE and SLE geometry of micro-scale single rotor, 12° collective setting.

standing of the reason for the disparities between the power distributions of the blunt and sharp leading edge geometries. Figure 4.9(a) and Fig. 4.9(b), respectively show the spanwise distribution of viscous and pressure power. From the figures, it is seen that in contrast to the total power, the viscous power distribution resulting from the blunt leading edge geometry cases are lower than that from the sharp leading edge geometries at all span locations. The reason for this is that when there is separated flow, the skin friction is actually in the upstream direction, which lowers the skin friction drag. The distribution of the pressure component of power can be seen to be very similar to that of the total power. Since the viscous component of power is about an order of magnitude smaller than the pressure component, the disparities in the total powers of various geometries arises mainly from the differences in the pressure components and the reason for this dissemblance will be understood better when looking at the blade



(a) Power due to viscous forces



(b) Power due to pressure forces

Figure 4.9: Spanwise distributions of components of power for micro-scale single rotor, 12° collective setting.

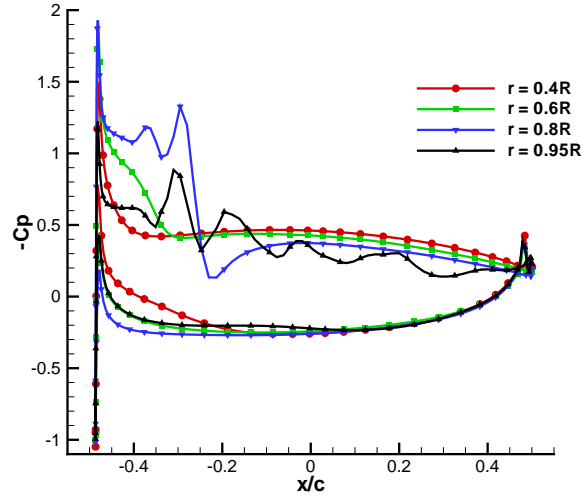
pressure distributions at various spanwise stations.

4.6 Blade Pressure Distributions

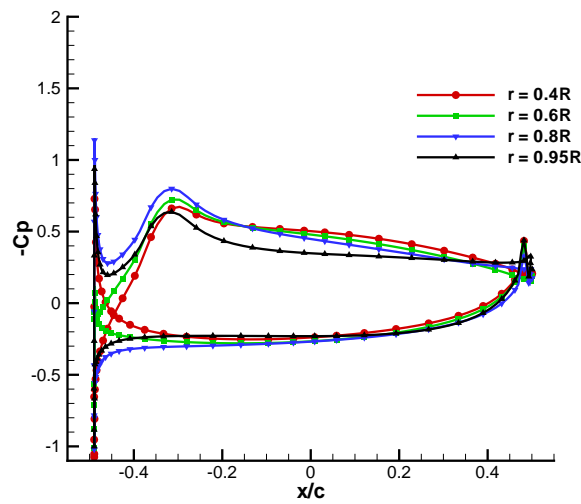
A better understanding of the spanwise distributions of thrust and power can be obtained by looking at surface pressure plots at selected spanwise stations. Figure 4.10 shows the chordwise surface pressure distribution for all four geometries at 12° collective setting at four spanwise locations. The chordwise distributions for the sharp leading edge geometry cases do not show much variation with span, whereas those for the blunt leading edge geometries vary significantly with span, especially in the outboard regions because of the leading edge separation. The effect of the laminar separation bubble can be seen at the $0.6R$ and $0.8R$ span locations for the blunt leading edge geometries, where the pressure distributions become relatively constant near the leading edge. At the $0.95R$ span location, where the flow is completely separated, the pressure distribution on the upper surface is wavy and was seen to be quite unsteady.

Comparing the chordwise pressure distributions resulting from the blunt leading edge geometries with those for the sharp leading edge geometries having identical trailing edge profile, especially at the inboard locations, one observes that the distributions are different near the leading edge, whereas they are comparable near the trailing edge. The blunt leading edge geometries result in a larger suction peak which occurs at an earlier chordwise location compared to that for the sharp leading edge geometries.

Comparing the chordwise pressure distributions resulting from the blunt trailing edge geometries with those for corresponding sharp trailing edge geometries, it can be seen that the distributions are similar on the bottom surface of the airfoil. However, on the top surface of the airfoil, the blunt trailing edge geometries cause higher pressure through most of the chord. As a result, the blunt trailing



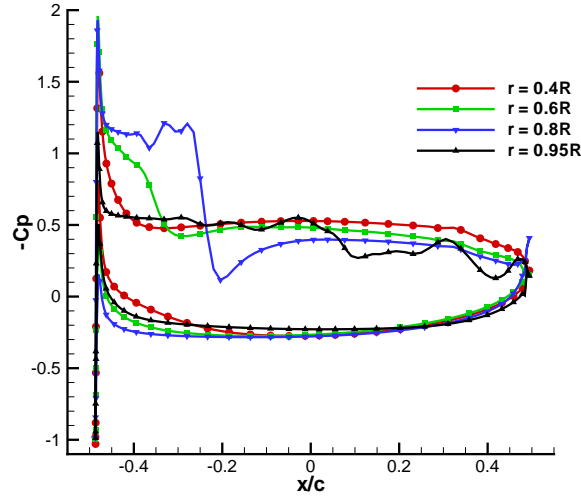
(a) BLTE geometry



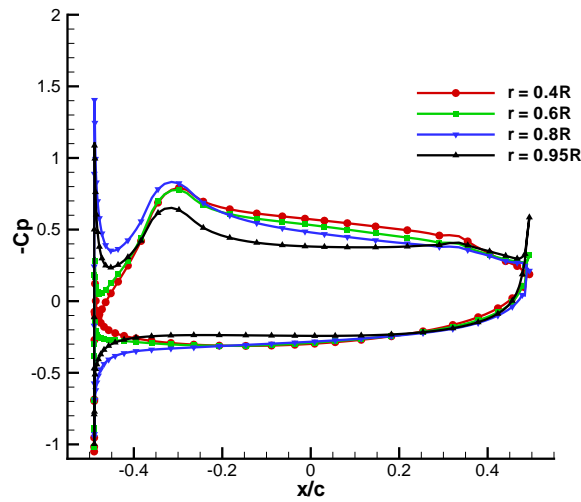
(b) SLE geometry

Figure 4.10: Blade pressure distributions at different spanwise location for micro-scale single rotor, 12° collective setting.

edge geometries have lower thrust compared to those from the corresponding sharp trailing edge geometries.



(c) STE geometry

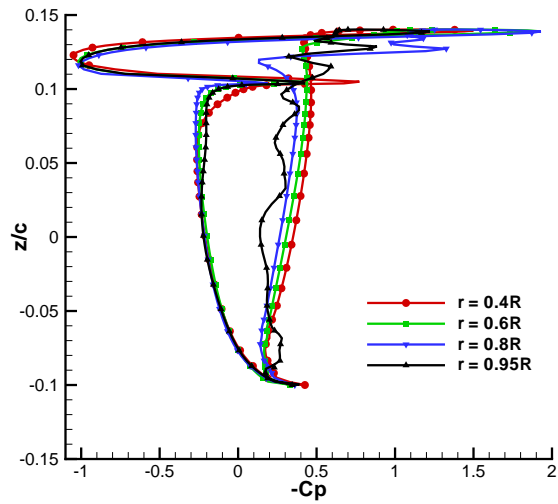


(d) SLTE geometry

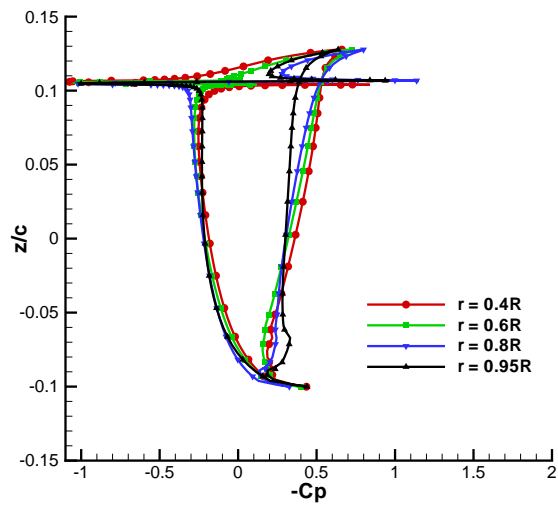
Figure 4.10: Blade pressure distributions at different spanwise location for micro-scale single rotor, 12° collective setting. (cont'd)

Figure 4.11 shows the variation of surface pressure along the vertical direction at the same four spanwise locations for all four geometries at 12° collective

setting. The surface pressures proceed in a clockwise manner around all geometries at all four spanwise locations, except right near the suction peaks at the leading edge (both at the top and bottom for the blunt leading edge geometries case). The area enclosed by the curve gives the sectional pressure drag coefficient. Clearly, the pressure drag for the blunt leading edge geometries are higher than that for the sharp leading edge geometries and the difference mainly occurs near the maximum z/c location which corresponds to the regions near the leading edge. The high pressure region created near the leading edge due to stagnating flow generates significant amount of pressure drag for the blunt leading edge geometry case. A small contribution to the pressure drag also comes from the reduction in suction peak due to the leading edge laminar separation bubble. It can also be seen that the pressure drag for the blunt trailing edge geometries are smaller compared to the corresponding sharp trailing edge geometries.

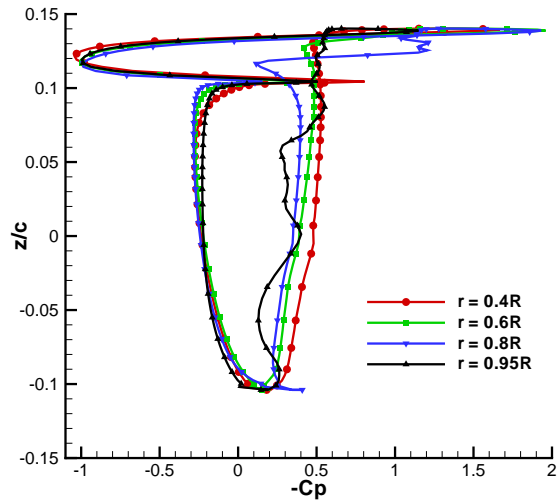


(a) BLTE geometry

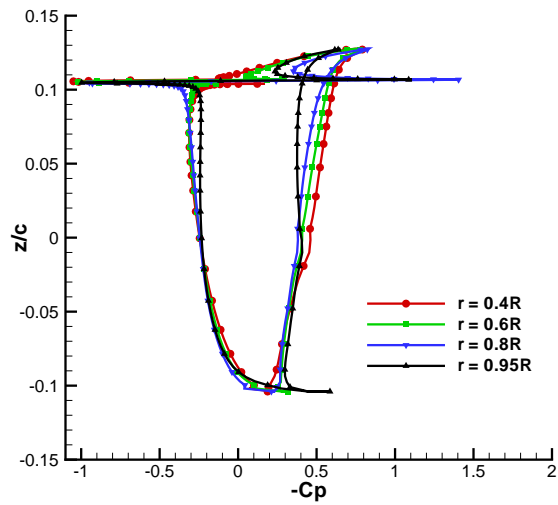


(b) SLE geometry

Figure 4.11: Blade pressure distributions at different spanwise location for micro-scale single rotor, 12° collective setting.



(c) STE geometry



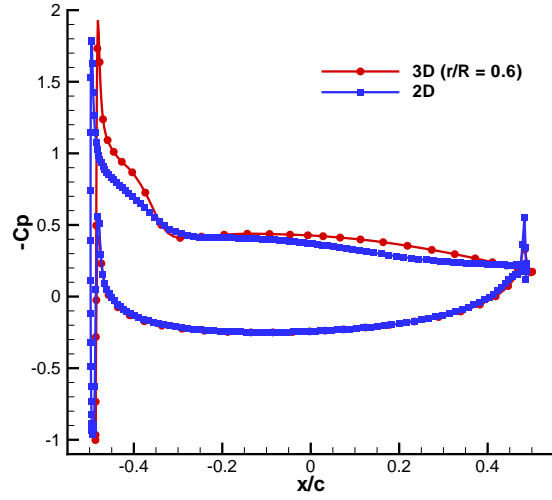
(d) SLTE geometry

Figure 4.11: Blade pressure distributions at different spanwise location for micro-scale single rotor, 12° collective setting. (cont'd)

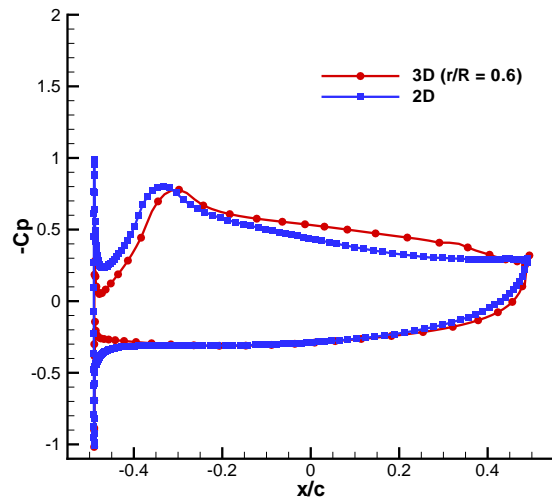
4.7 Two-Dimensional Analysis

Simple design tools like Blade Element Momentum Theory and Vortex Filament Method rely on two-dimensional CFD data. The applicability of these analyses to micro-rotor problems is determined by performing 2D computations for the flow conditions corresponding to one particular section in BLTE and SLTE blade and comparing the chordwise pressure contours with those obtained from the 3D analysis. The chosen section on the blade is $0.6R$. The corresponding Reynolds number is 19,440 and Mach number is 0.048. The local angle of attack is determined by using the inflow distribution (shown in Fig. 4.30) and is found to be approximately 3° at $0.6R$, when the collective setting is 12° for both the geometries.

Figure 4.12 shows the chordwise pressure distribution for 2D calculation at 3° angle of attack as well as that for the 3D calculation done at 12° collective setting, at $0.6R$ span location for both BLTE and SLTE geometry. The distributions are seen to compare fairly well. There is slight discrepancy on the upper surface distribution, which arises because of the discrepancy in determining the correct effective local angle of attack. Additional discrepancy on the upper surface of the 2D calculation for the BLTE geometry arise because of difference in separation prediction near the leading edge. Nevertheless, the overall prediction from 2D calculation is reasonably good, suggesting that simple tools can indeed provide reasonably good performance prediction when the flow is attached. However, the two-dimensional analyses are not capable of predicting the highly three-dimensional flow-field found near the tip of the BLTE geometry and therefore, can lead to inaccuracies in the performance prediction, when the flow is separated.



(a) BLTE geometry



(b) SLTE geometry

Figure 4.12: 2D and 3D pressure distributions for conditions found at $0.6R$ span location for micro-scale single rotor at 12° collective setting.

Figure 4.13 shows lift to drag ratio versus angle of attack for various leading and trailing edge geometries. At 3° angle of attack, the L/D ratio for various

geometries is seen to be close to maximum (~ 15). Note that the L/D ratio for the 2D calculation is much larger compared to what was seen in 3D (~ 5), see Fig. 4.8. The reason for this is because of the difference in the direction in which drag is determined. In 3D calculations, the local free-stream direction is not known a priori and therefore, the drag is measured along the rotational direction. However, in 2D computations the drag is measured along the free-stream direction. To provide proper comparison, the component of drag along the local free-stream direction needs to be taken in 3D and doing so would provide good comparison of L/D ratio with those obtained from 2D.

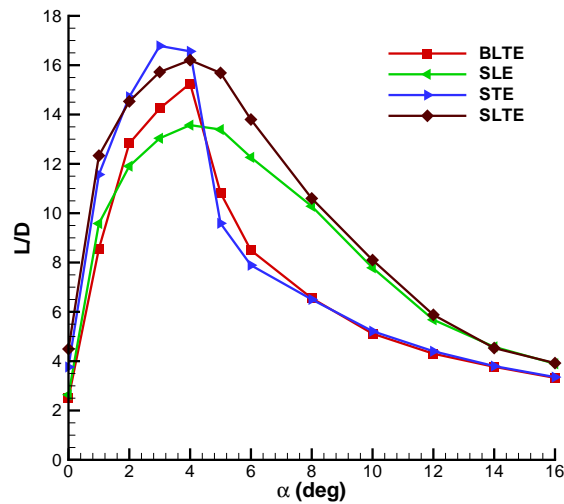


Figure 4.13: L/D versus angle of attack for various geometries using 2D calculation.

Having established the reliability of 2D calculation in the attached flow regions, the 2D analysis is used to provide further understanding of the differences between blunt and sharp leading edge geometries for a range of angles of attack. It is observed in Fig. 4.13 that, blunt leading edge geometries have slightly

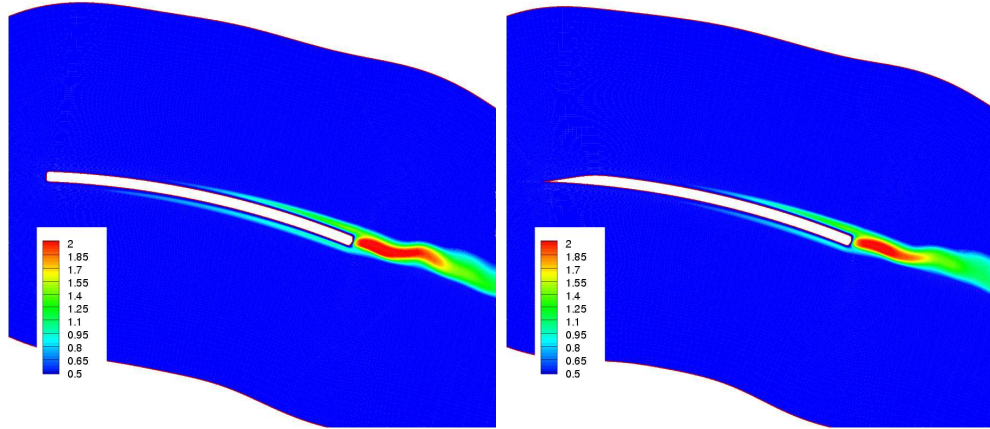
higher L/D ratio compared to sharp leading edge geometries with identical trailing edge at lower angles of attack. However, the L/D ratio for the blunt leading edge geometries is seen to rapidly decrease beyond 5° angle of attack, while the sharp leading edge geometries have a much more gradual drop. As a result, sharp leading edge geometries have better L/D ratio at higher angles of attack. In 3D calculations, high local angles of attack were found in outboard region at moderate collective settings and through most of the span at higher collective settings. As a result, blunt leading edge geometries show slightly degraded performance at moderate collective settings and significantly degraded performance at higher collective settings. The variation of 2D lift to drag ratio with angle of attack also suggests that for all geometries, it is preferable to operate at a local angle of attack of around 3° . This can be achieved by having a certain amount of negative twist.

4.8 Sectional Flow Contours

In order to attain a better understanding of the separation, spanwise contours of eddy viscosity for all four geometries at 12° collective setting are plotted in Figs. 4.14, 4.15, 4.16 and 4.17 at the same spanwise locations as the pressure plots, shown earlier. At the $0.4R$ station there is little difference between all of the cases. The leading edge separation bubble for the blunt leading edge geometries is very small. The high values of eddy viscosity are concentrated in the separated regions near the trailing edge and in the very near wake. The wake also seems to show the typical shear layer instabilities for low Reynolds number flow, clearly indicating that the flow is unsteady. It should be noted that over most of the airfoil, the eddy viscosity values are less than one and the flow

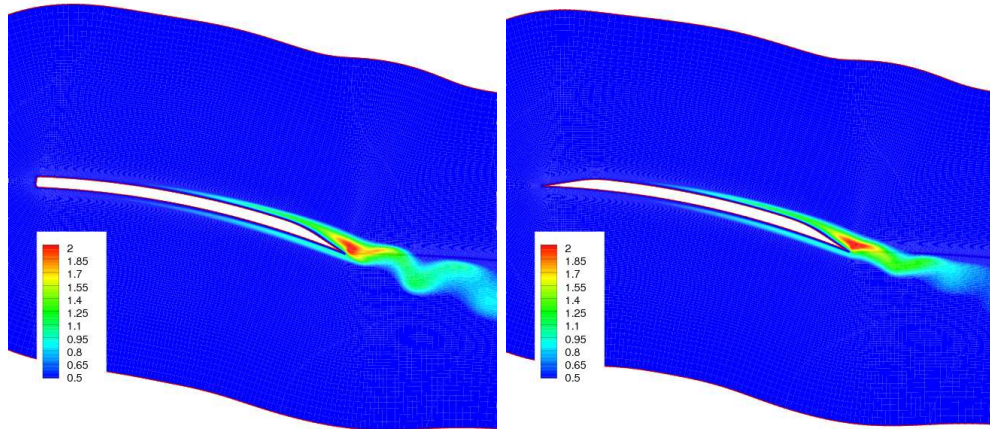
is substantially predicted to be laminar. By the $0.6R$ station, the separation is more pronounced for the blunt leading edge geometries in the leading edge region; as a result, the results do show a movement forward for the beginning of the growth in eddy viscosity. The region of higher eddy viscosity has grown slightly larger near the trailing edge for both geometries with clear shear layer instability. By the $0.8R$ location, there is now a region of high eddy viscosity near the leading edge region for the blunt leading edge geometries that connects to the high eddy viscosity region near the trailing edge. At the $0.95R$ station there is clearly a relatively massively separated flow region that extends over nearly the whole chord of the cross section for the blunt leading edge geometry cases, resulting in a large volume of high eddy viscosity flow. The eddy viscosity contours seem to show that the Spalart-Allmaras model fortuitously mimics a transition model. The eddy viscosity remains fairly low in the laminar regions and increases as the flow separates and the flow transitions to turbulent. This suggests that the separation pattern predicted in the present calculations might indeed be quite reasonable.

Figures 4.18 and 4.19 show radial velocity contours along with streamlines at spanwise locations of $0.4R$ and $0.8R$, respectively. The plots show similar separation features as those observed in the contours of eddy viscosity. It is interesting to note that in the regions of flow separation, the radial flow component of velocity is very strong as compared to the regions outside. This may result in the transport of eddy viscosity from within the leading edge separation bubble towards the tip, further elevating the level of eddy viscosity in the tip region.



(a) BLTE geometry

(b) SLE geometry



(c) STE geometry

(d) SLTE geometry

Figure 4.14: Eddy Viscosity contours at $0.4R$ for micro-scale single rotor, 12° collective setting.

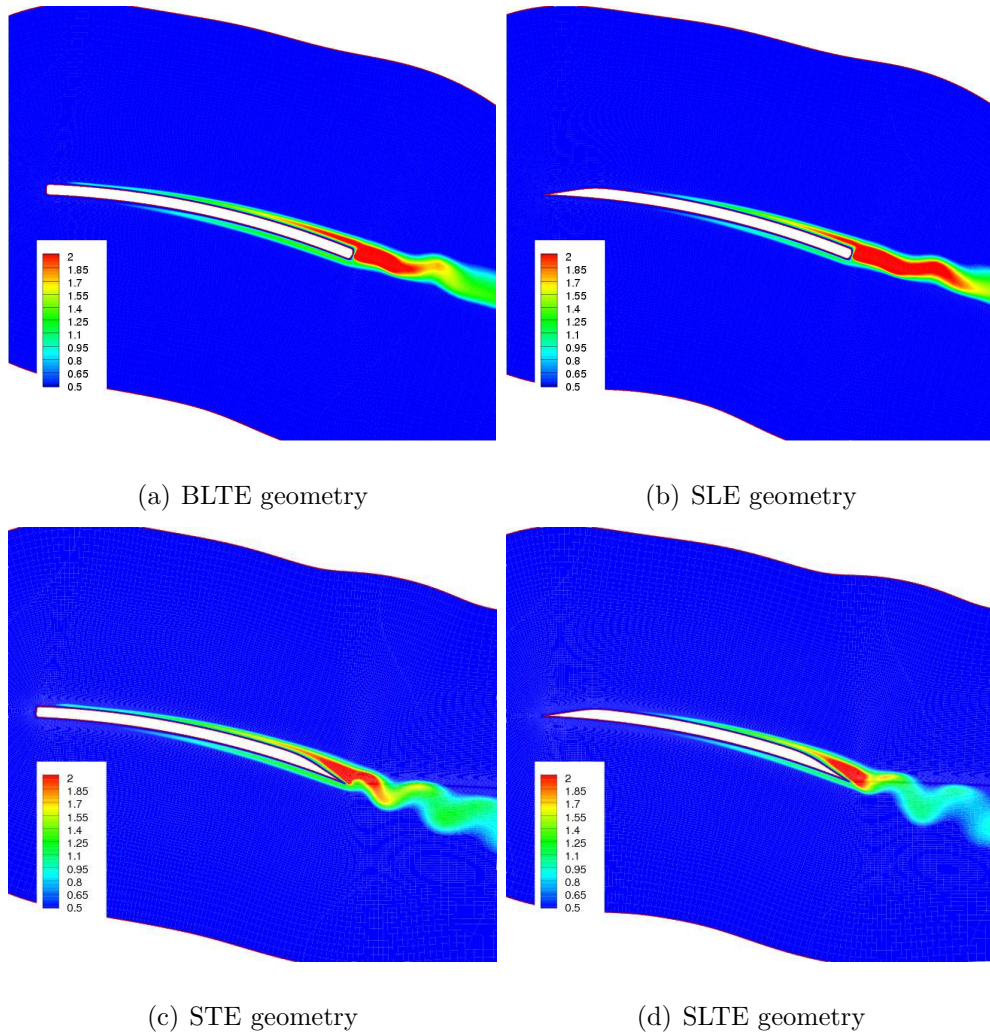
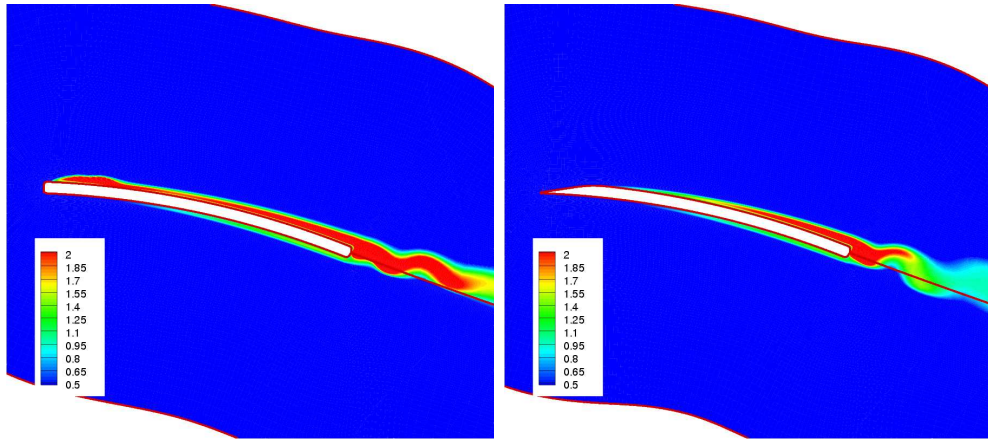
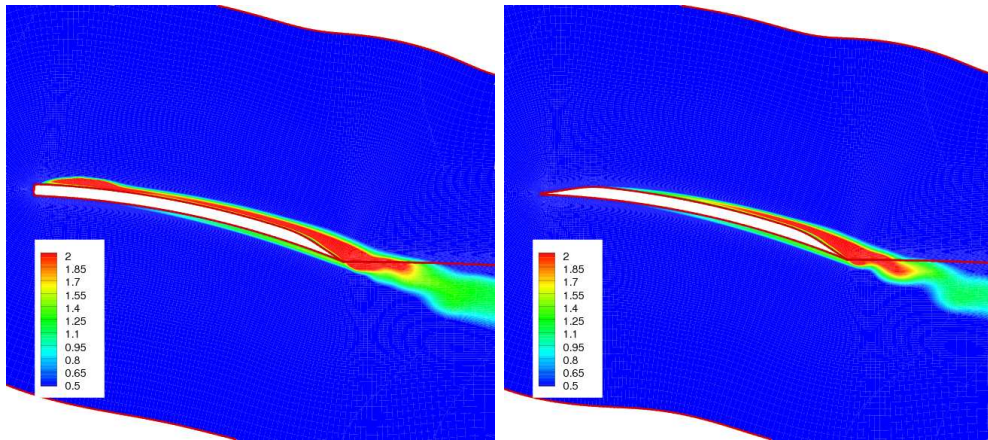


Figure 4.15: Eddy Viscosity contours at $0.6R$ for micro-scale single rotor, 12° collective setting.



(a) BLTE geometry

(b) SLE geometry



(c) STE geometry

(d) SLTE geometry

Figure 4.16: Eddy Viscosity contours at $0.8R$ for micro-scale single rotor, 12° collective setting.

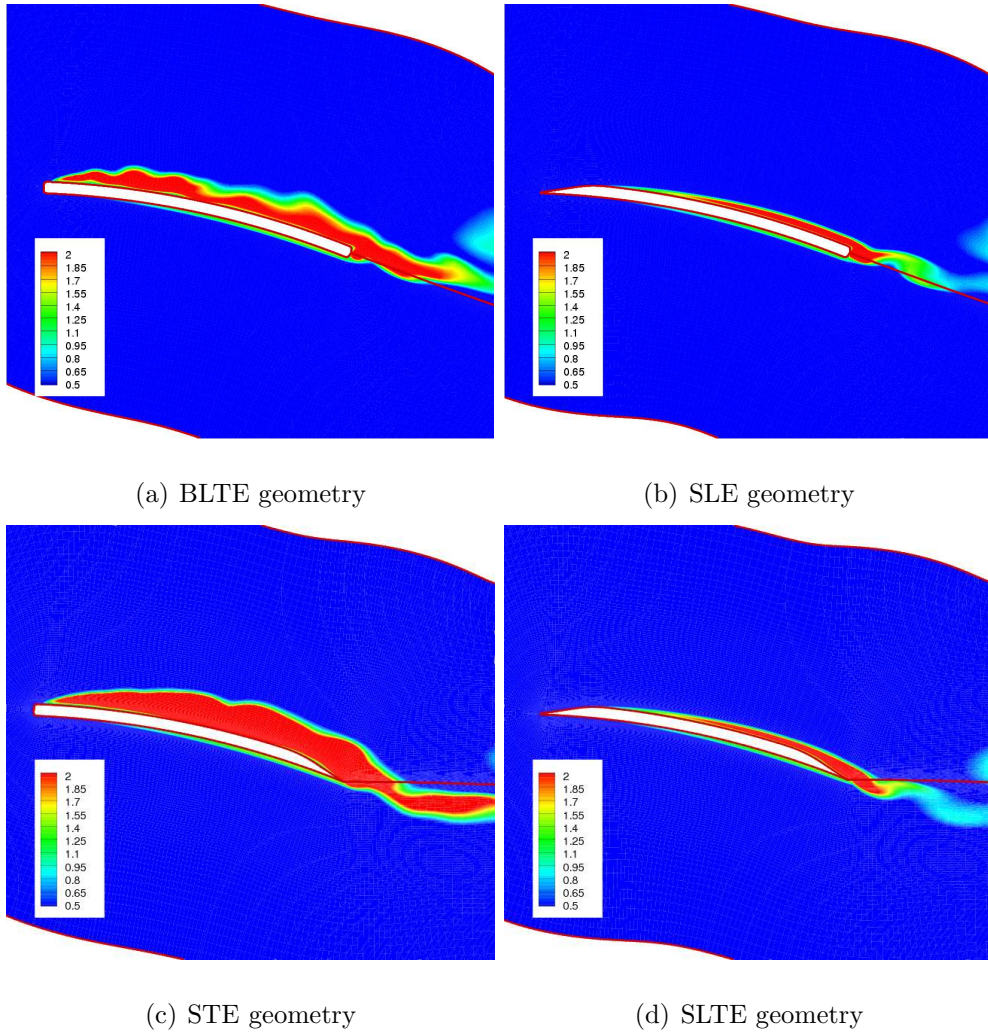


Figure 4.17: Eddy Viscosity contours at $0.95R$ for micro-scale single rotor, 12° collective setting.

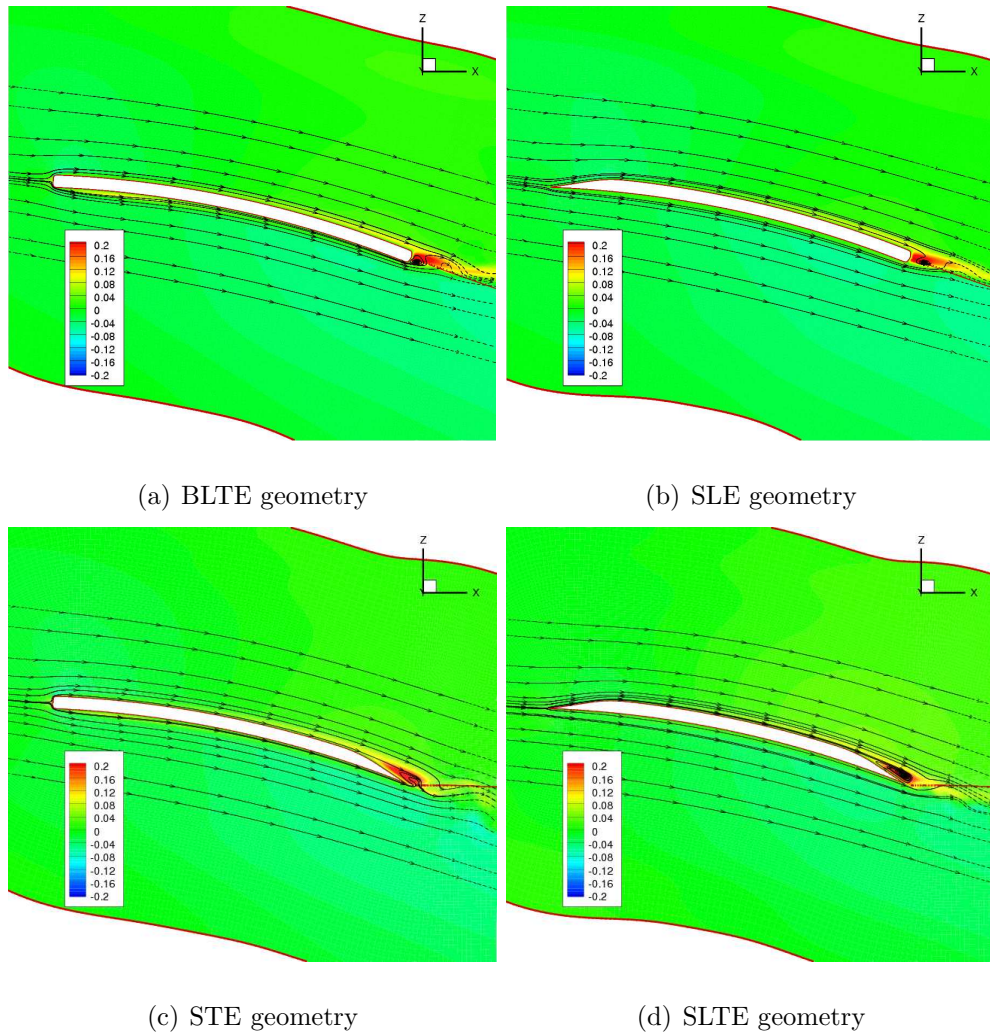


Figure 4.18: Radial Velocity contours along with streamlines at $0.4R$ for micro-scale single rotor, 12° collective setting.

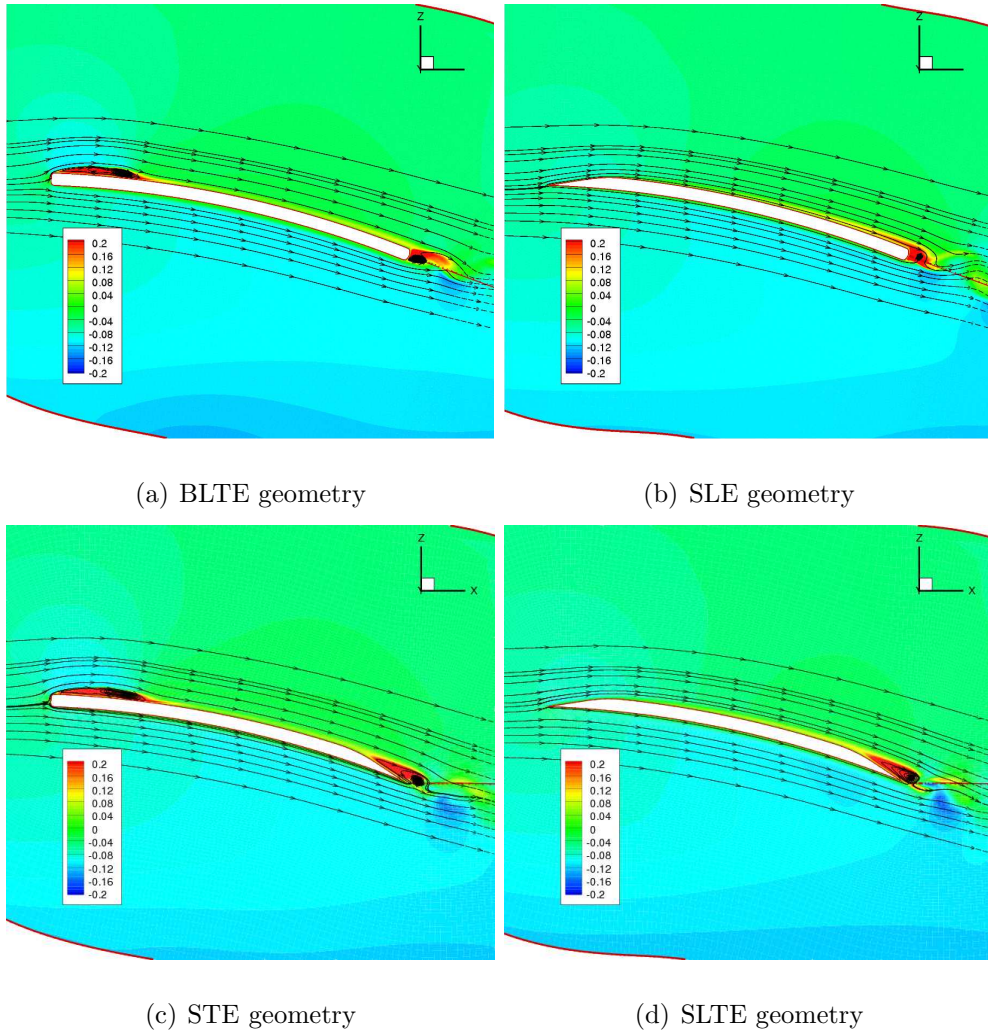


Figure 4.19: Radial Velocity contours along with streamlines at $0.8R$ for micro-scale single rotor, 12° collective setting.

4.9 Flow-field Visualizations

Next, qualitative features in the flow-field are examined. Figure 4.20 shows iso-surfaces of the so-called q -criterion [90] near the blade surface for 12° collective setting for all four geometries. While the flow is smooth near the tip of the sharp leading edge geometries, numerous vortical structures can be seen on the top of the blades with blunt leading edge geometries, due to flow separation. These structures can also be seen in Figs. 4.21 (a) & (c), which show the streamwise vorticity contours. Looking at the tip vortex, for both the leading edge geometries, it is evident that the tip vortex flow-field is extremely complicated because of the presence of a variety of secondary structures near the blade tip. The origin of these structures can be discerned from Fig. 4.21. While initial traces of the tip vortex can be seen slightly upstream of the quarter-chord point, secondary vortices originate from the leading edge as well as from the separation of the crossflow boundary layer rolling over the rounded tip. In addition to the secondary vortices, a large number of additional vortical structures are found near the trailing edge of the blade over most of the span for both cases as seen from Fig. 4.21; although they are better formed for the sharp leading edge geometries. Similar vortical structures can be seen even in the experimental flow visualization [29] shown in Fig. 4.22. These structures are formed as a result of flow separation near the blade trailing edge. Within a short distance downstream of the trailing edge, these structures appear to have merged with the tip vortex (as seen from the coherent iso-surface in Fig. 4.20).

Figure 4.23 shows the iso-surface of q -criterion (colored with vorticity magnitude contour) in the entire flow-field for the BLTE geometry at 12° collective setting. The resolution of the tip vortex until 3 blade passages is clearly evident.

Beyond this wake-age, the background mesh becomes too coarse to accurately represent the details of the tip vortex. An interesting feature revealed from this figure is the fact that while the tip vortex is smooth initially, it seems to get twisted near the first blade passage. This is because of the fact that it is embedded in a highly strained field due to the presence of the evolving tip vortex (note that the vertical convection of the tip vortex is relatively low before the first pass as has been well documented [1, 38]) and other near-blade structures. It is also seen that after the first pass, the vortex becomes wavy along its axis, thus suggesting a slight instability. Interestingly, such an instability was observed experimentally even for a full-scale rotor [1]. It should be mentioned here that the corresponding iso-surface for the other geometries at 12° collective setting is not too different from Fig. 4.23.

Further evidence of the interaction between different turns of the tip vortex can be seen in Fig. 4.24(a), in which vorticity magnitude contours are shown along a 0° azimuthal plane of the background mesh. The tip vortex, after its first blade passage, is seen to interact with the inboard wake as well as the second blade passage, both of which introduce a strain-field. The experimental flow visualization [29] plotted in Fig. 4.24(b) is qualitatively similar to the computed flow-field and shows similar interactions.

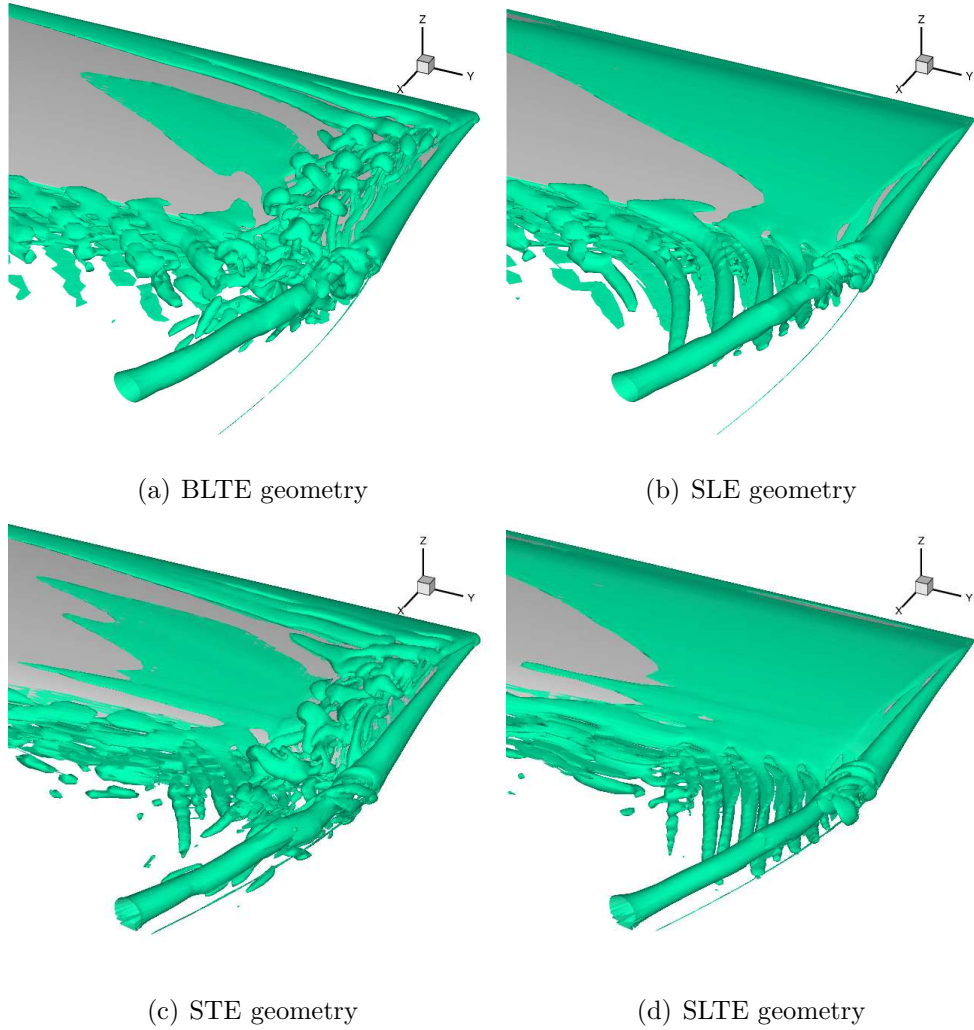


Figure 4.20: Iso-surfaces of second invariant of velocity magnitude, $q = 8.0$, at 12° collective setting for micro-scale single rotor.

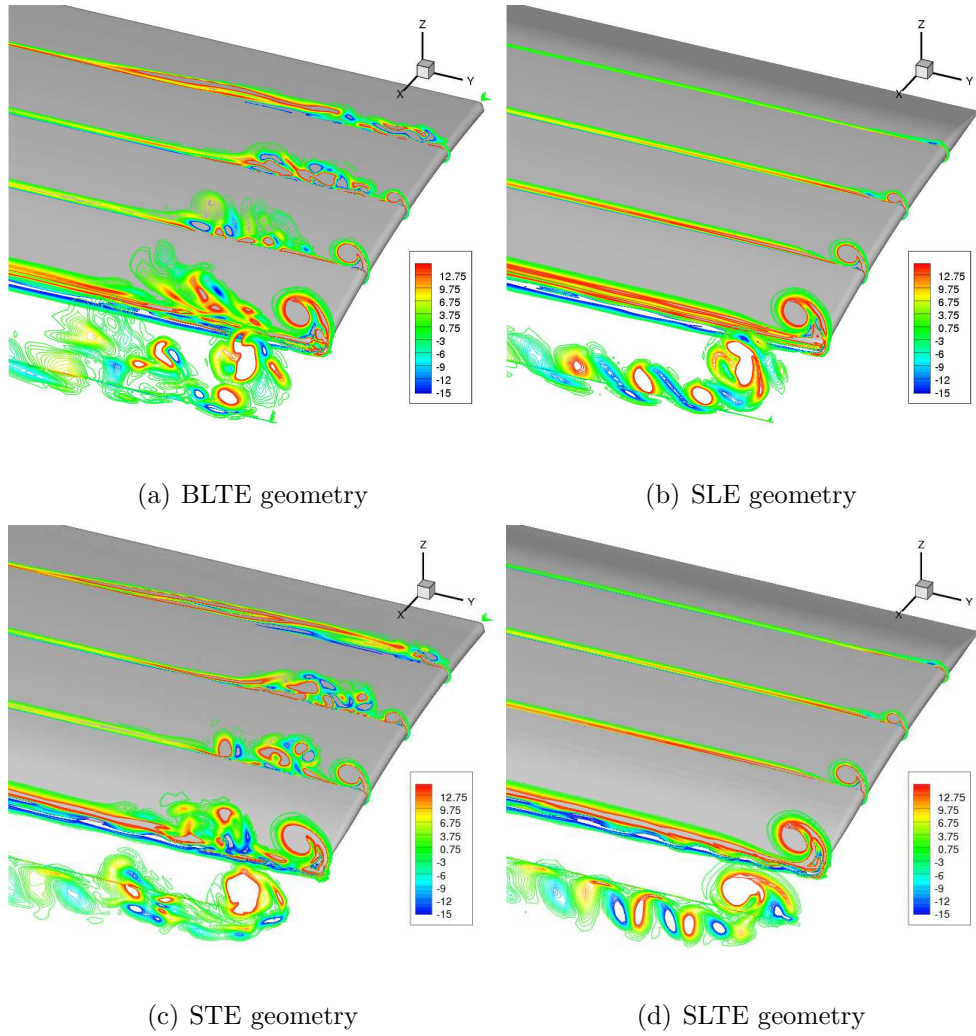


Figure 4.21: Contours of streamwise vorticity at 12° collective setting for micro-scale single rotor.

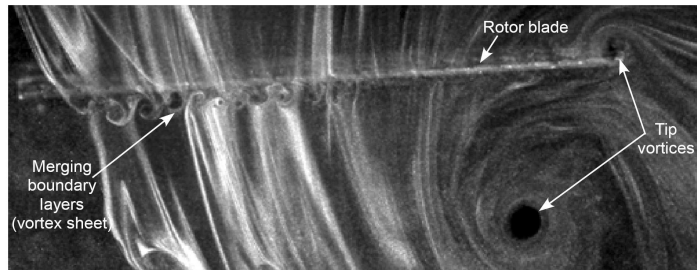


Figure 4.22: Experimental flow visualization [29].

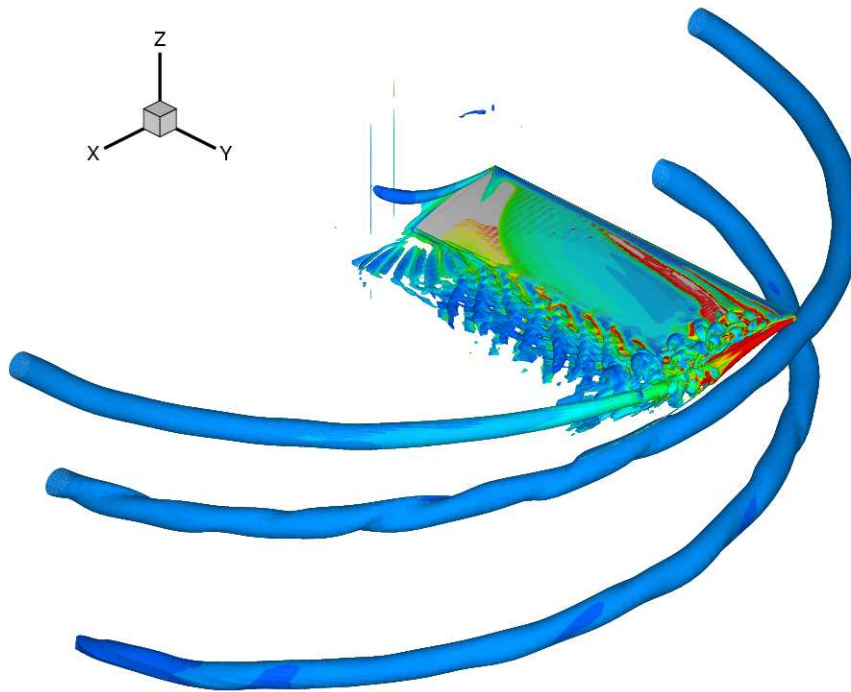
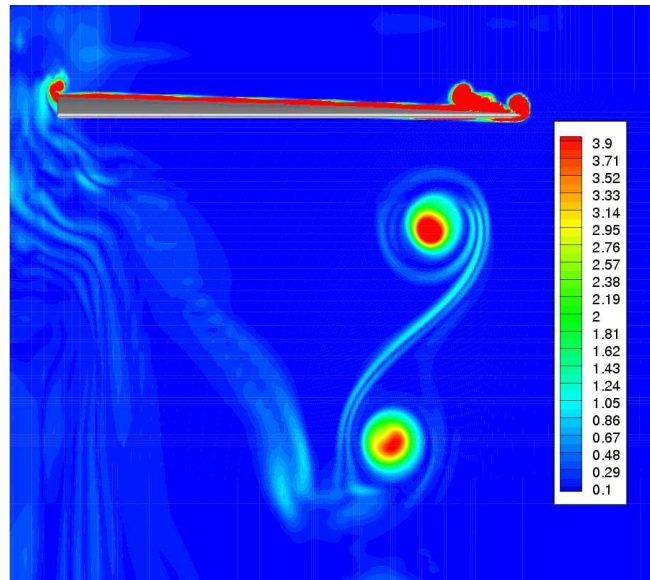
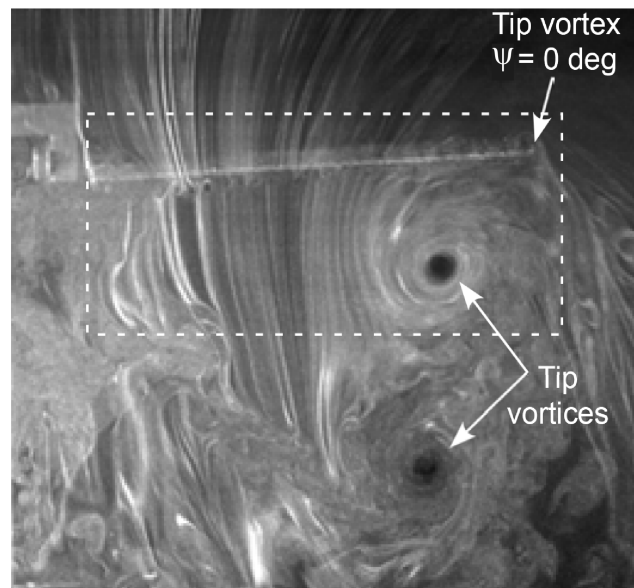


Figure 4.23: Iso-surfaces of second invariant of velocity magnitude (colored by vorticity magnitude), $q = 1.0$, at 12° collective setting for micro-scale single rotor, BLTE geometry.



(a) Contours of vorticity magnitude at $\psi = 0^\circ$ for BLTE geometry of micro-scale single rotor at 12° collective setting.



(b) Experimental flow visualization [29]

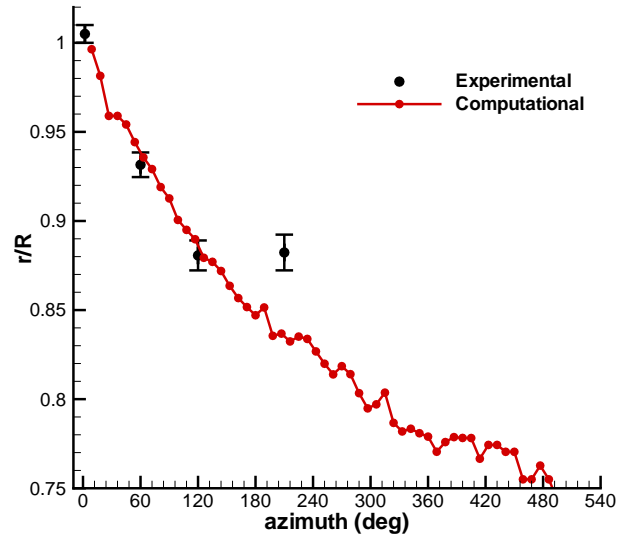
Figure 4.24: Flow-field comparison.

4.10 Wake Trajectory

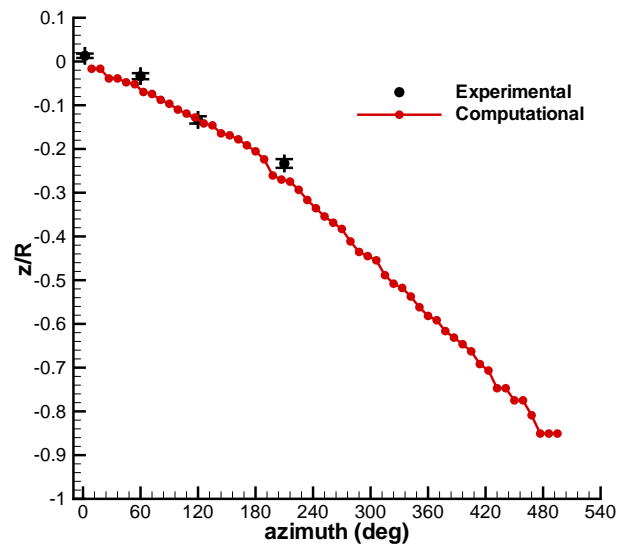
Figure 4.25 shows the computed wake trajectory for the BLTE geometry at 12° collective setting, along with the experimental data. The computed radial contraction of the wake (shown in Fig. 4.25(a)) shows good comparison with the experimental wake trajectory in the early wake ages. By the wake age of 210° , the experimental wake trajectory does not seem to contract, while the computed trajectory continues to contract. The difference could be because of the large separation near the root due to the mounting apparatus (hub) in the experiment, which prevents wake contraction (see Fig. 4.26). The instability in the computed wake, after the first blade passage, can be seen in the form of wiggles after 180° azimuth (discussed previously). Additionally, the contraction rate is seen to decrease, after the first blade passage at 180° azimuth, as a result of the interaction of the tip vortex before the first blade passage with the tip vortex after the blade passage. The blade passage effect is also seen in the vertical convection of the wake, see Fig. 4.25(b). After the blade passage, the vertical convection rate increases because of increased inflow. Note that, computed vertical convection is seen to compare well with the experimental measurements.

Figure 4.25(c) shows the spatial location of the wake. The computed trajectory is again seen to compare well with the experiments during the initial wake ages, but differs at the later wake ages, due to the differences in the radial contraction explained before. For the computed trajectory, it can be seen that the wake contracts to less than $0.8R$ and is not too different from that observed for full-scale rotors [1]. Recall that the theoretical momentum theory contraction is $0.707R$. The wake trajectories for the other geometries are not too different

from that of the BLTE geometry.

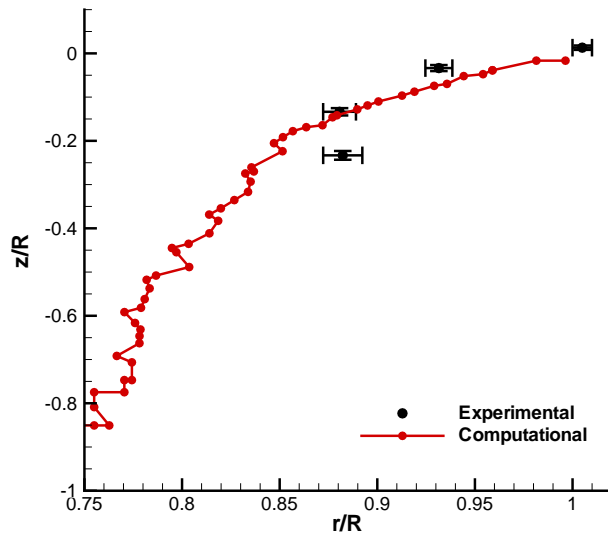


(a) r/R vs azimuth



(b) z/R vs azimuth

Figure 4.25: Comparison of wake trajectory with experimental data [29] for BLTE geometry of micro-scale single rotor at 12° collective setting.



(c) z/R vs r/R

Figure 4.25: Comparison of wake trajectory with experimental data [29] for BLTE geometry of micro-scale single rotor at 12° collective setting. (cont'd)

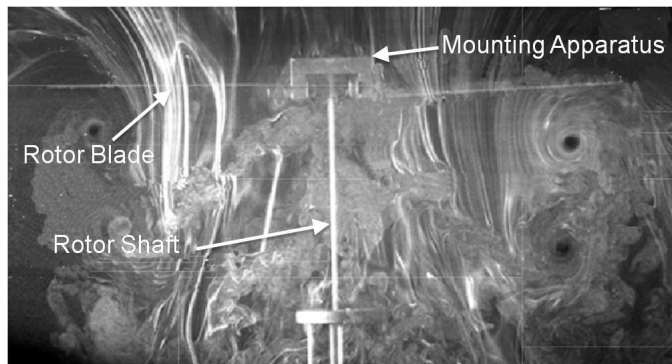
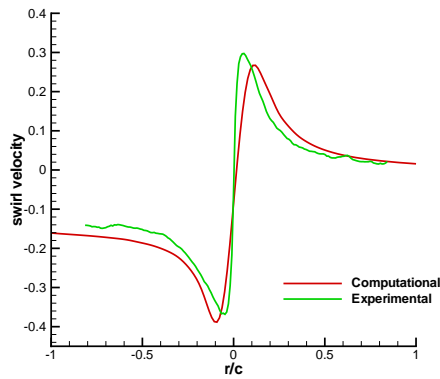


Figure 4.26: Experimental flow visualization [29].

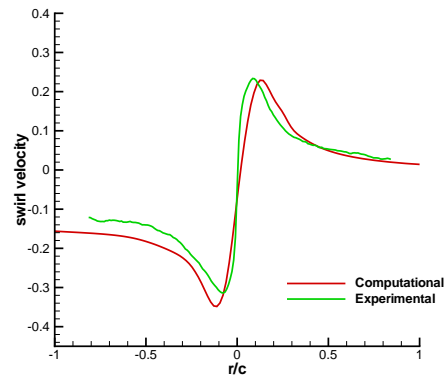
4.11 Vortex Structure Comparison

Experimental data [29] can be used to quantitatively validate the initial development and evolution of the tip vortex structure. Figures 4.27 and 4.28 show the comparison of swirl velocity and axial velocity profiles, respectively along a line passing through the center of the tip vortex at different wake ages at 12° collective setting for the BLTE geometry. It should be noted that the axial deficit in the core of the vortex is very large and is most likely due to the dominance of viscous forces for these small scale micro-rotors. In general, there is good agreement between the computational and the experimental results. The peak swirl velocity is predicted correctly at all azimuth locations, however, the peak axial deficit is over-predicted (less than $\sim 25\%$). The core radius, defined as half the distance between the peak-to-peak swirl velocity is also over-predicted at all wake ages. At 180° wake age, the core radius is over-predicted by about 20%. However, the rate of core growth and the rate of peak swirl decay is predicted accurately, see Fig. 4.29, indicating that the inconsistency mainly arises during tip vortex formation, while the tip vortex evolution is well resolved.

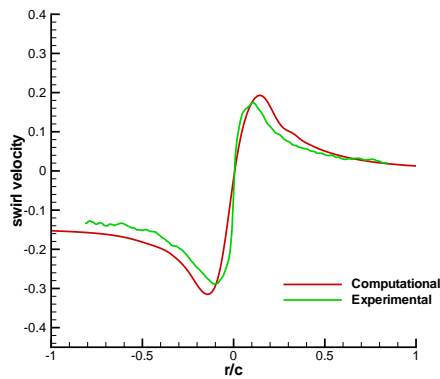
Apart from the experimental uncertainties, there are two possible reasons for the discrepancy. The main reason could be due to the inadequacy of the Spalart-Allmaras turbulence model in a non-isotropic environment such as those found near the regions of tip vortex formation. Additionally, better turbulence modeling is required to capture the separation correctly. It might be worthwhile to examine this issue using a DES approach in the tip region. The second reason for the discrepancy could be due to under-resolution of the tip vortex formation because of insufficient mesh resolution near the blade tip.



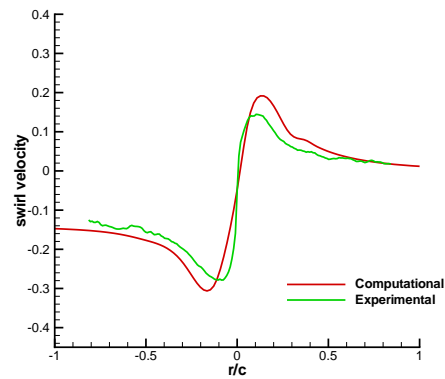
(a) $\Psi = 30^\circ$



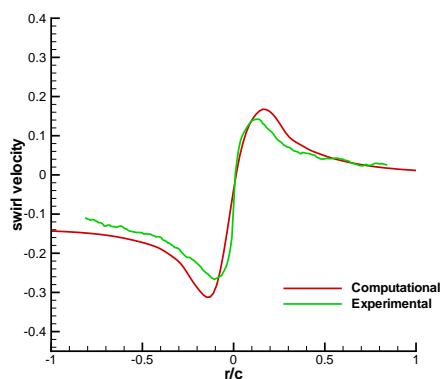
(b) $\Psi = 60^\circ$



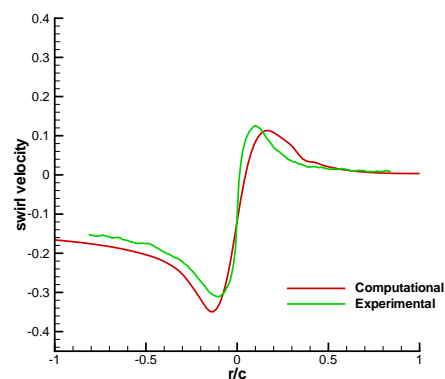
(c) $\Psi = 90^\circ$



(d) $\Psi = 120^\circ$

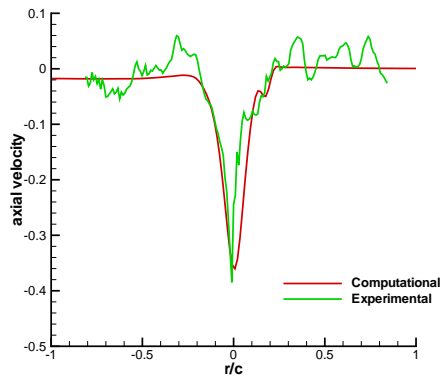


(e) $\Psi = 150^\circ$

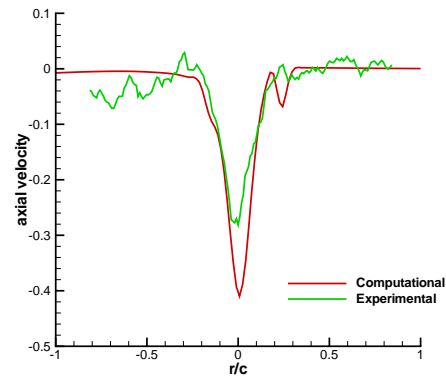


(f) $\Psi = 180^\circ$

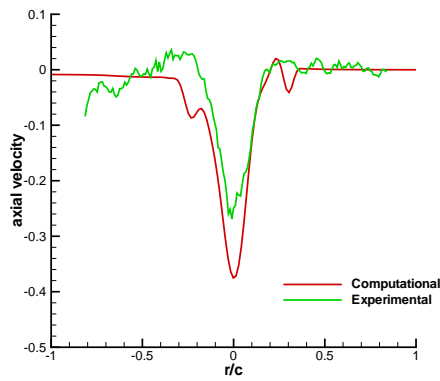
Figure 4.27: Vortex swirl velocity profile (non-dimensionalized by tip speed) comparison between computational BLTE geometry and experimental baseline geometry [29] for micro-scale single rotor, 12° collective setting.



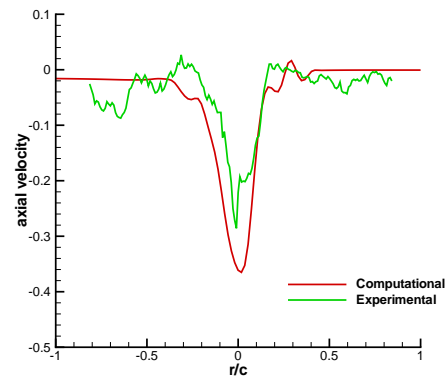
(a) $\Psi = 30^\circ$



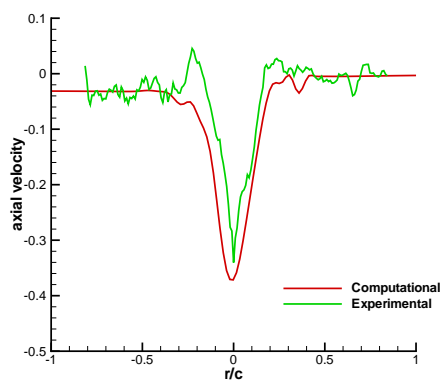
(b) $\Psi = 60^\circ$



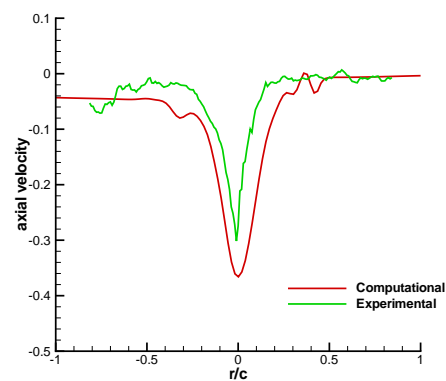
(c) $\Psi = 90^\circ$



(d) $\Psi = 120^\circ$

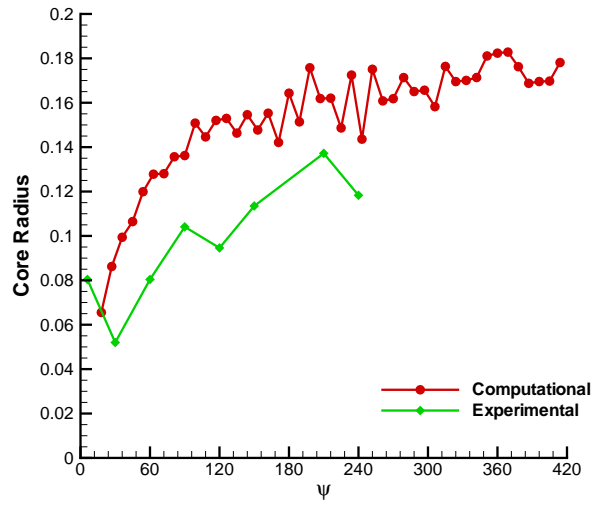


(e) $\Psi = 150^\circ$

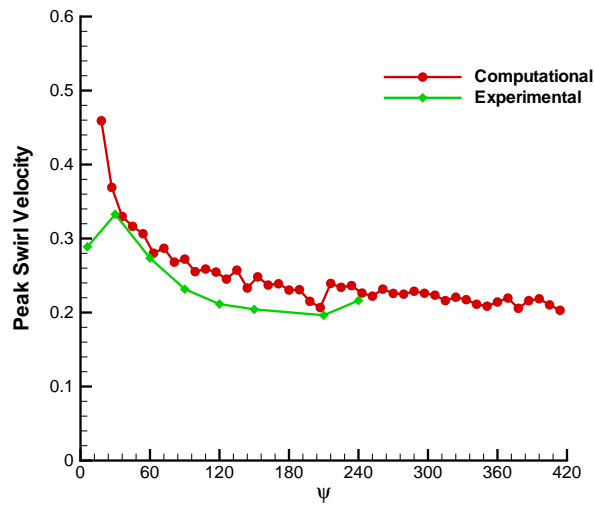


(f) $\Psi = 180^\circ$

Figure 4.28: Vortex axial velocity profile (non-dimensionalized by tip speed) comparison between computational BLTE geometry and experimental baseline geometry [29] for micro-scale single rotor, 12° collective setting.



(a)

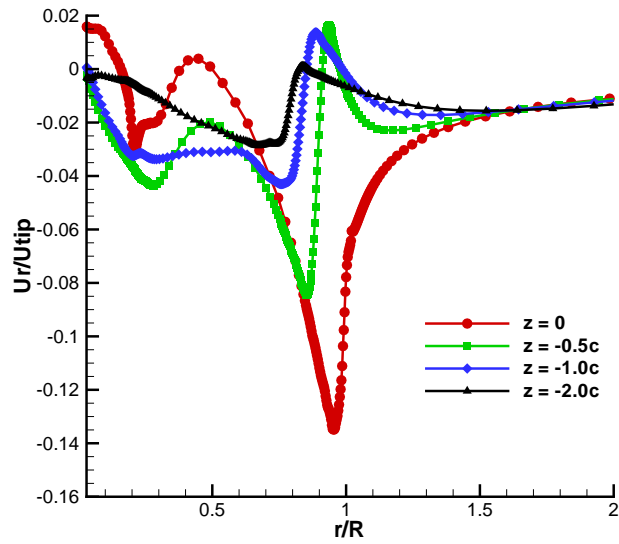


(b)

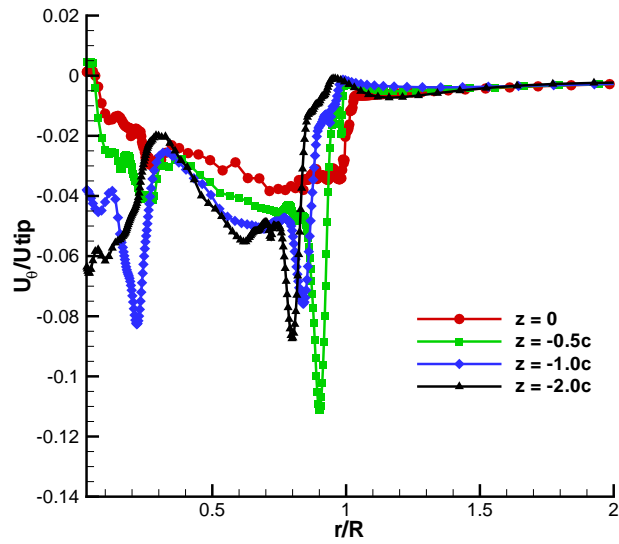
Figure 4.29: Tip vortex viscous core radius (a) and Peak tip vortex swirl velocity (b) comparison with experimental data [29] with wake age for micro-scale single rotor.

4.12 Average Velocity Profiles in Wake

The sectional drag for low Reynolds number airfoils is much larger than that at high Reynolds number and may alter the induced velocities in the rotor wake for small scale micro-rotors. Figure 4.30 shows the radial variation of various components of velocity averaged in the azimuthal direction. The variation is shown at different planes below the rotor. It should be noted that the results shown at $z = 0$ are obtained by averaging those at $z = 0.1c$ and $z = -0.1c$ (to minimize influence of the rotor blade). The velocities are non-dimensionalized by the tip speed. The peak magnitude of the radial velocity reaches about 15% of the tip speed in the plane of the rotor and it occurs near the tip of the blade. As one moves away from the rotor, the radial component becomes weaker and the location of peak radial velocity moves inboard as a result of wake contraction. Correspondingly, the location of peak swirl velocity and peak inflow also move inboard. The average magnitude of swirl velocity in the wake region remains fairly constant at about 5 – 6% of the tip speed at all distances from the blade, with the peak reaching about 10 – 12% of the tip speed. These values are significantly larger as compared to those for a full-scale rotor. Sample results for the full-scale Harrington single rotor-2 (studied in Chapter 3), operating at a thrust coefficient of 0.004, is plotted in Fig. 4.31. The thrust coefficient for the micro-scale rotor is about 0.0167. As a result, the inflow for the full-scale rotor is about half the value as that of the micro-rotor. The swirl velocity, however is only about one-fourth of that for the micro-rotor. The larger swirl velocity can be one of the reasons for additional power loss in micro-scale rotors. Note that a similar magnitude of swirl velocity component was seen for the other micro-scale rotor geometries.

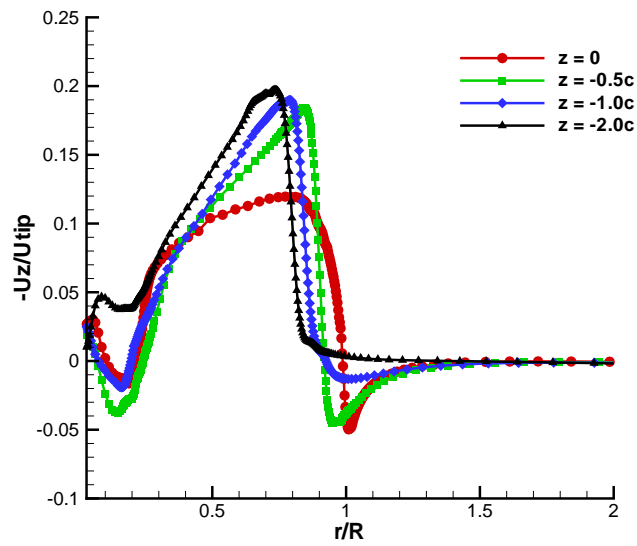


(a) Average radial velocity along span



(b) Average swirl velocity along span

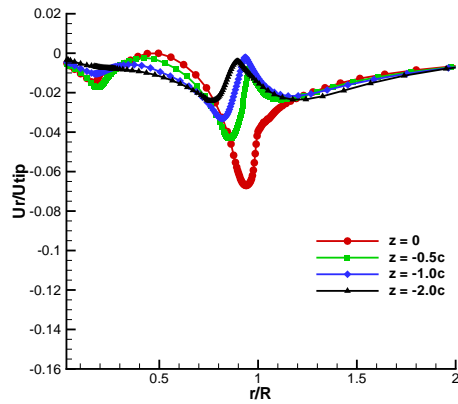
Figure 4.30: Average velocities along radial direction at different planes below the rotor for BLTE geometry for micro-scale single rotor, 12° collective setting.



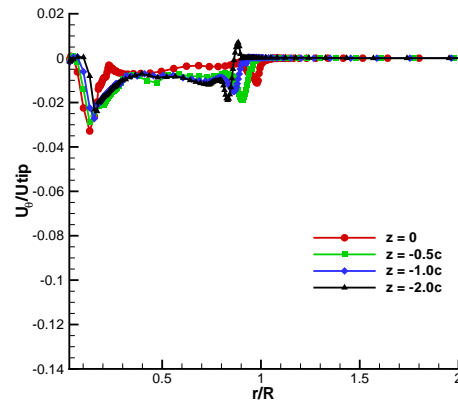
(c) Average inflow velocity along span

Figure 4.30: Average velocities along radial direction at different planes below the rotor for BLTE geometry for micro-scale single rotor, 12° collective setting.

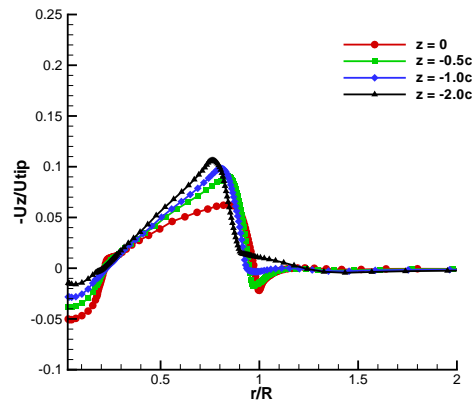
(cont'd)



(a) Average radial velocity along span



(b) Average swirl velocity along span



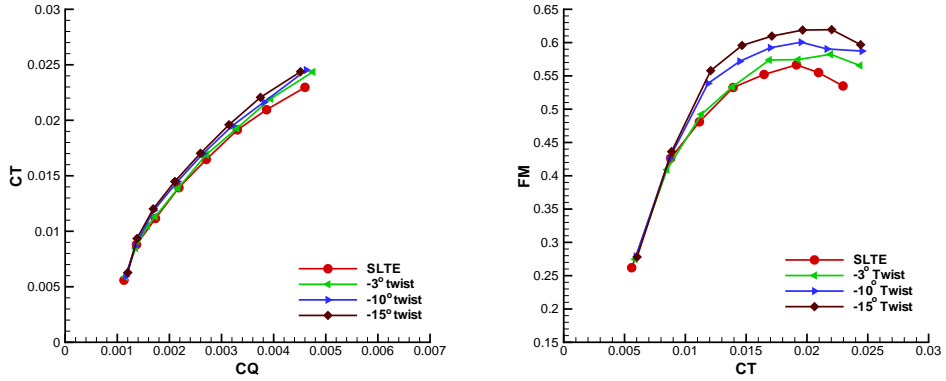
(c) Average inflow velocity along span

Figure 4.31: Average velocities along radial direction at different planes below the rotor for full-scale Harrington single rotor-2 [49], $C_T = 0.004$.

4.13 Effect of Twist and Taper

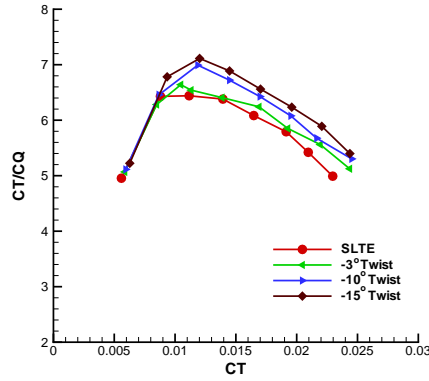
Having studied the effect of leading and trailing edge geometry profiles for micro rotors, an initial study is also performed on the effect of twist and taper on the performance of these small-scale rotors. Twist and taper are generally used to optimize the rotor performance in full-scale helicopters. Taper reduces the profile losses near the tip, apart from reducing the local solidity of the blades and consequently the inflow. On the other hand, introducing negative twist in the blades increases the inflow at the root while reducing it at the tips. This produces a more uniform inflow distribution, thus reducing the induced losses of the rotor. With the right combination of twist and taper, a more uniform inflow and higher lift to drag ratios can be achieved along the blade span. Twist and taper can also be expected to provide similar benefits in micro-scale rotors.

Past studies on the use of twist for micro-rotor blades have shown contradictory results. Use of twist was shown to be beneficial in the experimental studies of Ramasamy et al. [30]. However, in the experimental studies done by Bohorquez [2], the use of twist did not show any benefits compared to the untwisted blades, whereas, the blade element momentum theory (BEMT) analysis on the same blades did show improvements for the twisted blades. Similar to twist, past studies also show contradictory results for the use of taper on micro-rotor blades. The experimental results obtained by Bohorquez showed improvements with taper (asymmetric distribution showing maximum benefits). On the other hand, experimental results obtained by Ramasamy et al. showed no benefits with the use of taper. In this section, the computational methodology developed in this work is used to provide further insights into the use of twist and taper for the MAV rotors.



(a) C_T vs C_Q

(b) FM vs C_T



(c) C_T/C_Q vs C_T

Figure 4.32: Performance comparison for various blade twists for micro-scale single rotor, SLTE geometry.

Figure 4.32 shows the performance comparison for three different linear twists (-3° , -10° and -15°) along with the no twist case for the SLTE geometry. Clearly, we can see that the performance improves with larger negative twist, especially at higher thrust values. The FM for the -15° twist reaches a maximum value greater than 0.6 ($\sim 10\%$ increase from SLTE). The reason for the improved performance is clearly due to a more uniform inflow achieved by the

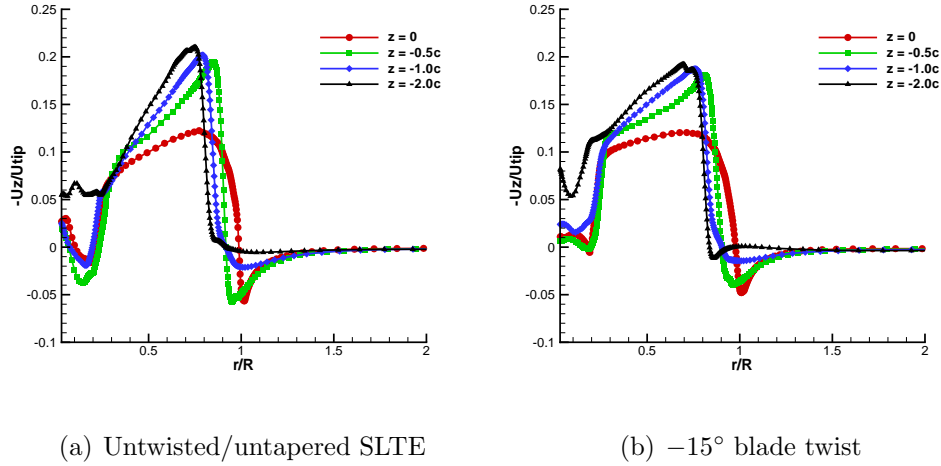


Figure 4.33: Average inflow velocity along radial direction at different planes below the rotor for micro-scale single rotor, $\theta_{0.75} = 12^\circ$.

twisted blades, see Fig. 4.33, where the inflow velocity at different planes below the rotor is plotted for the untwisted/untapered SLTE geometry and the -15° twisted planform. Additionally, the thrust level at which maximum C_T/C_Q is achieved also increases ($\sim 35\%$) as the twist increases. This is significant because the MAV can now operate at a higher thrust level to achieve maximum endurance.

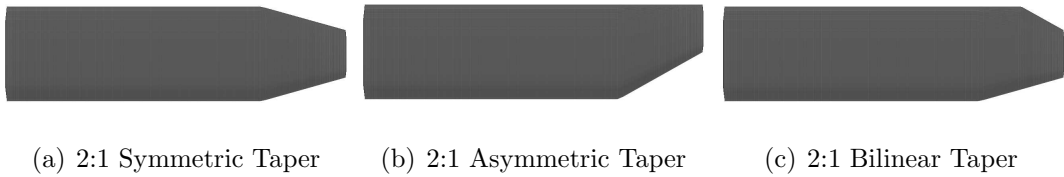


Figure 4.34: Blade taper planforms for micro-scale single rotor.

Effect of taper is investigated by simulating three different taper distributions; 2 : 1 symmetric linear taper, 2 : 1 asymmetric linear taper and 2 : 1 bilinear taper (shown in Fig. 4.34). Additionally, a blade that uses a combination of twist (-15°) and taper (2 : 1 bilinear) is studied. The taper starts at

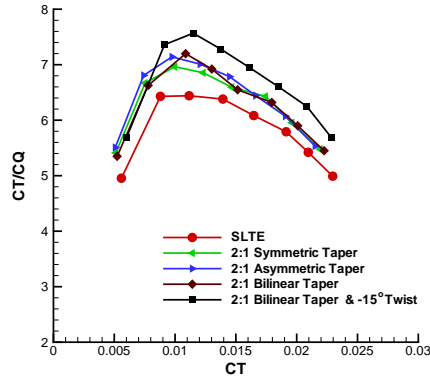
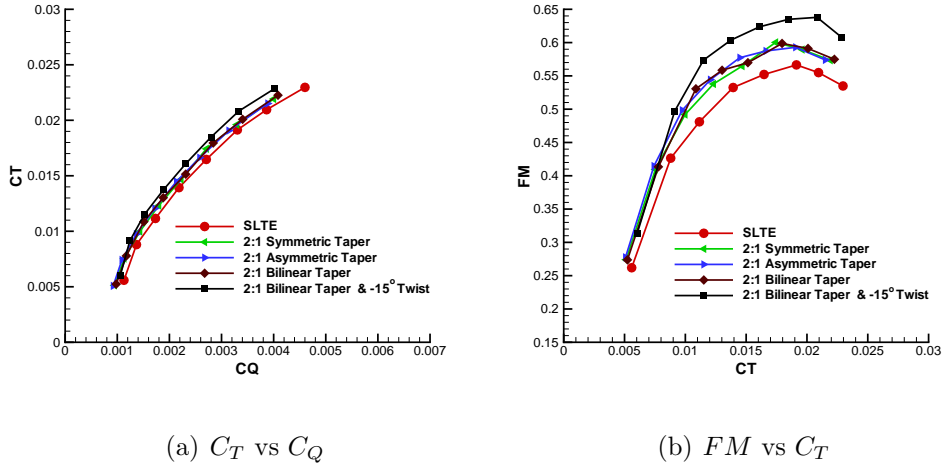


Figure 4.35: Performance comparison for various blade taper for micro-scale single rotor, SLTE geometry.

80% span. The symmetric and the asymmetric taper distributions are similar to those studied by Bohorquez [2]. For the symmetrically tapered blade, the mid-chord line remains unchanged, while for the asymmetrically tapered blade, the leading edge line remains unchanged. For the bilinearly tapered blade, the leading edge remains unchanged till 90% span. Both asymmetric and bilinear taper intrinsically introduces a negative twist. In order to maintain the thick-

ness ratio, the airfoil is thinned as the blade tapers. Taper introduces a very small change in solidity, which can be neglected. Figure 4.35 shows the performance comparison for that resulting from the untapered SLTE geometry along with those resulting from the various taper distributions. It can be seen that all the untwisted taper planforms provide similar performance improvements at all thrust levels. This suggests that the performance improvement mainly arises due to the reduction in profile power, as the difference in twist near the tip for the two tapered blades did not contribute to any significant difference in performance. This fact is also supported by Fig. 4.36, where spanwise sectional L/D is plotted for SLTE geometry along with symmetrically tapered geometry. Clearly, the sectional L/D for tapered geometry is larger near the tip because of the decrease in profile power, while there is no significant differences in the inboard untapered portions. Because of the performance improvements, maximum FM for the tapered blades reaches a value of about 0.58 ($\sim 5\%$ increase from SLTE). The thrust level at which C_T/C_Q reaches a maximum, increases marginally for the tapered blades.

The combined use of twist and taper can be seen to perform better than just having either twist or taper, achieving a maximum FM of about 0.63 ($\sim 14\%$ increase from SLTE), showing that performance in MAVs can be further improved by having a good blade planform. Further studies will be required to determine an optimal configuration.

4.14 Summary

In this chapter, time accurate computations of hovering micro-scale single rotors are validated with available experimental data and the resulting flow-field

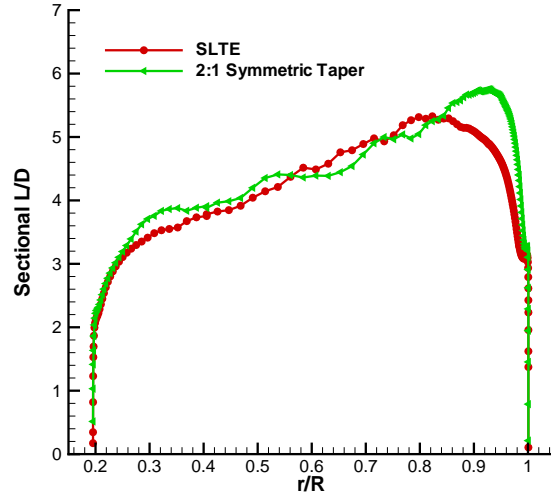


Figure 4.36: Sectional L/D distributions for SLTE and symmetrically tapered blade of micro-scale single rotor, 12° collective setting.

examined to determine the resulting flow physics. The solver is applied to study the effect of leading and trailing edge geometries on hovering micro rotors. Four different geometries comprising of two different leading and trailing edge profiles (blunt and sharp) for the blade section were studied. The performance of all the geometries show good comparison with the experimental data. Blunt leading edge geometries show poorer performance compared to the corresponding sharp leading edge geometries mainly because of large pressure drag acting at the blunt front. A blunt leading edge geometry also shows a significant leading edge laminar separation bubble which results in complete separation near the tip. Flow visualization shows that the tip vortex flow-field is very complicated with the presence of secondary vortices and additional vortices formed due to separation near the trailing edge. The tip vortex velocity profiles are reasonably well predicted as compared to experimental data, but the inadequacy of the

current turbulence model may lead to some discrepancies during tip vortex formation. The examination of the wake trajectory showed good comparison with the experimental data during the initial wake ages. However, the comparison was not good at a later wake age, because of the expansion of the experimental trajectory caused by the separation near the root due to the mounting apparatus. The swirl velocities for the micro-rotor are found to be significantly larger as compared to those from a full-scale rotor, which can be one of the reasons for additional power loss in the smaller scale rotors.

A preliminary study on planform shape shows that the use of twist and taper improves the performance of micro rotors, similar to that for full-scale rotors. Twist reduces the induced power, while taper decreases the profile power. Additionally, twist increases the thrust level at which the rotor has maximum thrust to power ratio. Combined use of twist and taper is seen to further improve the performance.

Chapter 5

Computational Investigation of Full Scale Coaxial Rotor Aerodynamics in Hover

After having performed computations on a hovering micro-scale single rotor, the next step is to validate the CFD model developed for a coaxial rotor in full-scale. In this chapter, high resolution computations are performed on a hovering full-scale coaxial rotor and validated with experimental performance results. Subsequently, detailed analysis of the flow physics is performed. A trim procedure is implemented to balance the torque and to trim the thrust to a particular value. The experimental results are torque-trimmed and therefore, it is appropriate to trim the CFD solution for the purpose of comparison.

5.1 Rotor Configuration

The hovering coaxial experimental setup of Harrington Rotor-2 [49] is used to validate the computational predictions for the coaxial rotors at full-scale. It

consists of two 2-bladed rotors arranged to form a coaxial system. The aspect ratio of the blade is 8.33 (blade chord is 18 inches and rotor diameter is 25 feet), resulting in an individual rotor solidity of 0.076 with rotor spacing, $H/D = 0.08$ (1.33 chords). The blade uses a NACA airfoil with a linearly varying thickness of 27.5% at 0.2R to 15% at R. The tip speed of the rotor is 392 ft/sec. The corresponding tip Reynolds number is 3.5×10^6 and the tip Mach number is 0.352. Thus, each rotor system is identical to the single rotor system examined in Chapter 3.

5.2 Mesh System

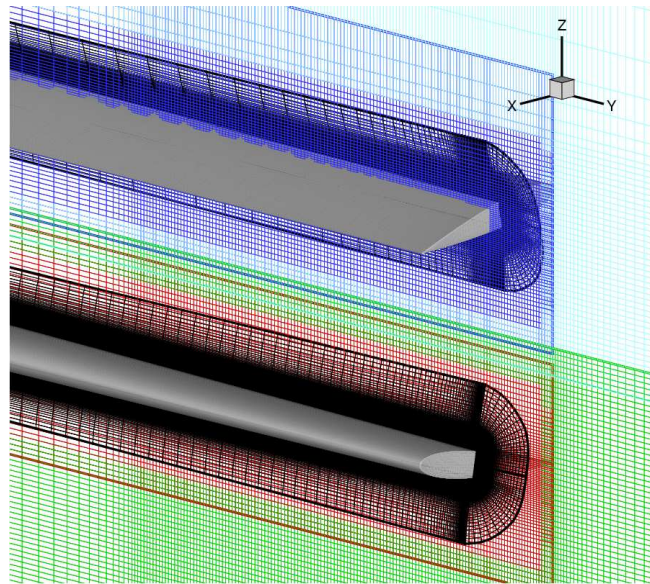
A six mesh system consisting of two blade meshes, two nested background meshes and two cylindrical outer background meshes is used. The blade mesh, the nested background mesh and the outer background mesh of each rotor form an overset system. It was mentioned before in Chapter 2, that the outer boundary of the blade mesh cannot be made to extend very far from the blade surface in a coaxial configuration and is limited by the rotor separation distance. Therefore, nested background meshes are used, which can transfer the solution smoothly from the blade mesh to the outer background mesh. The outer background meshes communicate with each other by means of a sliding mesh interface as explained earlier, allowing for a complete simulation using just one blade mesh in each rotor system. The solution is transferred from one mesh to the other by using a third order slope limited M3-quartic interpolation of Huynh [91]. Compared to first order (linear) interpolation, the higher order interpolation significantly reduces the oscillation in the forces of the bottom rotor arising due to the interpolation error, along with providing a better representation of the wake.

It should be mentioned here that, a spectral scheme was investigated to provide higher order interpolation. However, the results were unsatisfactory due to the presence of numerous spurious oscillations and therefore, in order to minimize these oscillations, a monotonic M3-quartic interpolation was chosen. The extra cost for the higher-order interpolation is minimal since the interpolation is only one-dimensional between the sliding mesh boundaries.

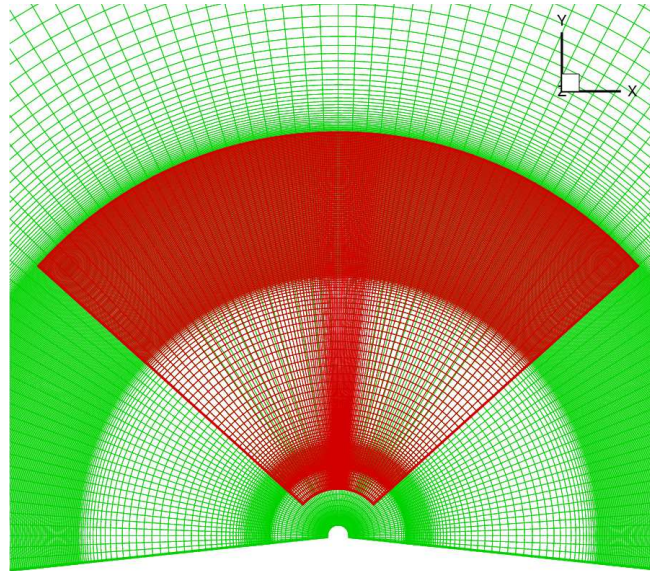
All the computations are performed on top and bottom rotor blade meshes having $267 \times 155 \times 111$ points in the streamwise, spanwise and normal directions, respectively, nested background meshes having $97 \times 204 \times 72$, top rotor outer background mesh having $97 \times 270 \times 61$ points and bottom rotor outer background mesh having $97 \times 270 \times 180$ in the azimuthal, radial and vertical directions, respectively. Thus, the total number of mesh points used is 18.3 million.

Figure 5.1 shows the blade and background meshes. The blade mesh of the top rotor is sufficiently fine in the tip region to resolve the tip vortex formation. For the bottom rotor, the grid is redistributed such that the inboard region is more highly refined, in order to resolve the wake interaction. In the most refined regions, the nested background mesh has a grid spacing of 0.0165 chords in the vertical direction, while the outer background mesh has a grid spacing of 0.033 chords in the same direction. In the radial direction, both the nested and outer background meshes have a grid spacing of 0.02 chords in the most refined region. Along the azimuthal direction, a grid plane is spaced every 2° in the outer background mesh. For the nested background mesh, the azimuthal spacing varies from 0.3° near the blade to 2° in its outer boundaries. The outer boundary of the outer background mesh extends to $3R$ above the top rotor, $4.5R$ below the bottom rotor and $4R$ from the tip of the blade. Each calculation

along with trimming takes about 30 days when run in parallel on 16 Intel Xeon 3.20GHz processors.



(a) Blade mesh with inner and outer cylindrical meshes of the top and bottom rotors



(b) Inner and outer cylindrical meshes of the bottom rotor (top view)

Figure 5.1: Computational mesh for full-scale coaxial rotor system.

5.3 Trimming Procedure

In the experimental test, the top and bottom rotors were torque balanced by selecting the appropriate collective pitch. In order to obtain a reasonable validation, the CFD results need to be yaw-trimmed. This is achieved by using a trimming procedure, by which the thrust is trimmed to a specific value in addition to balancing the torque. The CFD calculations are started using initial collective settings obtained from the vortex filament method for various target values of thrust. These settings were provided by Ananthan [53]. Using the initial results obtained from these collective angles, the collective settings are changed in a manner described below [92].

The rotor control input vector and the response vector are respectively given by

$$\begin{aligned}\mathbf{x} &= \{\theta_{0_1}, \theta_{0_2}\}^T \\ \mathbf{y} &= \{\Sigma C_T, \Sigma C_Q\}^T\end{aligned}$$

where, θ_{0_1} and θ_{0_2} are respectively the collective setting of the top and bottom rotor. Note that the sign of C_Q of the bottom rotor is taken negative.

The change in the response vector for a perturbation in the input vector \mathbf{x} can be written as a Taylor series expansion given by

$$\mathbf{y}(\mathbf{x} + \Delta\mathbf{x}) = \mathbf{y} + \frac{\partial\mathbf{y}}{\partial\mathbf{x}}\Delta\mathbf{x} + \dots$$

The Jacobian matrix, $[J]$ of the dependent quantities with respect to the independent quantities can be written as

$$[J] = \frac{\partial \mathbf{y}}{\partial \mathbf{x}} = \begin{bmatrix} \frac{\partial \Sigma C_T}{\partial \theta_{01}} & \frac{\partial \Sigma C_T}{\partial \theta_{02}} \\ \frac{\partial \Sigma C_Q}{\partial \theta_{01}} & \frac{\partial \Sigma C_Q}{\partial \theta_{02}} \end{bmatrix}$$

Neglecting the higher order terms, the expression for the perturbation in the control input vector \mathbf{x} can be written as

$$\Delta \mathbf{x} = [J]^{-1}(\mathbf{y}(\mathbf{x} + \Delta \mathbf{x}) - \mathbf{y}) = [J]^{-1} \begin{Bmatrix} \Sigma C_T - C_{T_{req}} \\ \Sigma C_Q \end{Bmatrix}$$

The Jacobian matrix obtained from the vortex filament code is used to determine the change in collective settings. The solution for the new collective settings are calculated using the previous solution as the initial condition. As a result, the convergence time reduces significantly, thereby making the trimming procedure feasible. The above step is repeated until the values are trimmed to within 1% of the target. For all cases the trim criteria was met in 3 to 4 iterations.

Table 5.1 shows the trim collective settings obtained for various target thrust values. These settings are not too different from that obtained using the vortex filament code.

Table 5.1: Trim collective settings for the top and bottom rotors of full-scale coaxial system.

Case	C_T (Target)	θ_0 (top rotor)	θ_0 (bottom rotor)
1	0.000	0.00°	0.00°
2	0.002	3.72°	4.10°
3	0.003	4.74°	5.22°
4	0.004	5.73°	6.22°
5	0.005	6.63°	7.11°
6	0.006	7.45°	7.95°
7	0.007	8.36°	8.85°
8	0.008	9.10°	9.60°
9	0.009	9.85°	10.30°

5.4 Performance Comparison

5.4.1 Mean Performance

Tables 5.2 and 5.3 respectively summarize the mean values of thrust (C_T) and power (C_Q) coefficients obtained from CFD for each individual rotor system as well as for the entire system. It can be seen that all the cases are trimmed to within the specified criteria of 1% error. As a general trend, it is observed that as the total thrust increases, the difference between the top and bottom rotor thrust also increases. Table 5.2 also shows the ratio of the top rotor thrust to the total thrust. It can be seen that at all thrust levels, the top rotor contributes to about 55% of the total value.

Table 5.2: Computed mean thrust coefficient for full-scale coaxial system.

Case	$C_{T_{top}}$	$C_{T_{bot}}$	$C_{T_{total}}$	$C_{T_{top}}/C_{T_{total}}$
1	-0.00006	0.00005	0.00001	-
2	0.00112	0.00086	0.00198	0.57
3	0.00164	0.00134	0.00298	0.55
4	0.00219	0.00177	0.00396	0.55
5	0.00274	0.00221	0.00495	0.55
6	0.00329	0.00271	0.00600	0.55
7	0.00385	0.00317	0.00702	0.55
8	0.00436	0.00364	0.00800	0.55
9	0.00490	0.00411	0.00901	0.54

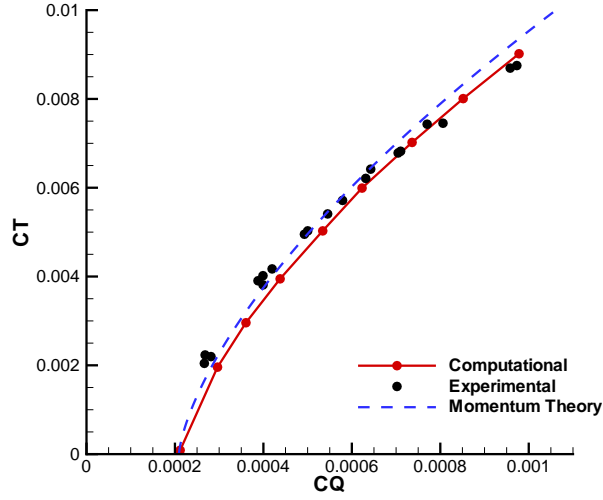
Figure 5.2(a) compares the computed variation of mean total thrust coefficient with mean total power coefficient with the measured values. The total performance is well predicted. At lower collectives, the power is slightly over-

Table 5.3: Computed mean power coefficient for full-scale coaxial system.

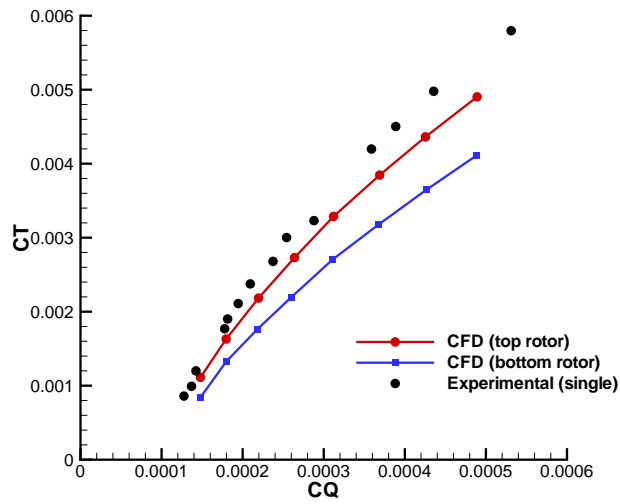
Case	$C_{Q_{top}}$	$C_{Q_{bot}}$	$C_{Q_{total}}$	$ C_{Q_{top}} - C_{Q_{bot}} $
1	0.000104	0.000107	0.000211	0.000003
2	0.000148	0.000148	0.000296	0.000000
3	0.000180	0.000180	0.000360	0.000000
4	0.000220	0.000218	0.000438	0.000002
5	0.000264	0.000261	0.000525	0.000003
6	0.000312	0.000311	0.000623	0.000001
7	0.000369	0.000367	0.000736	0.000002
8	0.000425	0.000426	0.000851	0.000001
9	0.000489	0.000489	0.000958	0.000000

predicted for a given thrust, whereas at higher collectives, the power is marginally under-predicted for a given thrust level. Plotted along with the experimental data and the CFD results is the curve fit using momentum theory for a coaxial rotor [89]. The results using momentum theory also show a similar trend as the CFD results.

Figure 5.2(b) shows the mean performances of the individual rotor systems (zero collective case is excluded). As expected, for the bottom rotor, the performance degrades significantly (about 40% increase in power at same thrust at higher thrust levels) compared to that of the single rotor because of the influence of the wake from the top rotor. It is interesting to note that even the performance of the top rotor is slightly degraded (about 15% increase in power at same thrust at higher thrust levels), indicating that the bottom rotor has some influence on the flow-field of the top rotor. Similar observations were made by Syal [55] for the Harrington rotor-1 using a Free Vortex Method (FVM).



(a) Total C_T (mean) versus total C_Q (mean)



(b) C_T (mean) versus C_Q (mean) for individual rotors.

Figure 5.2: Comparison of performance with experimental data [49] for full-scale coaxial rotor.

5.4.2 Unsteady Performance

A measure of the unsteadiness in thrust and power is the root mean square value of the temporal variations and this is summarized in Tables 5.4 and 5.5.

As a general trend, the absolute value of the fluctuation increases with increasing collective pitch settings, except for the bottom rotor torque. For the bottom rotor torque, the absolute fluctuations increase at lower thrust values, but reaches a plateau at higher thrust levels. Looking at the relative fluctuation with respect to the mean value, we see a reduction in value for all quantities except the top rotor power. For the top rotor power, the relative fluctuation is seen to remain constant over a large range of C_T . Additionally, when the fluctuations of the whole system are compared to that of the individual rotors, it is seen that though the absolute value is higher, the relative fluctuation is smaller. In general, there is 5 – 10% fluctuation in all integrated quantities, which could be significant for vibration and acoustic characteristics. Further details of the temporal variation will be presented later in this section.

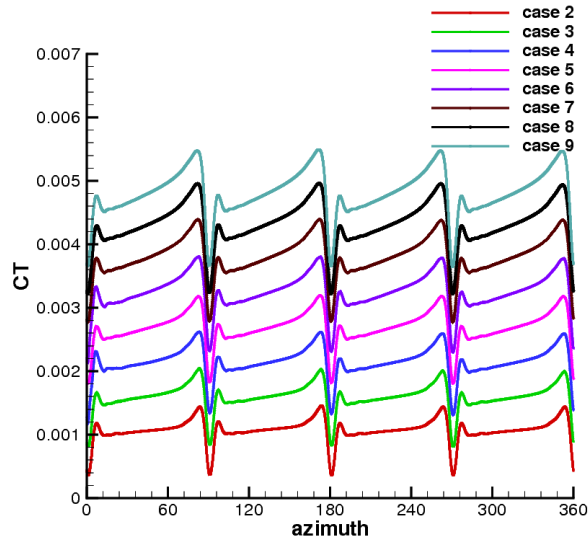
Table 5.4: Computed RMS fluctuation of thrust coefficient for full-scale coaxial system.

Case	$dC_{T_{rms}}$ (top rotor)	% fluctuation	$dC_{T_{rms}}$ (bottom rotor)	% fluctuation	$dC_{T_{rms}}$ (total)	% fluctuation
1	0.000131	–	0.000141	–	0.000027	–
2	0.000185	16.52%	0.000125	14.53%	0.000128	6.46%
3	0.000209	12.74%	0.000137	10.22%	0.000208	6.97%
4	0.000235	10.73%	0.000160	9.04%	0.000278	7.02%
5	0.000260	9.49%	0.000176	7.96%	0.000335	6.77%
6	0.000287	8.72%	0.000198	7.31%	0.000391	6.51%
7	0.000313	8.13%	0.000235	7.41%	0.000440	6.27%
8	0.000341	7.82%	0.000242	6.65%	0.000484	6.05%
9	0.000368	7.51%	0.000257	6.25%	0.000532	5.90%

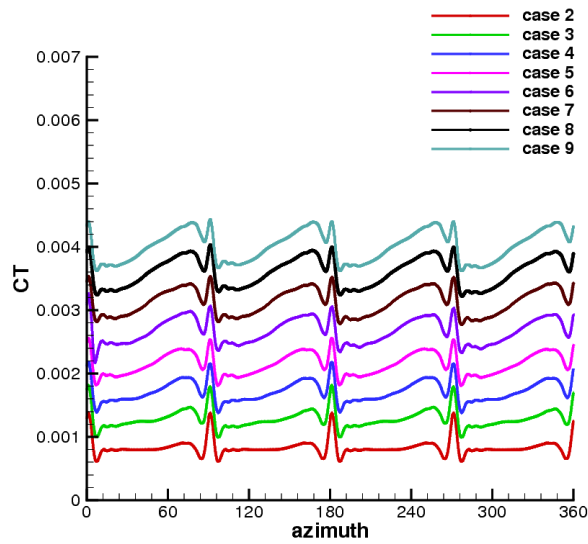
Table 5.5: Computed RMS fluctuation of power coefficient for full-scale coaxial system.

Case	$dC_{Q_{rms}}$ (top rotor)	% fluctuation	$dC_{Q_{rms}}$ (bottom rotor)	% fluctuation	$dC_{Q_{rms}}$ (total)	% fluctuation
1	0.0000114	10.96%	0.0000118	11.02%	0.0000231	10.94%
2	0.0000106	7.16%	0.0000144	9.73%	0.0000227	7.67%
3	0.0000121	6.72%	0.0000156	8.66%	0.0000234	6.50%
4	0.0000140	6.36%	0.0000175	8.03%	0.0000253	5.77%
5	0.0000166	6.29%	0.0000184	7.05%	0.0000268	5.10%
6	0.0000197	6.31%	0.0000191	6.14%	0.0000291	4.67%
7	0.0000235	6.37%	0.0000193	5.23%	0.0000322	4.38%
8	0.0000277	6.52%	0.0000193	4.54%	0.0000357	4.20%
9	0.0000317	6.48%	0.0000188	3.84%	0.0000383	4.00%

Figures 5.3 and 5.4, respectively shows the temporal variation of C_T and C_Q over one revolution for cases 2-9. Note that, when viewed from above, the top rotor rotates in an anti-clockwise fashion and the bottom rotor rotates clockwise. Therefore, the azimuthal locations of the top and bottom rotors are measured in their respective directions of rotation. From the figure, the unsteadiness is clearly seen with a dominant 4/rev frequency (number of times a blade of one rotor encounters a blade of the other rotor in one revolution). A higher frequency variation can be seen in the form of spikes when the blades are very close to each other. Such a variation can be attributed to the venturi effect caused by the thickness of the blades, which leads to a reduction in pressure between the rotors. As a result, the thrust of the top rotor spikes down whereas the thrust of the bottom rotor spikes up. Apart from the thickness effect, there is also a



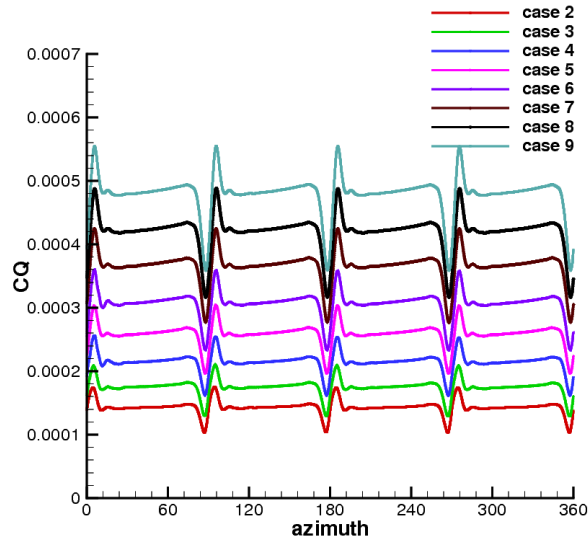
(a) Top rotor C_T variation



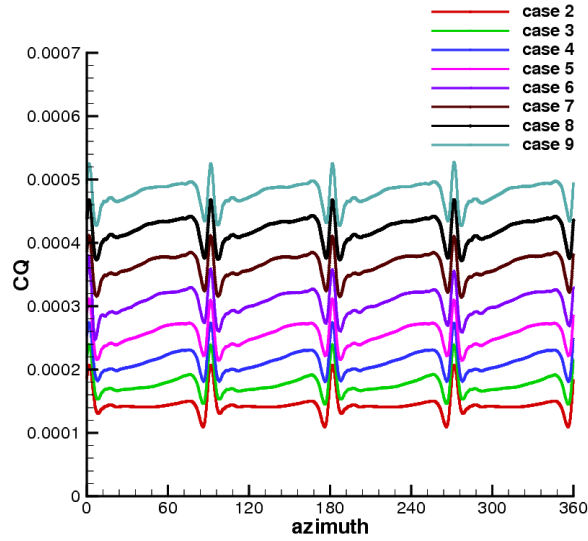
(b) Bottom rotor C_T variation

Figure 5.3: Temporal variation of C_T of the top and bottom rotors over one revolution for all cases for full-scale coaxial system.

loading effect created by the bound circulation of the blades. These effects are schematized in Fig. 5.5. As the blades of the top and bottom rotors approach



(a) Top rotor C_Q variation



(b) Bottom rotor C_Q variation

Figure 5.4: Temporal variation of C_Q of the top and bottom rotors over one revolution for all cases for full-scale coaxial system.

each other, each blade induces an upwash on the other blade. The upwash increases as the blades approach each other, but after a certain point it starts

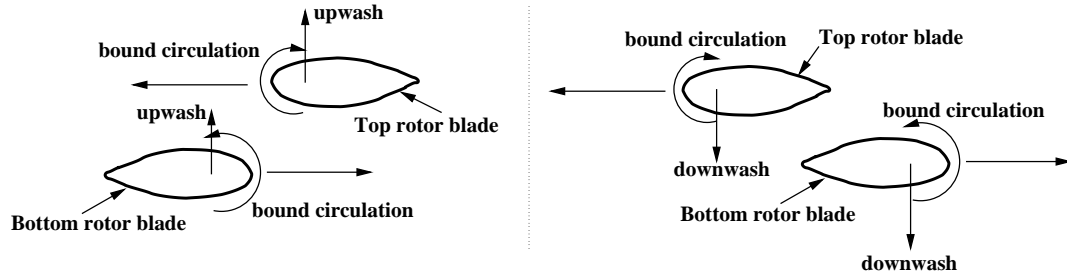
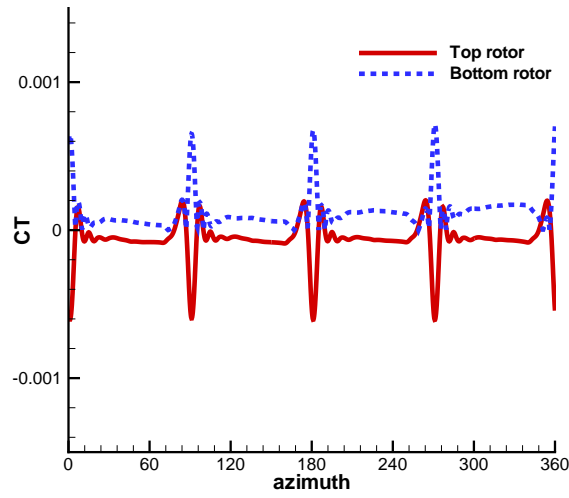


Figure 5.5: Schematic of the loading effect in coaxial system.

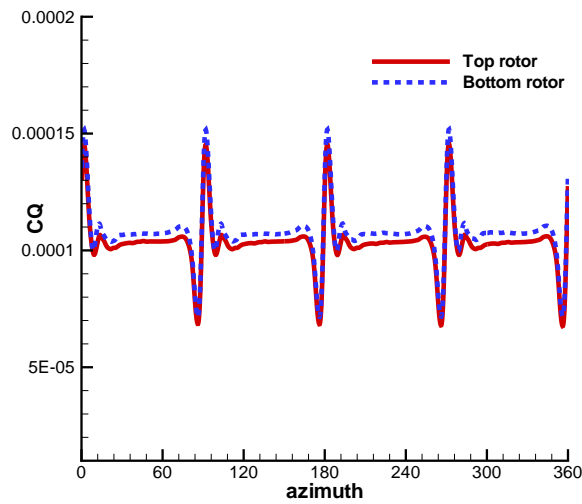
decreasing, changes sign and acts as a downwash. The strength of the downwash is seen to initially increase and then starts decreasing as the blades move away from each other. Correspondingly, the forces on both the top and the bottom rotor increase as the blades approach, then decrease and then increase again as they move away. Furthermore, while the thrust and the power of the top rotor show an impulsive but phased behavior, the features are more spread out and distinct for the bottom rotor which lies in the wake of the top rotor.

Figure 5.6 shows the temporal variation of thrust and power for the zero collective case. From the figure, it can be seen that, at all times, the top and bottom rotors produce almost equal and opposite thrust resulting in a net zero thrust, while the power of both rotors are almost identical. This behavior is expected, because for this zero collective case, the loading and wake effects are negligible and only the thickness effect is prominent. Therefore, for both top and bottom rotors, the forces remain constant for most of the time, being impulsive only when the blades pass each other.

Figure 5.7(a) shows the temporal variation of the power due to pressure and viscous forces for the top and bottom rotors for case 3. The viscous component of the power coefficient is almost constant with time and is equal for both the rotors. Figure 5.7(b) shows the temporal variation of the fraction of the total



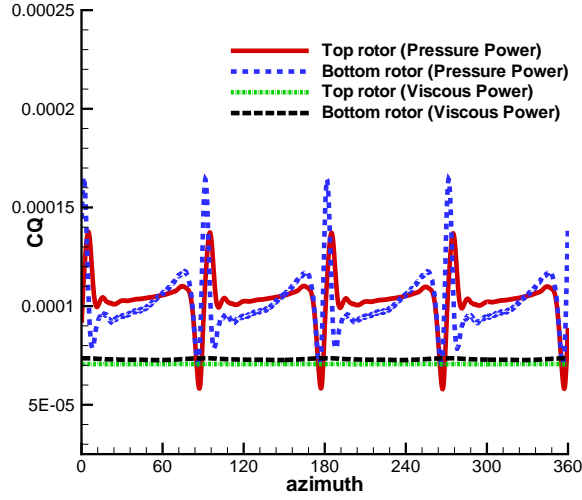
(a) C_T variation



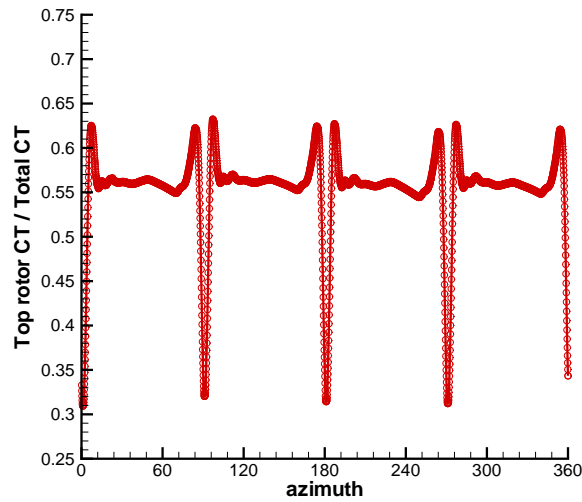
(b) C_Q variation

Figure 5.6: Temporal variation of C_T and C_Q of the top and bottom rotors over one revolution for full-scale coaxial system (case 1).

thrust shared by the top rotor. For most of the time, the fraction is close to the average value of 0.55. When the blades pass each other, the ratio briefly peaks



(a) Induced and profile power variation



(b) Ratio of Top Rotor C_T to Total C_T

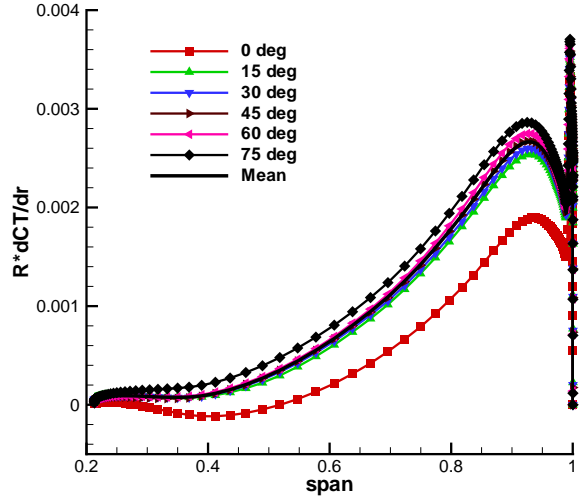
Figure 5.7: Temporal variation of components of power for the top and bottom rotors and thrust sharing over one revolution for full-scale coaxial system (case 3).

to a value of more than 0.6 and then impulsively dips to a value close to 0.3.

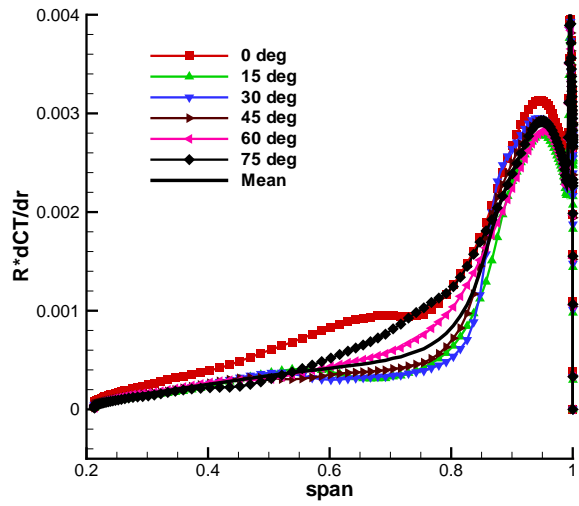
Figure 5.8 shows the spanwise thrust distribution for both the top and the

bottom rotors at different azimuthal locations for case 3. For the top rotor, the thrust distribution is similar at all azimuth locations except 0° . At 0° azimuth, due to the thickness effect discussed earlier, the thrust is lower. For the bottom rotor, variation in thrust with azimuth is more prominent. The thrust at 0° azimuth is clearly larger due to the thickness effect. A dip is noticeable in the thrust distribution at azimuth locations 15° , 30° and 45° and this is due to the interaction of the tip vortex from the top rotor with the bottom rotor. The steepness of the dip is seen to be a maximum at 30° , suggesting that the interaction occurs around this azimuth location, where the wake-age of the top rotor vortex is about 240° . This will be seen more clearly while looking at the temporal variation of sectional thrust of the bottom rotor at selected span locations. It should be noted that the azimuthal location of the blade-vortex interaction varies for the different thrust cases. The interaction occurs at an earlier wake-age as the thrust increases, due to faster vertical convection of the wake. Spatially the blade-vortex interaction occurs at a radial location of about $0.85R$, as seen from the relative location of the dip.

Contours of the sectional thrust ($R\frac{dC_T}{dr}$) and its fluctuation from the mean value are respectively plotted in Figs. 5.9 and 5.10 in the plane of the rotor, for both the top and bottom rotors for case 3. The figures clearly show the large fluctuations in the outer portions of the rotors as they pass by each other, as well as the additional unsteadiness on the bottom rotor as the wake from the top rotor encounters the plane of the bottom rotor. The interacting wake increases the thrust outboard and decreases the thrust inboard. This can be seen clearly in Fig. 5.11, which shows the temporal variation of the sectional thrust for the bottom rotor at selected span locations in the neighborhood of the region of



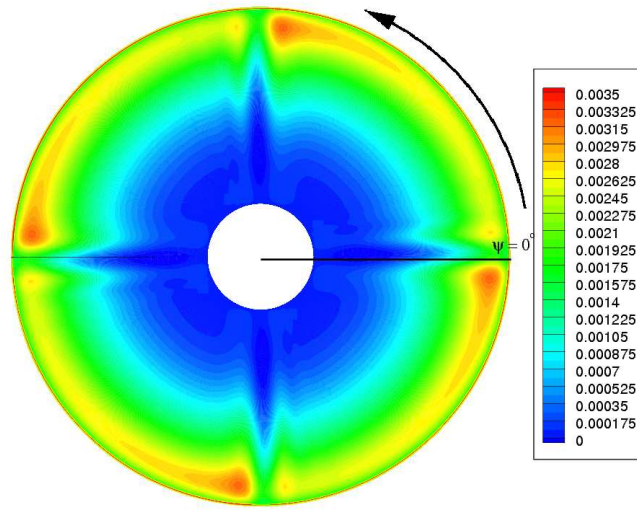
(a) Top Rotor



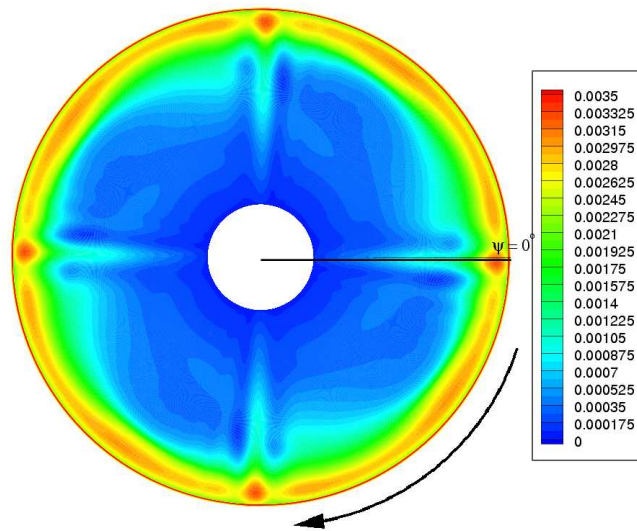
(b) Bottom Rotor

Figure 5.8: Spanwise thrust distribution at different azimuth locations for full-scale coaxial system (case 3).

blade-vortex interaction for case 3. From this plot, the azimuthal location of the interaction can be found to be close to 35° , where the difference in thrust



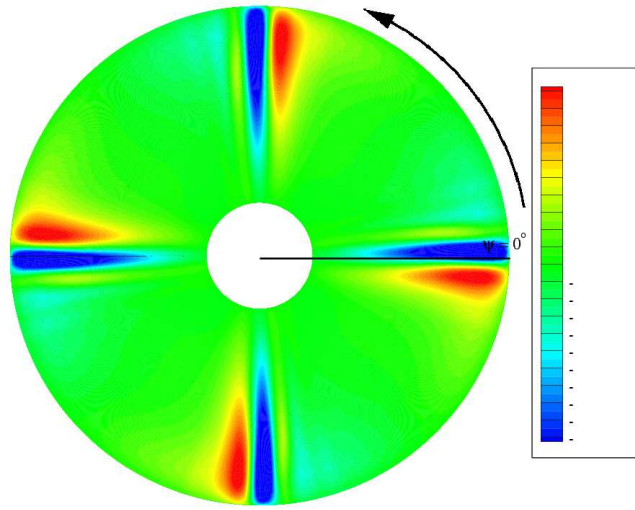
(a) Top rotor



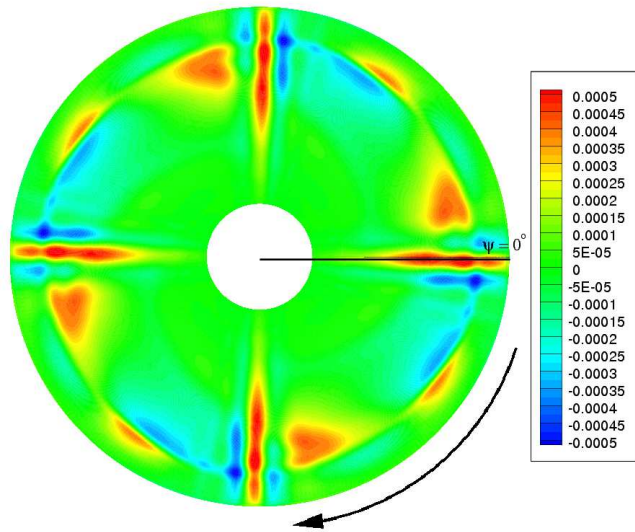
(b) Bottom rotor

Figure 5.9: Sectional thrust ($R\frac{dC_T}{dr}$) contour for full-scale coaxial system (case 3).

between inboard and outboard section is maximum. The radial location of the interaction is close to $0.84R$, inboard of which the thrust dips at the time of interaction and outboard of which it peaks.



(a) Top rotor



(b) Bottom rotor

Figure 5.10: Fluctuation in sectional thrust ($R \frac{dC_T}{dr}$) contour for full-scale coaxial system (case 3).

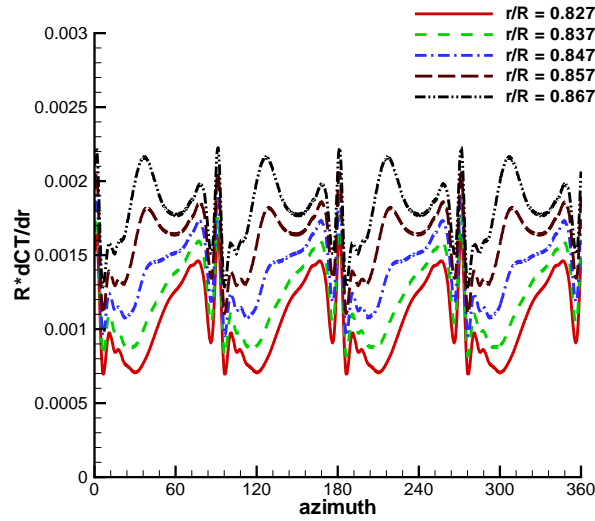
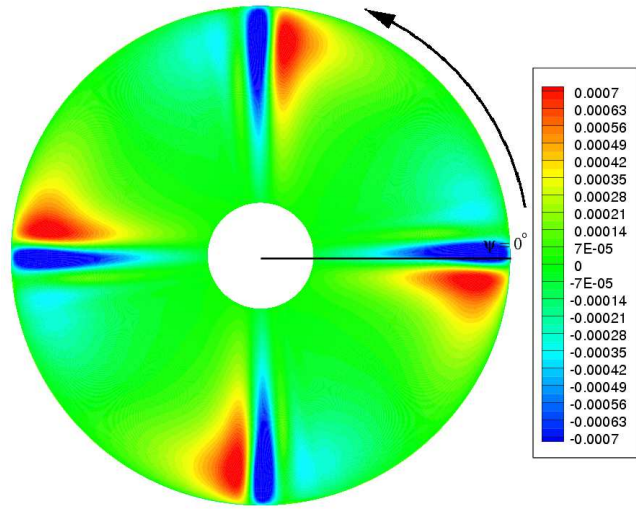
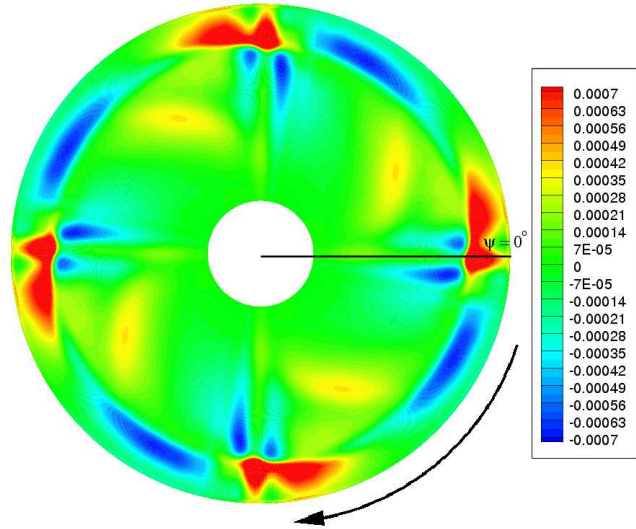


Figure 5.11: Temporal variation in sectional thrust ($R \frac{dC_T}{dr}$) at selected spanwise locations for the bottom rotor of full-scale coaxial system (case 3).

Figure 5.12 shows contours of the fluctuation of the sectional thrust for both the top and bottom rotors for case 7, which is a higher thrust case. The fluctuations for the top rotor are very similar to that of case 3, but have larger magnitude. For the bottom rotor, the fluctuations are slightly different, mainly because the wake from the top rotor now interacts with the bottom rotor at a different azimuth location (at 0° as will be seen from the flow visualization).



(a) Top rotor



(b) Bottom rotor

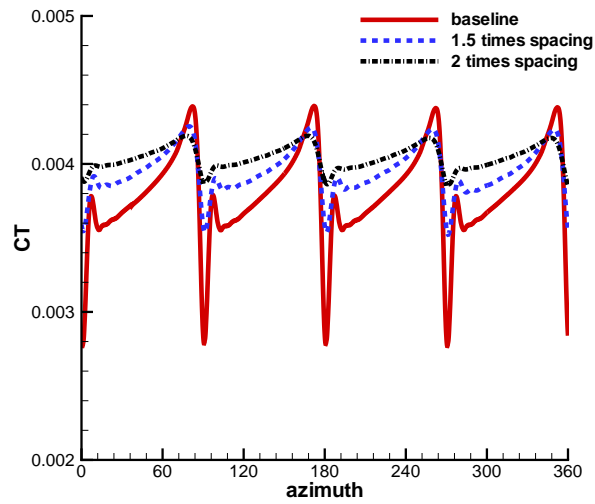
Figure 5.12: Fluctuation in sectional thrust ($R \frac{dC_T}{dr}$) contour for full-scale coaxial system (case 7).

5.5 Effect of Rotor Spacing

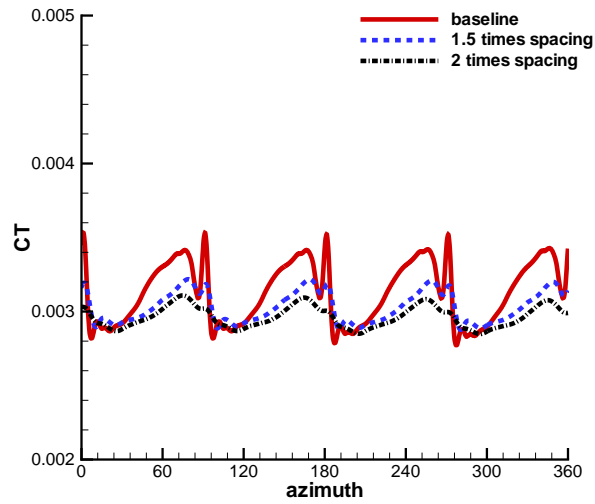
In order to analyze the effect of rotor spacing, case 7 was run for two other hypothetical rotor spacings, with one and half times (2 chords) and twice (2.66 chords) the original separation. These cases were run at the same collective settings as the baseline case and therefore are not trimmed. Figures 5.13 and 5.14 shows the temporal variation of the top and bottom rotor thrust and power over one revolution for all three cases. As the rotor spacing increases, both the thickness and loading effects decrease. Therefore, smaller spikes are observed with increasing separation. The mean values and the fluctuations of the integrated quantities are summarized in Table 5.6. For the top rotor, the mean values of the integrated quantities are seen to increase with the rotor spacing, whereas for the bottom rotor, they decrease. As a result, the system goes out of torque balance with increasing rotor spacing. However, the total thrust is seen not to vary significantly.

The effect of rotor spacing can be better quantified by investigating the frequency content in the integrated quantities. In Figs. 5.15 and 5.16, the amplitude of the frequency is normalized by the amplitude of the 4/rev frequency of the baseline case. It is seen that in all the cases (except the top rotor power), 4/rev is the dominant frequency. For the top rotor power, the dominant frequency is either 8/rev or 12/rev. The presence of these higher frequencies is due to the sharper nature of the impulses. Therefore, as expected, an increase in the rotor spacing decreases the high frequency content. This could be significant from the view point of acoustic noise propagation. Additionally, it is also evident that the relative amplitude of various frequencies decreases as the rotor spacing increases. It should also be noted that the bottom rotor has lesser high frequency content

relative to the dominant 4/rev frequency.

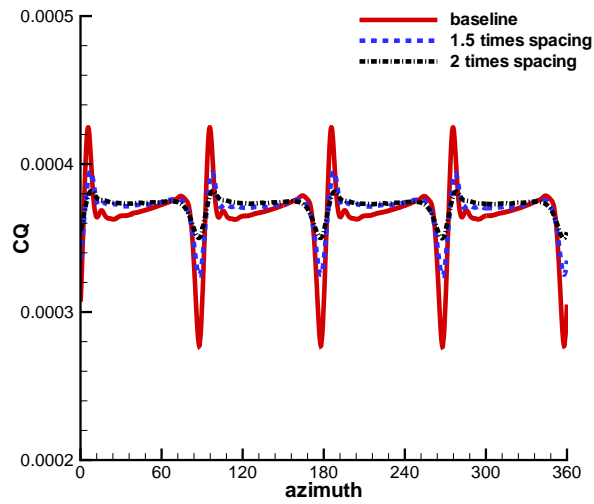


(a) Top rotor thrust

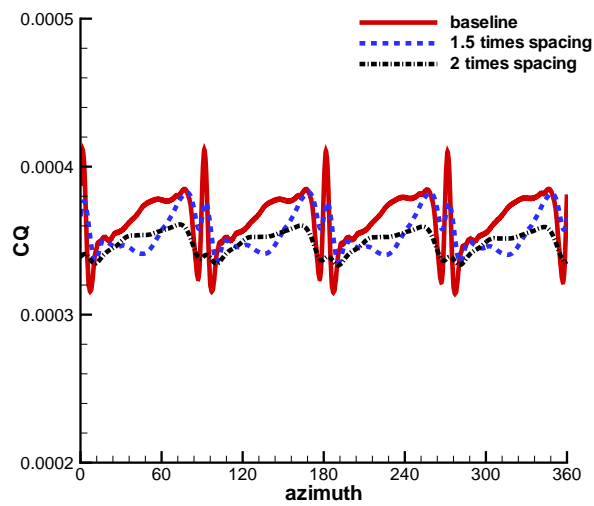


(b) Bottom rotor thrust

Figure 5.13: Effect of rotor spacing on the thrust for full-scale coaxial system (case 7).



(a) Top rotor power

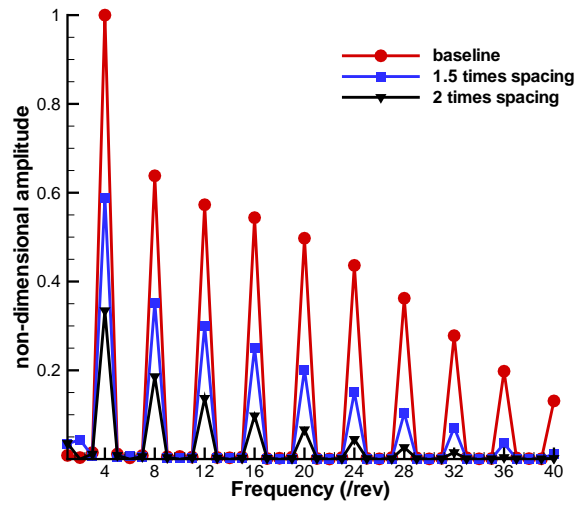


(b) Bottom rotor power

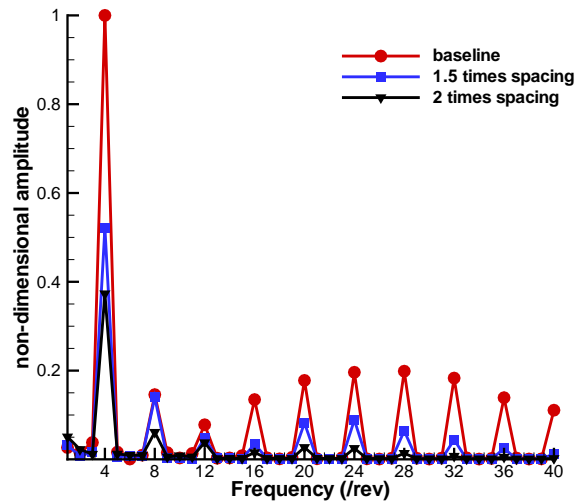
Figure 5.14: Effect of rotor spacing on the power for full-scale coaxial system (case 7).

Table 5.6: Effect of rotor spacing for full-scale coaxial system (case 7).

	Baseline	1.5X spacing	2X spacing
Top rotor			
C_T	0.00385	0.00399	0.00407
$dC_{T_{rms}}$	0.000313	0.000161	0.000091
C_Q	0.000369	0.000374	0.000377
$dC_{Q_{rms}}$	0.0000235	0.0000128	0.0000079
Bottom rotor			
C_T	0.00317	0.00306	0.00298
$dC_{T_{rms}}$	0.000235	0.000108	0.000072
C_Q	0.000367	0.000360	0.000352
$dC_{Q_{rms}}$	0.0000193	0.0000138	0.0000118

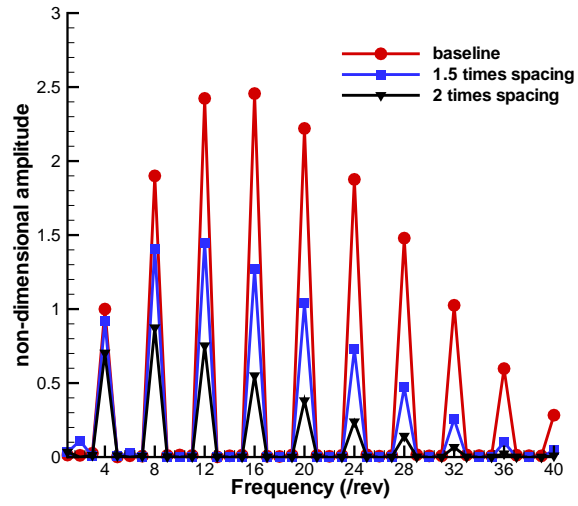


(a) Top rotor thrust

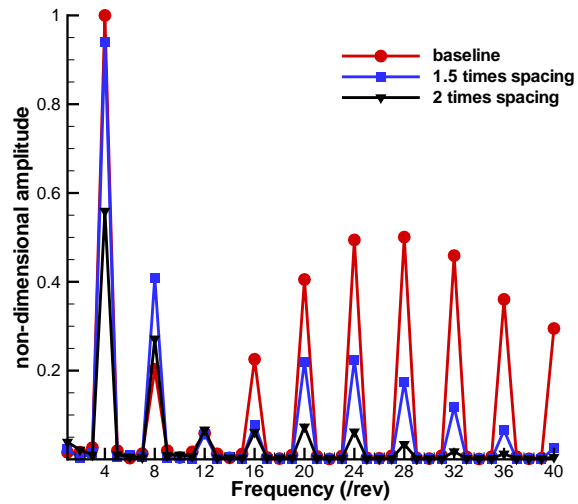


(b) Bottom rotor thrust

Figure 5.15: Effect of rotor spacing on the frequency distribution of thrust, normalized by the amplitude of 4/rev frequency of the baseline case, for full-scale coaxial system (case 7).



(a) Top rotor power

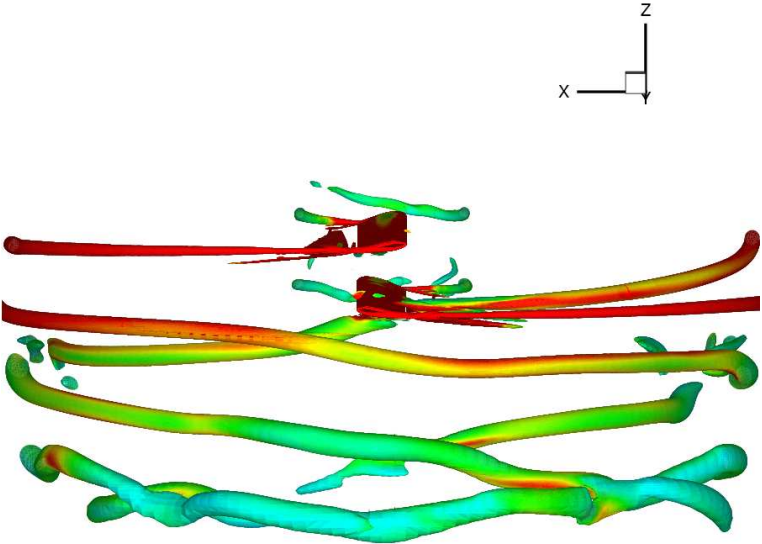


(b) Bottom rotor power

Figure 5.16: Effect of rotor spacing on the frequency distribution of power, normalized by the amplitude of 4/rev frequency of the baseline case, for full-scale coaxial system (case 7).

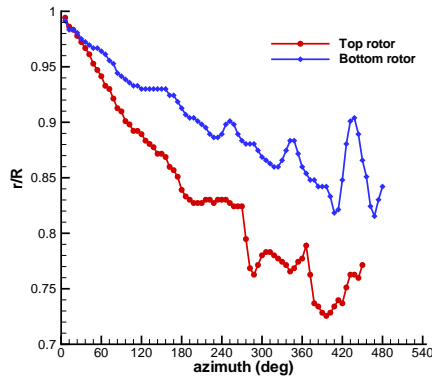
5.6 Wake Trajectory

In order to extract only the rotational flow regions and not the highly strained regions, an iso-surface of so-called q -criterion [90] is shown in Fig. 5.17 for case 7. The plot is colored using vorticity magnitude and is obtained when the top and bottom rotors are aligned with each other. From the figure, it can be seen that the tip vortices are well resolved for two blade passages. Beyond this wake-age, the background mesh becomes too coarse to accurately represent the details of the tip vortex. After passing the bottom rotor, there is a significant interaction between the tip vortices. There is also some evidence of straining in the tip vortex from the preceding bottom rotor blade as it passes under the subsequent bottom rotor blade.

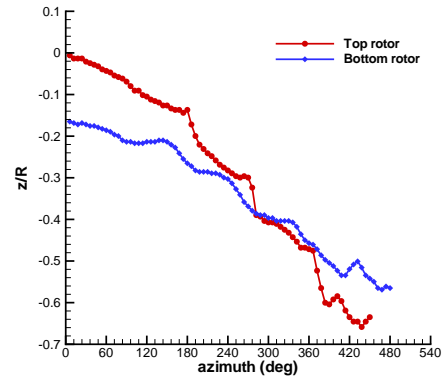


(a) $q = 0.025$

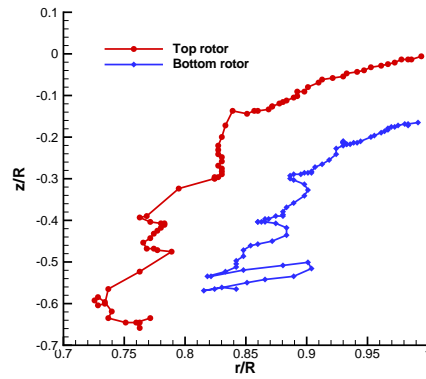
Figure 5.17: Iso-surfaces of the second invariant of vorticity magnitude for full-scale coaxial system (case 7) when the blades are aligned.



(a) r/R vs azimuth



(b) z/R vs azimuth



(c) z/R vs r/R

Figure 5.18: Wake trajectory for full-scale coaxial system (case 7) when the blades are aligned.

Figure 5.18 shows the wake trajectory at the same instant of time. The radial contraction of the wakes with azimuth is plotted in Fig. 5.18(a). It can be seen that the wake of the top rotor contracts at a much faster rate as compared to that of the bottom rotor. This is a result of the interaction between the two wakes, which forces the top rotor wake inward, while pushing the bottom rotor wake outward. Figure 5.18(b) shows the vertical convection of the wakes with

the azimuth. Clearly, the wake of the top rotor convects at a faster rate due to the presence of increased inflow. Both the wakes show an increased vertical convection rate after the first blade passage at 180° azimuth. Figure 5.18(c) shows the spatial location of both the wakes. It can be seen that the wake of the top rotor contracts to about $0.85R$ by the time it reaches the bottom rotor.

5.7 Flow-field Visualization

Figure 5.19 shows the vorticity magnitude contours for case 7 in a fixed plane in space at various instances in time. At the first instance both the top and bottom rotor blades are aligned at the plane. As the time increases, the wake age of the tip vortices from both the rotors at this plane increases. At all wake ages, the bottom rotor tip vortices are clearly visible. On the other hand, the top rotor vortices, which impinge upon the bottom rotor blade at around the plane shown for this particular case, remains distorted after the interaction. However, when similar contours are viewed on a plane which is located at different azimuth location in space, the tip vortices from both the rotors are clearly distinguished.

The tip vortices from the rotors can also be clearly distinguished from Figures 5.20 and 5.21. Figure 5.20 shows the vorticity magnitude contours for case 7 in a plane that is at 30° azimuth with respect to the top rotor blade, at different instances in time. At this plane, wake age of the tip vortices trailed from the top rotor remains constant, while the wake age of those trailed from the bottom rotor increases. At the first instance, the top and the bottom rotor blades are aligned. At a later time, the bottom rotor blade can be seen to intersect the plane of interest. The plot clearly shows the interaction of the vortices from the two rotors with each other and also with the inboard sheet. Additionally, we can

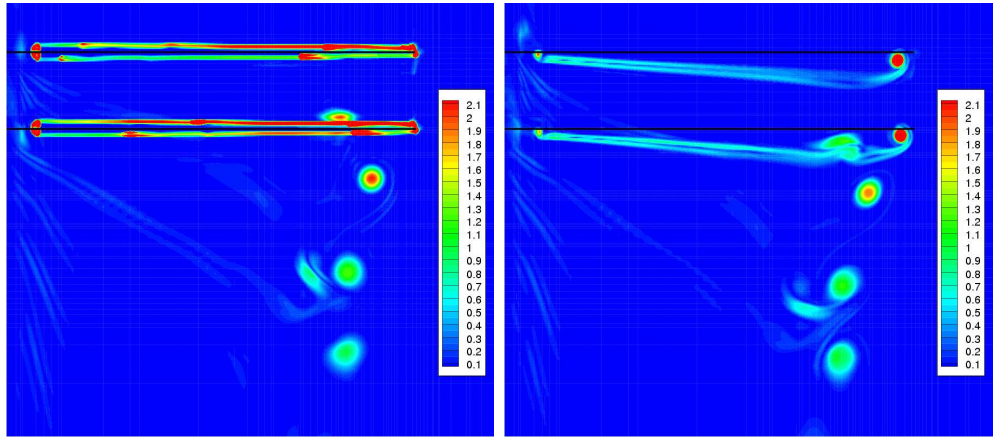
observe that, even though the vortices trailing from the top rotor vortices are at constant wake age, they are not at a fixed position. Due to the various vortex-vortex and blade-vortex interactions, the tip vortices trailing from the top rotor (especially the ones after the first blade passage) show significant wandering. Figure 5.21 shows the vorticity magnitude contours for case 7, but in a plane that is at 30° azimuth with respect to the bottom rotor blade. At this plane, the wake age of the bottom rotor vortices are fixed and the wake age of the top rotor vortices increases. Again, significant wandering of the bottom rotor tip vortices can be seen.

Figure 5.22 shows similar plots as in Fig. 5.19, but for a lower thrust level (case 3). The vortices from both the rotors are clearly distinguished in this plane. Recall that for this case, top rotor vortices impinge the bottom rotor at about 30° azimuth location. As a result, these vortices do not show the same distortion in the plane shown, as was observed for case 7. Comparing the locations of the vortices of the top and bottom rotors with those for case 7, we see that for this case the vortices convect vertically down at a slower rate due to decreased inflow. As a result, the number of vortex-vortex interactions in the same frame is larger, therefore resulting in a more complicated flow-field.

5.8 Summary

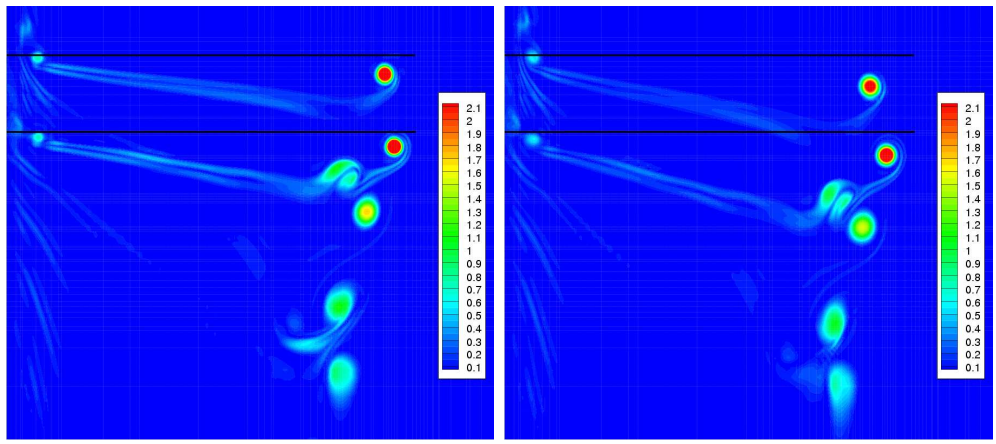
In this chapter, high resolution computations are performed on a hovering full-scale coaxial rotor and validated with experimental performance results. A trimming procedure is implemented, which allows for detailed yaw and thrust trim. The interaction between the rotor systems is seen to generate significant impulses in the instantaneous thrust and power. The characteristic signature of

this impulse is explained in terms of the blade thickness effect and loading effect. As expected, increased rotor spacing is seen to reduce both the thickness and loading effects. Further, interaction of the top-rotor wake with the blades of the bottom rotor results in low-harmonic unsteadiness. The flow-field of the full-scale coaxial system is very complicated due to the various blade-vortex and vortex interactions.



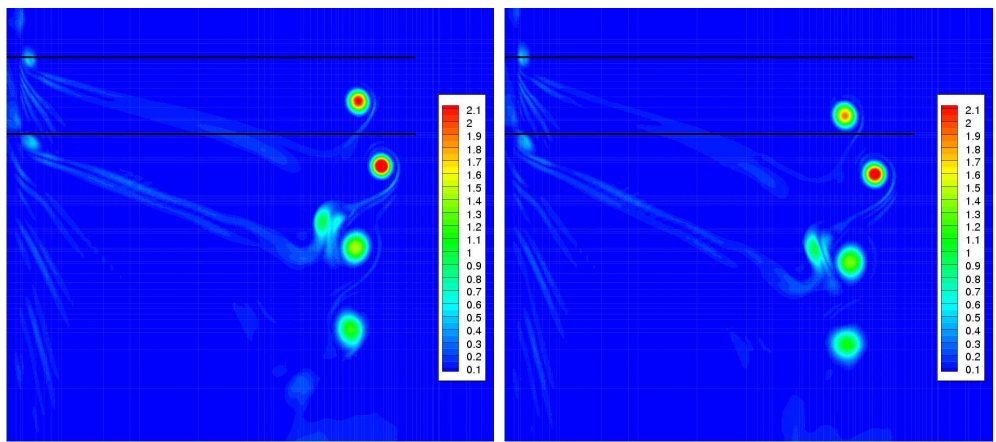
(a) $\Psi_{b_1} = \Psi_{b_2} = 0^\circ$

(b) $\Psi_{b_1} = \Psi_{b_2} = 30^\circ$



(c) $\Psi_{b_1} = \Psi_{b_2} = 60^\circ$

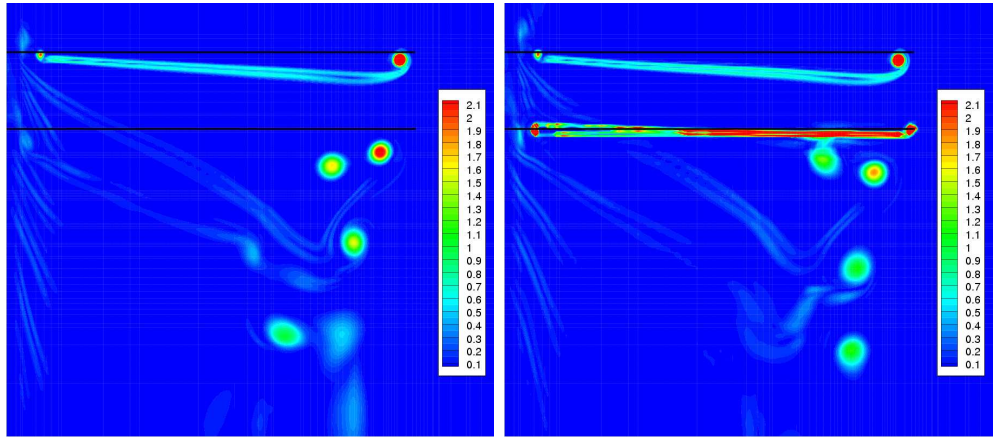
(d) $\Psi_{b_1} = \Psi_{b_2} = 90^\circ$



(e) $\Psi_{b_1} = \Psi_{b_2} = 120^\circ$

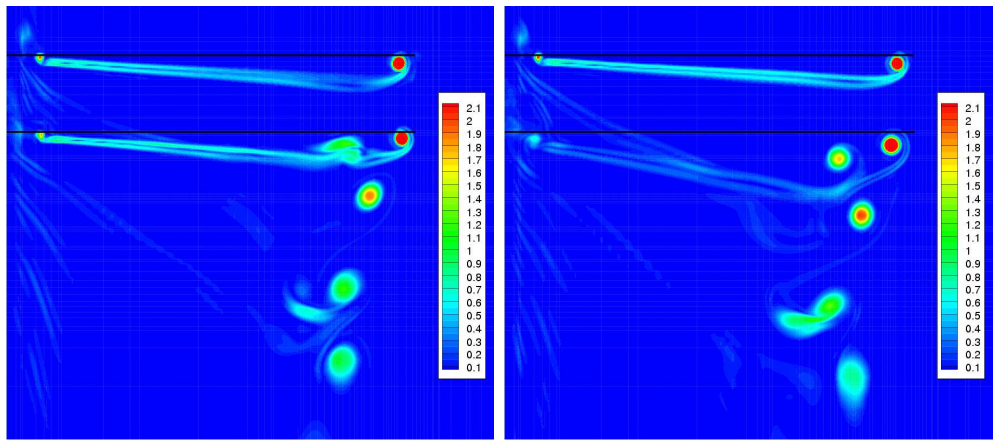
(f) $\Psi_{b_1} = \Psi_{b_2} = 150^\circ$

Figure 5.19: Vorticity magnitude contours in a fixed plane in space for full-scale coaxial system at different instances in time for full-scale coaxial system (case 7).



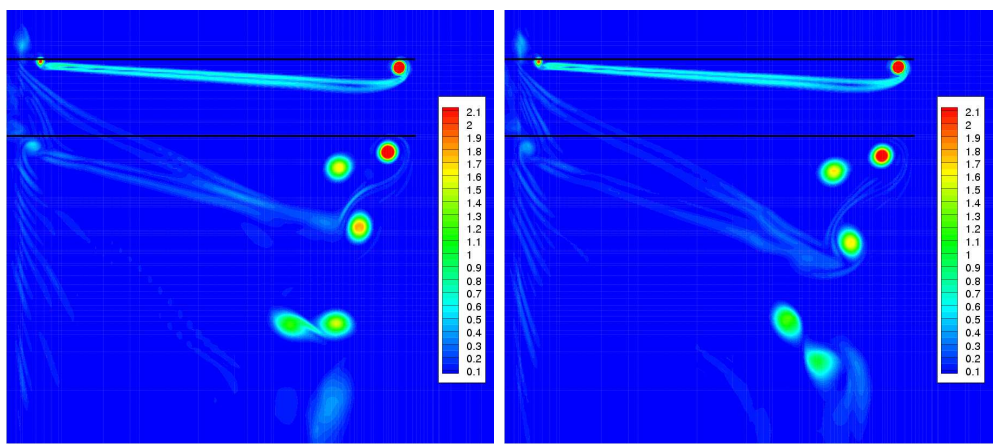
(a) $\Psi_{b_1} = 30^\circ, \Psi_{b_2} = 150^\circ$

(b) $\Psi_{b_1} = 30^\circ, \Psi_{b_2} = 6^\circ$



(c) $\Psi_{b_1} = 30^\circ, \Psi_{b_2} = 30^\circ$

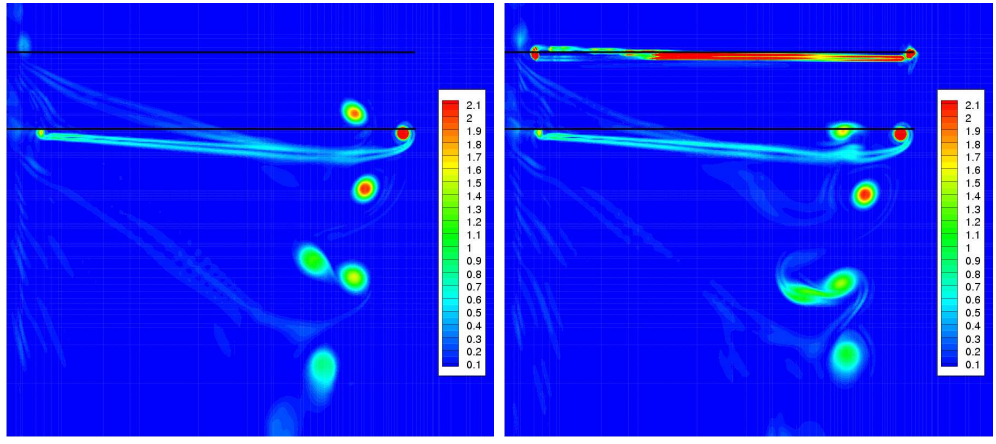
(d) $\Psi_{b_1} = 30^\circ, \Psi_{b_2} = 66^\circ$



(e) $\Psi_{b_1} = 30^\circ, \Psi_{b_2} = 90^\circ$

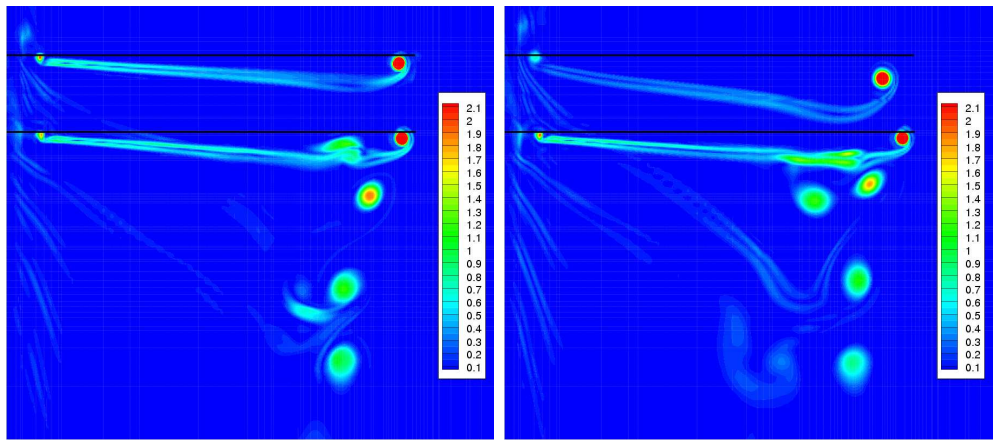
(f) $\Psi_{b_1} = 30^\circ, \Psi_{b_2} = 126^\circ$

Figure 5.20: Vorticity magnitude contours in a plane that is at 30° azimuth from the top rotor blade at different instances in time for full-scale coaxial system (case 7).



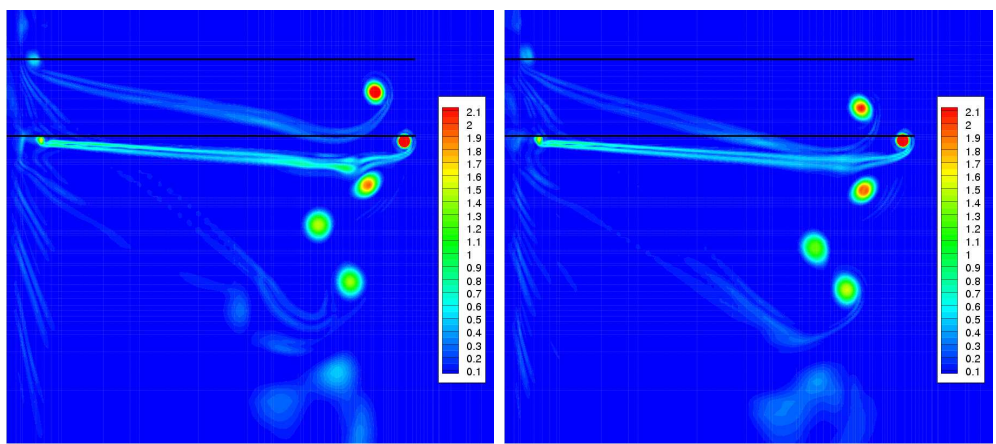
(a) $\Psi_{b_1} = 150^\circ, \Psi_{b_2} = 30^\circ$

(b) $\Psi_{b_1} = 6^\circ, \Psi_{b_2} = 30^\circ$



(c) $\Psi_{b_1} = 30^\circ, \Psi_{b_2} = 30^\circ$

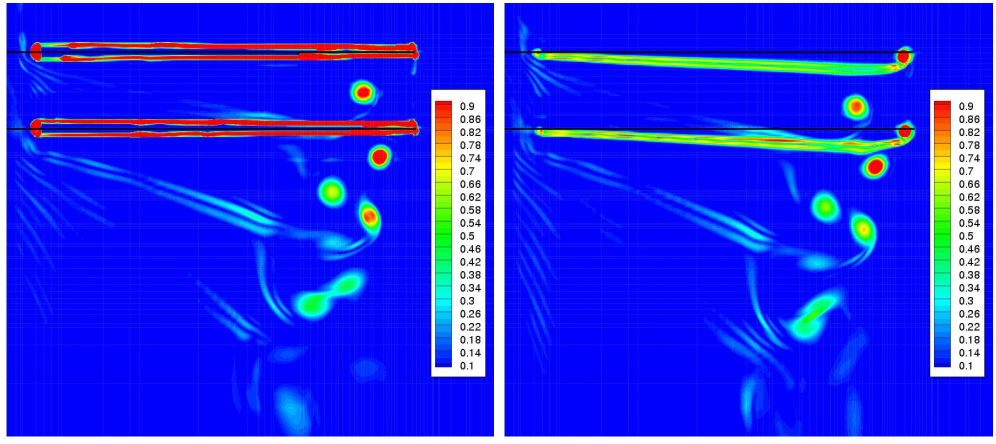
(d) $\Psi_{b_1} = 66^\circ, \Psi_{b_2} = 30^\circ$



(e) $\Psi_{b_1} = 90^\circ, \Psi_{b_2} = 30^\circ$

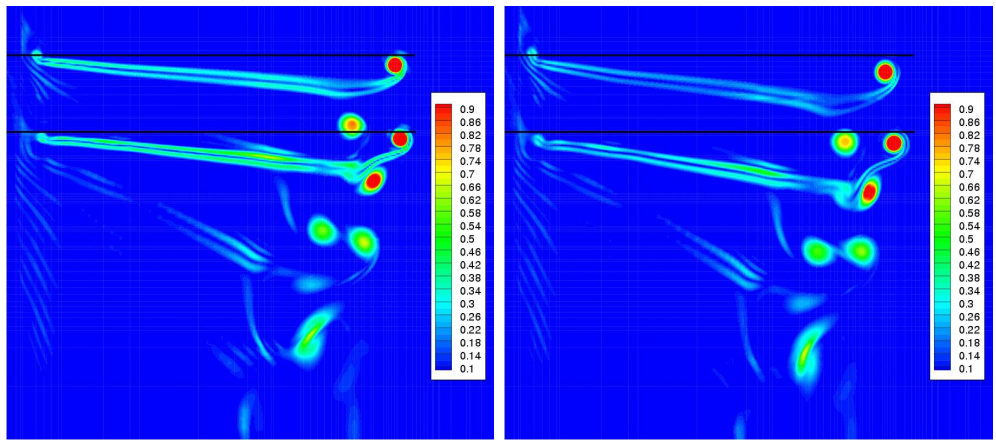
(f) $\Psi_{b_1} = 126^\circ, \Psi_{b_2} = 30^\circ$

Figure 5.21: Vorticity magnitude contours in a plane that is at 30° azimuth from the bottom rotor blade at different instances in time for full-scale coaxial system (case 7).



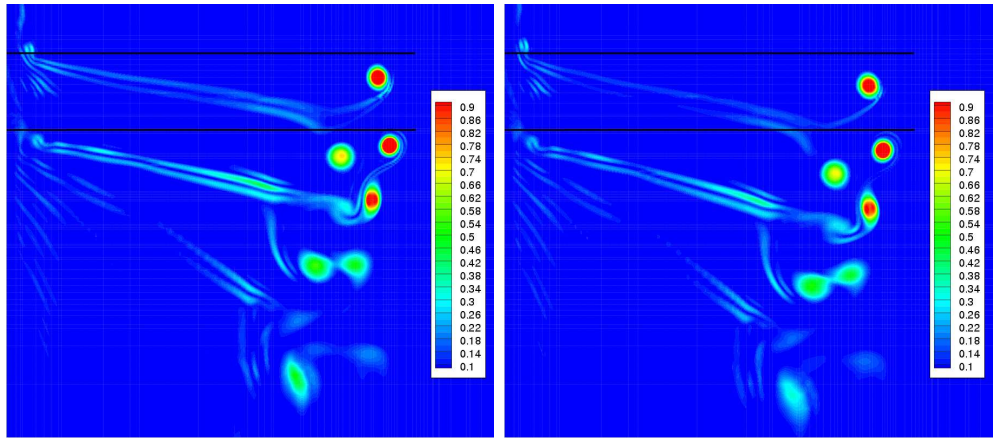
(a) $\Psi_{b_1} = \Psi_{b_2} = 0^\circ$

(b) $\Psi_{b_1} = \Psi_{b_2} = 30^\circ$



(c) $\Psi_{b_1} = \Psi_{b_2} = 60^\circ$

(d) $\Psi_{b_1} = \Psi_{b_2} = 90^\circ$



(e) $\Psi_{b_1} = \Psi_{b_2} = 120^\circ$

(f) $\Psi_{b_1} = \Psi_{b_2} = 150^\circ$

Figure 5.22: Vorticity magnitude contours in a fixed plane in space for full-scale coaxial system at different instances in time for full-scale coaxial system (case 3).

Chapter 6

Computational Investigation of Micro-Scale Coaxial Rotor Aerodynamics in Hover

After gaining sufficient confidence in full-scale coaxial rotor computations, the methodologies developed for micro-scale single rotor and full-scale coaxial rotor is combined to simulate micro-scale coaxial rotor in this chapter. Computations performed on a hovering micro-scale coaxial rotor are validated with experimental performance results. Next, a detailed study examining the influence of rotor spacing on unsteadiness is presented. The primary differences in the flow-field of micro-scale and full-scale coaxial rotor are identified.

6.1 Rotor Configuration

Micro-scale coaxial rotor simulations are validated by exploring the experimental results obtained by Bohorquez et al. [2] on a hovering coaxial system having two 2-bladed rotors. The aspect ratio of blade each is 4.98 (rotor radius is 112 mm

and blade chord is 22.5 mm), resulting in an individual rotor solidity of 0.128. The blades have an untwisted planform with the airfoil cross section geometry consisting of a circular arc airfoil with sharpened leading and trailing edges. The airfoil has a camber of 6% and a thickness of 2.2%. The experiment was conducted at various rotor RPM and inter-rotor spacing. The collectives of both the top and bottom rotors are fixed at 16° .

In the experimental test, the top and bottom rotors were torque balanced by changing the RPM of the bottom rotor, while keeping the top rotor RPM fixed. However, it was found that the percentile difference in rotational speed required for torque balance is less than 2%. Therefore, it should be reasonable to approximate the rotational speed of the bottom rotor to be the same as that of the top rotor. Consequently, all the computations are performed assuming identical top and bottom rotor rotational speeds.

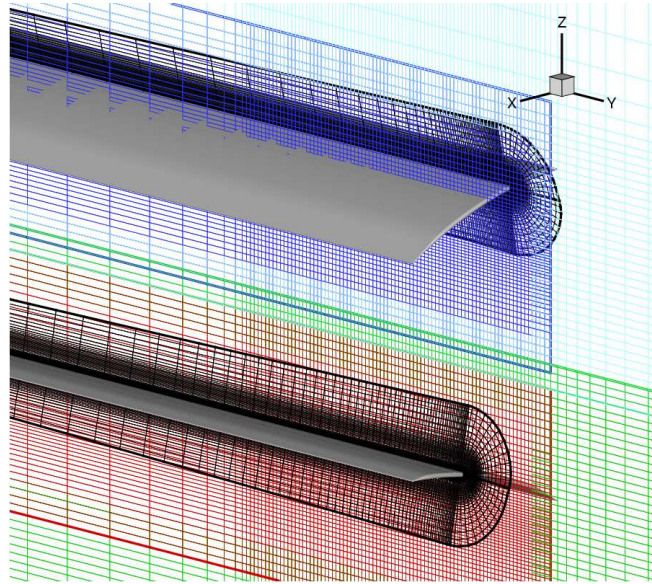
6.2 Mesh System

The mesh system used for the computation is similar to that used for the full-scale coaxial rotor calculation. A six mesh system consisting of two blade meshes, two nested background meshes and two cylindrical outer background meshes is used. Computations are performed on top and bottom rotor blade meshes having $267 \times 93 \times 50$ points in the streamwise, spanwise and normal directions, respectively, nested background meshes having $97 \times 124 \times 56$, top rotor outer background mesh having $97 \times 149 \times 49$ points and bottom rotor outer background mesh having $97 \times 149 \times 143$ in the azimuthal, radial and vertical directions, respectively. The total number of mesh points used is 6.6 million. A smaller number of mesh points can be used for the micro-scale rotor due to the lower

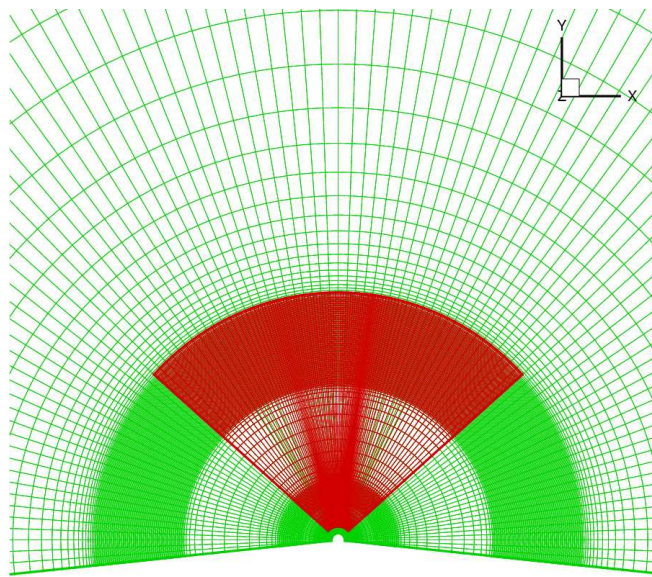
aspect ratio and the relatively larger expected sizes of the boundary layers and the core of the vortices as compared to the full-scale rotor. Figure 6.1 shows the blade and background meshes. In the most refined regions, the nested background mesh has a grid spacing of 0.02 chords in the vertical direction, while the outer background mesh has a grid spacing of 0.04 chords in the same direction. In the radial direction, both the nested and outer background meshes have a grid spacing of 0.025 chords in the most refined region. Along the azimuthal direction, a grid plane is spaced every 2° in the outer background mesh. For the nested background mesh, the azimuthal spacing varies from 0.3° near the blade to 2° towards its outer boundaries. The outer boundary of the background mesh extends to $3R$ above the top rotor, $4.5R$ below the bottom rotor and $4R$ from the tip of the blade. The chosen time-step size corresponds to 0.125° of azimuth. Each calculation takes about 5 days when run in parallel on 21 Intel Xeon 3.20GHz processors.

6.3 Effect of RPM

Experiments were conducted for a range of RPM varying from 1900 to 2700. Correspondingly, the tip Reynolds number varied from 19,000 to 27,000 and the tip Mach number ranged from 0.0665 to 0.0945. The rotor spacing is fixed at $h/R = 0.446$. Figure 6.2(a) shows the comparison between the computed and the measured variation of mean thrust with RPM for individual rotors as well as the entire system. The total system thrust is seen to be well predicted (within 3%) at all rotational speeds. Top rotor thrust is under-predicted by approximately $< 2\%$ at all speeds, whereas the bottom rotor thrust is over-predicted by approximately $< 8\%$. Figure 6.2(b) shows the comparison of mean



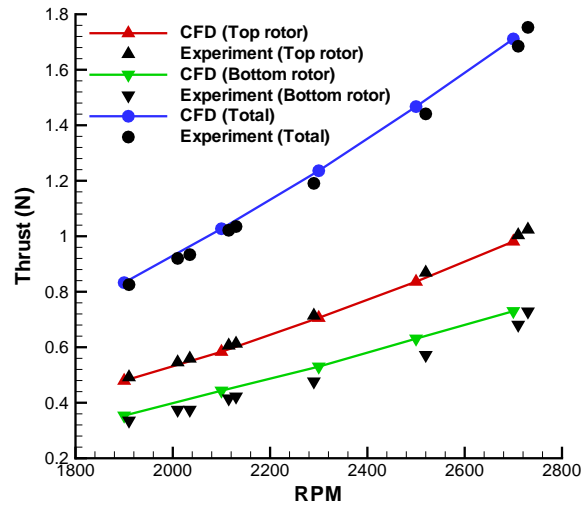
(a) Blade meshes along with cylindrical meshes



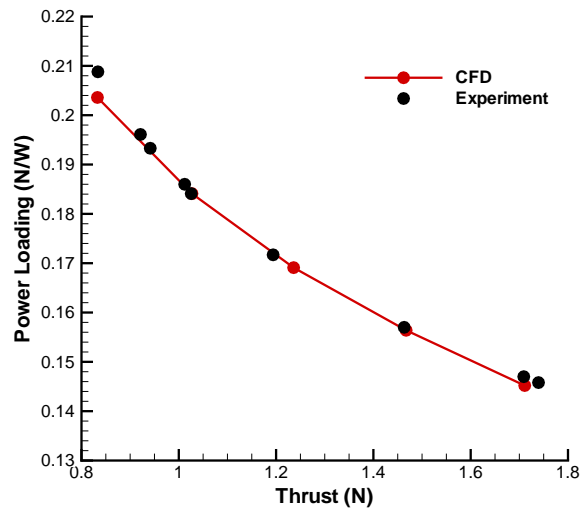
(b) Inner and outer cylindrical meshes

Figure 6.1: Computational mesh for micro-scale coaxial rotor system.

Power Loading (PL) versus mean thrust for the total system. Clearly, the power is very well predicted.



(a) Thrust (mean) versus RPM



(b) Power loading (mean) versus Thrust (mean)

Figure 6.2: Performance comparison with experimental data [2] at different RPM for micro-scale coaxial rotor.

6.4 Effect of rotor spacing

Five different rotor spacings given by $h/R = 0.268, 0.357, 0.446, 0.536$ and 0.625 are studied. The RPM for this study is fixed at 2000. Correspondingly, the tip Reynolds number is 20,000 and the tip Mach number is 0.07.

6.4.1 Mean Performance

Table 6.1 summarizes the mean values of torque (C_Q) coefficient obtained from CFD for individual rotors as well as for the entire system for all the rotor spacings. It can be seen that for all cases, torque is trimmed to within 5% error, showing that it is reasonable to assume identical rotational speeds for the top and bottom rotors. Table 6.2 summarizes the mean values of thrust (C_T) coefficient obtained from CFD for individual rotors as well as for the entire system. Also shown is the total thrust obtained from the experiments. It can be seen that the computed top and bottom rotor thrusts show opposite trends as the rotor spacing increases. While the top rotor thrust increases with the rotor spacing, the bottom rotor thrust decreases as the rotor separation increases. Both the rotor thrusts approach a constant value at very large rotor spacing. Because of the opposing trends in the top and bottom rotor thrusts, the total thrust of the system is seen to remain fairly constant with the rotor spacing, apart from the marginal increase in value at smaller rotor separation distances. Similar trend can be seen even in the experimental results. Tab 6.2 also shows the ratio of the top rotor thrust to the total thrust. Top rotor contributes to about 55% of the total value at smaller rotor spacing and increases to about 58% at the largest rotor separation. Note that, the full-scale coaxial rotor also showed similar thrust sharing.

Table 6.1: Computed mean torque coefficient for micro-scale coaxial system.

h/R	$C_{Q_{top}}$	$C_{Q_{bot}}$	$C_{Q_{total}}$	$ C_{Q_{top}} - C_{Q_{bot}} $
0.268	0.00384	0.00422	0.00806	0.00038
0.357	0.00387	0.00410	0.00797	0.00023
0.446	0.00388	0.00407	0.00795	0.00019
0.536	0.00389	0.00407	0.00796	0.00018
0.625	0.00392	0.00408	0.00800	0.00016

Table 6.2: Computed mean thrust coefficient for micro-scale coaxial system.

h/R	$C_{T_{top}}$	$C_{T_{bot}}$	$C_{T_{total}}$	$C_{T_{top}}/C_{T_{total}}$	$C_{T_{total}}$ (Expt. [2])
0.268	0.0199	0.0163	0.0362	0.55	0.0349
0.357	0.0205	0.0158	0.0363	0.56	0.0349
0.446	0.0208	0.0157	0.0365	0.57	0.0350
0.536	0.0210	0.0155	0.0365	0.58	0.0350
0.625	0.0212	0.0153	0.0365	0.58	0.0350

6.4.2 Unsteady Performance

A measure of the unsteadiness in thrust and power is the root mean square value of the temporal variations and this is summarized in Tables 6.3 and 6.4. For the top rotor, the absolute value of the fluctuation decreases with increasing rotor spacing, however surprisingly, for the bottom rotor, the absolute fluctuations initially decrease and then increase again as the rotor separation increases. The reason for this will be discussed later in the section. The fluctuations of the integrated quantities of the whole system follows similar trend as that of the bottom rotor. In general, there is 3 – 8% fluctuation in all integrated quantities, which could be significant for vibration and acoustic characteristics. Note that,

experiments typically provide only the mean performance data, while obtaining the unsteady data is very challenging.

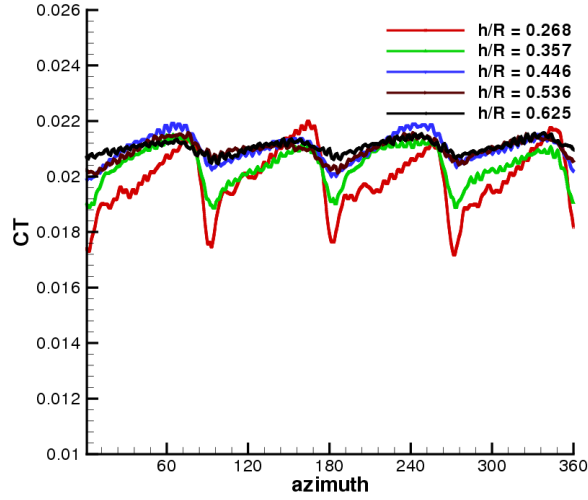
Table 6.3: Computed RMS fluctuation of power coefficient for micro-scale coaxial system.

h/R	$dC_{Q_{rms}}$ (top rotor)	% fluctuation	$dC_{Q_{rms}}$ (bottom rotor)	% fluctuation	$dC_{Q_{rms}}$ (total)	% fluctuation
0.268	0.000141	3.67%	0.000626	14.83%	0.000628	7.79%
0.357	0.000094	2.43%	0.000304	7.41%	0.000234	2.93%
0.446	0.000053	1.37%	0.000168	4.13%	0.000204	2.57%
0.536	0.000048	1.23%	0.000357	8.77%	0.000376	4.71%
0.625	0.000039	0.99%	0.000405	9.93%	0.000405	5.06%

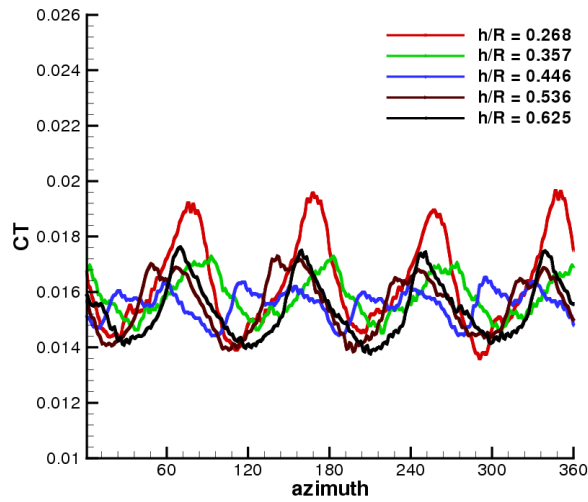
Table 6.4: Computed RMS fluctuation of thrust coefficient for micro-scale coaxial system.

h/R	$dC_{T_{rms}}$ (top rotor)	% fluctuation	$dC_{T_{rms}}$ (bottom rotor)	% fluctuation	$dC_{T_{rms}}$ (total)	% fluctuation
0.268	0.00105	5.28%	0.00164	10.06%	0.00237	6.55%
0.357	0.00065	3.17%	0.00074	4.68%	0.00074	2.04%
0.446	0.00040	1.92%	0.00057	3.63%	0.00088	2.41%
0.536	0.00036	1.71%	0.00091	5.87%	0.00120	3.29%
0.625	0.00024	1.13%	0.00105	6.86%	0.00117	3.21%

Figures 6.3 and 6.4, respectively, show the temporal variation of C_T and C_Q over one revolution for all rotor spacings. As seen for the full-scale coaxial rotor, the figure clearly shows the unsteadiness with a dominant 4/rev frequency. A high frequency noise-like variation is seen at all times due to shedding near the



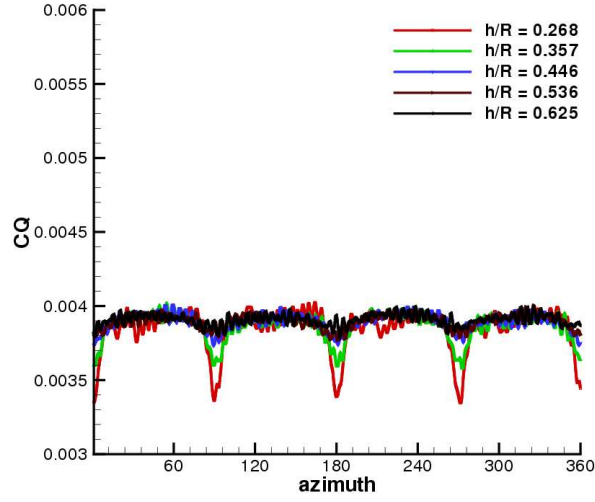
(a) Top rotor C_T variation



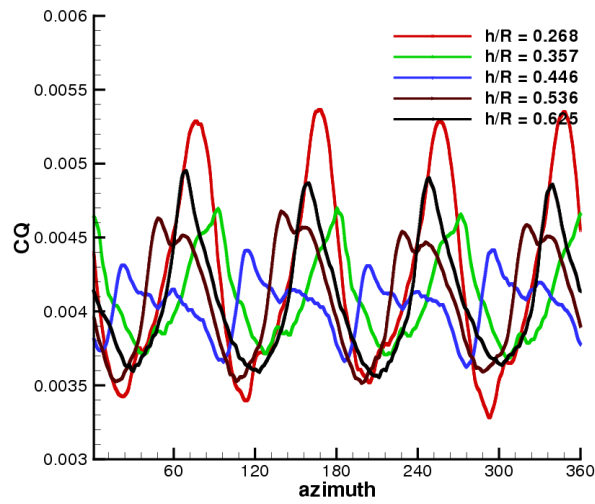
(b) Bottom rotor C_T variation

Figure 6.3: Temporal variation of C_T of the top and bottom rotors over one revolution for various rotor spacing for micro-scale coaxial system.

trailing edge, which was seen even for the micro-scale single rotor (Fig. 4.23). This variation is more obvious in the top rotor forces. The higher frequency



(a) Top rotor C_Q variation



(b) Bottom rotor C_Q variation

Figure 6.4: Temporal variation of C_Q of the top and bottom rotors over one revolution for various rotor spacing for micro-scale coaxial system.

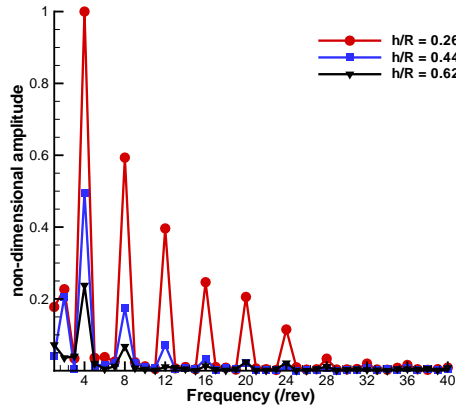
variation seen in the full-scale coaxial rotor near the blade passage due to venturi effect is not very prominent. This is because, the airfoil sections used in

the blades here are relatively thin and therefore, do not produce a significant thickness effect. The upwash-downwash (loading) effect is seen to be present, which decreases with the rotor spacing, similar to that for the full-scale coaxial rotor. This is particularly clear from the temporal variation of the integrated quantities of the top rotor, where the unsteadiness decreases with the increasing rotor separation.

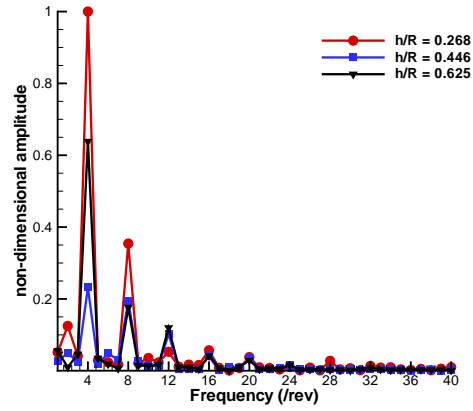
However, for the bottom rotor, the unsteadiness is not seen to follow any particular trend as the rotor spacing increases. This is in contrast to that for the full-scale system, for which the unsteadiness in the bottom rotor forces also decrease with the rotor spacing. The reason for the differences can be understood by comparing the temporal variation of thrust and power for the bottom rotor of the micro-scale system along with that of the full-scale system (Fig. 5.3(b) and 5.4(b)). All the plots show two peaks (apart from the peak due to venturi effect on the full-scale system). The peak which occurs close to the blade-passage is due to the loading effect and the other peak occurs when the vortex from the top rotor impinges upon the bottom rotor (for some of the plots, the peaks coincide). Clearly, as opposed to the full-scale system, the peak due to vortex impingement is more prominent and at times larger than the peak due to loading effect for the micro-scale rotor. This suggests that, contrary to what occurs for the full-scale system, the wake effect for the micro-scale system is comparable or maybe even predominant over the loading effect when the rotor spacing is large. Therefore, the unsteadiness in the integrated quantities for the bottom rotor of the micro-scale coaxial system need not necessarily decrease as the rotor spacing increases. On the other hand, because of the decrease in the dominant loading effect for the full-scale systems, an increase in rotor spacing almost always results in a decrease

in the unsteadiness of the bottom rotor forces. In Fig. 6.3, the peak due to vortex impingement is seen to move to a later azimuth as the rotor spacing increases, as the tip vortex from the upper rotor takes longer to convect down vertically. The peak due to vortex impingement for $h/R = 0.268, 0.357, 0.446, 0.536$ and 0.625 respectively occur at $76^\circ, 2^\circ, 22^\circ, 48^\circ$ and 68° azimuth location. For $h/R = 0.268$ and $h/R = 0.625$, the peaks due to vortex impingement and the loading effect are almost coincident, whereas for $h/R = 0.446$, the peaks are farthest apart. Clearly, the unsteadiness in the forces of the bottom rotor is smallest for $h/R = 0.446$, indicating that the phasing of the vortex impingement upon the bottom rotor can play a significant role in reducing unsteadiness for the micro-scale coaxial systems.

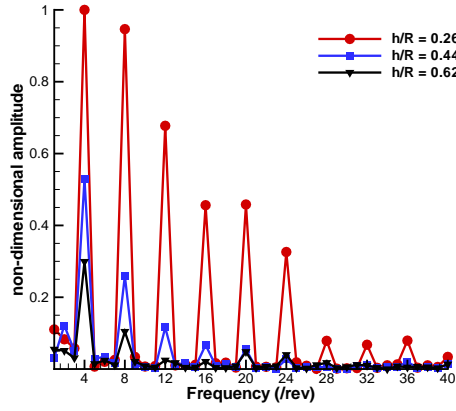
The effect of rotor spacing can be better quantified by investigating the frequency content in the integrated quantities. In Fig. 6.5, the amplitude of the frequency is normalized by the amplitude of the $4/\text{rev}$ frequency of the $h/R = 0.268$ case. It is seen that for all the cases, $4/\text{rev}$ is the dominant frequency. The presence of these higher frequencies is due to the sharper nature of the impulses. Therefore, as expected, an increase in the rotor spacing decreases the high frequency content of the top rotor forces. Additionally, it is also evident that the relative amplitude of various frequencies decreases for the top rotor as the rotor spacing increases. However, the trends for the bottom rotor are not so obvious due to the reasons discussed earlier. As expected, the bottom rotor for $h/R = 0.446$ case has the smallest $4/\text{rev}$ content. It should also be noted that the bottom rotor has lesser high frequency content relative to the dominant $4/\text{rev}$ frequency when $h/R = 0.268$.



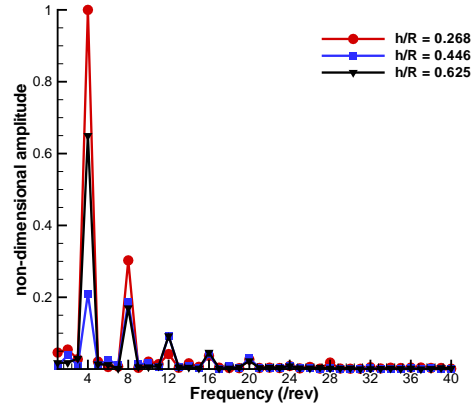
(a) Top rotor thrust



(b) Bottom rotor thrust



(c) Top rotor power



(d) Bottom rotor power

Figure 6.5: Effect of rotor spacing on the frequency distribution, normalized by the amplitude of 4/rev frequency of the $h/R = 0.268$ case, for micro-scale coaxial system.

6.4.3 Effect of Top Rotor Wake on Bottom Rotor

In order to better visualize the effect of top rotor wake on the bottom rotor, an azimuthal contour of the sectional thrust ($R \frac{dC_T}{dr}$) and its fluctuation from the mean value are respectively plotted in Figs. 6.6 and 6.7, for the bottom rotors

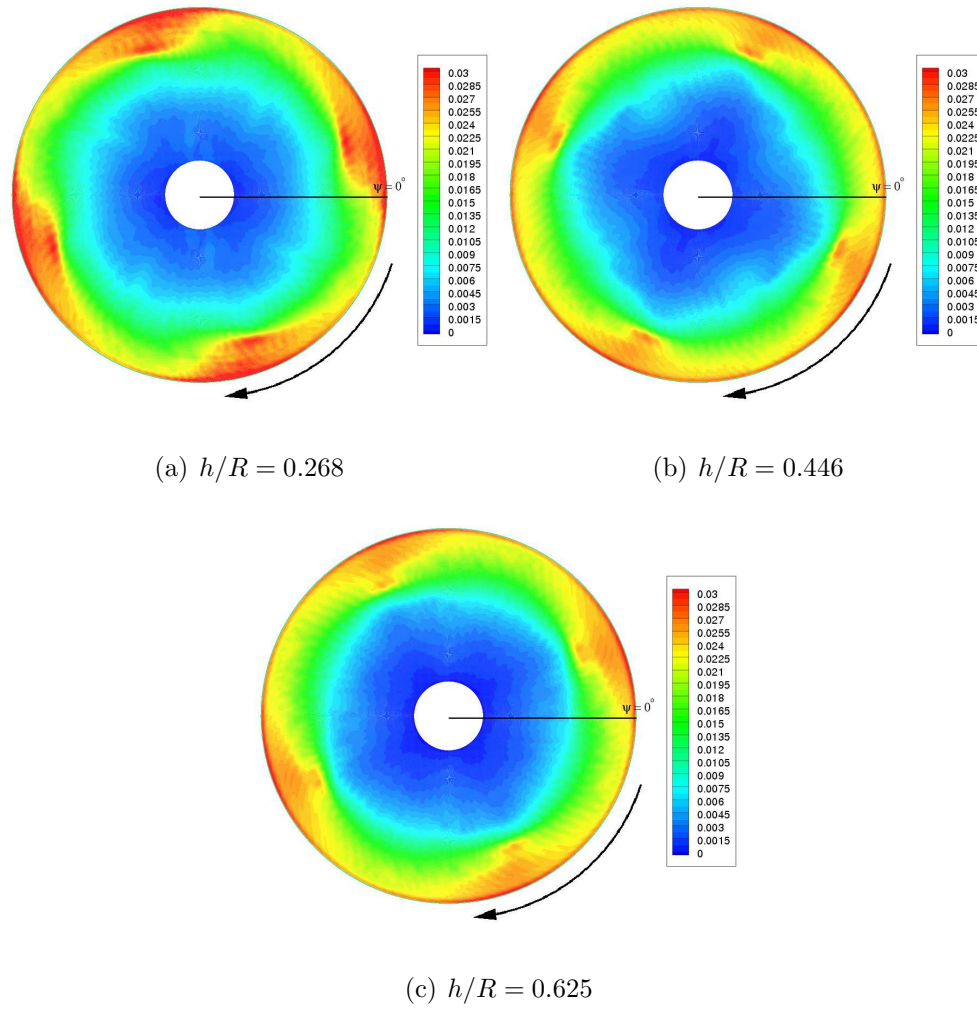


Figure 6.6: Sectional thrust ($R \frac{dC_T}{dr}$) contour for the bottom rotor of micro-scale coaxial system.

for the cases with $h/R = 0.268$, $h/R = 0.446$ and $h/R = 0.625$. The figures clearly show the unsteadiness on the bottom rotor as the wake from the top rotor encounters the plane of the bottom rotor. The interacting wake increases the thrust outboard and decreases the thrust inboard. The sectional thrust fluctuation contour plots for the $h/R = 0.268$ and $h/R = 0.625$ cases are very similar, whereas the corresponding plot for $h/R = 0.446$ case looks different.

The reason for the differences is again explained by the different location of the impingement of the top rotor vortex on the bottom rotor.

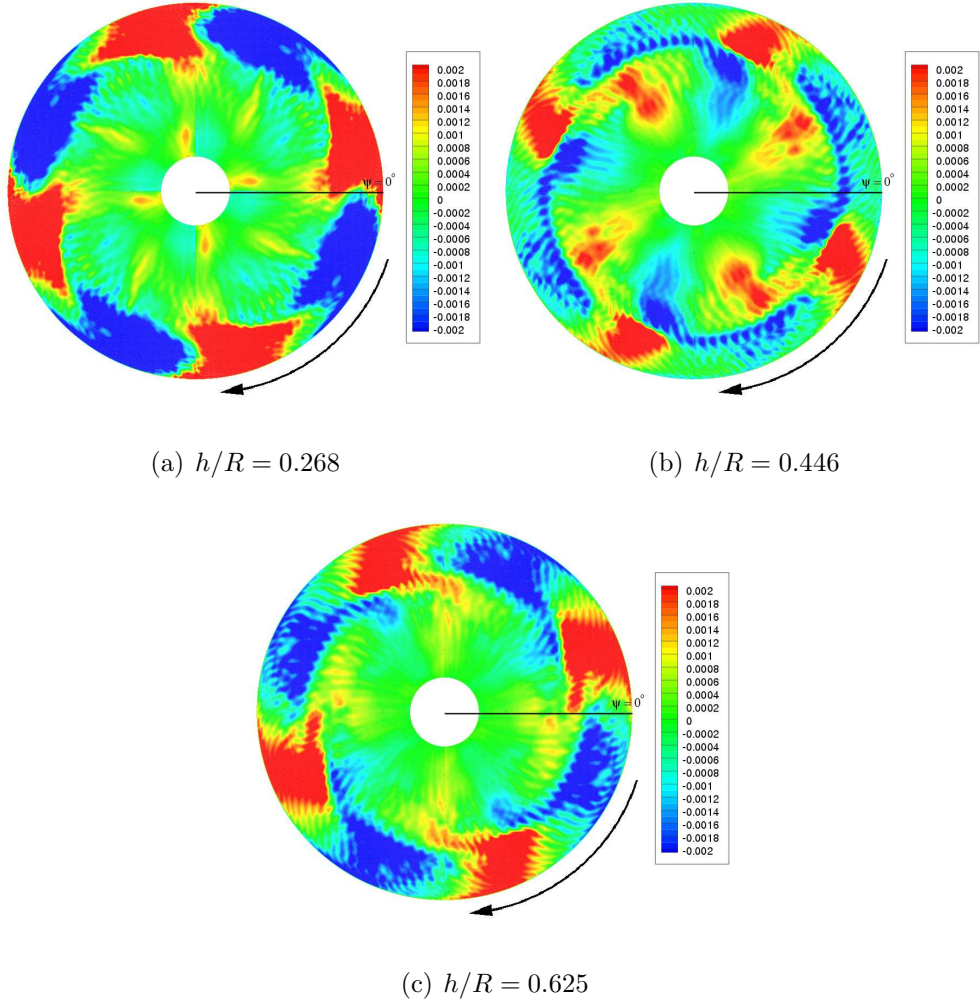
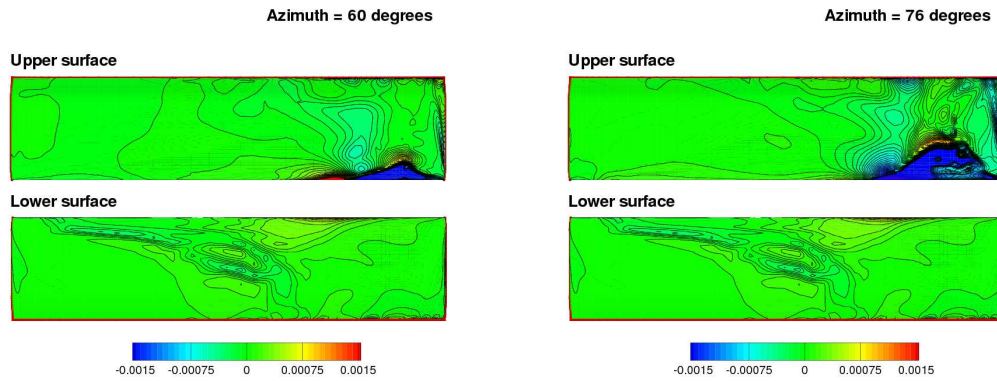


Figure 6.7: Fluctuation in sectional thrust ($R \frac{dC_T}{dr}$) contour for the bottom rotor of micro-scale coaxial system.

In order to further understand the effect of the top rotor vortex impingement on the bottom rotor, blade pressure fluctuation contours of the bottom rotor are plotted at three different instances in time (instance 1 : 16° before the impingement of the vortex, instance 2 : at the time of impingement of vortex,

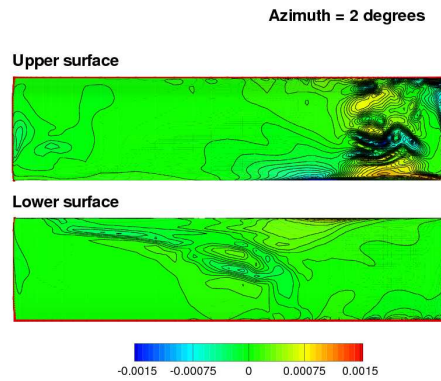
instance 3 : 16° after the impingement of the vortex) for the three rotor spacings of $h/R = 0.268$, $h/R = 0.446$ and $h/R = 0.625$ in Figs. 6.8, 6.9 and 6.10, respectively. In these plots, the leading edge of the blade is towards the middle for both the upper and lower surfaces. At instance 1, a strong suction pressure starts to build on the upper surface of the outboard region of the blade for all cases. On the lower surface, the signature of the inboard vortex sheet impinging on the blade can be seen, which is particularly clear for the $h/R = 0.446$ case. At instance 2, the strong suction on the upper surface of the outboard portion of the blade is getting ready to separate from the leading edge for all cases, which can be seen more clearly in Fig. 6.11, which shows the sectional pressure contour at an outboard spanwise location of $0.9R$. At the same instance, a vortex has already shed from the lower surface of the inboard portion of the blade with a higher pressure peak wave further downstream (the acoustic wave seen on the surface plots), see Fig. 6.12 which shows the sectional pressure contour at an inboard spanwise location of $0.55R$ at instance 2. The suction peak associated with the separated vortex on the lower surface is not very strong on the actual surface. At instance 3, all the cases show a three dimensional shedding in the outboard section of the blade.

As a summary to this section, the interaction of the top rotor vortex and inboard sheet with the bottom rotor results in unsteady shedding from the leading-edge region both in the outboard and inboard portions of the blade; a phenomenon not seen for the full-scale coaxial rotor. In the outboard portion of the blade, a highly three-dimensional shedding occurs on the upper surface of the blade, whereas the shedding at the inboard portion of the blade occurs on the lower surface and it is more two-dimensional in nature. The reason for this



(a) Instance 1

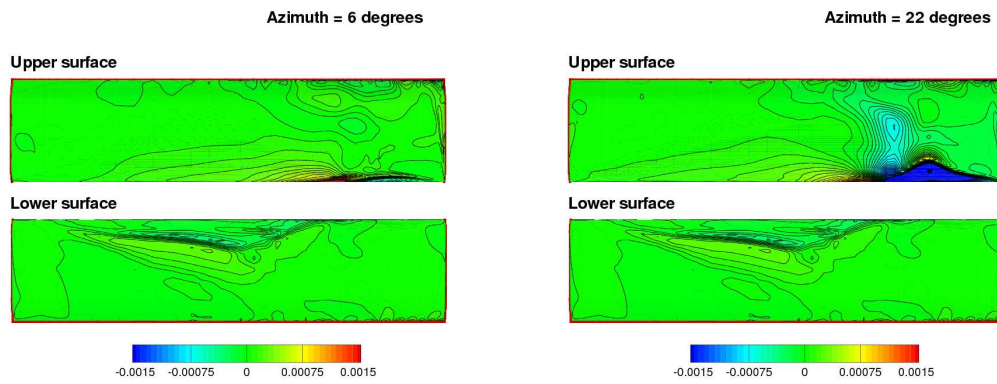
(b) Instance 2



(c) Instance 3

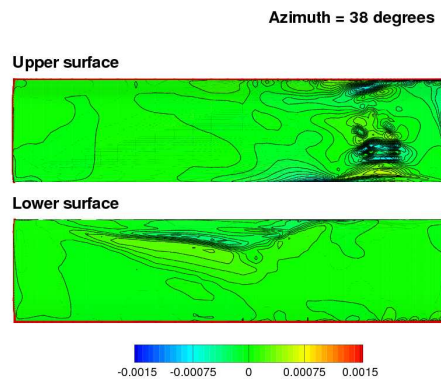
Figure 6.8: Fluctuation in the surface pressure for the $h/R = 0.268$ case of micro-scale coaxial system.

shedding is because of the change in local angle of attack due to velocity induced by the tip vortex, which might result in significant movement of the stagnation point about the sharp leading edge. In the outboard portion of the bottom rotor blade, the angle increases as the top rotor vortex impinges upon it, whereas the angle decreases in the inboard portion.



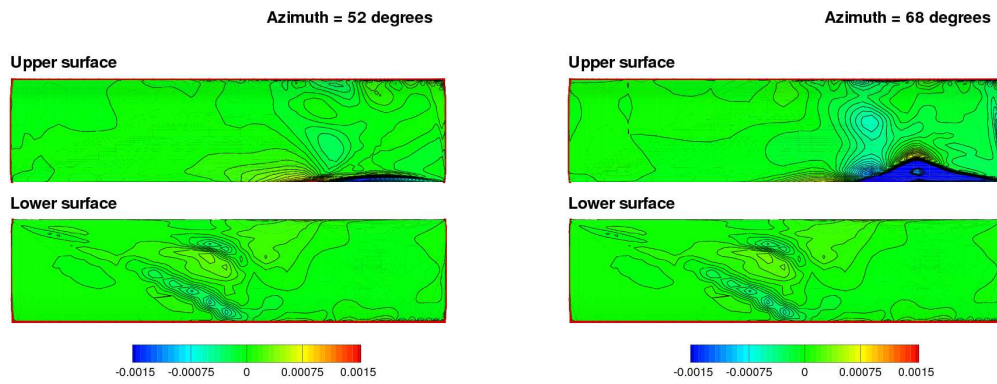
(a) Instance 1

(b) Instance 2



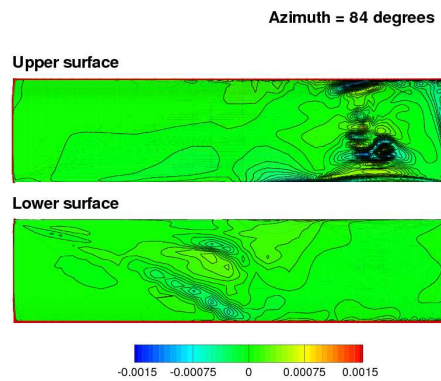
(c) Instance 3

Figure 6.9: Fluctuation in the surface pressure for the $h/R = 0.446$ case of micro-scale coaxial system.



(a) Instance 1

(b) Instance 2



(c) Instance 3

Figure 6.10: Fluctuation in the surface pressure for the $h/R = 0.625$ case of micro-scale coaxial system.

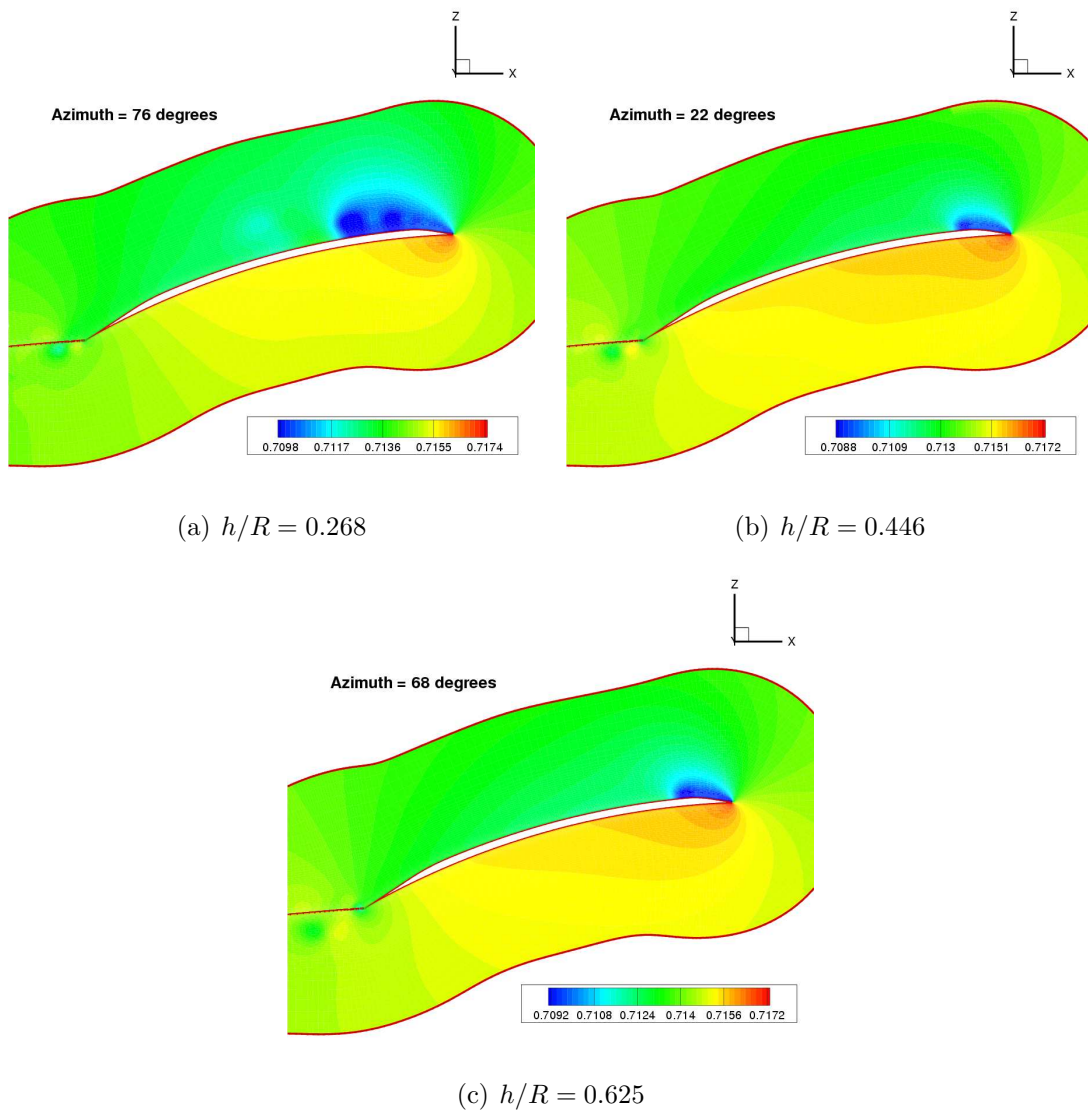


Figure 6.11: Spanwise pressure contour at $r/R = 0.9$ for micro-scale coaxial system.

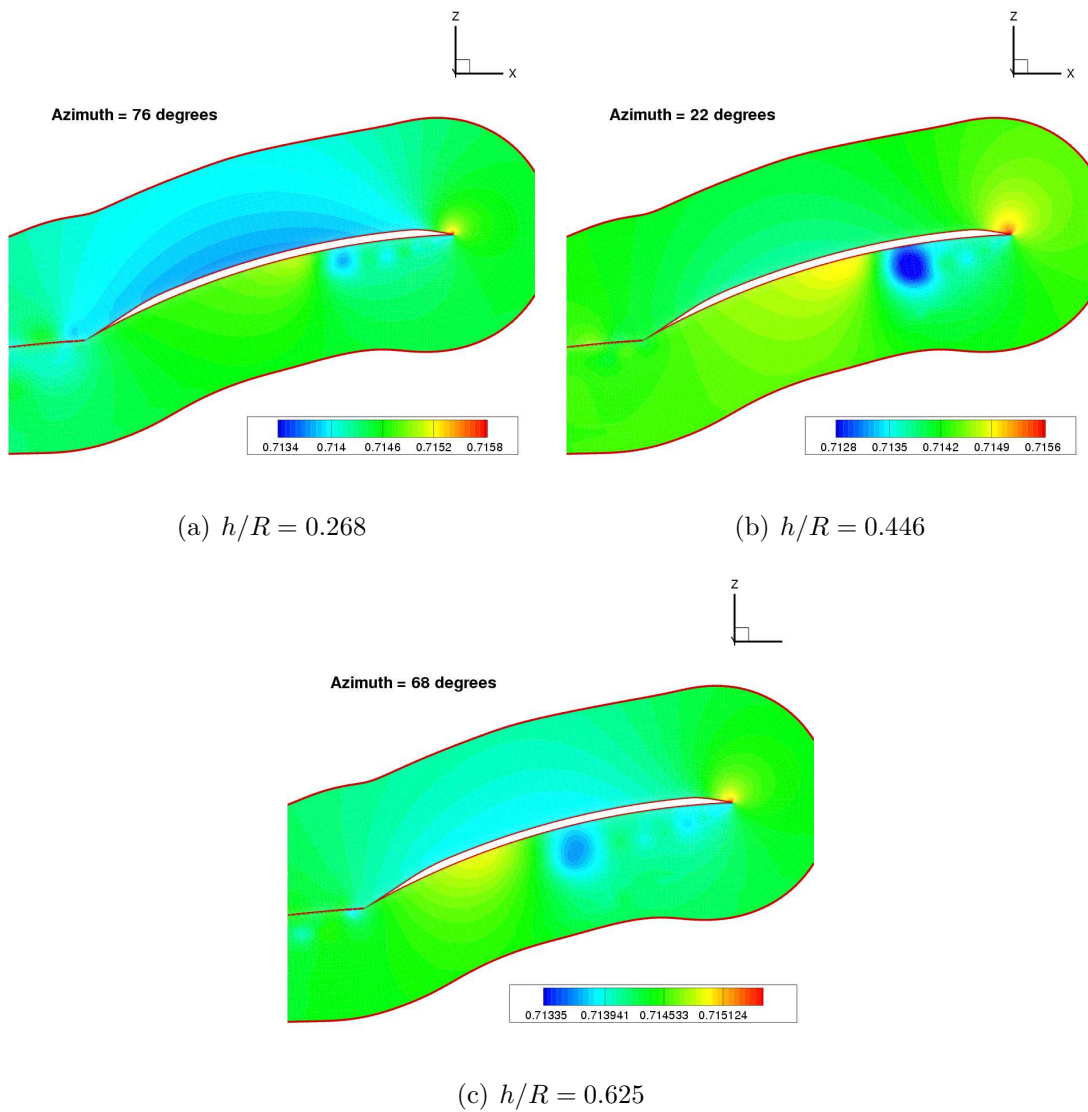


Figure 6.12: Spanwise pressure contour at $r/R = 0.55$ for micro-scale coaxial system.

6.4.4 Wake Trajectory

In order to extract only the rotational flow regions and not the highly strained regions, the iso-surfaces of so-called q-criterion [90] are shown in Fig. 6.13 for the rotor spacings of $h/R = 0.268$, $h/R = 0.446$ and $h/R = 0.625$ at the instant in time where the top and the bottom rotor are at the same azimuth. From the figure, it can be seen that the tip vortices are well resolved for two blade passages for all cases. Beyond this wake-age, the background mesh becomes too coarse to accurately represent the details of the tip vortex. After passing through the bottom rotor, there is a significant interaction between the tip vortices. There is also some evidence of straining in the tip vortex from the preceding bottom rotor blade as it passes under the subsequent bottom rotor blade.

Figure 6.14 shows the wake trajectory at the same instant of time for all the three rotor spacings. The radial contraction of the wake of the top and bottom rotors with azimuth are respectively plotted in Figs. 6.14(a) and (b). Similar to that for the full-scale rotor, the wake of the top rotor contracts at a much faster rate compared to that of the bottom rotor for all the cases. This is a result of the interaction between the two wakes, which forces the top rotor wake inward, while pushing the bottom rotor wake outward. Also, as this interaction occurs at an earlier wake age for smaller rotor spacings, the amount of contraction of the top rotor wake is larger at the same azimuth location for smaller rotor separation distances. For the same reason, the top rotor wake gets wavy at an earlier azimuth when the rotor separation is smaller. Comparing the contraction of the bottom rotor wakes for the three rotor spacings, we can see that the contraction rate is slightly larger for the $h/R = 0.268$ case, but it is not too different for the other two rotor spacing cases. The reason for this could be due to stronger

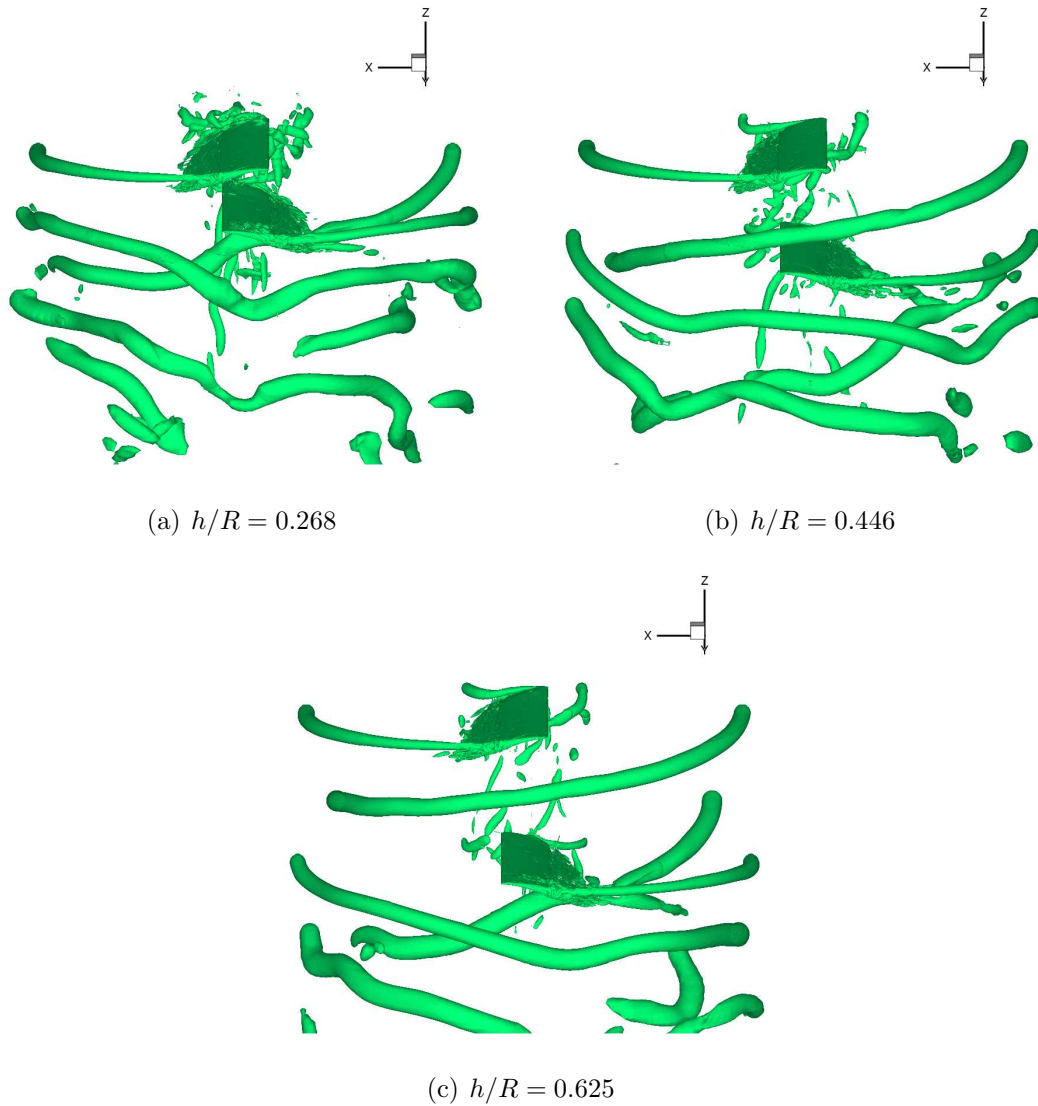
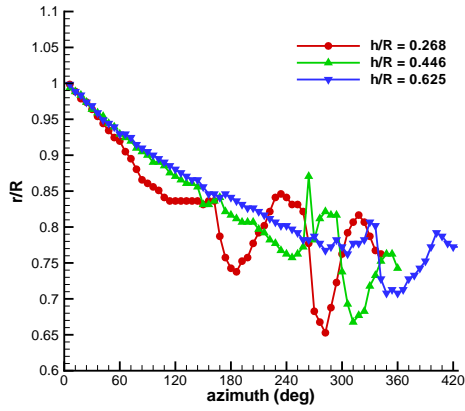


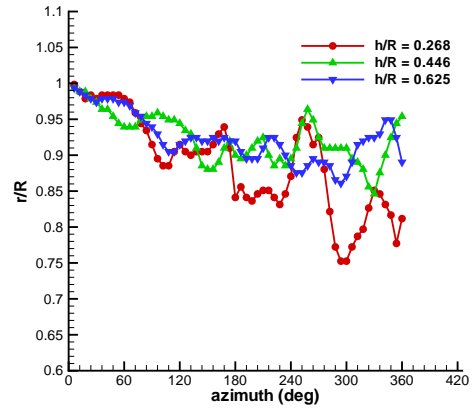
Figure 6.13: Iso-surfaces of the second invariant of vorticity magnitude ($q = 0.2$) for micro-scale coaxial system when the blades are aligned.

interactions between the wakes for the smallest rotor spacing.

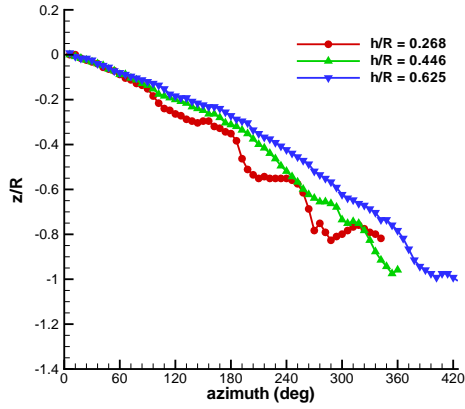
Figures 6.14(c) and (d) respectively show the vertical convection of the top and bottom rotors wake with the azimuth for all the three rotor spacing cases. Clearly, the wakes of the top rotor convect at a faster rate compared to bottom rotor wakes due to the presence of increased inflow. Both the wakes show an



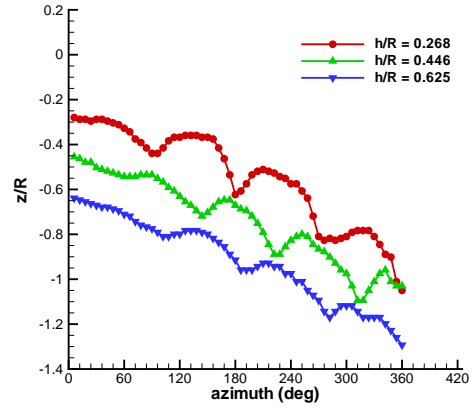
(a) r/R vs azimuth(top rotor)



(b) r/R vs azimuth (bottom rotor)



(c) z/R vs azimuth (top rotor)



(d) z/R vs azimuth (bottom rotor)

Figure 6.14: Wake trajectories for various rotor spacing for micro-scale coaxial system when the blades are aligned.

increased vertical convection rate after the first blade passage at 180° azimuth. The top rotor wakes show an additional increase in vertical convection rate when they encounter the bottom rotor. As a result, when the rotor spacing is smaller, the vertical convection rate of the top rotor wake increases at an earlier azimuth, therefore showing larger convection at the same azimuth location compared to a

larger rotor spacing case. The vertical convection rate of the bottom rotor wake is not too different for all the rotor spacings.

6.4.5 Flow-field Visualization

Figure 6.15 shows the vorticity magnitude contours for the $h/R = 0.446$ case in a fixed plane in space at various instances in time. At the first instance both the top and bottom rotor blades are aligned at the plane. As the time increases, the wake age of the tip vortices from both the rotors at this plane increases. At all wake ages, the top and bottom rotors tip vortices are clearly visible. The interaction between the top and bottom rotor vortices results in significant wandering. The figure also indicates that the tip vortices from the two rotor systems are entering into a leap-frogging system, similar to that for vortex smoke rings.

Figure 6.16 shows the vorticity magnitude contours for the $h/R = 0.268$ case in a plane that is fixed with respect to the bottom rotor blade, at different instances in time. At this plane, the wake age of the tip vortices trailed from the bottom rotor remains constant (0° , 180° , 360° etc.), while the wake age of those trailed from the top rotor increases. At the first instance, the top and the bottom rotor blades are aligned. The plot clearly shows the interaction of the vortices from the two rotors with each other and also with the inboard sheet. The impingement of the top rotor vortex upon the bottom rotor can be seen to have occurred at an instance just before Fig. 6.16(f) which corresponds to 156° wake-age of the top rotor vortex (78° azimuth in time). Recall that, for this rotor spacing, a peak in integrated quantities of the bottom rotor had occurred at about 76° azimuth in time and this plot confirms that the peak is

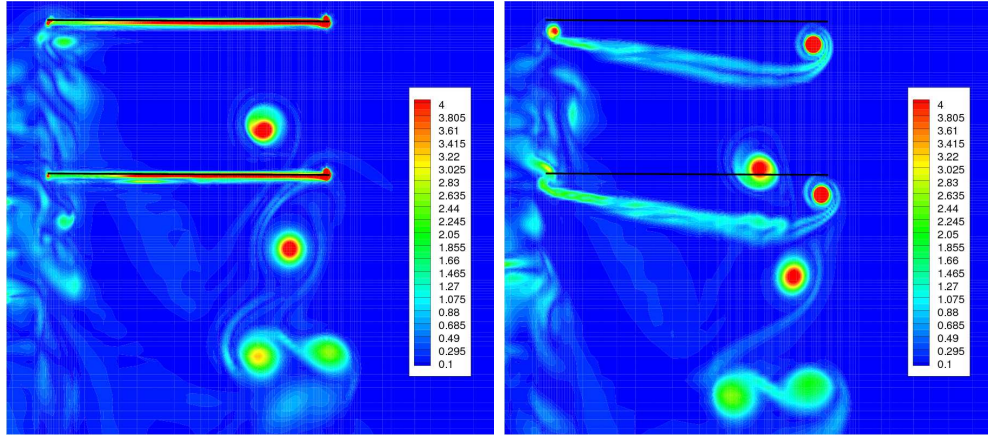
indeed due to the vortex impingement. Similar conclusions can be made for the rotor spacing of $h/R = 0.446$ and $h/R = 0.625$ from their corresponding plots, Figs. 6.17 and 6.18. For all cases, we can observe that, even though the vortices trailing from the bottom rotor vortices are at constant wake age, they are not at a fixed position. Due to the various vortex-vortex and blade-vortex interactions, the tip vortices trailing from the bottom rotor (especially the ones after the first blade passage) show significant wandering.

Figure 6.19 shows the vorticity magnitude contours for the $h/R = 0.446$ case in a plane that is 30° in azimuth behind the top rotor blade, at different instances in time. At this plane, the wake age of the tip vortices trailed from the top rotor remains constant (30° , 210° , 390° etc.), while the wake age of those trailed from the bottom rotor increases. At the first instance, the top and the bottom rotor blades are aligned. At a later time, the bottom rotor blade can be seen to intersect the plane of interest. Again, significant wandering of the top rotor tip vortices can be seen due to various interactions, even though they are at a constant wake age.

6.5 Summary

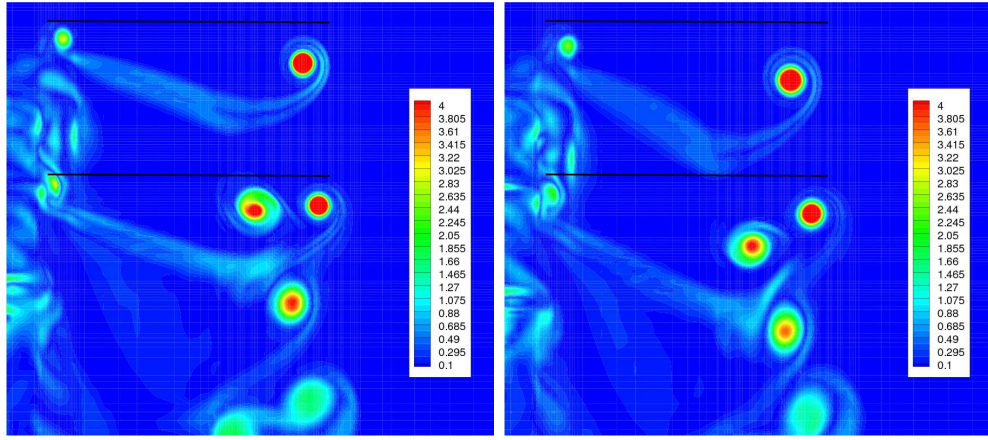
In this chapter, computations are performed on a hovering micro-scale coaxial rotor and validated with experimental performance results. The overall performance is well predicted for a range of RPMs and rotor spacing. As the rotor spacing increases, the top rotor thrust increases and the bottom rotor thrust decreases, while the total thrust remain fairly constant. The interaction between the rotor systems is seen to generate significant impulses in the instantaneous thrust and power. Unsteadiness is mainly caused due to blade loading (for both

top and bottom rotor) and the wake impingement effect (for the bottom rotor). Additional high frequency unsteadiness is also seen due to shedding near the trailing edge. The phasing of the top vortex impingement upon the bottom rotor plays a significant role in the amount of unsteadiness for the bottom rotor. Interaction of the top rotor vortex and inboard sheet with the bottom rotor results in a highly three-dimensional shedding on the upper surface of the blade in the outboard region and a two-dimensional shedding on the lower surface at the inboard portion of the blade, most likely due to the sharp leading edge geometry. An analysis of the vortex trajectories and flow-field visualization shows the expected faster contraction and vertical convection of the top rotor wake as compared to bottom rotor wake. Significant wandering is observed and it is expected that the tip vortices from the two rotor systems are entering into a leap-frogging system, similar to that for vortex smoke rings.



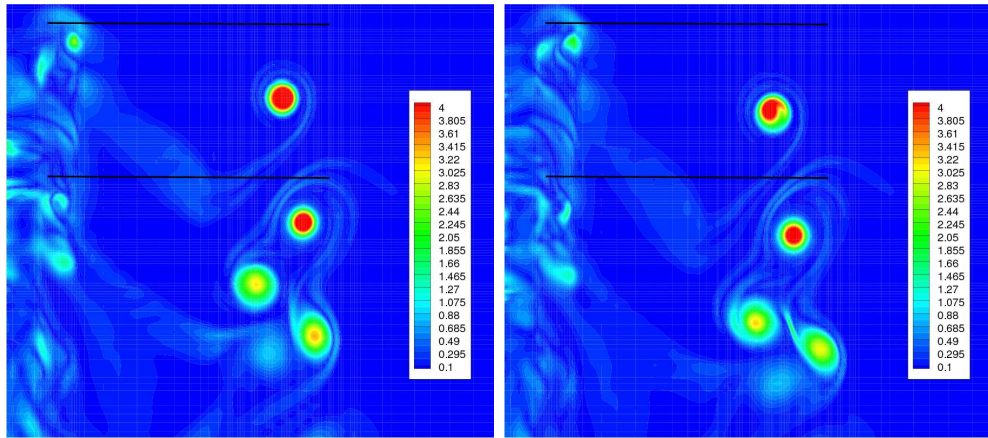
(a) $\Psi_{b_1} = \Psi_{b_2} = 0^\circ$

(b) $\Psi_{b_1} = \Psi_{b_2} = 30^\circ$



(c) $\Psi_{b_1} = \Psi_{b_2} = 60^\circ$

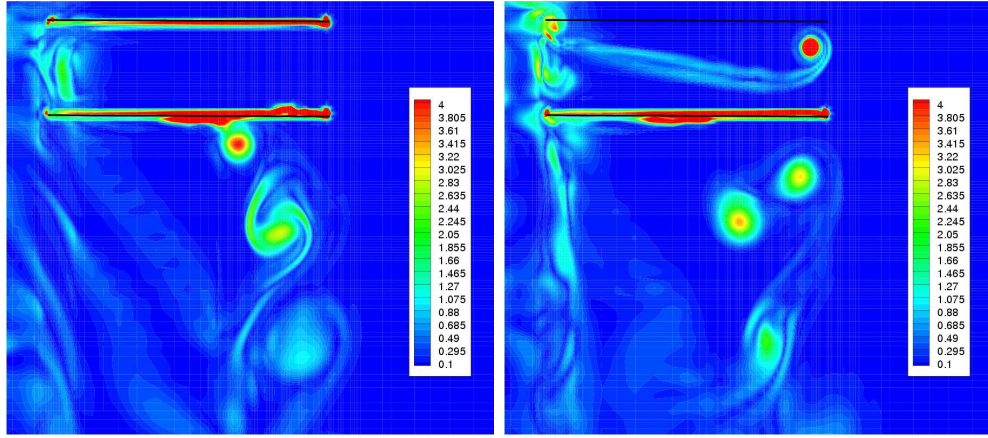
(d) $\Psi_{b_1} = \Psi_{b_2} = 90^\circ$



(e) $\Psi_{b_1} = \Psi_{b_2} = 120^\circ$

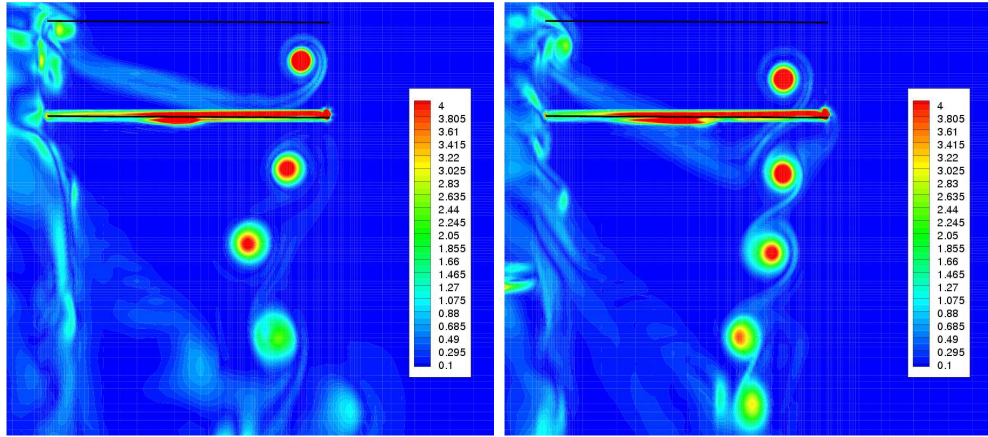
(f) $\Psi_{b_1} = \Psi_{b_2} = 150^\circ$

Figure 6.15: Vorticity magnitude contours in a fixed plane in space at different instances in time for micro-scale coaxial system, $h/R = 0.446$.



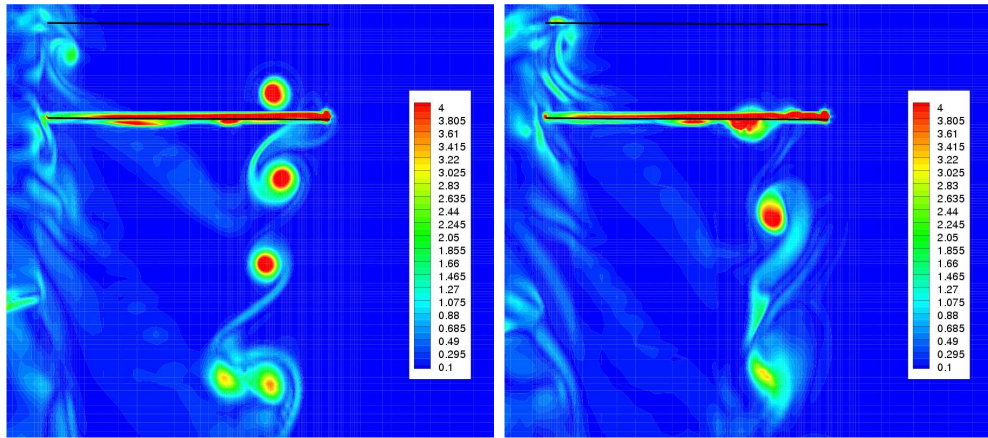
(a) $\Psi_{b_1} = 0^\circ, \Psi_{b_2} = 0^\circ$

(b) $\Psi_{b_1} = 36^\circ, \Psi_{b_2} = 0^\circ$



(c) $\Psi_{b_1} = 60^\circ, \Psi_{b_2} = 0^\circ$

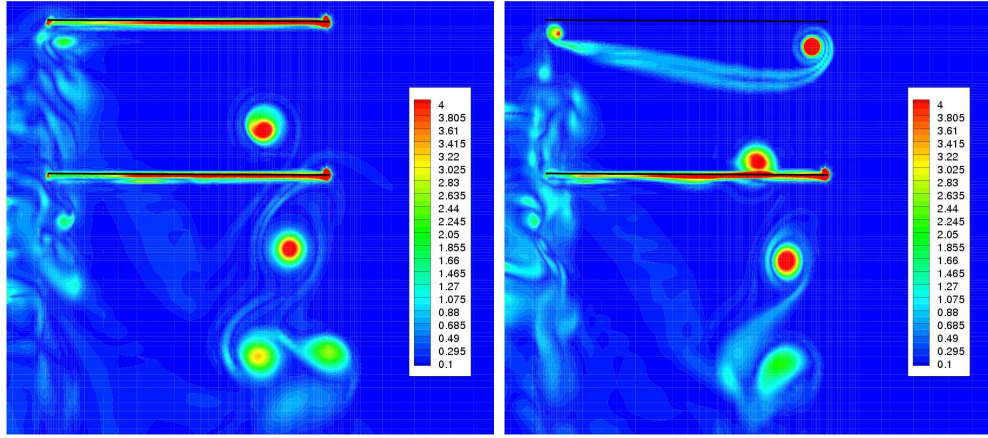
(d) $\Psi_{b_1} = 96^\circ, \Psi_{b_2} = 0^\circ$



(e) $\Psi_{b_1} = 120^\circ, \Psi_{b_2} = 0^\circ$

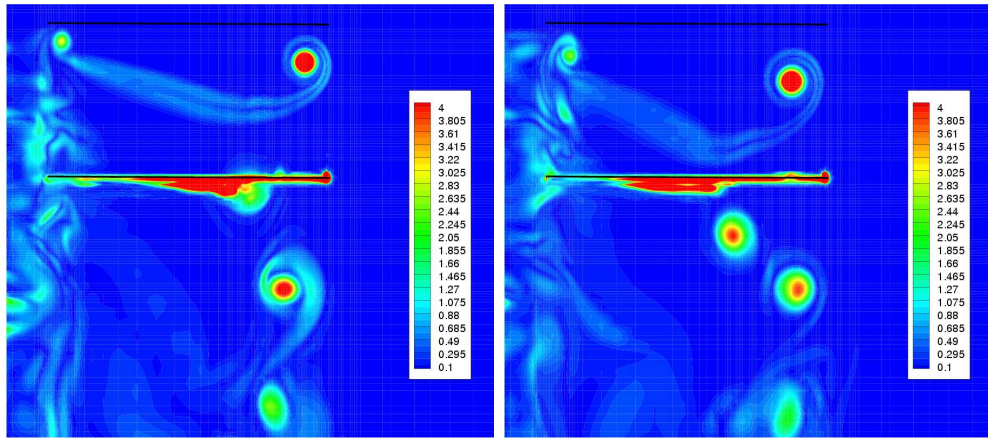
(f) $\Psi_{b_1} = 156^\circ, \Psi_{b_2} = 0^\circ$

Figure 6.16: Vorticity magnitude contours in the plane of the bottom rotor blade at different instances in time for micro-scale coaxial system, $h/R = 0.268$.



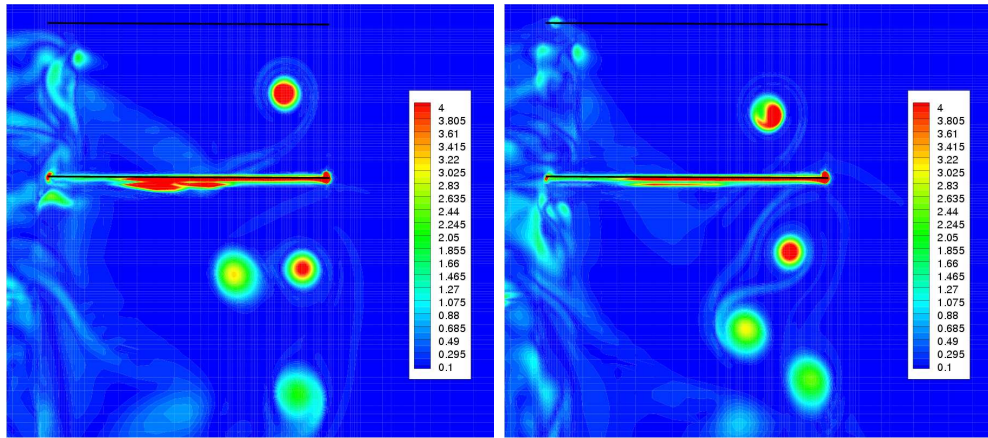
(a) $\Psi_{b_1} = 0^\circ, \Psi_{b_2} = 0^\circ$

(b) $\Psi_{b_1} = 36^\circ, \Psi_{b_2} = 0^\circ$



(c) $\Psi_{b_1} = 60^\circ, \Psi_{b_2} = 0^\circ$

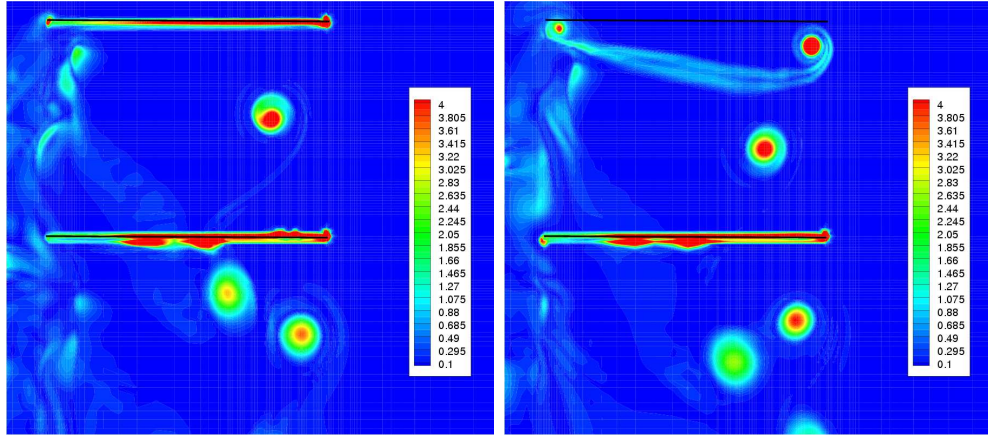
(d) $\Psi_{b_1} = 96^\circ, \Psi_{b_2} = 0^\circ$



(e) $\Psi_{b_1} = 120^\circ, \Psi_{b_2} = 0^\circ$

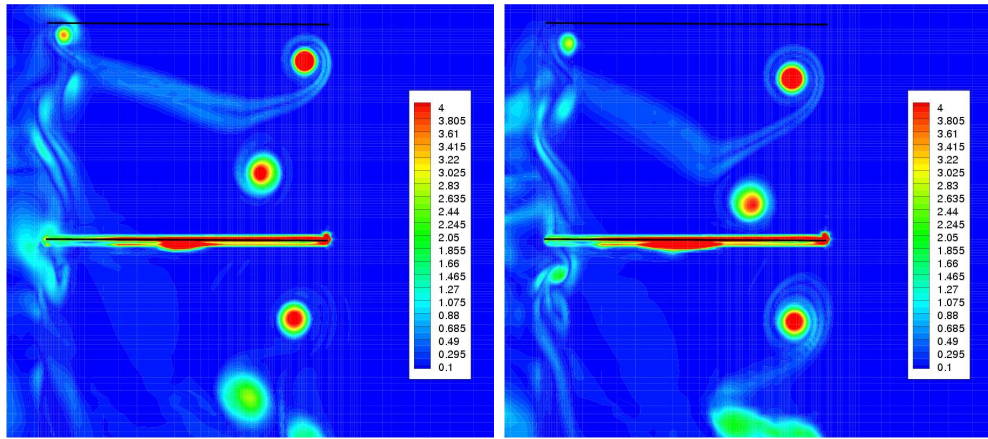
(f) $\Psi_{b_1} = 156^\circ, \Psi_{b_2} = 0^\circ$

Figure 6.17: Vorticity magnitude contours in the plane of the bottom rotor blade at different instances in time for micro-scale coaxial system, $h/R = 0.446$.



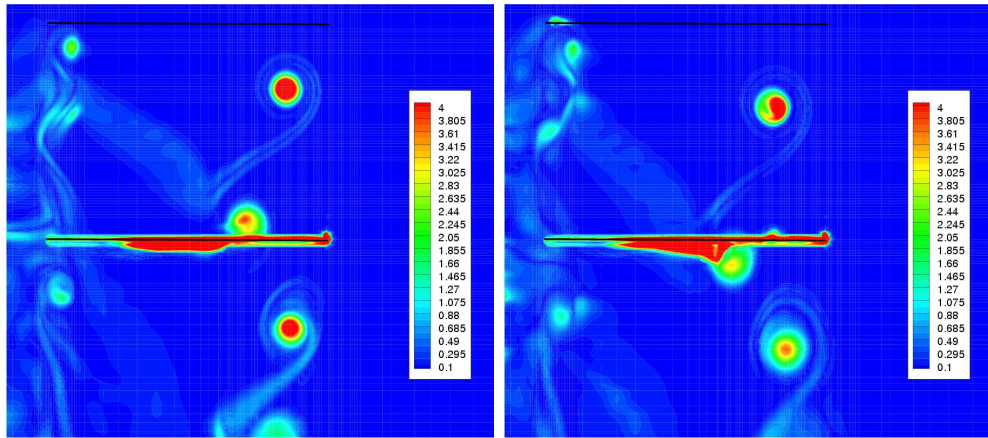
(a) $\Psi_{b_1} = 0^\circ, \Psi_{b_2} = 0^\circ$

(b) $\Psi_{b_1} = 36^\circ, \Psi_{b_2} = 0^\circ$



(c) $\Psi_{b_1} = 60^\circ, \Psi_{b_2} = 0^\circ$

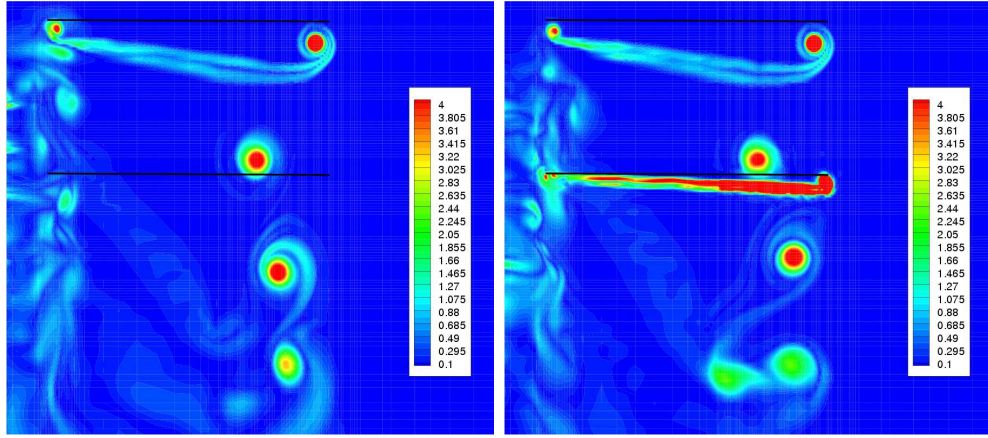
(d) $\Psi_{b_1} = 96^\circ, \Psi_{b_2} = 0^\circ$



(e) $\Psi_{b_1} = 120^\circ, \Psi_{b_2} = 0^\circ$

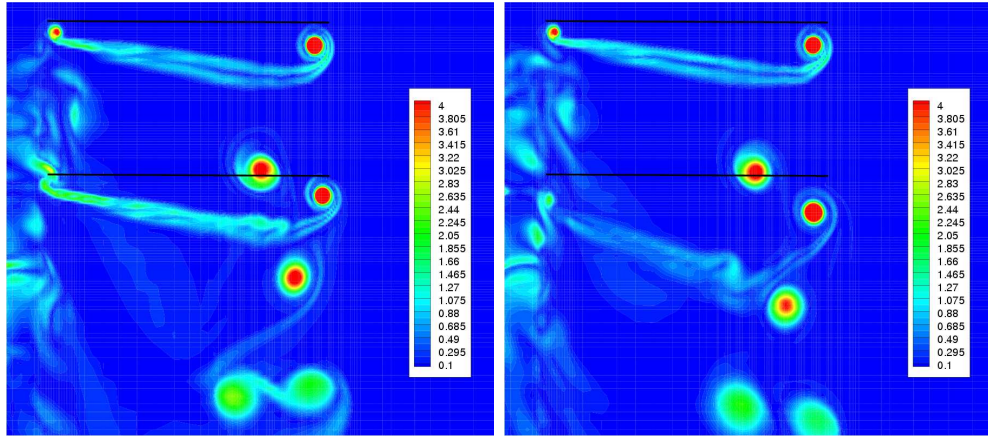
(f) $\Psi_{b_1} = 156^\circ, \Psi_{b_2} = 0^\circ$

Figure 6.18: Vorticity magnitude contours in the plane of the bottom rotor blade at different instances in time for micro-scale coaxial system, $h/R = 0.625$.



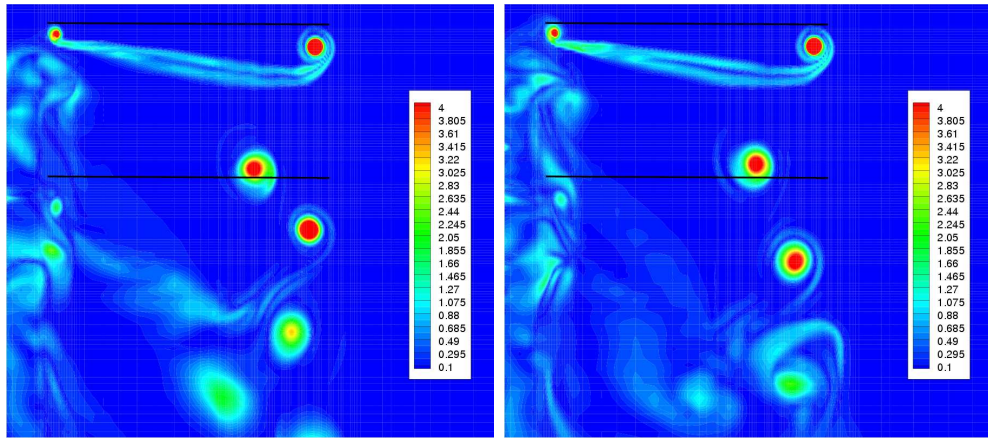
(a) $\Psi_{b_1} = 30^\circ, \Psi_{b_2} = 150^\circ$

(b) $\Psi_{b_1} = 30^\circ, \Psi_{b_2} = 6^\circ$



(c) $\Psi_{b_1} = 30^\circ, \Psi_{b_2} = 30^\circ$

(d) $\Psi_{b_1} = 30^\circ, \Psi_{b_2} = 66^\circ$



(e) $\Psi_{b_1} = 30^\circ, \Psi_{b_2} = 90^\circ$

(f) $\Psi_{b_1} = 30^\circ, \Psi_{b_2} = 126^\circ$

Figure 6.19: Vorticity magnitude contours in a plane that is at 30° azimuth from the top rotor blade at different instances in time for micro-scale coaxial system, $h/R = 0.446$.

Chapter 7

Conclusions

Micro air vehicles are an emerging technology that can provide an inexpensive and expendable platform to a wide array of military and civilian missions where larger vehicles are impractical to transport or operate. Rotary-wing MAVs are particularly attractive for indoor missions because of their hovering and tight-maneuvering capability. However, the capabilities of current rotary-wing MAVs fall way short of various mission requirements due to limitations arising from aerodynamic as well as non-aerodynamic issues. The work reported in this dissertation attempts to develop and validate a high resolution computational platform that can be used to address the various aerodynamic challenges associated with the current rotary-wing MAV configurations.

This final chapter summarizes the contributions made in this work, along with briefly discussing the main observations and conclusions drawn. Suggestions for future research are also provided.

7.1 Summary

The overall objective of this dissertation was to develop and validate a high resolution computational methodology to study performance and flow physics of conventional and a non-conventional (coaxial) micro-rotor configurations in hover. This required the modification of an existing compressible Reynolds-Averaged Navier Stokes (RANS) solver. The various improved methodologies were then systematically verified for simpler problems before being applied to rotor problems.

The solver was then applied to simulate a series of hovering rotors - micro-scale single rotors, full-scale coaxial rotors and micro-scale coaxial rotors. Full-scale coaxial rotor calculations were done as a part of the validation of methodologies developed for coaxial rotor simulation, before extending them to the micro-scale coaxial rotors. All these computations were performed on structured overset meshes, consisting of blade and background meshes.

Hovering micro-scale single rotor simulations were done using a blade mesh overset in a background mesh. Four different geometries comprising of two different leading and trailing edge profiles (blunt and sharp) for the blade section were studied. The computations were validated with experimentally measured performance data, wake trajectory and also with tip vortex profile data. Apart from validating the methodology, the details of flow physics were studied. Finally, a preliminary study of the effect of twist and taper on the micro-rotor blades was performed.

Next, the solver was applied to simulate the aerodynamics of full-scale coaxial rotor configurations in hover. Due to the large aspect ratio and the small vortex core size, a nested background mesh was found necessary to properly

transfer information from the blade mesh to the outer background mesh. A trim procedure was implemented to trim the coaxial system to a particular thrust value and to balance the torque. The computations were validated with experimentally measured mean thrust and power and the sources of unsteadiness were examined. To understand the details of the flow physics, the tip vortices from both the top and bottom rotor blades were preserved until two blade passages.

After gaining sufficient confidence in full-scale coaxial rotor computations, the solver was then extended to simulate the aerodynamics of micro-scale coaxial rotor configuration in hover. This was achieved by combining the methodologies developed for micro-scale single rotor calculations and those for full-scale coaxial rotor calculations. Again, a nested background mesh was found necessary to properly transfer information from the blade mesh to the outer background mesh. The computations were validated with experimentally measured mean thrust and power. Subsequently, the effect of rotor spacing was studied and the sources of unsteadiness along with the details of flow physics were investigated.

7.2 Observations

Specific observations and conclusions drawn from the CFD methodology and from the study of hovering rotors (micro-scale single rotor, full-scale coaxial rotor and micro-scale coaxial rotor) are detailed below.

7.2.1 CFD Methodology

The low Mach preconditioning parameter was controlled by varying the pseudo-time step. The value of pseudo-time step size in the order of actual time step

size was found to be optimum when considering both convergence and accuracy. The use of the low Mach preconditioning for the study of low speed evolution of 2D inviscid isentropic vortex, showed better convergence compared to the no-preconditioning case, especially at very low speeds and higher time step. Low Mach preconditioner increased accuracy near stagnation points, increased the convergence rate, and resulted in lift coefficients that scale with the Prandtl-Glauert compressible factor for the steady 2D flow over an airfoil. The comparisons of 3D finite-span wing results with experiment showed good capture of the axial velocity deficit, peak swirl velocity and core radius size.

The sliding mesh interpolation boundary condition allowed the use of periodicity in the flow-field and enabled the simulation of multi-bladed coaxial rotor system using just one blade from each rotor system. The use of third order slope limited M3-quartic interpolation instead of first order (linear) interpolation for the sliding mesh interface boundary, reduced the oscillation in the forces of the bottom rotor arising due to the interpolation error along with providing a better representation of the wake. However, the use of a spectral scheme for higher order interpolation resulted in numerous spurious oscillations.

Using the implicit hole-cutting method, the exchange of information always occurred at regions where cell sizes of the various meshes are comparable, whereas, this was not guaranteed using conventional hole-cutting technique. The use of improved blanking technique along with implicit hole-cutting method for steady 2D airfoil problem simulated using a two mesh overset system having optimally thin fringe layers resulted in less than 2% difference in lift, drag and moment coefficients from those obtained using single mesh simulations. However, the corresponding two mesh system simulation without the use of the improved

blanking technique resulted in a difference of greater than 20% in the moment coefficient and about 8–10% difference in the lift and drag coefficients from those obtained using single mesh simulations. The new blanking technique along with the implicit hole-cutting methodology provided improved performance predictions compared to those obtained using a traditional hole-cutting methodology, for full-scale single rotor simulation. The prediction accuracy improved from $\sim 20\%$ error in power at lower thrust levels to within 3% error.

7.2.2 Micro-Scale Single Rotor

The performance validation study on a micro-scale single rotor showed good comparison with the experimental data for all geometries (blunt leading and trailing edge, sharp leading edge and blunt trailing edge, sharp leading and trailing edge). At higher thrust levels, the power for the sharp leading edge geometries were under-predicted by about 4–5%, while the power for the blunt leading and trailing edge geometry was over-predicted by 1–2%. The following are the conclusions drawn on the performance of a micro-scale single rotor:

1. The performance of the sharp leading edge geometries are better compared to that of corresponding blunt leading edge geometries ($\sim 8–16\%$ increase in maximum figure of merit and $\sim 4\%$ increase in maximum power loading). The total thrust produced by the geometries with identical trailing edges are similar. However, the geometries having blunt leading edge require larger power ($\sim 12–18\%$ at higher thrust level). The large pressure drag created by the near stagnation pressure along the leading edge for the blunt leading edge geometries is the main reason for the increased power. A small contribution to the additional power for the blunt leading edge

geometry cases also comes from the presence of a significant leading edge separation bubble, which increased in chordwise extent towards the tip, eventually leading to complete separation near the tip.

2. Methods that use 2D airfoil characteristics, such Blade Element Momentum Theory (BEMT) and Free Vortex Methods (FVM) should be suitable for preliminary design. However, their accuracy should deteriorate if there is significant leading edge separation with the accompanying significant spanwise flow and transport of vorticity.
3. Sharpening the trailing edge improves the performance of the geometry with blunt leading edge, but not for the geometry with sharp leading edge. Blunt trailing edge geometries has lower thrust ($\sim 5 - 8\%$ at higher thrust levels) and power ($\sim 7 - 10\%$ at higher thrust levels) compared to the sharp trailing edge geometry with identical leading edge due to higher pressure on the upper surface of the airfoil.
4. Similar to full-scale rotors, use of twist and taper improves the performance of micro rotor using sharp leading and trailing edge geometry. The performance improvement due to twist ($\sim 10\%$ increase in maximum figure of merit and $\sim 11\%$ increase in maximum power loading) is mainly due to the reduction in induced power. Twist also increases the thrust level ($\sim 35\%$) at which maximum C_T/C_P is achieved. The improvement in tapered blade ($\sim 5\%$ increase in maximum figure of merit and $\sim 11\%$ increase in maximum power loading) occurs as a result of decrease in profile power. The combination of twist and taper provides further benefits over the untwisted rectangular planform ($\sim 14\%$ increase in maximum figure of

merit and $\sim 18\%$ increase in maximum power loading) over the untwisted rectangular planform.

In the validation of the flow-field of a micro-scale single rotor, the wake trajectory showed good comparison with the experimental data during the initial wake ages. However, the comparison was not good at a later wake age, because of the expansion of the experimental trajectory, possibly caused by the separation near the root due to the mounting apparatus. The computed wake contracts to about $0.75R$, which is similar to the wake contraction for a full-scale rotor. The effect of blade passage was seen as an increase in the vertical convection rate and a decrease in the radial contraction rate. Comparison of tip vortex profiles showed that the peak swirl velocity was predicted reasonably well at all wake ages, whereas the axial deficit along the vortex center and the vortex core radius were over-predicted at all wake ages (less than $\sim 25\%$ for axial deficit and $\sim 20\%$ for vortex core radius at 180° wake age). The discrepancy in the tip vortex profile was found to arise during the initial tip vortex formation. The inadequacy of the Spalart-Allmaras turbulence model in a non-isotropic environment could be the main reason for the disparity. Additionally, the separation may not be predicted accurately by the Spalart-Allmaras model. Sectional flow contours showed larger turbulence in separated regions and in the very near wake for all the geometries. In the separated regions, the radial velocity was also larger and was directed towards the tip of the blade. The contour plots showed shear layer instabilities in the wake, which are typical for low Reynolds number flows.

The following are the conclusions drawn on the flow-field of a micro-scale single rotor:

1. Tip vortex flow-field of micro-rotor is very complicated with the presence

of secondary vortices. Additional vortices are found near the trailing edge of the blade over most of the span, a feature which has been observed in experiments. The tip vortex formed on the micro-rotor blade interacts with secondary vortices early in its development along the chord. After the first passage of the tip vortex under the blade, the vortex experiences some destabilization as it is influenced by the strain field from both the blade and the inboard wake sheet. The instabilities in the wake after the blade passage show oscillations in the radial location of the wake.

2. The swirl component of azimuthally averaged velocities is twice as large as compared to a full-scale rotor operating at the same thrust level and could lead to significant power losses.

7.2.3 Full-Scale Coaxial Rotor

The performance validation study on a full-scale coaxial rotor showed that the overall performance was reasonably well predicted, with the thrust and power trimmed to less than 1% error. It was observed that the top rotor contributes to approximately 55% of the total thrust at all thrust levels. From the flow-visualization, the tip vortices from both the top and bottom rotors were clearly identifiable. The interaction of top rotor vortex with bottom rotor, along with that between tip vortices from the two rotors with each other and the inboard sheet, produce a highly complicated flow-field. Significant wandering of the tip vortex was observed due to interactions for both the top and the bottom rotor. Wake trajectory showed that the wake of the top rotor contracts at a faster rate compared to that of the bottom rotor because of the vortex-vortex interaction. The top rotor wake contracted to about $0.82R$ by the time it reaches the bottom

rotor. Additionally, the top rotor wake convected vertically down at a faster rate due to increased inflow. Following are the specific conclusions drawn on the full-scale coaxial system:

1. The bottom rotor shows significant degradation in performance due to the influence of the top rotor wake ($\sim 40\%$ increase in power at same thrust at higher thrust levels). Interestingly, even the top rotor shows slight degradation in performance ($\sim 15\%$ increase in power at same thrust at higher thrust levels), showing that the bottom rotor has some influence on the top rotor.
2. The flow-field of hovering coaxial rotor is unsteady with a dominant $2N/\text{rev}$ frequency (where N is the number of blades for each rotor). The unsteadiness in hovering coaxial system is explained in terms of blade thickness effect, loading effect and wake effect. Thickness of the blade surfaces results in an impulsive behavior when the blades of the top and bottom rotor are aligned. Additional impulsiveness is generated due to the blade loading. For the bottom rotor, the added influence of the top rotor wake makes the features more spread out and distinct. The interactions result in fluctuations ($5 - 10\%$) in the integrated quantities. Such a fluctuation could be significant for vibration and acoustic characteristics. Increasing the rotor spacing decreases the fluctuation in performance data.

7.2.4 Micro-Scale Coaxial Rotor

The overall performance of a micro-scale coaxial system was well predicted for a range of RPMs. Top rotor thrust was under-predicted by less than $\sim 2\%$ at all speeds, whereas the bottom rotor thrust was over-predicted by less than

$\sim 8\%$. The total power was well predicted. In the experiment, torque was balanced by changing the bottom rotor RPM, while keeping the top rotor RPM fixed. Assuming identical rotational speed for the top and bottom rotors in computation introduced only an error within 5% in the torque balance. As the rotor spacing increases, the top and bottom rotor thrusts showed opposite trends. While the top rotor thrust increased with the rotor spacing, the bottom rotor thrust decreased as the rotor separation increases. Both the rotor thrusts approached a constant value at very large rotor spacing. The total thrust of the system was seen to remain fairly constant with the rotor spacing, which was seen even in the experimental results. Top rotor contributed to about 55% of the total thrust at smaller rotor spacing and increased to about 58% at the largest rotor separation, which was similar to what was seen for full-scale coaxial rotor. Similar to full-scale system, the computed performance data showed that the flow-field is unsteady with a dominant $2N/\text{rev}$ frequency (where N is the number of blades for each rotor). The interactions resulted in a fluctuation of 3–8% in the integrated quantities. Similar to full-scale coaxial rotors, significant wandering of the tip vortex was observed for both the top and the bottom rotors. Following are the specific conclusions drawn on a micro-scale coaxial system:

1. Unsteadiness in micro-scale coaxial rotor is mainly caused due to blade loading and wake effect. The venturi effect due to thickness of the blade (seen in full-scale coaxial rotors) was negligible because of the thin airfoil used. Additional high frequency unsteadiness is also seen due to shedding near the trailing edge, which was also seen for micro-scale single rotor.
2. As the rotor spacing increases, the unsteadiness in the top rotor decreases, however the unsteadiness in the bottom rotor does not follow any particular

trend. For the micro-scale coaxial system, the wake effect is comparable or even predominant over the loading effect when the rotor spacing is large. This is in contrary to the full-scale systems, where the loading effect was more predominant over the wake effect and therefore, increase in rotor spacing almost always results in a decrease in unsteadiness of the forces on bottom rotor.

3. In micro-scale coaxial system, the phasing of the impingement of the top rotor vortex upon the bottom rotor plays a significant role in the amount of unsteadiness for the micro-scale coaxial systems. To have least unsteadiness on the bottom rotor, the vortex impingement should occur farthest away from the location at which the loading effect peaks. The phasing can be controlled by adjusting the rotor-spacing.
4. Interaction of top rotor vortex and inboard sheet with the bottom rotor results in unsteady shedding both in the outboard and inboard portions of the blade; a phenomenon not seen for the full-scale coaxial rotor. In the outboard portion of the blade, a highly three-dimensional shedding occurs on the upper surface of the blade, whereas the shedding at the inboard portion of the blade occurs on the lower surface and it is more two-dimensional in nature. Sharp leading edge geometry on the bottom rotor is believed to be the main reason for such a drastic separation and slight amount of roundness at the leading edge could possibly alleviate this issue.

7.3 Recommendations

The verification of the techniques used to improve the state-of-the-art in the CFD modeling of micro-rotors, along with their validation with available experimental data, gives confidence in the ability of using the resulting methodology to be part of a tool that could aid in developing MAVs, which meet the targets set by DARPA.

Specifically, regarding CFD methodology, the following recommendations are made:

1. Time accurate low Mach preconditioning should be used for micro-rotors with pseudo-time step size in the order of actual time step size.
2. The improved blanking technique with proper treatment of fringe points should be used for all overset calculations.
3. The Spalart-Allmaras turbulence model appears to be sufficient for simulating micro-rotors. However, the current methodology can further be improved by implementing a transition model to provide better quantitative prediction of the separation pattern for micro-rotors.

Furthermore, based on the physical insights gained by examining the various simulations, the following recommendations are made:

1. Blunting leading edge geometries should be avoided due to the increase in pressure drag.
2. The limitations in the aerodynamic efficiency of micro-rotors is still possibly because of the large profile power. Further efforts should be made to design airfoils that have low profile drag at low Reynolds numbers.

3. Similar to full-scale rotors, twist and taper should be used to improve performance of micro-rotors.
4. Optimal rotor spacing for a micro-scale coaxial system can be used to reduce fluctuations on the bottom rotor.
5. Some degree of leading edge roundness might be desirable to avoid separation on coaxial rotors due to the blade-vortex interactions on the bottom rotor.
6. CFD should be used to investigate the feasibility for optimizing the bottom rotor geometry in coaxial micro-rotors.

7.4 Future Work

Some of the suggested future work are:

1. More validation of simple design tools like Blade Element Momentum Theory and Free Vortex Method for micro-rotors need to be done using the results obtained from the CFD methodology developed in this work.
2. Assuming periodicity in coaxial rotor simulation serves as a first approximation, which reduce the simulation time significantly. However, this assumption restricts the aperiodicity that can develop between different blades of a rotor system. Therefore, simulation using all the blades of each rotor system must be performed to check the validity of the current approximation.
3. Additional experiments need to be performed for further validation of coaxial rotors, especially, the measurement of unsteady thrust and power. In

addition, wake measurements for the coaxial rotors needs to be performed.

4. To understand the aerodynamics of coaxial rotors in non-hovering flight conditions, CFD methodology need to be extended for axial and forward flights; corresponding experiments need to be performed for the continued validation.
5. To develop a comprehensive computational platform that can be used for building MAVs, the methodology developed in this work needs to be extended to other non-conventional micro-rotors such as ducted rotors, flapping rotors etc.

Bibliography

- [1] Leishman, J. G., "Principles of Helicopter Aerodynamics," Cambridge University Press, 2002.
- [2] Bohorquez, F., "Rotor Hover Performance and System Design of an Efficient Coaxial Rotary Wing Micro Air Vehicle," Ph.D. Dissertation, Department of Aerospace Engineering. University of Maryland. College Park, MD. 2007.
- [3] Schmitz, F. W., "Aerodynamics of Model Aircraft Wing Measurements. Part I. Airfoil Measurements," NASA-TM-X-60976, November 1967.
- [4] Althaus, D., "ProfilePolaren Fur den Modellflug," Institut Fur Aerodynamik u. Gasdynamik der Universitat Stuttgart Neckar-Verlag, Postfach 1820, 7730 Villingen-Schwenningen, Germany, 1980.
- [5] Carmichael, B. H., "Low Reynolds Number Airfoil Survey, Volume 1," NASA-CR-165803-VOL-1, November 1981.
- [6] Mueller, T. J., "Aerodynamic Measurements at Low Reynolds Numbers for Fixed Wing Micro-Air Vehicles," Presented at the RTO AVT/VKI Special Course on Development and Operation of UAVs for Military and Civil Applications, VKI, Belgium, September 1999.

- [7] Mueller, T. J., and Batill, S. M., “Experimental Studies of Separation on a Two-Dimensional Airfoil at Low Reynolds Numbers,” *AIAA Journal*, Vol. 20, No. 4, April 1982, pp. 456–463.
- [8] Mueller, T. J., “The Influence of Laminar Separation and Transition on Low Reynolds Number Airfoil Hysteresis,” *AIAA Journal of Aircraft*, Vol. 22, No. 9, September 1985, pp. 763–770.
- [9] Selig M. S., Donovan J. F., and Fraser D. B., “Airfoils at Low Speeds,” Soar Tech Publications, 1989.
- [10] Selig M. S., Donovan J.F., and Fraser D. B., “Summary of Low Speed Airfoil Data, Volumes 1, 2, 3 and 4,” Soar Tech Publications, 1989–2004.
- [11] Selig M. S., and Maughmer, M. D., “A Multi-Point Inverse Airfoil Design Method Based on Conformal Mapping,” *AIAA Journal*, Vol. 30, No. 5, May 1992, pp. 1162–1170.
- [12] Selig M. S., and Maughmer, M. D. “Generalized Multipoint Inverse Airfoil Design,” *AIAA Journal*, Vol. 30, No. 11, November 1992, pp. 2618–2625.
- [13] Laitone, E. V., “Wind Tunnel Tests of Wings at Reynolds Numbers Below 70000,” *Experiments in Fluids*, Vol. 23, No. 5, November 1997, pp. 405–409.
- [14] Laitone, E. V., “Aerodynamic Lift at Reynolds Numbers Below 7×10^4 ,” *AIAA Journal*, Vol. 34, No. 9, September 1996, pp. 1941–1942.
- [15] Hein, B. R., and Chopra, I., “Hover Performance of a Micro Air Vehicle: Rotors at Low Reynolds Number,” Proceedings of the American Helicopter

Society International Specialists' Meeting on Unmanned Rotorcraft, Chandler, AZ, January 2005.

- [16] Singh, A. P., "A Computational Study on Airfoils at Low Reynolds Numbers," Proceedings of the ASME Fluids Engineering Division, Boston, MA, June 2000.
- [17] Drela, M., "XFOIL: An Analysis and Design System for Low Reynolds Number Airfoils," Conference on Low Reynolds Number Airfoil Aerodynamics, University of Notre Dame, IN, June 1989.
- [18] Kellogg, M. I., and Bowman, W. J., "Parametric Design Study of the Thickness of Airfoils at Reynolds Numbers from 60,000-150,000," 42nd AIAA Aerospace Sciences Meeting and Exhibit, AIAA paper-2004-1054, Reno, Nevada, January 2004.
- [19] Schroeder, E., and Baeder, J. D., "Using Computational Fluid Dynamics for Micro-Air Vehicle Airfoil Validation and Prediction," 23rd AIAA Applied Aerodynamics Conference, AIAA paper 2005-4841, Toronto, Canada, June 2005.
- [20] Schroeder, E., "Low Reynolds Number Flow Validation using Computational Fluid Dynamics with Applications to Micro Air Vehicles," Master's Thesis, Department of Aerospace Engineering, University of Maryland at College Park, 2005.
- [21] Srinivasan, G. R., and Baeder, J. D., "TURNS: A Free-wake Euler/ Navier-Stokes Numerical Method for Helicopter Rotors," *AIAA Journal*, Vol. 31, No. 5, May 1993.

- [22] Gupta, V., "An Investigation of Quad Tilt Rotor Aerodynamics in Helicopter mode," Ph.D. Dissertation, Department of Aerospace Engineering, University of Maryland at College Park, 2005.
- [23] Caradonna, F. X., and Tung, C., "Experimental and Analytical Studies of a Model Helicopter Rotor in Hover," NASA-TM-81232, September 1981.
- [24] Tangler, J. L., "Experimental Investigation of the Sub-wing Tip and its Vortex Structure" NASA-CR-3058, November 1978.
- [25] Thompson T. L., Komerath N. M., and Gray R. B., "Visualization and Measurement of the Tip Vortex Core of a Rotor Blade in Hover," *AIAA Journal of Aircraft*, Vol. 25, No. 12, December 1988, pp. 1113–1121.
- [26] Martin, P. B., Pugilese, G. J., and Leishman, J. G., "High Resolution Trailing Vortex Measurements in the Wake of a Hovering Rotor," *Journal of the American Helicopter Society*, Vol. 48, No. 1, January 2003, pp. 39–52.
- [27] Ramasamy, M., and Leishman, J. G., "A Generalized Model for Transitional Rotor Blade Tip Vortices," *Journal of the American Helicopter Society*, Vol. 51, No. 1, January 2006, pp. 92–103.
- [28] McAlister, K. W., "Rotor Wake Development during the First Revolution," *Journal of the American Helicopter Society*, Vol. 49, No. 4, October 2004, pp. 371–390.
- [29] Ramasamy, M., Leishman, J.G., and Timothy E. Lee., "Flow Field of a Rotating Wing MAV," Proceedings of the 62nd Annual Forum of the American Helicopter Society, Phoenix, AZ, May 2006.

- [30] Ramasamy, M., Johnson, B., and Leishman, J. G., “Toward Understanding the Aerodynamic Efficiency of a Hovering Micro-Rotor,” Proceedings of the American Helicopter Society International Specialists’ Meeting on Unmanned Rotorcraft, Chandler, AZ, January 2007.
- [31] Russell, J. W., Sankar, L. N., Tung, C., and Patterson, M. T., “Alterations of Tip Vortex Structure from a Hovering Rotor using Passive Tip Devices,” Proceedings of the 53rd Annual Forum of the American Helicopter Society, Virginia Beach, VA, May 1997.
- [32] Russell, J. W., Sankar, L. N., and Tung, C., “High Accuracy Studies of the Tip Vortex Structure from a Hovering Rotor,” 28th AIAA Fluid Dynamics Conference, AIAA Paper 1997-1845, Snowmass Village, CO, July 1997.
- [33] McAlister, K. W., Schuler, C. A., Branum, L., and Wu, J.C., “The 3-D Wake Measurements Near a Hovering Rotor for Determining Profile and Induced Drag,” NASA-TP-3577, August 1995.
- [34] Usta, E., “Application of a Symmetric Total Variation Diminishing Scheme To Aerodynamics of Rotors,” Ph.D. Dissertation, Department of Aerospace Engineering, Georgia Institute of Technology, 2002.
- [35] Yee, H. C., Sandham, N. D., and Djomehri, M. J., “Low-dissipative High-order Shock-capturing Methods Using Characteristic-based Filters,” *Journal of Computational Physics*, Vol. 150, No. 1, 1999, pp. 199–238.
- [36] Tang, L., “Improved Euler Simulation of Helicopter Vortical Flows,” Ph.D. Dissertation, Department of Aerospace Engineering, University of Maryland at College Park, 1998.

- [37] Duraisamy, K., “Studies in Tip Vortex Formation, Evolution and Control,” Ph.D. Dissertation, Department of Aerospace Engineering, University of Maryland at College Park, 2005.
- [38] Duraisamy, K., and Baeder, J., “High Resolution Wake Capturing Methodology for Hovering Rotors,” *Journal of the American Helicopter Society*, Vol. 52, No. 2, April 2007, pp. 110–122.
- [39] Duraisamy, K., Ramasamy, M., Baeder, J., and Leishman, G., “High Resolution Computational and Experimental Study of Hovering Rotor Tip Vortex Formation,” *AIAA Journal*, Vol. 45, No. 11, November 2007, pp. 2593–2602.
- [40] Precision Heli R/C Helicopters. <http://www.precisionheli.com/>, 2007.
- [41] Sirohi, J., Tishchenko, M., and Chopra I., “Design and Testing of a Micro-Aerial Vehicle with a Single Rotor and Turning Vanes,” Proceedings of the 61st Annual Forum of the American Helicopter Society, Grapevine, TX, June 2005.
- [42] Hrishikeshavan, V., Sirohi, J., Tishchenko, M., and Chopra, I., “Design and Stability of a Shrouded Rotor Micro Air Vehicle with Anti-torque Vanes,” Proceedings of the American Helicopter Society International Specialists’ Meeting on Unmanned Rotorcraft, Chandler, Arizona, January 2007.
- [43] Lipera, L., Colbourne, J. D., Tischler, M. B., Mansur, M. H., Rotkowitz, M. C., and Patangu, P., “The Micro Craft iSTAR Micro Air Vehicle: Control System Design and Testing,” Proceedings of the 57th Annual Forum of the American Helicopter Society, Washington, D.C., May 2001.

- [44] Seiko Epson Corporation. “Epson Develops World’s Smallest Flying Robot,” http://www.epson.co.jp/e/newsroom/news_2003_11_18_2.htm. November 17, 2003.
- [45] Boulet, J., “The History of the Helicopter as Told by its Pioneers 1907-1956,” Editions France-Empire, Paris, 1984.
- [46] Liberatore, E. K., “Helicopters Before Helicopters,” Krieger Publishing, Malabar, FL, 1998.
- [47] Russian Military. <http://www.military.cz/russia/air/helicopters/Ka-50/>
- [48] Coleman, C. P., “A Survey of Theoretical and Experimental Coaxial Rotor Aerodynamic Research,” Proceedings of the 19th European Rotorcraft Forum, Cernobbio, Italy, September 1993. Also published as NASA-TP-3675, March 1997.
- [49] Harrington, R. D., “Full-Scale-Tunnel Investigation of the Static-Thrust Performance of a Coaxial Helicopter Rotor,” NACA-TN-2318, March 1951.
- [50] Dingledein, R. C., “Wind-Tunnel Studies of the Performance of Multirotor Configurations,” NACA-TN-3236, August 1954.
- [51] Nagashima, T., and Nakanishi, K., “Optimum Performance and Wake Geometry of Coaxial Rotor in Hover,” Proceedings of the 7th European Rotorcraft and Powered Lift Forum, Paper No. 41, September 1981.
- [52] McAlister, K. W., Tung, C., Rand, O., Khromov, V., and Wilson, J.S., “Experimental and Numerical Study of a Model Coaxial Rotor,” Proceedings of the 62nd Annual Forum of the American Helicopter Society, Phoenix, AZ, May 2006.

- [53] Leishman, J. G., and Ananthan, S., “Aerodynamic Optimization of a Coaxial Proprotor,” Proceedings of the 62nd Annual Forum of the American Helicopter Society, Phoenix, AZ, May 2006.
- [54] Griffiths, D. A., and Leishman, J. G., “A Study of Dual-Rotor Interference and Ground Effect Using a Free-Vortex Wake Model,” Proceedings of the 58th Annual Forum of the American Helicopter Society, Montreal, Canada, June 2002.
- [55] Syal, M., “Contributions to the Aerodynamic Optimization of a Coaxial Rotor system,” Master’s Thesis, Department of Aerospace Engineering, University of Maryland at College Park, 2008.
- [56] Kim, H. W., and Brown, R. E., “Coaxial Rotor Performance and Wake Dynamics in Steady and Manoeuvring flight,” Proceedings of the 62nd Annual Forum of the American Helicopter Society, Phoenix, AZ, May 2006.
- [57] Lim, J. W., McAlister, K. W., and Johnson, W., “Performance Correlation for Full-Scale and Model-Scale Coaxial Rotors,” Proceedings of the 63rd Annual Forum of the American Helicopter Society, Virginia Beach, VA, May 2007.
- [58] Ruzicka, G. C., and Strawn, R. C., “Computational Fluid Dynamics Analysis of a Coaxial Rotor Using Overset Grids,” Proceedings of the American Helicopter Society International Specialists’ Meeting on Aeromechanics, San Francisco, CA, January 2008.

- [59] Barth, T. J., Puliam, T. H., and Buning P. G., “Navier-Stokes Computations for Exotic Airfoils,” 23rd AIAA Aerospace Sciences Meeting, AIAA Paper 1985-0109, Reno, NV, January 1985.
- [60] White, F. M., “Viscous Fluid Flow,” McGraw-Hill, 1991.
- [61] Van Leer, B., “Towards the Ultimate Conservative Difference Scheme V. A Second-Order Sequel To Godunov’s Method,” *Journal of Computational Physics*, Vol. 135, No. 2, August 1997, pp. 229–248.
- [62] Koren, B., “Upwind Schemes, Multigrid and Defect Correction for the Steady Navier-Stokes Equations,” Proceedings of the 11th International Conference on Numerical Methods in Fluid Dynamics, Williamsburg, VA, June 1988.
- [63] Roe, P., “Approximate Riemann Solvers, Parameter Vectors and Difference Schemes,” *Journal of Computational Physics*, Vol. 135, No. 2, August 1997, pp. 250–258.
- [64] Hoffman, K. A., and Chiang, S. T., “Computational Fluid Dynamics, Vol. 2,” EES Books, 2000.
- [65] Jameson, A., and Yoon, S., “Lower-Upper Implicit Schemes with Multiple Grids for Euler Equations,” *AIAA Journal*, Vol. 25, No. 7, July 1987, pp. 929-935.
- [66] Yoon, S., and Jameson, A., “Lower-Upper Symmetric-Gauss-Seidel Method for the Euler and Navier-stokes Equations,” *AIAA Journal*, Vol. 26, No. 9, September 1988, pp. 1025–1026.

- [67] Pulliam, T., “Time Accuracy and the use of Implicit Methods,” 11th AIAA Computational Fluid Dynamics Conference, AIAA Paper 1993-3360, Orlando, FL, July 1993.
- [68] Baldwin, B., and Lomax, H., “Thin Layer approximation and Algebraic Model for Separated Flows,” 16th AIAA Aerospace Sciences Meeting, AIAA paper 1978-257, Huntsville, AL, January 1978.
- [69] Durbin, P., “A Reynolds Stress Model for Near Wall Turbulence,” *Journal of Fluid Mechanics*, Vol. 249, 1993, pp. 465-498.
- [70] Srinivasan, G.R., Ekaterinaris J. A., and McCroskey, W. J., “Evaluation of Turbulence Models for Unsteady Flows of an Oscillating Airfoil,” *Computers and Fluids*, Vol. 24, No. 7, 1995, pp. 833–861.
- [71] Spalart, P.R., and Allmaras, S.R., “A One-equation Turbulence Model for Aerodynamic Flows,” 30th AIAA Aerospace Sciences Meeting and Exhibit, AIAA Paper 1992-0439, Reno, NV, January 1992.
- [72] Hirsch, C., “Numerical Computation of Internal and External Flows, Volume 2,” Wiley Publishers, 1990.
- [73] Turkel, E., “Preconditioning Techniques in Computational Fluid Dynamics,” *Annual Review of Fluid Mechanics*, Vol. 31, January 1999, pp. 385-416.
- [74] Turkel, E., “Preconditioning Techniques for Solving the Incompressible and Low Speed Compressible Equations,” *Journal of Computational Physics*, Vol. 72, No. 2, October 1987, pp. 277-298.

- [75] Turkel, E., Radespiel, R., and Kroll, N., “Assessment of Preconditioning Methods for Multidimensional Aerodynamics,” *Computers and Fluids*, Vol. 26, No. 6, 1997, pp. 613–635.
- [76] Buelow P. E. O., Schwer D. A., Feng J., and Merkle C. L., “A Preconditioned Dual-Time, Diagonalized ADI scheme for Unsteady Computations,” 13th AIAA Computational Fluid Dynamics Conference, AIAA paper 1997-2101, Snowmass Village, CO, July 1997.
- [77] Pandya, S. A., Venkateswaran, S., and Pulliam, T. H., “Implementation of Preconditioned Dual-Time Procedures in OVERFLOW,” 41st AIAA Aerospace Sciences Meeting and Exhibit, AIAA paper 2003-0072, Reno, NV, January 2003.
- [78] Pulliam, T., and Chaussee, D., “A Diagonal Form of an Implicit Approximate Factorization Algorithm,” *Journal of Computational Physics*, Vol. 39, No. 2, February 1981, pp. 347–363.
- [79] Warming, R., and Beam, R., “On the Construction and Application of Implicit Factored Schemes for Conservation Laws,” *SIAM-AMS Proceedings*, Vol. 11, 1978, pp. 85–129.
- [80] Atwood, C. A., and Smith, M. H., “Nonlinear Fluid Computations in a Distributed Environment,” 33rd AIAA Aerospace Sciences Meeting and Exhibit, AIAA paper 1995-0224, Reno, NV, January 1995.
- [81] Brown, D., Chesshire, G., Henshaw, W., and Quinlan, D., “Overture: An Object-Oriented Software System for Solving Partial Differential Equations

- in Serial and Parallel Environments,” 8th SIAM Conference on Parallel Processing for Scientific Computing, Minneapolis, MN, March 1997.
- [82] Ryan, J. S., and Weeratunga, S., “Parallel Computation of 3D Navier-Stokes Flowfields for Supersonic Vehicles,” 31st Aerospace Sciences Meeting and Exhibit, AIAA Paper 1993-0064, Reno, NV, January 1993.
- [83] Wissink, A. M., and Meakin, R. L., “On Parallel Implementations of Dynamic Overset Grid Methods,” Proceedings of the 1997 ACM/IEEE Conference on Supercomputing, San Jose, CA, November 1997.
- [84] Lee, Y., “On Overset Grids Connectivity and Automated Vortex Tracking in Rotorcraft CFD,” Ph.D. Dissertation, Department of Aerospace Engineering, University of Maryland at College Park, 2008.
- [85] Buning, P. G., Jespersen, D. C., Pulliam, T. H., Chan, W. M., Slotnick, J. P., Krist, S. E., and Renze, K. J., “OVERFLOW User’s Manual, Version 1.8g,” NASA Langley Research Center, March 1999.
- [86] Zuhail, L. R., “Formation and Near-Field Dynamics of a Wing Tip Vortex,” Ph.D. Dissertation, California Institute of Technology, 2001.
- [87] Batchelor, G. K., “Axial Flow in Trailing Line Vortices,” *Journal of Fluid Mechanics*, Vol. 20, No. 4, 1964, pp. 645-658.
- [88] Heyes, A. L., Jones, R. F., and Smith, D. A. R., “Wandering of Wing-tip Vortices,” Proceedings of 12th International Symposium on Application of Laser Techniques to Fluid Mechanics, Lisbon, Portugal, July 2004.

- [89] Leishman, J. G., and Syal, M., “Figure of Merit Definition for Coaxial Rotors,” *Journal of the American Helicopter Society*, Vol. 53, No. 3, July 2008, pp. 290–300.
- [90] Jeong, J. and Hussain, F., “On the Identification of a Vortex,” *Journal of Fluid Mechanics*, Vol. 285, 1995, pp. 69–94.
- [91] Huynh, H. T., “Accurate Monotone Cubic Interpolation,” *SIAM Journal of Numerical Analysis*, Vol. 30, No. 1, February 1993, pp. 57–100.
- [92] Ananthan, S., “Analysis of Rotor Wake Aerodynamics during Maneuvering Flight using a Free-Vortex Wake Methodology,” Ph.D. Dissertation, Department of Aerospace Engineering, University of Maryland at College Park, 2006.